Title
Investigations of Low-Mass Star Formation: Simulations and Simulated Observations

Author
Offner, Stella S. R.

Publication Date
2009

Peer reviewed|Thesis/dissertation

Investigations of Low-Mass Star Formation: Simulations and Simulated Observations

by

Stella Susannah Reber Offner

B.A. (Wellesley College) 2003
M.A. (University of California, Berkeley) 2005

A dissertation submitted in partial satisfaction of the
requirements for the degree of
Doctor of Philosophy

in

Physics

in the

GRADUATE DIVISION
of the
UNIVERSITY OF CALIFORNIA, BERKELEY

Committee in charge:
Christopher McKee, Co-Chair
Richard Klein, Co-Chair
Jon Arons
James Graham

Fall 2009

Investigations of Low-Mass Star Formation: Simulations and Simulated Observations

Abstract

Investigations of Low-Mass Star Formation: Simulations and Simulated Observations

by

Stella Susannah Reber Offner
Doctor of Philosophy in Physics

University of California, Berkeley

Christopher McKee, Co-Chair

Richard Klein, Co-Chair

I investigate the role of gravitation, turbulence, and radiation in forming low-mass stars. Molecular clouds are observed to be turbulent, but the origin of this turbulence is not well understood. Using a gravito-hydrodynamics adaptive mesh refinement (AMR) code, I study the properties of cores and protostars in simulations in which the turbulence is driven to maintain virial balance and where it is allowed to decay. I demonstrate that cores forming in a decaying turbulence environment produce high-multiplicity protostellar systems with Toomre-Q unstable disks that exhibit characteristics of competitive accretion. In contrast, cores forming in a virialized cloud produce smaller protostellar systems with fewer low-mass members.

Observations of molecular clouds are limited by projection, resolution, and the coupling between density and velocity information that is inherent in the molecular tracers commonly used to map molecular clouds. To compare with observations of core kinematics and shapes, I post-processs the simulations to obtain dust emission maps and molecular line information. I demonstrate that some simulated observations are significantly different in the driven and decaying turbulence simulations, making them potential diagnostics for characterizing turbulence in observed star-forming clouds.

Although forming stars emit a substantial amount of radiation into their natal environment, the effects of radiative feedback on the star formation process have not been well studied. I perform simulations of protostars forming in a turbulent molecular cloud including grey flux-limited diffusion radiative transfer. I compare the distributions of stellar masses, accretion rates, and temperatures in simulations with and without radiative transfer, and I demonstrate that radiative feedback has a profound effect on accretion, multiplicity, and mass by reducing the number of stars formed and the total rate at which gas turns into stars. I also show that protostellar radiation is the dominant source of energy in the simulation, exceeding viscous dissipation and compressional heating by at least an order of magnitude. Although heating from protostars is mainly confined within the core envelope, I find that it is sufficient to suppress disk fragmentation that would otherwise result in very low-mass companions or brown dwarfs. I compare the simulation results with recent observations of local low-mass star forming regions and discuss the "luminosity problem." For future radiative transfer studies of star formation, I add multigroup radiative diffusion capability to the ORION AMR code.

Christopher McKee
Dissertation Committee Co-Chair

Richard Klein
Dissertation Committee Co-Chair

To my parents

Contents

List of Figures

List of Tables

Acknowledgments

This thesis has been improved and produced through invigorating collaboration with Christopher McKee, Richard Klein, Mark Krumholz, and Alek Shestakov. I would like to thank my advisors and committee members for helpful comments during the revision process. Papers contributing to this manuscript also benefited from helpful discussions with numerous astrophysicists including but not limited to Robert Fisher, Robert Crockett, Pak Shing Li, Andrew Cunningham, and Kaitlin Kratter. Suggestions from anonymous referees have also significantly improved the contributing papers.

Funding for my work was provided by AX division at the Lawrence Livermore National Laboratory under the auspices of the UC Department of Energy and the National Science Foundation. Computing time was provided by the San Diego Supercomputing Center and the National Energy Research Scientific Computer Center.

I would like to recognize all those people who made the graduate process more cheerful, amusing, and fun. This includes my office family of Eric, Holly, Linda, and Pancho, who were there to provide a sympathetic ear and on-the-spot scientific help. I would like to thank my generous housemates Shareena, Kevin, and Jen for providing a quiet and homey sanctuary. I am also indebted to Atticus and Isabeau for cuddling and inadvertent hilarity. Finally, I would like to thank my parents, Vera and John, who encouraged me throughout my academic journey and were there for me every step of the way. Their guidance as role models, financial assistance, and support as patient confidants were essential for reaching this point.

Chapter 1

Overview: Role of Gravity, Turbulence, and Radiative Transfer in the Formation of Low-Mass Stars

Formulating a complete theory of star formation is essential to understanding the origins of the solar system and its galactic neighborhood. Developing such a theory remains one of the most challenging and most important goals of astrophysics.

Fundamental physical processes such as gravity, turbulence, radiation, and magnetic fields act over a staggering range of scales to assemble stars from molecular gas that is initially only a few 10^2 particles per cm^{-3}. These molecular regions are quite dense by cosmic standards, and they are optically thick to dissociating UV radiation, a requirement to maintain a cool 10 K temperature. In the galaxy, molecular clouds sizes range from a few pc to 100 pc with observed masses of up to a few 10^6 $M_\odot$ (Williams & McKee 1997). The molecular cloud environment is regulated by a combination of supersonic turbulence and gravity (Mac Low & Klessen 2004; McKee & Ostriker 2007). Due to near equilibrium between turbulence and gravity, star formation is characteristically slow, such that only a few percent of cloud material undergoes gravitational instability and collapses to form stars over a dynamical time

(Wu et al. 2005; Krumholz & Tan 2007).

Star formation is typically divided into two regimes. Low-mass star formation encompasses masses $M_* \leq 8\mathrm{M}_\odot$, while high-mass stars are considered to have masses $M_* > 8\mathrm{M}_\odot$. Although low-mass stars far outnumber high-mass stars and comprise most of the stellar mass budget, high-mass stars are responsible for the majority of the luminosity output, making them important cosmic beacons. However, high-mass stars are much rarer, require particularly dense initial conditions, and form in clouds located fairly distantly from earth (Krumholz & McKee 2008). In this thesis, we instead focus on the formation of low-mass stars. The many nearby low-mass star-forming regions have allowed high-resolution observations and detailed study, supporting the formulation of a generally accepted star formation paradigm.

The early formation process of low-mass stars occurs in several stages. First, cores of dense gravitationally bound gas develop, seeded by shocks or initial inhomogeneities in the cloud. Once these cores reach sufficient mass, they become gravitationally unstable and begin inside-out collapse, a process that is likely modulated by magnetic fields (Shu et al. 1987; Ward-Thompson et al. 2007). As collapse proceeds, a protostar forms and gains mass via an accretion disk that channels low angular momentum gas onto the protostar. After the formation of an efficient accretion disk, the system launches an outflow, ejecting or entraining $\sim 50\%$ of the incoming mass along the rotational axis (Matzner & McKee 2000; Alves et al. 2007; Enoch et al. 2008). Deuterium burning begins when the central temperature reaches 10^6 K. Once most of the surrounding gas is accreted or expelled, the protostar contracts along the Hayashi track towards the main sequence where it begins hydrogen burning. At this point, the remnant circumstellar debris undergoes the complex process that may lead to planet formation.

Despite this general picture of star formation, many of the details of the process remain poorly understood. For example, despite the ubiquity of turbulent motions observed in molecular clouds, both the origin and the maintenance mechanism of turbulence are unknown. Numerical simulations suggest that turbulence decays quickly (Mac Low et al. 1998; Stone et al. 1998), leading to the quandary of why molecular clouds do not collapse rapidly into stars. producing a high star formation rate. Var-

ious sources of turbulent energy have been suggested to solve this problem, however, debate continues as to whether the turbulence may be driven purely from large scale processes like shearing, expanding HII regions, and supernova explosions or local processes such as outflows (Mac Low & Klessen 2004).

The collapse process from pre-stellar cores to protostars is also uncertain. Debate continues about the relative importance of magnetic fields (Shu et al. 1987; Li et al. 2004; Padoan et al. 2007), ambipolar diffusion (Mouschovias 1976, 1977; Hujeirat et al. 2000; Adams & Shu 2007), turbulence (Padoan & Nordlund 2002, 2004), radiative transfer (Boss et al. 2000; Krumholz et al. 2007b; Bate 2009b), protostellar outflows (Li & Nakamura 2006; Nakamura & Li 2007), and many other effects.

Despite a large variety of star forming initial conditions, observations indicate that throughout the galaxy the initial mass function (IMF) of stars is universal (Chabrier 2005). The similarity extends from 0.1-10 $M_{\odot}$, including the typical distribution peak of $\sim 0.2\ M_{\odot}$, suggesting that some fundamental process is at work. The origin of this common shape remains a mystery, although different authors have attributed it to turbulent cloud conditions (Padoan & Nordlund 2002, 2004; Hennebelle & Chabrier 2008), thermal physics (Larson 2005), or competitive accretion of gas onto small seed protostars (Bonnell et al. 1997, 2001; Klessen & Burkert 2000, 2001). Recent observations have demonstrated that the mass function of dense cores strongly resembles the shape of the IMF for some low-mass star forming regions (Motte et al. 1998; Testi & Sargent 1998; Johnstone et al. 2001; Onishi et al. 2002; Alves et al. 2007; Enoch et al. 2008). A direct mapping between the starless core mass function and the stellar IMF is complicated by the presence of unbound cores (Lada et al. 2008), fragmentation of the core into multiple stars (Clark et al. 2007), and the existence of outflows, which may eject a variable and signficant amount of the core gas (Matzner & McKee 2000).

Although nearly half of stars are observed to be members of multiple systems (Lada 2006), no quantitative theory exists to explain the origin, frequency, and mass ratios of such systems. Fragmentation of cores or circumstellar disks have been suggested as mechanisms to form multiple systems (Padoan & Nordlund 2002; Whitworth & Stamatellos 2006; Kratter et al. 2008). The gravitational collapse of a

region and the characteristic fragmentation size depend sensitively upon the scale at which thermal energy is no longer sufficient to support against gravity. This scale, the Jeans length, depends sensitively on the local temperature and density, and it is responsible for the onset of gravitational instability. The local gas temperature is influenced by compressional and accretion heating, molecular chemistry, as well as by radiation emitted by nearby protostellar sources, posing a challenging problem.

Due to the complexity of the physics involved, simulations serve as a powerful research tool for addressing these issues (Klein et al. 2007). Adaptive mesh refinement (AMR) is particularly well suited to problems of gravitational collapse, because additional grids are automatically inserted in regions of interest (Truelove et al. 1998; Klein 1999). Since collapsed objects like protostars fill a relatively small volume of the grid, AMR is both highly accurate and enormously efficient in both computational time and memory usage. In contrast, conventional fixed-grid codes must cover the entire computational domain with a grid sufficiently fine to resolve the smallest forming structures. Alternatively, Lagrangian N-body methods such as smoothed-particle hydrodynamics (SPH) are superb at modeling dense regions, fast, and robust, but they inaccurately render shocks and instabilities, which are essential for modeling star formation (Agertz et al. 2007).

In this thesis, I perform a series of computational studies to investigate the role of turbulence, gravity, and radiative transfer in the process of low-mass star formation. In particular, the latter topic has been largely neglected and yet has important consequences for understanding the key problems in star formation. I gauge the importance of these physical processes via simulated observations and comparisons with observations of local low-mass star-forming regions.

Simulations of star formation typically model turbulence via one of two methods. In driven turbulence, energy is continually injected through velocity or momentum perturbations to maintain constant kinetic energy, while decaying turbulence simulations begin with a turbulent velocity field that is allowed to decay. In Chapter 2, I use the ORION AMR code to model the formation of cores and protostars in molecular clouds with driven and decaying turbulence. I analyze the properties of bound cores such as size, shape, line width, and rotational energy, and I compare these with

observations. At high-resolution, I find that different core accretion rates in the two cases lead to significant differences in protostellar system development. I show that cores forming in a decaying turbulence environment produce high-multiplicity protostellar systems with unstable disks that exhibit characteristics of the competitive accretion model for star formation. In contrast, cores forming in the context of continuously driven turbulence form smaller protostellar systems with fewer low-mass members.

Observational information of molecular clouds is obtained via radiation signatures, such as dust and molecular line emission, which comprise an incomplete picture in scale, wavelength, and perspective. This information may be very distinct from quantities reported by simulators, complicating comparisons between observations and computations. In Chapter 3, I model observations of the simulated cores described in Chapter 2 in the $C^{18}O(2 \rightarrow 1)$, $NH_3(1, 1)$, and $N_2H^+(1 \rightarrow 0)$ molecular lines. From the simulated observations I measure the line widths of individual cores, the line widths of the surrounding gas, and the motions of the cores relative to one another. I find that some of these distributions are significantly different in the driven and decaying runs, making them potential diagnostics for determining whether the turbulence in observed star-forming clouds is driven or decaying.

Core shapes potentially reflect molecular cloud properties, such as local turbulence or magnetic field geometry. In Chapter 4, I investigate the shapes of simulated starless and protostellar cores. I model observations of the cores in dust emission, including realistic noise and telescope resolution, and I compare to the core shapes measured in the Orion molecular cloud by Nutter & Ward-Thompson (2007). I show that the turbulent simulations and the observations have generally high statistical similarity, with particularly good agreement between simulations and Orion B. Due to the high level of agreement between the non-magnetic hydrodynamic simulations and observation, I suggest that the presence of magnetic fields does not strongly influence core shapes in Orion.

Due to the computational expense and complexity of radiative transfer algorithms, radiative processes have largely been neglected in the field of star formation. In Chapter 5, I use ORION to simulate low-mass star formation in a turbulent

molecular cloud including radiative feedback from forming protostars. I compare the distributions of stellar masses, accretion rates, and temperatures in the cases with and without radiative transfer, and I demonstrate that radiative feedback has a profound effect on accretion, multiplicity, and mass by reducing the number of stars formed and the total rate at which gas turns into stars. I also show that once star formation reaches a steady state protostellar radiation is by far the dominant source of energy in the simulation, exceeding viscous dissipation and compressional heating by at least an order of magnitude. I conclude that calculations omitting radiative feedback from protstars significantly underestimate the gas temperature, resulting in excess disk fragmentation that would otherwise result in very low-mass companions or brown dwarfs.

Observations of young protostars find luminosities that are significantly smaller than predicted by current theories of star formation (e.g., Kenyon et al. 1990). In Chapter 6, I investigate the nature of the luminosity problem by comparing a radiation-hydrodynamics simulation of protostars forming in a turbulent molecular cloud to protostars observed in the Perseus molecular cloud. I post-process the simulations to adjust for protostellar outflows, and I demonstrate that the simulation produces protostellar luminosities that are in reasonable agreement with observations.

Even the most sophisticated radiation transfer methods currently applied in star formation require simplifying assumptions due to computational limitations. In Chapter 7, I review the multigroup approach to the radiative transfer problem. This approach improves upon the gray method adopted in Chapter 5 by including frequency information. I present two tests of the three-dimensional AMR multigroup radiative diffusion method implemented in ORION. I conclude with a discussion of future applications of multifrequency methods to remaining puzzles in the field of star formation.

Chapter 2

Driven and Decaying Turbulence Simulations of Low-Mass Star Formation: From Clumps to Cores to Protostars

Offner, Klein, & McKee, 2008, ApJ, 686, 1174. [1]

2.1 Introduction

Contemporary star formation occurs exclusively in dense molecular clouds (MCs). Such regions exhibit large non-thermal linewidths generally attributed to supersonic turbulence (Larson 1981). Although debate continues on the origin and characteristics of this turbulence, it is now recognized that turbulence is a necessary element of star formation and plays an important role in the shape of the core initial mass function (IMF), the lifetimes of molecular clouds, and the star formation rate (Mac Low & Klessen 2004).

Simulations have shown that supersonic turbulence decays with an e-folding

time of approximately one cloud crossing time if there is no energy input to sustain it (Stone et al. 1998; Elmegreen & Scalo 2004; Mac Low & Klessen 2004). If turbulence decays as quickly in molecular clouds then star formation must happen rapidly as the cloud looses turbulent pressure support and undergoes global collapse. In this senario, star formation occurs on a dynamical timescale and MCs must be transient dynamic structures (Elmegreen 2000; Hartmann et al. 2001). If however, turbulence is fed from large scales or protostellar winds, expanding HII regions, and other processes provide sufficient energy injection to balance dissipation produced by shocks, then MCs may arrive at a quasi-equilibrium state (Tan et al. 2006; Krumholz & Tan 2007). Although there are many possible sources for turbulent energy, the dominant source and the specific characteristics of turbulence remain poorly understood. Recent effort has been directed at this issue and some observations of low-mass star forming regions, e.g., L1551, find evidence for ongoing turbulence injection in the form of winds and jets (Swift & Welch 2008). While turbulent support is maintained, only a small volume of gas will become gravitationally unstable and form stars in a dynamical time, leading to a low star formation rate and allowing MCs to live for several dynamical times.

The two different views of cloud dynamics are related to, but distinct from, the two major approaches to simulating turbulent molecular clouds. The fact that there are two competing approaches to the simulation of such clouds is a direct reflection of our lack of understanding of the origin of the turbulence in these clouds (McKee & Ostriker 2007). In one method, the turbulence is initialized and then allowed to decay (e.g., Klessen et al. 1998; Bonnell et al. 2003; Bate et al. 2002; Tilley & Pudritz 2004). The primary problem with this approach is that the turbulence decays to levels that are much lower than those observed. Advocates of this method argue that the gravitational collapse that ensues after the decay of the turbulence can be observationally confused with turbulence (Vázquez-Semadeni et al. 2006), but it is difficult to see how to maintain a low star formation efficiency if much of the gas is in a state of gravitational collapse. The other approach to cloud simulation is to drive the turbulence by perturbing the gas velocity or momentum so that it does not decay (e.g., Padoan & Nordlund (1999); Gammie et al. (2003); Li et al. (2004);

Jappsen & Klessen (2005)). This approach allows one to study the processes that occur at a given level of turbulence, which can be set to match that in a given cloud, but it suffers from the disadvantage that the driving is unphysical. Thus, turbulently driven simulations are a good representation of quasi-equilibrium clouds. They can also be consistent with transient clouds if it is assumed that the simulation box represents only a small part of the molecular cloud, so that the decay time for the turbulence is long compared to the dynamical time of the simulation.

The near universal shape of the stellar IMF across diverse star forming environments has sparked much debate and generated diverse theories. Padoan & Nordlund (2002) suggest that the functional form of the IMF can be derived from the power spectrum and probability density function characteristic of supersonic turbulence. Larson (2005) proposes that the peak of the IMF is set by the Bonnor-Ebert mass at the minimum cloud temperature, which is related to the dust-gas coupling and gas cooling efficiency. In the competitive accretion model, Bonnell et al. (2004) invoke high stellar densities at the centers of clusters to propose that the relative position of the stars in the gas reservoir determines their mass. In this model, the IMF is determined by mass segregation, such that low-mass stars form in the lower density gas at the edges of the cluster, while higher mass stars form in the center, where their masses can be augmented by the coalescence of smaller protostars. In addressing the origin of the IMF, numerical simulations have been largely inconclusive in discriminating between models given that a wide range of conditions (e.g., virial parameters, resolution, code algorithms, included physics) have all succeeded in reproducing the IMF shape.

A large amount of computational effort has been directed towards studying self-gravitating turbulent clouds both with and without magnetic fields (Klessen 2001; Bonnell et al. 2003; Li et al. 2004). A number of simulations succeed in reproducing various observed core properties such as the IMF and Larson's laws (Padoan & Nordlund 1999; Gammie et al. 2003; Tilley & Pudritz 2004; Li et al. 2004; Jappsen & Klessen 2005; Bate & Bonnell 2005). However, most simulations lack the resolution to span the turbulent inertial range to accurately render the evolution of cores into stars in a cluster environment (Klein et al. 2007).

In this paper, we perform numerical AMR simulations with our code ORION to investigate the role of driven and decaying turbulence on low-mass star formation. We follow the evolution of star forming cores in a turbulent box to show that turbulent feedback is correlated with the multiplicity of stellar systems, the shape of the IMF, and the protostellar accretion model. In §2, we discuss the methodology of ORION and the initial conditions. In §3, we analyze core properties in driven and decaying turbulence at low-resolution. In §4, we present results from a few high-resolution studies of the protostellar evolution inside selected cores formed in the context of driven and decaying turbulence. Finally, §5 contains conclusions. In a companion paper (Offner et al. 2008, hereafter Paper II) we investigate the effects of driven and undriven turbulence on the properties of the cores from which the stars form.

2.2 Calculations

2.2.1 Numerical Methods

Our simulations are performed using the parallel adaptive mesh refinement (AMR) code, ORION, which uses a conservative second order Godunov scheme to solve the equations of compressible gas dynamics (Truelove et al. 1998; Klein 1999). ORION solves the Poisson equation using multi-level elliptic solvers with multi-grid iteration. Throughout our calculations, we use the Truelove criterion to determine the addition of new AMR grids (Truelove et al. 1997),

$$\rho < \rho_{\rm J} = \frac{J^2 \pi c_{\rm s}^2}{G(\Delta x^l)^2}, \tag{2.1}$$

where Δx^l is the cell size on level, l, and we adopt a Jeans number of $J = 0.25$. We insert sink particles in regions of the flow that have exceeded this density on the maximum level (Krumholz et al. 2004). Sink particles serve as numerical markers of collapsing regions and also, after sufficient mass accretion and lifetime, protostellar objects. We impose a merger criterion that combines sink particles that approach within two grid cells of one another but prohibits nearby objects from merging

if both have masses exceeding 0.1 $M_\odot$. This limit divides stars from substellar objects such as brown dwarfs and has the effect of tracking all significantly massive objects. Particles that represent temporary violations of the Jeans condition and have little bound mass tend to accrete little and ultimately merge with their more substantial neighbors. The combination of sink particles and AMR with the Jeans criterion allows us to accurately and efficiently continue our calculation to high-resolution without the time constraints imposed by a large base grid and without the consequences of artificial fragmentation.

2.2.2 Initial Conditions and Simulation Parameters

Isothermal self-gravitating gas is scale free, so we give the key cloud properties as a function of fiducial values for the mean number density of hydrogen nuclei, $\bar{n}_{\rm H}$, and gas temperature, T. We adopt a characteristic 3D turbulent Mach number, $\mathcal{M}$=8.4, such that the cloud is approximately virialized:

$$\alpha_{\rm vir} = \frac{5\sigma^2}{GM/R} \sim 1.67. \tag{2.2}$$

It is then easy to scale the simulation results to the astrophysical region of interest. For the adopted values of the virial parameter and Mach number, the box length, mass, and 1D velocity dispersion are given by

$$L = 2.9\ {T_1}^{1/2} \bar{n}_{\rm H,3}^{-1/2}\ {\rm pc}\,, \tag{2.3}$$

$$M = 865\ {T_1}^{3/2} \bar{n}_{\rm H,3}^{-1/2}\ {\rm M}_\odot\,, \tag{2.4}$$

$$\sigma_{\rm 1D} = 0.9\ {T_1}^{1/2}\ {\rm km\ s^{-1}}\,, \tag{2.5}$$

$$t_{\rm ff} = 1.37\ \bar{n}_{\rm H,3}^{-1/2}\ {\rm Myr}\,, \tag{2.6}$$

where $\bar{n}_{\rm H,\,3} = \bar{n}_{\rm H}/(10^3\ {\rm cm^{-3}})$ and $T_1 = T/(10\ {\rm K})$ and where we have also listed the free-fall time for the gas in the box for completeness. For $\bar{n}_{\rm H,\,3} \sim T_1 \sim 1$, the simulation approximately satisfies the observed linewidth-size relation (Solomon et al. 1987; Heyer & Brunt 2004). For the remainder of this paper, all results will be given assuming the fiducial scaling values $\bar{n}_{\rm H} = 1100\ {\rm cm^{-3}}$ and T=10 K, which are appropriate for the Perseus MC (Paper II), but they may be adjusted to different

conditions using equations (2.2)-(2.5). In terms of the Bonnor-Ebert mass,

$$M_{\rm BE} = \frac{1.182c^3}{\left(G^3\bar{\rho}\right)^{1/2}} = 4.71\frac{T_1^{3/2}}{\bar{n}_{\rm H,\,3}^{1/2}} \quad M_\odot, \tag{2.7}$$

the simulation has a mass of $184M_{\rm BE}$. If the Jeans mass is defined as $M_{\rm J} = \rho L_J^3$, where $L_J = (\pi c_s^2/G\bar{\rho})^{1/2}$ is the Jeans length, then $M_J = (\pi^{3/2}/1.18)M_{\rm BE} = 18.9T_1^{3/2}/\bar{n}_{\rm H,\,3}^{1/2}\ M_\odot$.

Our turbulent periodic box study is comprised of two stages. The first stage simulates the large-scale isothermal environment of a turbulent molecular cloud with self-gravity. In this "low-resolution" stage, we only add enough AMR levels to resolve the shape and structure of collapsing clumps and cores. This first stage has two parts. First, to obtain the initial turbulent spectrum, we turn off self-gravity and use the method described in Mac Low (1999), in which velocity perturbations are applied to an initially constant density field. These perturbations correspond to a Gaussian random field with flat power spectrum in the range $3 \leq k \leq 4$ where k is the wavenumber normalized to $k_{\rm phys}L/2\pi$. At the end of two cloud crossing times, the turbulence follows a Burgers $P(k) \propto k^{-2}$ power spectrum as expected for hydrodynamic systems of supersonic shocks. For the second part, we turn on gravity and follow the subsequent gravitational collapse for two scenarios. It should be noted that some workers (e.g., Bate et al. 2002) do not allow self-consistent turbulent density fluctuations to build up before turning on gravity. Any choice of initialization for a turbulent, self-gravitating cloud is necessarily approximate, but in our view it is preferable to have self-consistent density and velocity fluctuations in the initial conditions. In the simulation that we will refer to with the letter D (driven), we continue turbulent driving to maintain virial equilibrium, while in the other, noted with U (undriven), we halt the energy injection and allow the turbulence to decay.

In the second stage, we select a few emerging cores for further study in each turbulent box, and we follow their fragmentation and evolution into protostellar systems at high-resolution using a barotropic equation of state (EOS). We add additional grid refinement to the regions we select, which continue to evolve within the low-resolution context of the box. This method capitalizes on the AMR methodology

to achieve a high-resolution study of the development and properties of protostellar cores with realistic initial and boundary conditions. Following all the cores over a free-fall time with AMR rather than a subset to the maximum resolution would require more than a million CPU hours on 1.5 GHz processors. In contrast, our stage two approach with AMR requires ∼50,000 CPU hours per high-resolution box.

In the first stage, it is reasonable to assume that the low density gas in the cluster is isothermal and scale-free, reflecting the efficient radiative cooling of the gas. However, as the gas compresses and becomes optically thicker there is a critical density at which the radiation is trapped. Ideally, we would directly solve for the radiation transfer using an appropriate opacity model to accurately determine the gas temperature at these high densities. However, even approximations such as the Eddington and diffusion approximations do not sufficiently economize the equations of radiation transfer such that they are affordable over the resolution and timescales necessary for this calculation. Consequently, we adopt a bartotropic EOS to emulate the effect of radiation transfer. The gas pressure is given by

$$P = \rho c_{\rm s}^2 + \left(\frac{\rho}{\rho_{\rm c}}\right)^{\gamma} \rho_{\rm c} c_{\rm s}^2, \tag{2.8}$$

where $c_{\rm s} = (k_{\rm B}T/\mu)^{1/2}$ is the sound speed, $\gamma = 5/3$, the average molecular weight $\mu = 2.33 m_{\rm H}$, and the stiffening density $\rho_{\rm c}$ is given by $\rho_{\rm c}/\rho_0 = 2.8 \times 10^8$. The value of μ reflects an assumed gas composition of $n_{\rm He} = 0.1 n_{\rm H}$. The value of the stiffening density determines the transition from isothermal to adiabatic regimes. It introduces a characteristic scale into the previously scale-free isothermal conditions. The isothermal scaling relations above remain valid as long as the ratio of stiffening density to the average box density is presumed to be constant. We chose a value of the stiffening density, $\rho_{\rm c} = 2 \times 10^{-13}$ g cm^{-3}, to agree with the $\rho(T)$ relation calculated by Masunaga et al. (1998), who perform a full angle-dependent radiation hydrodynamic simulation of a spherically symmetric collapsing cloud core. Unfortunately, we sacrifice some accuracy in using the barotropic approximation in lieu of radiative transfer, since an EOS assumes that gas temperature is a single valued function of density. Simulations have shown that gas temperature in calculations using radiation transfer vs. a barotropic EOS can differ by a factor of several and

potentially produce different fragmentation (Boss et al. 2000; Whitehouse & Bate 2006; Krumholz et al. 2007b).

The low-resolution initial stage uses a 128^3 base grid with 4 levels of factors of 2 in grid refinement, giving an effective resolution of 2048^3. The high-resolution core study has 9 levels of refinement for an effective resolution of $65,536^3$ such that the smallest cell size corresponds to $\sim$10 AU for our fiducial values.

2.3 Bound Clump Properties

2.3.1 Clump Definition

At the end of a free-fall time with gravity, we analyze the core properties and compare the driven and decaying turbulent results. At this time, the large-scale driven turbulent simulation has 32 sink particles with 14.2% of the total mass accreted. The decaying turbulence simulation has 20 sink particles containing 13.6% of the mass. Because the sink particles mark collapsing cores rather than individual protostars at this stage, these percentages should be viewed as an upper limit to the actual star formation rate. Nonetheless, these numbers are not too much larger than the the prediction of a 7% star formation rate per free-fall time given by Krumholz & McKee (2005) for our assumed conditions and neglecting outflows. In the undriven simulation, the turbulence decays significantly in $1t_{\rm ff}$ and no new sink particles are formed after $\sim 0.75t_{\rm ff}$. Without continued driving, there is insufficient energy to create the large scale compressions responsible for seeding new cores. After significant turbulent support is lost, the cloud deviates from virial equilibrium and the gas falls onto existing over-densities rather than forming new cores.

In presenting the results from the low-resolution simulations, we restrict ourselves to the analysis of objects that can best be described as "star-forming bound clumps" (see McKee & Ostriker (2007)), which are generally gravitationally bound but may form several systems of stars. In the following sections, we will adopt the terminology "core" to refer to the bound condensations out of which a single protostar (i.e., sink particle) or small multiplicity protostellar system forms. Hence, we

do not apply a Clumpfind algorithm, as described by Williams et al. (1994), which also captures unbound and transient over-densities. Instead, we define a bound core as a sink particle with envelope satisfying four criteria. First, the density in the included cells must exceed the average shock compressions, i.e., $\rho \geq \rho_0 {\mathcal{M}_{1\mathrm{D}}}^2$, which also ensures a single peak for each core. Second, the total mass in the core must be greater than the local Bonner-Ebert mass, signifying that the core will collapse. Each cell, i, forming a core must also be individually gravitationally bound to it such that $|E^i_{\mathrm{KE}}| < |E^i_{\mathrm{PE}}|$. Finally, the cells included must lie inside a virial radius, R, such that $\alpha_{\mathrm{vir}} \leq 2$, where the 1D velocity dispersion, σ, is given by the sum of the turbulent and thermal components of the gas velocity: $\sigma^2 = \sigma^2_{\mathrm{NT}} + c^2_{\mathrm{s}}$. We vary the density cutoff by a factor of two and find that changes in the data fits remain within 1-sigma error. Thus, our results are not overly sensitive to our core definition. The larger of these cores may eventually form a cluster of stars and may best be described as star-forming clumps. The smaller cores will likely form only a single protostellar system. At the low-resolution stage of analysis it is difficult to predict the outcome, and so the line between star-forming clumps and cores is ill-defined.

Note that in our methodology, the presence of a sink particle does not *guarantee* the eventual formation of a protostar, only that the Jeans condition has been exceeded at some time during the simulation. In each simulation, there are a few sink particles that do not posses envelopes satisfying these criteria. However, all cores included in our analysis are defined to be gravitationally bound, collapsing objects rather than transient overdensities in the flow and hence are predisposed to develop protostellar systems.

2.3.2 Clump Properties

There are a number of core physical properties that are comparable to observations, and we investigate these here at 1 t_{ff}. Figures 2.1 - 2.5 show the bound core data plotted with best fit lines. We exclude objects from the fit that have $R = \sqrt{\mathrm{ab}} \leq 4\Delta x$, where a and b are the lengths of the major and minor axes.

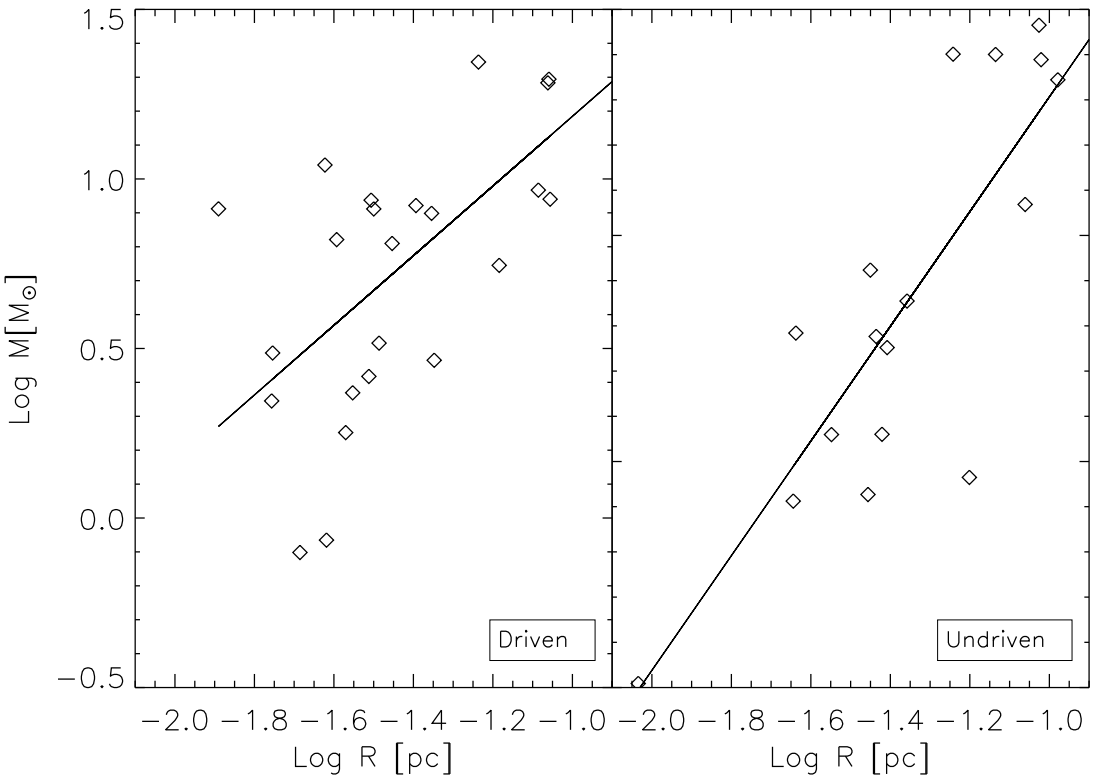

Figure 2.1 The figure shows the log of the core masses as a function of log size ($R = \sqrt{ab}$) for the driven (left) and decaying (right) boxes at 1 $t_{\rm ff}$. The slopes have fits of 1.03±0.26 and 1.27±0.19, respectively.

Density Profiles

As plotted in Figure 2.1, we find that compared to cores in run U, the cores in run D have a slightly flatter trend of $M(R) \propto R$, consistent with Bonnor-Ebert spheres, which are characterized by $\rho(r) \propto r^{-2.0}$. In run U, the cores have profiles that are closer to a free-fall profile, where $\rho(r) \propto r^{-1.5}$. Cores that are supported or collapsing slowly will tend to resemble pressure-confined isothermal spheres (Kirk et al. 2005; di Francesco et al. 2007) as in run D, where turbulence is providing more external pressure support. In run U, where the turbulence has decreased significantly, cores tend quickly to collapse as unbound gas becomes gravitationally attracted to the largest overdensities. However, the slopes of the cores in the two simulations are within 1-sigma error due to significant scatter, so that the trends are not significantly different.

Shape

As shown in Figure 2.2, both distributions of bound cores have similar morphologies and tend to be mainly tri-axial. It is thought that in the presence of magnetic fields, which we do not include, cores will flatten along the field lines (Basu & Ciolek 2004). However, ideal MHD simulations by Li et al. (2004) also find that their cores are mostly prolate and triaxial. In any event, the difficulty of deprojecting observed cores makes the true shape distribution ambiguous. Run D has median major and minor aspect ratios of b/a =0.76 and c/a=0.40, while the decaying cores have median aspect ratios of b/a=0.73 and c/a=0.54. The net medians of the shape distributions 0.58 (D) and 0.52 (U) are similar to those observed for different star-forming regions which fall in the range 0.50-0.67 (Jijina et al. 1999).

Velocity Dispersion

In Figure 2.3, we plot the velocity dispersion as a function of core size for comparison against Larson's linewidth-size relation. For low-mass star forming regions, $\sigma_{NT} \propto R^{0.5}$ with some sensitivity to core sizes and clustering (Jijina et al. 1999). We find exponents of 0.54 (D) and 0.19 (U). The slope of run D is within the range of

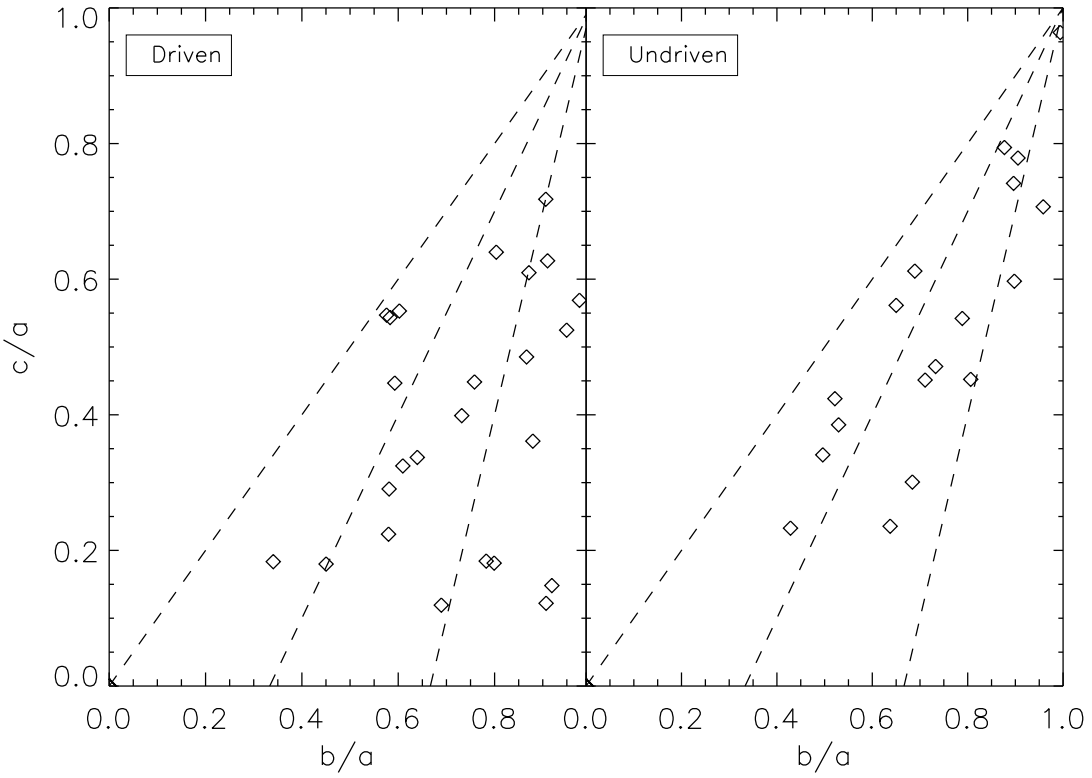

Figure 2.2 The figure shows the core aspect ratios for the driven (left) and decaying (right) boxes at 1 $t_{\rm ff}$. The median aspect ratios for each case are (b/a, c/a) = (0.76, 0.40) and (b/a, c/a) = (0.73,0.54), respectively.

observed slopes for low-mass regions. Although the scatter in our data appears large, our χ^2 fit slope error is comparable to the range of fit errors ($\pm 0.1 - \pm 0.19$) that Jijina et al. report. Plume et al. (2000) observed massive cores with a completely flat slope, and indeed, the cores in run U are more massive with a mean mass of 12 $M_\odot$ versus 8 $M_\odot$ for the driven, but not significantly so (see §3.2.6). The Kolmogorov-Smirnov (K-S) test quantifies the difference between the empirical distribution functions of two data sets. A K-S test of the distributions of velocity dispersions indicates definitively that the populations are quite dissimilar at the $>> 99\%$ level. The difference in slope between the two simulations is possibly due to crowding in the decaying turbulent case caused by insufficient global turbulent support against gravity. Jijina et al. (1999) showed that clustered objects have a significantly flatter linewidth-size relation slope. We note that the velocity dispersions in run U, although flatter with size, are larger, which is consistent with quickly collapsing rather than turbulently supported cores.

Rotation

Typically, rotational energy makes up only a small fraction of the core gravitational energy. The rotational parameter β is defined as the ratio of the rotational kinetic energy to the gravitational potential energy. For a uniform density sphere this can be written:

$$\beta_{\rm rot} = \frac{1}{3}\frac{\Omega^2 R^3}{GM} \tag{2.9}$$

Observationally, $\Omega_{\rm pos} = \Omega_x^2 + \Omega_y^2$ is the angular velocity projected in the plane of the sky, such that $\beta_{\rm rot,obs} = \frac{2}{3}\beta_{\rm rot}$. Goodman et al. (1993), studying a selection of dense cores in NH_3, find that $\beta_{\rm rot,obs}$ is roughly constant as a function of size, where $2 \times 10^{-3} < \beta_{\rm rot,obs} < 1.4$ with median $\beta_{\rm rot} \sim 0.02$. Observations of dense cores using N_2H^+, which primarily traces $n > 10^5$ cm^{-3}, find a similar median value of $\beta_{\rm rot,obs} \sim 0.01$ (Caselli et al. 2002). For the purpose of comparison, we evaluate $\beta_{\rm rot}$ in two ways. First, we follow the convention of the observers and evaluate $\beta_{\rm rot,obs}$ by assuming that the cores are projected constant density spheres. Second

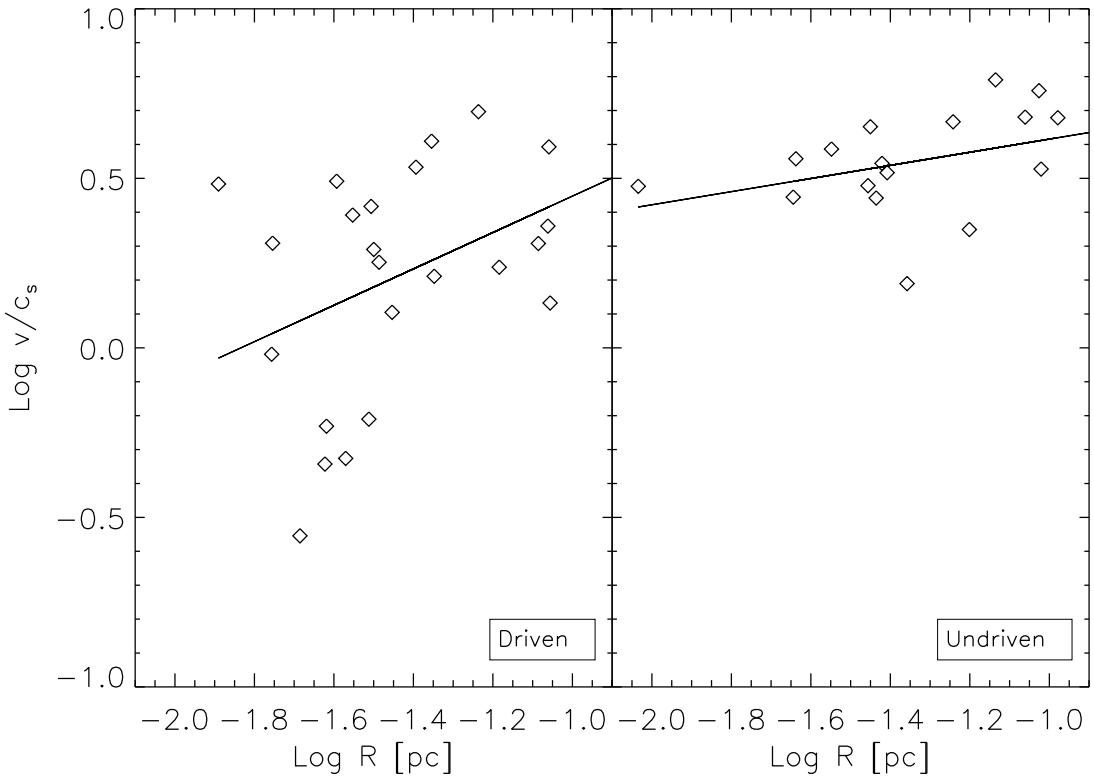

Figure 2.3 The figure shows the log core velocity dispersions as a function of log size ($R = \sqrt{ab}$) for the driven (left) and decaying (right) boxes at 1 $t_{\rm ff}$. The slopes have fits of 0.54 ± 0.25 and 0.19 ± 0.11, respectively.

we sum over all the 3D data to calculate $E_{\rm rot}/E_{\rm grav}$. For a singular isothermal sphere, $E_{\rm rot}/E_{\rm grav} = \frac{1}{3}\beta_{\rm rot}$.

Figure 2.4 confirms that $\beta_{\rm rot}$ for both runs is independent of the core size, and there is fairly large scatter. The total range of $\beta_{\rm rot}$ values for observation and simulation is roughly the same. We find a range of $0.0005 < \beta_{\rm rot,obs} < 0.2$ for the driven case and $0.006 < \beta_{\rm rot,obs} < 0.3$ for the decaying case. However, overall our values are a factor of 2 to 4 higher than those found by Goodman et al. Run D has a lower median $\beta_{\rm rot,obs} \sim 0.05$, while run U has very few low $\beta_{\rm rot,obs}$ cores and so has a median $\beta_{\rm rot,obs} \sim 0.08$. When we use the complete gas properties to calculate $E_{\rm rot}/E_{\rm grav}$, we find median values of 0.05 and 0.19 for the D and U cores, respectively. Jappsen & Klessen (2005) perform gravoturbulent driven simulations of cores and find a median $E_{\rm rot}/E_{\rm grav} \sim 0.05$, in agreement with our result. The higher $\beta_{\rm rot,obs}$ values measured in the cores in the undriven simulation may be a side effect of reduced turbulent support: Since the U cores are moving more slowly, they may more easily accrete gas from farther away, which has higher angular momentum [2].

Although a K-S test verifies that the two $\beta_{\rm rot,obs}$ populations are distinct, neither is a good match for observation since both have median values that are higher than observed.

One possible explanation for the factor of 3-5 difference between simulation and observation is that magnetic fields play a significant role in decreasing core rotation. A number of recent simulations of isolated rotating magnetized cloud cores have shown that magnetic braking is an efficient means of outward angular momentum transport (Hosking & Whitworth 2004; Machida et al. 2004, 2006; Banerjee & Pudritz 2006). The oblate cores formed in the ideal MHD simulation of Li et al. (2004) show a median $\beta_{\rm rot,3D}$ similar to ours (Li, private communication), however, all the cores are supercritical by an order of magnitude.

Another possibility to account for the difference in median β is that observers typically investigate isolated cores, which are easier to distinguish and analyze but tend to be less turbulent. However, our study specifically concerns bound cores forming in a turbulent cluster. Using Larson's laws, we would expect $\beta_{\rm rot} \propto v_{\rm rot}^2/(GM/R) \propto$

[2] We thank the referee for this comment.

$R/(GM/R) \propto 1/\Sigma \simeq$const, where Σ is the cloud column density. However, there is large scatter and a few examples of clouds with non-constant column density, such that measurements of β_{rot} could be sensitive to column density differences in various MCs.

Angular Momentum

There is also a substantial difference between the specific angular momentum in the two cases as illustrated in Figure 2.5. We plot both the 3D total specific angular momentum of the cores, which is obtained by directly summing the angular momentum of the individual cells comprising a clump, and the 2D specific angular momentum, by totaling the projected momentum along a line of sight. In run D, the specific angular momentum fits, $j_{2D}(R) \propto R^{1.1}$ and $j_{3D}(R) \propto R^{1.9}$, bracket the expected $j(R) \propto R^{1.5}$ based upon the linewidth, $\delta v \propto R^{1/2}$, and assumption of virial balance (Goodman et al. 1993; this argument suggests the same value for both the 2D and 3D cases). The specific angular momentum fits in run U are more similar but still a little flat, such that $j_{2D}(R) \propto R^{1.5}$ and $j_{3D}(R) \propto R^{1.1}$. Because the decaying cores are less turbulent, they will be inclined to have less angular momentum variation than their driven counterparts. The cores in run D overshoot the expected relationship for j_{3D}, while the decaying cores undershoot by a similar amount. In either case, we expect that the simulated angular momenta is affected by the absence of braking effects from magnetic fields, which we do not include. Nonetheless, we find that the measured range of $j \sim 10^{21} - 10^{22}$ cm^2 s^{-1} to be consistent with observational estimates, and we find the 2D angular momentum estimates to be statistically similar to one another, albeit flatter than the measured $j_{2D} \propto R^{1.6\pm0.2}$ (Goodman et al. 1993; see Figure 2.5).

Core Mass Function

Measurements of the core mass function (CMF) show that its shape strongly resembles the stellar IMF (Lada 2006). The high mass end, in particular, seems to share a similar power law index. As a key characteristic of star formation, the core and star mass functions for driven and undriven turbulence have been extensively

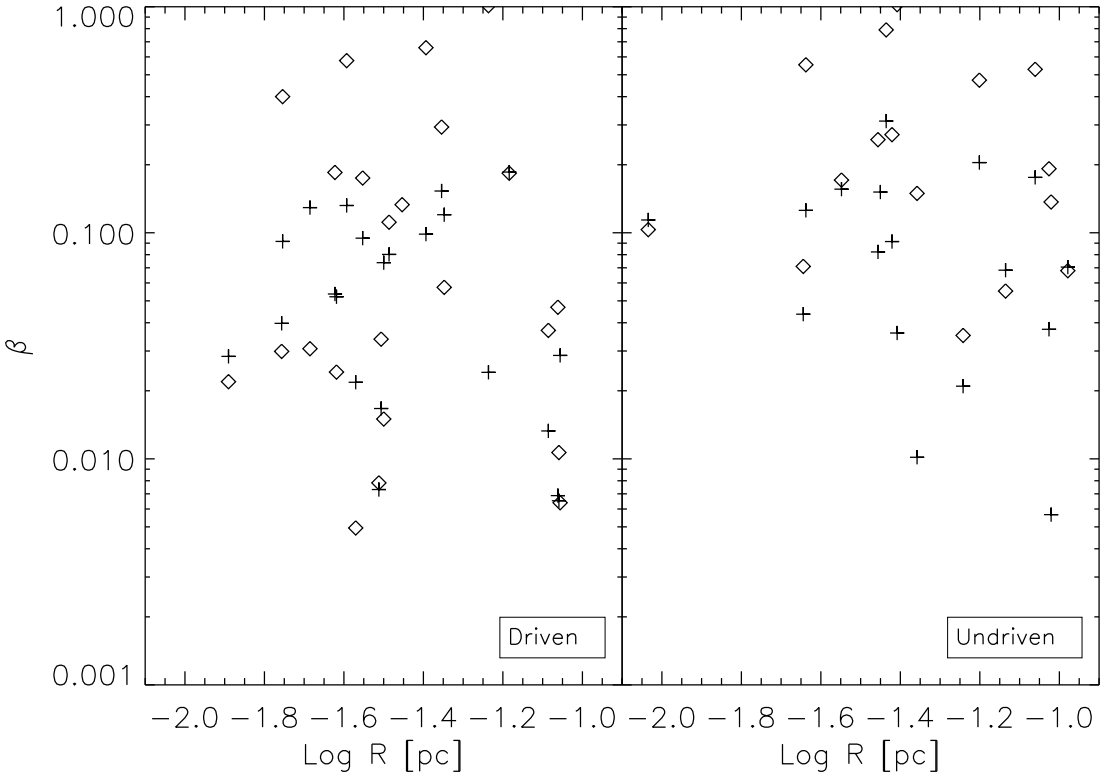

Figure 2.4 The figure shows the rotational parameter, β, as a function of size ($R = \sqrt{ab}$) for the driven (left) and decaying (right) boxes at 1 $t_{\rm ff}$. The crosses give the 2D projected value, while the diamonds give the 3D value. For run D, the median β values are 0.05 (crosses) and 0.05 (diamonds). For run U, the median β values are 0.08 (crosses), 0.19 (diamonds).

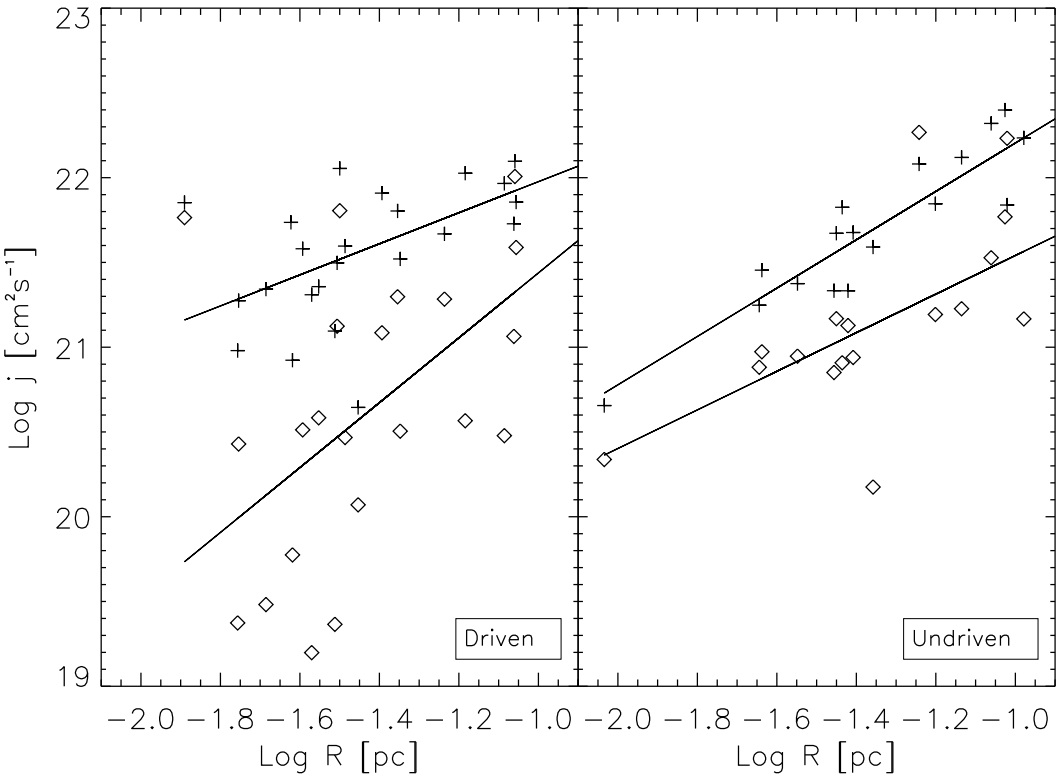

Figure 2.5 The figure shows the log of the core specific angular momentum as a function of log size ($R = \sqrt{ab}$) for the driven (left) and decaying (right) boxes at 1 $t_{\rm ff}$. The crosses give the 2D projected value, while the diamonds give the 3D value. For run D, the slopes have fits of 1.91 ± 0.65 (diamonds), 1.14 ± 0.31 (crosses). For run U, the slopes have fits of 1.14 ± 0.35 (diamonds), 1.50±0.23 (crosses).

numerically studied. Ballesteros-Paredes et al. (2006) and Padoan et al. (2007) find a mass function of the form $d\mathcal{N}/d\log(m) \propto m^{-1.3}$ for cores in driven hydrodynamic turbulence, even without the presence of self-gravity. Klessen (2001) finds that both driven turbulence with $1 \leq k \leq 2$ and undriven turbulence produce a core spectrum with a similar slope to that of the measured IMF. A number of isothermal SPH simulations of decaying turbulence have shown agreement with the observed IMF despite initial turbulent conditions in which a turbulent velocity spectrum is initialized on a constant density field and then allowed to decay in the presence of self-gravity (Klessen & Burkert 2001; Bate et al. 2002; Bonnell et al. 2003; Tilley & Pudritz 2004; Bonnell et al. 2006). In such calculations, the turbulence does not reach a steady state and the simulated cloud is not virialized as expected from observations.

For the purpose of comparison, we plot the CMF for the simulations D and U at 1 $t_{\rm ff}$ in Figure 2.6. The two runs produce 30 and 19 bound cores, respectively. Unfortunately, the statistics at the high mass end are too small to be able to rule out either distribution on the basis of agreement with the Salpeter slope. Although the agreement looks better for the driven cores, we find that the mass distributions are in fact statistically similar according to a K-S test.

Overall, the simulations have statistically different distributions of angular momentum, rotational parameter, and velocity dispersion. The decline of turbulent compressions in the undriven run appears to make some significant changes and cause fewer new condensations to be formed. As turbulent pressure support is lost, the contracting gas instead falls onto existing cores resulting in less turbulent, more quickly rotating cores than in the driven case. However, it is not possible to definitively conclude which approach corresponds more closely with observation, and agreement with a particular observed region may depend upon cloud properties such as clustering and the magnetic field strength.

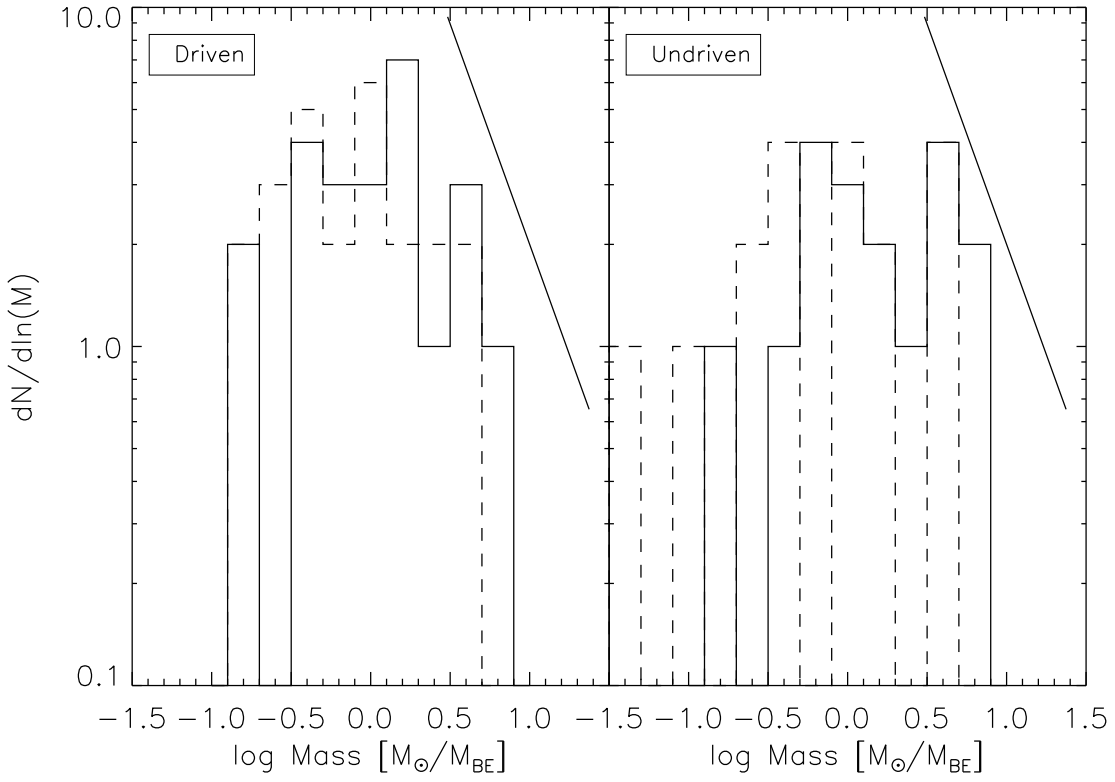

Figure 2.6 The figure shows the sink (dashed line) and core (solid line) mass distributions for the driven (left) and decaying (right) runs at 1 $t_{\rm ff}$. The straight time has a slope of -1.3.

2.4 Protostellar Cores at High Resolution

2.4.1 Overview

In this section, we present our computational results for the evolution of the protostellar systems contained in a few selected cores using 5 or 6 additional levels of refinement. We accomplish our study by inserting a refinement box around the core of interest before a sink particle is introduced on level 4 so that cells inside the box continue to higher densities and refine according to the Jeans criterion, while cells in the remainder of the simulation refine only to a maximum level of 4 as before. The lengths of the high-resolution boxes are typically 0.25-0.5 pc depending on the size of the enclosed clump. As a result, the boxes contain a region $\sim$200-2000 times volumetrically smaller than the simulation domain. The total initial mass in the boxes ranges from 4-12 $M_{\odot}$, which easily encompasses the bound core and all collapsing regions associated with it. In this way, we can perform a high-resolution study of selected collapsing cores with realistic initial conditions and consistent boundary conditions taken from the surrounding lower resolution grids computationally cheaply and efficiently. In each portion of the box, sink particles are introduced when the corresponding maximum refinement level is reached. At high-resolution, each sink particle represents a single "protostellar core." Thus, we are able to follow the clump fragmentation at high-resolution, without the need to re-run the entire calculation at that resolution.

We chose six cores for further study. In cases U1a and U1b, we test for convergence by following the same cores at two different resolutions. In cases D2 and U2, we choose an early collapsing object that is present in both the driven and decaying simulations to highlight the differences between the calculations. The cores U1, D2, and U2 have initial bound masses greater than 2.5 $M_{\odot}$. We also study two smaller driven and undriven cores, D3 and U3. By comparing the cases, we observe the effect of turbulent support on protostellar system development. The physical properties of the selected cores are given in Table 5.1.

Table 5.2 gives the three dimensionless quantities relating to the box surrounding

each core: $\mathcal{M}$, α_{vir}, and the self-gravity parameter,

$$\mu \equiv \frac{M}{c_s^3/(G^{3/2}\bar{\rho}^{1/2})}, \tag{2.10}$$

where $\alpha_{\rm vir}$ can then be written as

$$\alpha_{\rm vir} = \frac{5}{6}\left(\frac{\mathcal{M}^2}{\mu^{2/3}}\right). \tag{2.11}$$

These three parameters characterize the amount of turbulence in the core vicinity, the degree of self-gravitization of the gas, and the extent to which balance is achieved between the two. Table 5.2 indicates that all the small boxes are subsonic, and thus, the force of gravity rather than turbulence dominates the gas around the cores.

Note that when we cease driving in run U, the turbulent cascade continues and the turbulent decay rate is determined by the Mach number and the domain size as described by Mac Low (1999). At any given time, the effect of the decay on the cores forming in the high-resolution subdomain depends upon the amount of turbulent decay in the large box. The 1D velocity dispersion in Table 5.1 is an indicator of the change in turbulent energy when the core of interest is collapsing.

2.4.2 Convergence Study

Before embarking on further analysis, it is important to show that the results at the calculation resolution are suitably converged. In particular, it is necessary to show not only that there is no artificial fragmentation but that the number of fragments is constant with increasing resolution. For the convergence study we consider a box in the decaying turbulence run, U1, which encloses a long filament that collapses to form a number of small over-dense fragments along its length. We run this calculation with 9 (U1b) and 10 (U1a) levels of refinement, which corresponds to a minimum cell size of $\sim$10 AU and 5 AU, respectively. Figures 2.7, 2.8, and 2.9 show the two simulations at 16 kyr, 23 kyr, and 53 kyr, respectively, after the formation of the first sink particle. Tables 2.3 and 2.4 give the sink particle masses and the fragment masses at these times. We define the fragments as discrete cores of bound gas with density greater than 2×10^{-16} g cm^{-3}.

Table 2.1. Low resolution core properties

	U1a/U1b	D2	U2	D3	U3
Core Mass ($M_\odot$)[a]	10.71	5.05	4.32	1.59	2.80
$L_{\rm max}$ (pc)	0.45	0.23	0.19	0.03	0.08
Shape	1:0.28:0.05	1:0.37:0.09	1:0.66:0.26	1:0.69:0.60	1:0.78:0.24
$v_{\rm rms}$ (km/s)	0.42	0.32	0.36	0.33	0.45
$n_{\rm ave}(10^5 cm^{-3})$	1.44	1.08	1.01	4.06	1.25
$\alpha_{\rm vir}$	1.5	1.12	1.90	1.06	2.24
$\beta_{\rm rot}$	0.052	0.025	0.011	0.028	0.047
$t_{\rm ff}(10^4 yr)$	8.9	10.3	10.7	5.3	5.9
$\mathcal{M}_{\rm 1D}$ [b]	2.4	4.9	3.9	4.9	3.0

[a]Masses for each case when the sink particle is 0.1 $M_\odot$.

[b] $\mathcal{M}_{\rm 1D}$ is the velocity dispersion of the entire box, which is fixed at 4.9 for the driven cases.

We find that both resolutions produce the same number of collapsing fragments and yield a similar collection of sink particles. Most of the fragment masses for the two resolutions differ by at most a few percent, while sink particle masses may differ by 50%. At a particular instant in time, discrepancies between the number of sink particles in the two runs can occur due to several factors. First, the addition of extra levels allows the higher resolution simulation to collapse for a longer time without exceeding the Jeans criterion. Thus, a sink particle ultimately forms in both cases at the same location but at slightly different times. Another possibility is that a sink particle forms in both simulations at similar locations, but in one it mergers with a larger neighbor. A final possibility is that the region that collapses in the higher resolution becomes thermally supported before a sink is formed. In all these cases the gas physics can be quite similar but the introduction of sink particle can differ due to small details. For example, at 16 kyr the low-resolution simulation has formed sink particles in each filamentary fragment with condensation masses ranging from 1.5×10^{-2} $M_\odot - 8 \times 10^{-2}$ $M_\odot$ (see Table 2.4), while the higher resolution run has not reached sufficient density for any sink particles to form. This rather odd filamentary structure is created and confined by the ram pressure of intersecting shocks. The smallest sink particles formed in the filament later merge as shown in Figure 2.8 when the gas in the filament streams onto the disk-protostar system.

At later times and for small masses the corresponding sink particle properties differ the most significantly, particularly at the lower mass end as shown in Table 2.3. Due to the intrinsically chaotic and dynamically unstable nature of three or more body systems, the evolution of the two calculations begins to diverge at late times. This is unsurprising because not only do the calculations have different AMR grid structures, but the particle members of the system are introduced at slightly different times and initial masses. Despite this, the masses and configuration still show reasonable agreement at 80 kyr.

2.4.3 Influence of Turbulence on Stellar Properties

Interstellar turbulence undoubtedly has a substantial effect on cloud lifetimes and core creation, however, its relationship with core fragmentation and evolution is

less certain. The level of turbulence in cores is partially dependent on how much mass and energy the envelope exchanges with the surrounding turbulent gas. In turn, the properties of the parent core influence the rate of protostellar core formation and accretion. If substantial mass continues to fall onto the clump, as in the case of global contraction, then external flow patterns will impinge upon on the system development, increasing the accretion rate and possibly causing fragmentation. If however, the core accretes at a relatively low level in the manner of Bondi-Hoyle accretion in a turbulent medium then the core will accrete much less over time (Krumholz 2006; Krumholz et al. 2005a). Protostars forming in such a core limit to the Bondi-Hoyle accretion rate as the high density gas is depleted.

In cases D2 and D3 we continue turbulent driving to maintain virial equilibrium. To avoid directly adding artificial perturbations that may affect the core development or seed new fragmentation, we do not apply any velocity perturbations to the high-resolution regions inside the refinement box. Thus, the turbulence cascades into the highly-refined box from the outside in a self-consistent manner. In cases U2 and U3, the simulation continues without any turbulent injection.

We find striking differences in the protostellar systems formed in the driven and decaying cores. The most obvious difference between the D and U runs is the difference in the number and mass of sink particles formed (Table 2.5). For example, initially the fragmentation of D2 and U2 is similar temporally and spatially, but U2 eventually forms a slightly larger number of objects particularly at small masses as the level of turbulence in the two simulations diverges. The small D3 core forms a small stable binary system at early times, whereas U3, which is also fairly small, fragments into a number of protostellar members.

Despite the modest number of objects, we can compare the protostellar IMF to the observed IMF via a K-S test, which is accurate for input sets of four or more data points. A one-sided K-S test compares a given data set with a specified statistical distribution, in this case, the single star IMF given by Chabrier (2005). We achieve a best fit by scaling the masses by an adjustable normalization, $\epsilon = m_*/m_{\rm sink}$, where $m_{\rm sink}$ is the mass of the sink particle. Given that this simulation lacks feedback effects such as outflows and radiation transfer, the sink particle masses represent an

upper limit and the scaling factor corresponds to an efficiency factor of ϵ=0.25-0.75 (Matzner & McKee 2000).

Figure 2.10 shows the scaled cumulative distribution function (CDF) for the runs D2, U2, and U3, where the CDF of the Chabrier is overlaid for comparison. Although all three runs have a high confidence level of agreement with the measured IMF, the normalization values and the shapes of the distributions are quite different. For example, the smaller stellar population of D2 has fewer low-mass objects and hence has a smaller efficiency scaling factor of ~ 0.4 with 67% likelihood of being drawn from the Chabrier IMF. Conversely, U2+U3 distribution contains collections of low-mass objects and intermediate mass objects, such that the largest disagreement occurs in the middle of the two populations. A scaling factor of 1.0 gives the best agreement of 59%. A scaling factor near unity implies that protostellar mass loss has a negligible effect on the final mass of the star, contrary to some theoretical expectations (Shu et al. 1987; Nakano et al. 1995; Matzner & McKee 2000). For the D2 distribution, the largest disagreement occurs at the higher mass end, indicating that if the protostars continue to accrete mass and no new protostars are formed, then it is likely that the high probability of agreement with the IMF will be maintained even as the scale factor shifts to a lower value. The U2+U3 have a larger scale factor due to the significant number of low mass objects with accretion halted by dynamical ejection. These objects will be unlikely to accrete much additional mass, and so we can assume they have reached their final mass. For the undriven runs, the largest disagreement occurs in the middle of the distribution, indicating a widening difference between the sub-stellar fixed-mass ejected objects and those that remain in the gas reservoir and continue accreting. Further running time will more likely make the gap wider and agreement worse.

The efficiency scale factor is also dependent upon the normalization we have chosen. The minimum mass that we are able to resolve in these simulations is proportional to the Jeans mass evaluated at the maximum level of refinement. Because the Jeans mass is inversely related to the density, normalizing the results to a density higher than our fiducial value of $n = 1100$ cm^{-3} will produce lower mass objects and shift the IMF peak towards lower mass. This will increase the efficiency factor used

Table 2.2. Turbulent box properties

	D/U at t=0	U1a/U1b	D2	U2	D3	U3
$\mathcal{M}_{3D}$	8.37	0.71	0.80	0.72	0.38	0.74
μ_{box}	206.82	19.03	10.74	12.41	2.6	4.59
α_{vir}	1.67	0.06	0.11	0.08	0.06	0.16

Note. — The values for the small boxes are determined using the box length L_{small}=0.25 pc.

to scale the distribution to the universal IMF.

Studying the time evolution of the two simulations shows the origin of the different stellar populations. In simulation D2, the initial collapse and core fragmentation produces three well separated objects that remain fairly far apart. A few additional objects form, but they do not undergo large gravitational interactions with the primaries, and so they remain within the core and continue accreting. In contrast, in U2 and U3 the lack of global turbulent support causes mass to fall onto the early formed protostellar cores resulting in contraction of the clump. This causes all the protostars to gravitate towards the core center. As the protostellar proximity increases, the accretion disks interact and become gravitationally unstable (see discussion in § 4.6). Fragmentation ensues. The stellar systems become increasingly dynamically unstable with the addition of these small latecomers, which rapidly gravitationally interact with the larger protostars and are thrown out of the high density reservoir of gas. Their small envelopes are stripped away, thus truncating the accretion process and effectively fixing their stellar masses (see Figure 2.11). This truncation process occurs for approximately half of the objects formed in the undriven simulations (see discussion of brown dwarfs in § 4.5).

Table 2.3. Stellar Masses ($M_\odot$)

Δ t[a]	23 kyr		53 kyr	
Resolution	5 AU	10 AU	5 AU	10 AU
	0.834	0.705	1.224	0.925
	0.000	0.216	0.000	0.369
	0.264	0.262	0.571	0.455
	0.171	0.175	0.762	0.768
	0.000	0.036	0.106	0.141
	···	···	0.061	0.036
	···	···	0.128	0.180

[a]Time estimated from formation of the first sink particle.

Note. — The subscripts 10 (U1a) and 9 (U1b) represent the number of AMR levels. The sink particle absence in the second row of the high-resolution column is due to an early merger ($m < 0.1$ M$_\odot$ with the neighbor listed in the first row.)

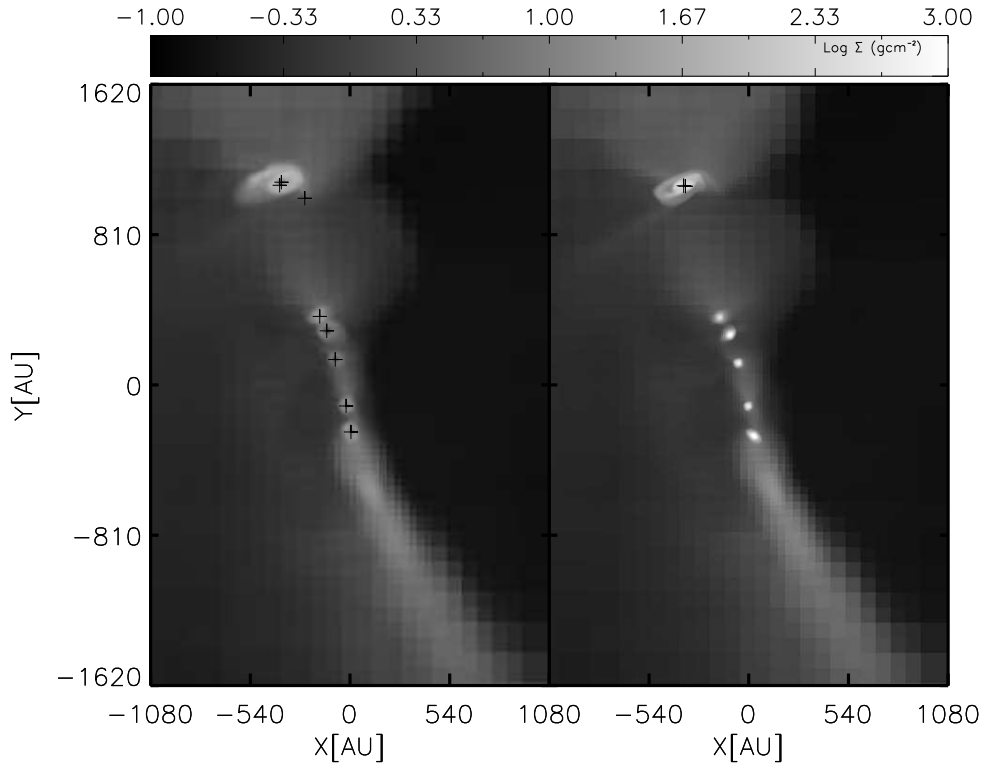

Figure 2.7 The figure shows the log column density of a core in the decaying turbulence simulation U1b (left) and U1a (right) with resolution of 10 AU and 5 AU 16 kyr after the formation of the first sink particle.

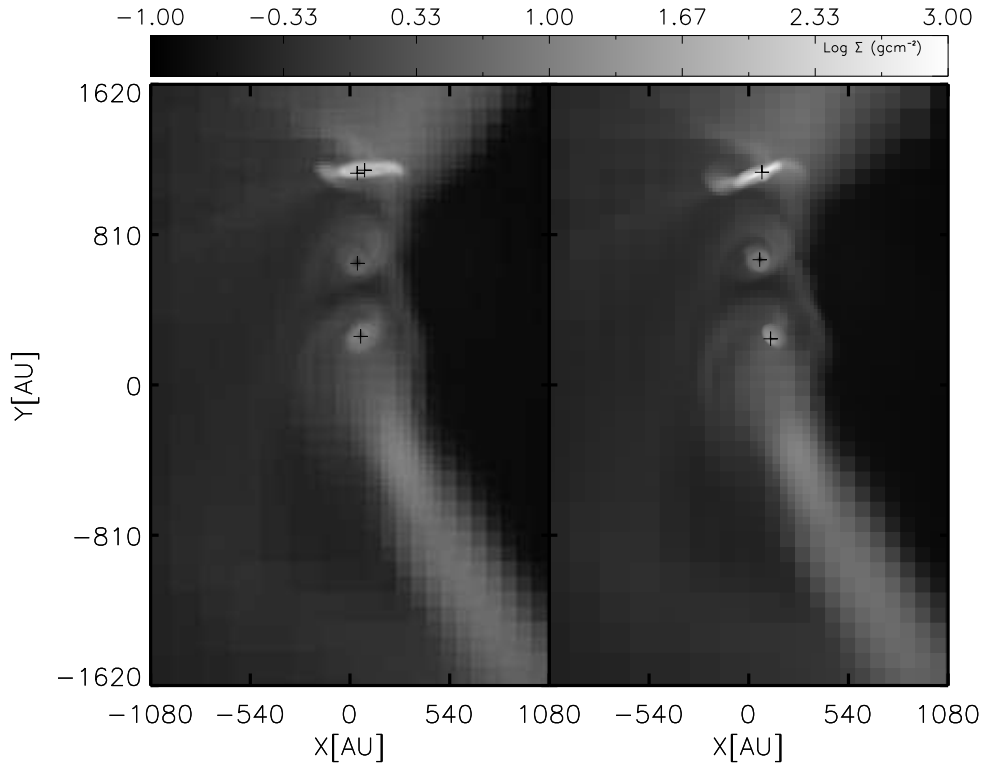

Figure 2.8 The figure shows the log column density of a core in the decaying turbulence simulation U1b (left) and U1a (right) 23 kyr after the formation of the first sink particle.

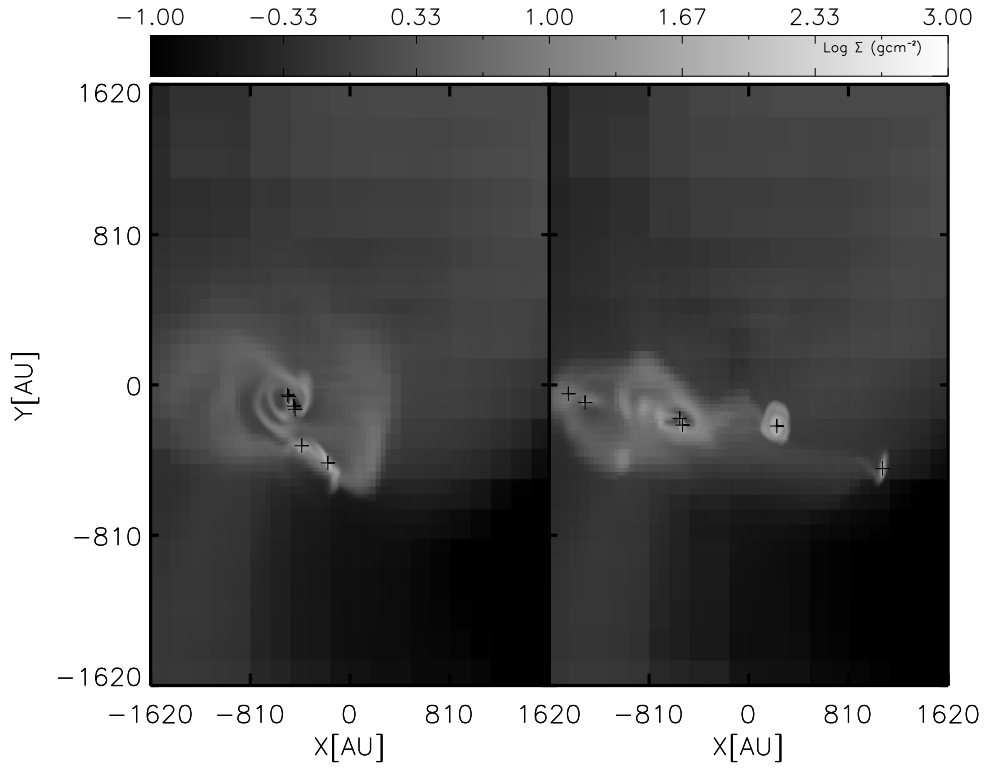

Figure 2.9 The figure shows the log column density of a core in the decaying turbulence simulation U1b (left) and U1a (right) 53 kyr after the formation of the first sink particle.

2.4.4 Accretion

There are two main accretion paradigms. In both models, star formation begins with the outside-in formation of gravitationally bound cores and their inside-out collapse. However, the core accretion model proposes that the main protostellar accretion phase takes place early on and continues until the entire core mass is accreted or expelled, after which accretion becomes negligible (Shu et al. 1987; Nakano et al. 1995; Matzner & McKee 2000). Thus, the initial core size and subsequent feedback effects limit the mass of the protostars. In contrast, the competitive accretion model proposes that stars begin in a cloud as wandering, accreting 0.1 $M_\odot$ seeds, whose final mass is determined by the protostar's location in the clump (Bonnell et al. 1997, 2001). Mass segregation is a common feature of this model, such that the largest mass objects inhabit the region of highest gravitational potential and the smallest objects inhabit the less dense gas, usually having been ejected from the center by gravitational interactions.

In our results, there are two accretion phases. Initially, there is a transient period of high accretion during which the initial infalling gas accretes onto the newly formed sink particle and gas is depleted from the cells inside the accretion region. This phase is model independent and occurs while the newly created sink particle region reaches pressure equilibrium with the surrounding gas. Generally less than 10% of the accretion occurs during this time. During the second phase, the accretion rate approaches the Shu model for core accretion,

$$\dot{M}_* = 0.975 c_s^3/G, \tag{2.12}$$

Shu et al. (1987), although in most cases the accretion rate is gradually declining. This solution is valid until the rarefaction wave reaches the core, i.e., when approximately half of the original core mass has been accreted (McLaughlin & Pudritz 1997; McKee & Tan 2002). Following this phase, the accretion rate is expected to diminish as the density of the surrounding gas decreases. Our simulations end before the accretion rate definitively declines.

To illustrate the differences between the protostellar systems, we plot the mass as a function of time for all sink particles, the instantaneous mass accretion rate for

the first two formed objects, the time-averaged accretion rate, and the total mass in sink particles as a function of time. The turbulent core accretion and competitive accretion models describe the evolution of the stellar population in cases D2 and U2, respectively. In the former case, objects are mainly formed from core fragmentation with separations larger than 1000 AU. The average accretion onto the protostars initially agrees with the Shu model but, modulo fluctuations, diminishes over time as the core mass depletes (Figure 2.12). Meanwhile, the core envelope accretes according to the Bondi-Hoyle model of turbulent accretion Krumholz et al. (2006b). For driven turbulent environments the box Mach number remains sufficiently high such that the core does not gain a substantial amount of mass during the core dynamical time and the main accretion phase of the forming protostars will be limited by this time. However, in the decaying turbulent case loss of turbulent pressure support potentially causes significant additional mass to accrete onto the core, resulting in a more constant protostellar accretion rate (Figure 2.12, bottom row). However, the differences in the accretion rates of the most massive objects are subtle due to the significant fluctuations.

Perturbations to the accretion disks and clumpiness of the infalling gas cause fairly large variability in the sink particle accretion rate as illustrated in Figure 2.12. However, we do not observe that most of the mass is deposited in short intervals by clumpiness in the disk as noted by Vorobyov & Basu (2006), who model 2D axi-symmetric disks with magnetic fields. The absence of this effect in our calculations is most likely due to our Cartesian grid geometry and resolution rather than lack of magnetic fields (Basu, private communication). The $r-\phi$ geometry used by Vorobyov & Basu (2006) is more suitable for disk treatment and has lower numerical viscosity, which may suppress small-scale clumpiness.

Due to differences in core accretion, the two cases produce very different stellar populations. In the driven cases, which form fewer objects, protostars accrete more smoothly and do not undergo strong dynamical interactions with their neighbors. However, in the decaying cases collapse pushes the protostars to the core center, where the large number and close proximity of protostars accreting from the gas reservoir precipitates the ejection of the smallest members. This can be observed in

Figure 2.12 (U3) as a precipitous drop off in the accretion rate for individual objects or as flatlining of the object mass (Figure 2.13, bottom row). Differences in object number are caused by turbulent support, which prohibits or delays collapse and infall. High accretion causes fragmentation and drives forming objects to the gravitational center, where dynamical interaction occurs. This close proximity results in object ejection and destabilization of the accretion disks, leading to new fragmentation. The differences in accretion rates and stellar population between the two cases support the intimate connection between the maintenance of turbulence, protostellar accretion, and stellar population (Krumholz et al. 2005a). In spite of individual accretion fluctuations, the total accretion of the objects from the core is dominated by the largest objects, such that the fraction of the core accreted is relatively smooth over time as shown by Figure 2.14.

2.4.5 Brown Dwarfs

Brown dwarfs (BD), defined as objects with masses $M_* \leq 0.08 M_\odot$, are observed to comprise ∼10-30 % of all luminous objects in star forming regions (Andersen et al. 2006; Luhman et al. 2007). In the Chabrier (2005) IMF, with which we compare, BDs comprise ∼20% of the total population. Understanding the population, origins, and connection between planets and hydrogen-burning stars is essential to formulating a successful theory of star formation. Observations remain particularly ambiguous concerning the primary formation mechanism of BDs, but a number of theories exist. Of these, proposals for BD formation by turbulent fragmentation, ejection, or disk fragmentation have the most potential for generating BDs in sufficient numbers (Padoan & Nordlund 2004; Reipurth & Clarke 2001; Whitworth & Stamatellos 2006; Stamatellos et al. 2007). Simulations provide an important vehicle for testing these theories, and we discuss the BD population of our simulations in this section.

Our driven turbulence high-resolution cores do not produce any sink particles with final substellar mass, However, this conclusion is sensitive to the assumed constant efficiency scaling factor. If BDs are formed via the same mechanism as stars, accrete from a disk, and produce outflows (Luhman et al. 2007) then the same efficiency factor will likely be valid for both stars and BDs in the simulation. In

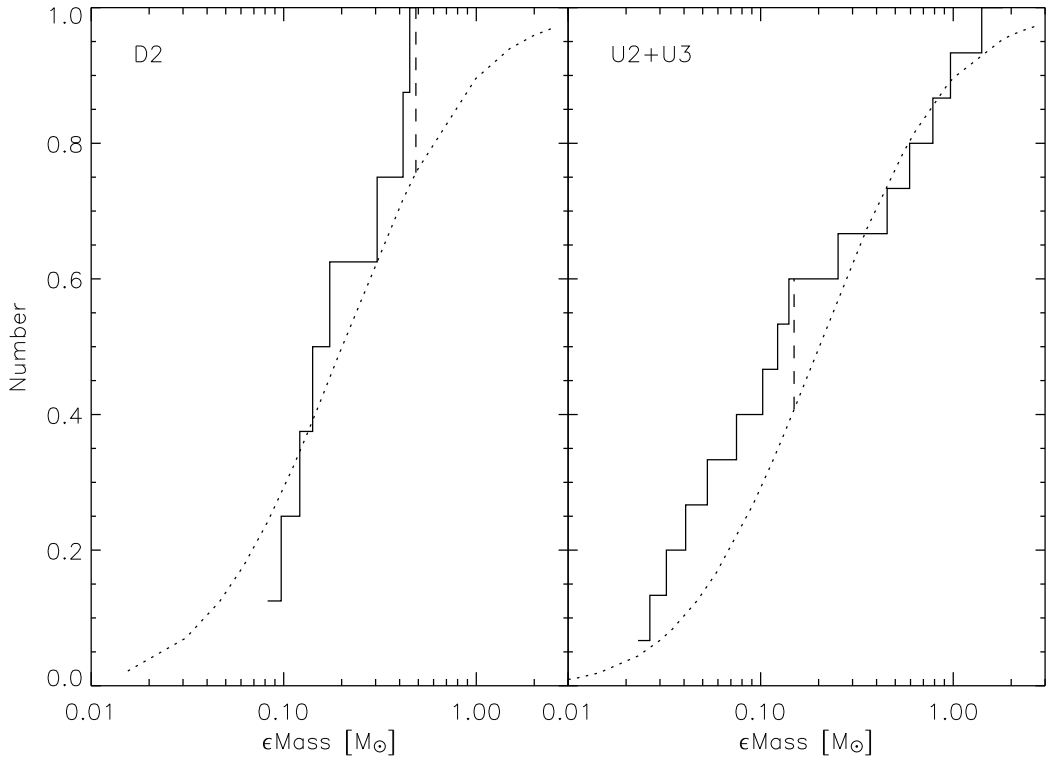

Figure 2.10 The figure shows the cumulative distribution function (solid line) at t=0.26 Myr for D2 (*left*), U2+U3 (*right*), where the dotted line is the Chabrier (2005) IMF fit. The dashed vertical line represents the point of largest disagreement. The probability that the data are drawn from the Chabrier IMF is 67% and 59% with efficiency scale factors of 0.4 and 1.0, respectively.

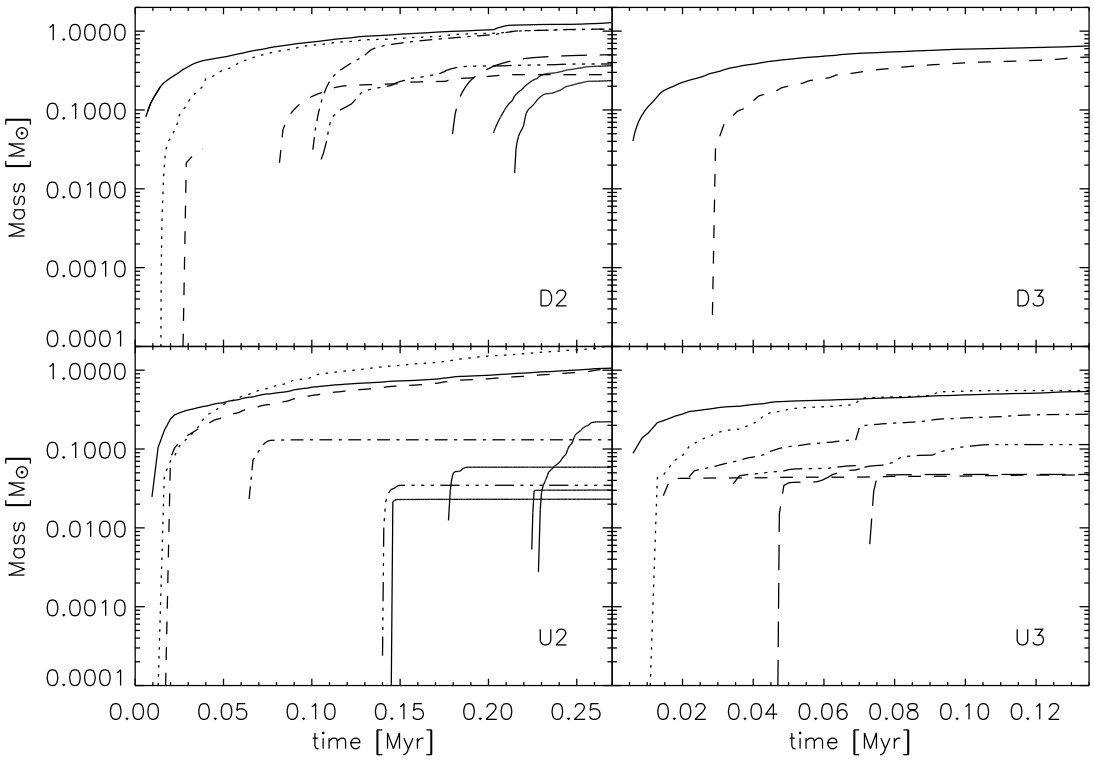

Figure 2.11 The figures show the sink particle mass as a function of time for runs D2, D3, U3, and U2 shown clockwise from top left. Each line style represents a different particle.

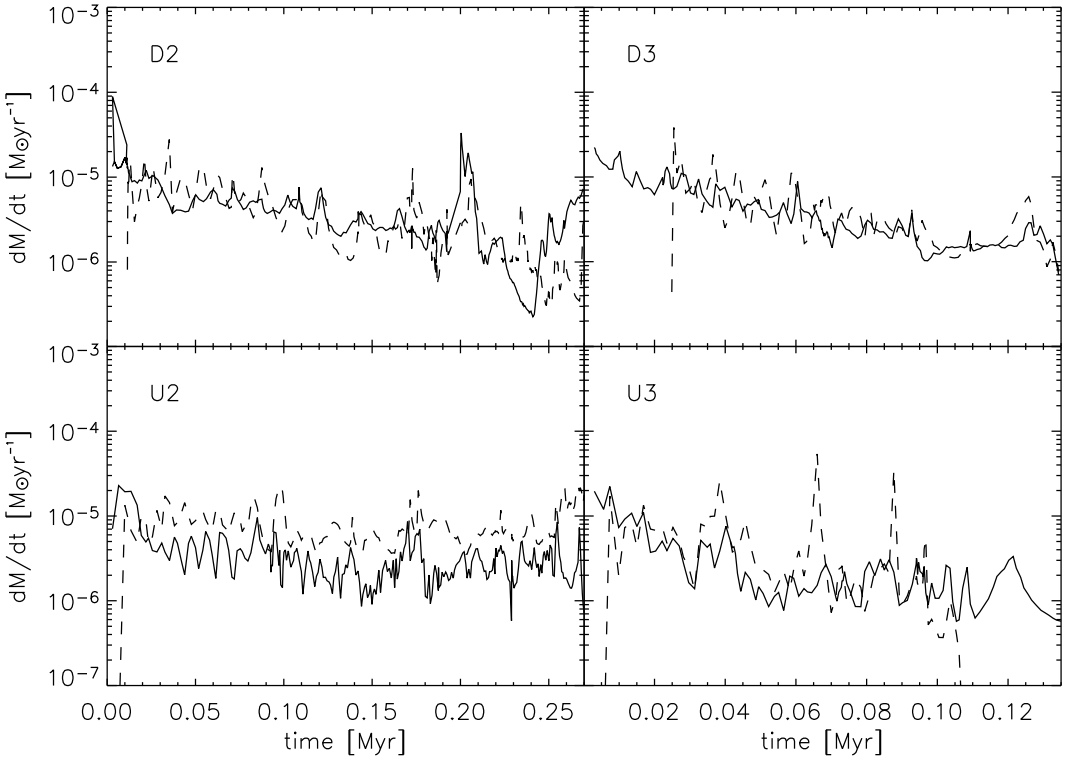

Figure 2.12 The figures show the instantaneous sink particle accretion rate as a function of time for runs D2, D3, U3, and U2 shown clockwise from top left. Only the history of the two first forming particles is shown for clarity.

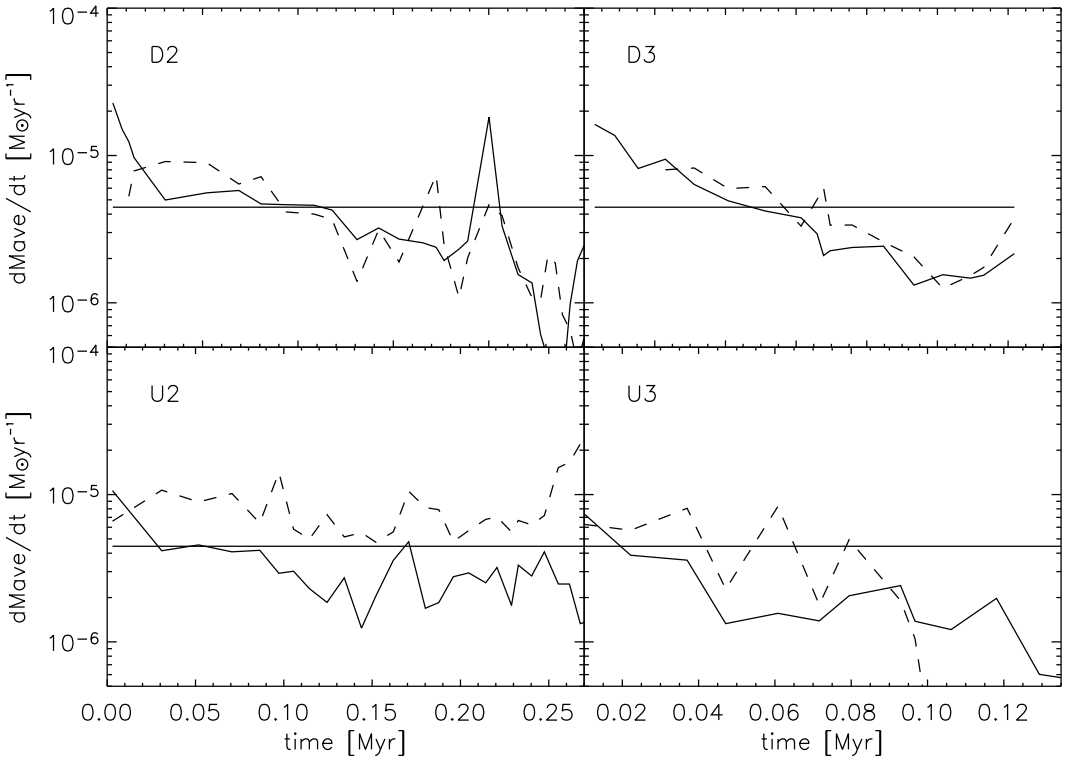

Figure 2.13 The figures show the averaged sink particle accretion rate for the first two sink particles as a function of time for runs D2, D3, U3, and U2 shown clockwise from top left. The average is taken over 10 consecutive timesteps, and the solid horizontal line indicates the value of $c_{\rm s}^3/G$.

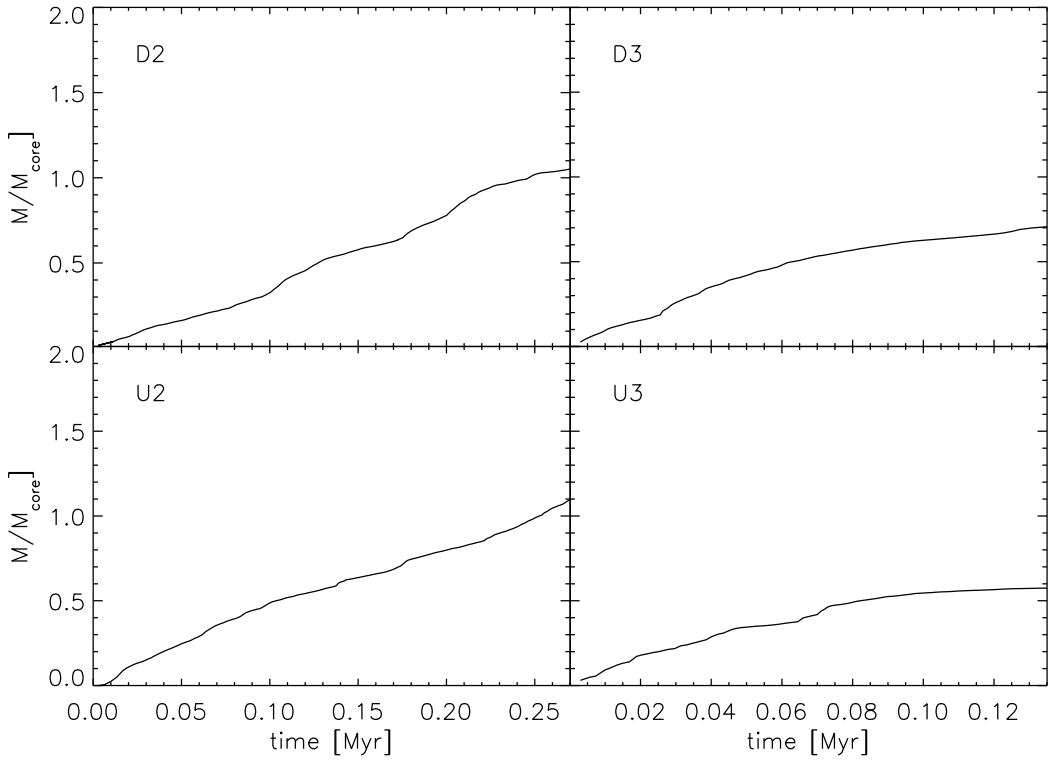

Figure 2.14 The figures show the total mass accreted normalized to the initial bound core mass as a function of time for runs D2, D3, U3, and U2 shown clockwise from top left.

contrast, the decaying turbulence cores form BDs comprising 33% of the number of objects, where the BDs are primarily created by prematurely truncated accretion. This result agrees with the competitive accretion paradigm. For example, Bate et al. (2002) find that ∼44 % of the objects that form in their 50 $M_{\odot}$ decaying turbulent cloud simulation qualify as BDs. We note that their calculation is initialized with uniform density and turbulent velocity field, but the turbulence never achieves a steady relaxed state. Despite this difference, our decaying turbulence runs form BDs in a similar manner and proportion.

Ideally, we would like to understand the BD population in various star forming regions as a function of their general properties. The turbulent fragmentation model predicts an upper limit on the total mass available for the formation of BDs as a function of the Mach number and average number density (Padoan & Nordlund 2004). According to their model, the total gas mass *available* to make BDs from turbulent compressions is 0.4% of the total gas mass or 3.7 $M_{\odot}$ as a function of our simulation Mach number and density. If the SFR per free-fall time for the driven and decaying runs is respectively 14.3% and 13.6% then the total maximum possible mass in BD due to turbulent fragmentation as a fraction of the actual mass turned into stars is 2.8% and 2.9%. For comparison, the fraction of the actual luminous mass turned into BDs according to the Chabrier IMF is ∼2%. Our high-resolution protostellar systems have a BD mass fraction of 0.0% and 3.2% for D2 and U2 + U3, respectively, using the efficiency factor from Figure 2.10. However, the turbulent fragmentation model gives only the maximum fraction of gas that can be converted to BDs by turbulent compressions and it does not include possible BD formation in disks (Goodwin et al. 2007). Fragmentation of disks and dynamical ejection is responsible for all of the BDs in the decaying simulation. Thus, comparison between the decaying turbulence models and turbulent fragmentation prediction is misleading.

The absence of BDs in the driven runs is reasonable if BDs actually form via turbulent fragmentation. In such a process, small low-mass objects form from small low-mass cores. Since we have not chosen any particularly small cores for high-resolution study, we would not expect to find many BDs. Thus, scaling to the

stellar IMF, which has a peak at ~ 0.2 $M_\odot$, requires a small efficiency factor. The core distribution is also constrained by the turbulent resolution. The minimum expected core mass is the Bonnor-Ebert mass evaluated at the maximum turbulent gas density. According to the turbulent fragmentation model, this maximum is set by the probability density function (PDF) of the gas density. The resolution and Mach number of our simulation yield a density PDF that falls off at $\sim 1.3 \times 10^{-18}$ g cm^{-3} or $M_{\rm BE} \simeq 0.2\ M_\odot$. The minimum mass estimated from this density agrees with the minimum sink particle mass at the end of a free-fall time at low-resolution. Since this mass is well above the maximum BD mass, it also explains the low abundance of low-mass objects at high-resolution in the driven simulation. Moreover, this suggests that the driven high-resolution IMF distribution is incomplete at the low-mass end such that scaling to the actual IMF may be optimistic and result in underestimating the core efficiency factor.

One observational measure of BDs is given by the ratio of low-mas stars to BDs: $R = N(0.08 - 1.0{\rm M}_\odot)/(N(0.02 - 0.08)$. Measurements of local star-forming regions give a range of $R_{\rm BD} \simeq 2 - 5$ (Andersen et al. 2006). For the driven and decaying simulations, respectively, we find $R_{\rm BD} > 7$ and $R_{\rm BD} = 3.0$, although these values are clearly sensitive to the statistics of our simulations. These ratios represent lower limits because we have not included radiative transfer, which has been shown to suppress fragmentation Krumholz et al. (2007b); Whitehouse & Bate (2006). Given that BD formation via disk fragmentation dominates in the undriven case, it is unsurprising that these statistics do not agree well with the turbulent fragmentation model prediction. Overall, we find that the driven BD mass fraction agrees more closely with the turbulent fragmentation prediction, whereas the undriven BD mass fraction agrees better with competitive accretion model.

2.4.6 Disk Stability

Analytically, gravitational disk instability is dictated by the Toomre Q parameter, which is given by

$$Q = \frac{c_{\rm s}\kappa}{\pi G \Sigma}, \tag{2.13}$$

Table 2.4. Core mass ($M_\odot$)

Δ t	16 kyr		23 kyr		53 kyr	
Resolution	5 AU	10 AU	5 AU	10 AU	5 AU	10 AU
	0.741	0.758	0.997	0.997	1.907	1.905
	0.124	0.124	0.280	0.283	0.827	0.806
	0.077	0.077	0.177	0.180	0.136	0.191
	0.040	0.037	...	...	...	...
	0.035	0.033	...	...	...	...
	0.291	0.259	...	...	...	...
	...	...	...	...	0.106	0.036

Note. — Decaying simulation data. Masses include the mass of the embedded sink particles. The subscripts 10 (U1a) and 9 (U1b) represent the number of AMR levels. The minimum density of the gas is $\rho = 2 \times 10^{-16}$ g cm^{-3}. The '...' represent cores that have merged with others and cannot be individually distinguished.

Table 2.5. Masses of the protostars ($M_\odot$)

D2 ($M_\odot$)	U2 ($M_\odot$)	D3 ($M_\odot$)	$U3(M_\odot)$
1.221	1.811	0.639	0.586
1.047	1.002	0.453	x 0.552
1.049	0.933	···	0.348
0.490	x 0.223	···	x 0.114 [3]
x 0.382	x 0.131	···	0.048
0.329	0.059	···	x 0.047
0.281	x 0.034	···	···
0.207	x 0.030	···	···
···	x 0.023	···	···

Note. — The larger core masses, D2 and U2, are reported at 260 kyr, while the smaller core masses, D3 and U3, are reported at 130 kyr. The x's represent particles that are ejected from the system by dynamical interactions. The time of first sink particle formation after the onset of gravity for each of the cores is 270, 680, 250, and 660 kyr after the formation of the first sink particle for D2, D3, U2, and U3, respectively.

where κ is the epicyclic frequency, and Σ is the surface density. For values of $Q \lesssim 1$, the disk becomes unstable to gravitational fragmentation. Spiral arms develop for low Q values and fragmentation ensues when Q approaches 1 from above. This fragmentation manifests as a density increase at those locations. The early fragmentation in D2 and U2 generally occurs near the disk perimeters, where it is coldest (see Figure 2.15). In the simulations, sources of disk instability are due to a combination of perturbations from clumpy infalling gas, gravitational influence of nearby bodies (i.e., other sink particles), and from actual collisions between disks. Since the sink accretion radius is $r_{\rm acc} = 4\Delta x$, we neglect the innermost 4 cells in the analysis. We define the disk gas where $\rho \geq 2 \times 10^{-16}$ g cm^{-3}, which agrees fairly well with disk boundaries determined visually. In general, we find disk radii between 150-300 AU and surface densities of a few g cm^{-2}, values similar to observed properties of low-mass disks (Williams & Andrews 2006).

Disk stability and the onset of gravitational instability have been shown to be correlated with the accretion rate of the disk itself (Bonnell 1994; Whitworth et al. 1995; Hennebelle et al. 2004; Matzner & Levin 2005). Higher disk accretion rates increase the likelihood of disk instability. This fact agrees with our observation that more disk fragmentation occurs in simulations U2 and U3, where there is larger infall onto the clump, in contrast to case D2, where disks remain fairly stable. The level of disk instability is directly visible in the plots of the sink particle accretion rates (Figure 2.12); very noisy and irregular accretion corresponds to clumping and disk disturbance. The simulations where sinks have many close neighbors show the highest rates of disk instability and episodic accretion. Note that in Figure 2.12 of run U3 the ejection of a companion substantially reduces the accretion rate fluctuations of the remaining protostar.

There has been considerable recent discourse on the necessary criteria for resolving disks and preventing artificial fragmentation (Nelson 2006; Klein et al. 2007; Durisen et al. 2007). Since we do find that our disks fragment, this is a topic of concern. Most recent simulations, including ours, have used the Jeans condition as defined by Truelove et al. (1997) or Bate & Burkert (1997) to set the minimum refinement of meshes and particles, respectively, in the disk under investigation.

However, Nelson (2006) argues that this criterion is inadequate and inappropriate for cylindrical disk geometry. Additional possible sources of error in our calculation may arise from sink particle gravitational softening, numerical viscosity, and the cartesian nature of the AMR grid. We address these issues here.

In calculating the gravitational sink particle-particle and sink particle-gas interactions, we use a constant softening length $0.5\Delta x^{max}$, where Δx^{max} is the grid spacing on the maximum level. This is much smaller than both the disk radius and the size of the accretion region, so it should have little effect on the behavior of the disk. In general, we find that disk fragmentation tends to occur at the ends of spiral arms, well away from the center of the disk (see Figure 2.15).

Nelson (2006) requires two specific criteria for adequate disk resolution. The first is a Toomre condition,

$$T \geq \frac{\Delta x^l}{\lambda_{\rm T}}, \tag{2.14}$$

where T is the Toomre number, Δx^l is the cell spacing on level l, and $\lambda_{\rm T}$ is the neutral stable wavelength defined by:

$$\lambda_{\rm T} = \frac{2c_{\rm s}^2}{QG\Sigma}. \tag{2.15}$$

The above criterion is analogous to the Jeans criterion defined in Truelove et al.:

$$J \geq \frac{\Delta x^l}{\lambda_{\rm J}}. \tag{2.16}$$

For our simulations, a disk radius of 200 AU is covered by 20 or 40 cells, which is fairly marginal resolution, but we will show it is, in fact, sufficient. We plot the azimuthally averaged density and Toomre Q parameter (equation 2.13) as a function of radius in Figure 2.16. Density enhancements are correlated with low Toomre Q in each refinement case. We also plot the right hand sides of equations (2.14) and (5.12) as functions of radius in Figure 2.17. In all cases, these quantities are under the fiducial value of 1/4. The excess resolution in the central disk is due to the requirement that all cells surrounding a sink particle be refined to the maximum level in order to encompass the accretion region.

Figure 2.15 indicates the borders between AMR grids, so some disk regions within 200 AU become derefined, and $\Delta x^l \rightarrow \Delta x^{l-1}$. However, these regions still satisfy the refinement criteria by a good margin as illustrated by Figure 2.16.

The second criterion formulated by Nelson applies specifically to SPH codes. It postulates the necessity of resolving the disk scale height at the midplane by four smoothing lengths. Nelson argues that insufficient resolution of the vertical structure produces errors in the force balance, thus favoring artificial fragmentation. If we assume a one-to-one conversion between smoothing lengths and grid cells, we can apply it to our calculation. Figure 2.17 shows azimuthally averaged quantities for an accretion disk for ∼2.5, 5, and 10 AU maximum resolution. The lowest resolution run fails to adequately resolve the disk scale height, but we do not see extra fragmentation. This may be because Nelson formulated and tested his criteria for SPH rather than grid-based codes. It is also possible that the one-to-one analog of smoothing length to Δx is not the correct conversion. However, most disagreement between the simulations occurs in the inner regions where the artificial viscosity is high, potentially suppressing fragmentation. In order to determine the cause of the discrepancy, a more detailed high-resolution investigation of disks is necessary.

Krumholz et al. (2004) presents a careful study of the accretion algorithm we use in our sink particle methodology. For a Keplerian disk, ORION agrees well with analytic predictions except when the radius of the disk is comparable to the Bondi radius, $r \sim r_{\rm B} = GM/c_{\rm s}^2$. However, our simulations have $r << r_{\rm B}$ during the main accretion phase and should be unaffected. Also of concern is the magnitude of the numerical viscosity, which has the potential to suppress fragmentation if it is sufficiently high. Using the definition of α viscosity defined in Krumholz et al. (2004), we can estimate the magnitude of the viscosity as a function of disk radius:

$$\alpha \simeq 78\frac{r_{\rm B}}{\Delta x}\left(\frac{r}{\Delta x}\right)^{-3.85} \tag{2.17}$$

$$\simeq 0.8 M_1 T_{10}^{-1} \Delta x_5^{2.85} r_{150}^{-3.85}, \tag{2.18}$$

where r_{150} is the radial distance from the central star in units of 150 AU, M_1 is the stellar mass is units of $M_\odot$, Δx_5 is the cell size in units of 5 AU, normalized to the maximum level of refinement, and T_{10} is the gas temperature in units of 10 K.

This expression is fairly sensitive to the cell size and disk radius. Due to the large α value in the inner region of the disk, artificial viscosity is likely to significantly influence the disk properties within the inner 100 AU. Protostellar disks around low-mass protostars, which are fairly thin and have a low ionization fraction, have been measured to have viscosities of $\alpha \sim 0.01$ (King et al. 2007; Williams & Andrews 2006).

In the resolution study, we find that all disks form exactly two fragments at the same radial locations where $Q \sim 1$. Convergence of the disk density distribution and number of fragments is our main concern. The averaged quantities are slightly different in the three cases, although the general trends are the same. In the lower resolution case the fragmentation is less pronounced, however, this is because sink particles are already present at these locations. It is certainly true that the fragments are not well resolved at the lowest resolution, and we are only marginally resolving the disks. Serious study of accretion disks requires much higher resolution than we adopt in this paper and is best studied in cylindrical or polar coordinate geometry to minimize the effects of numerical viscosity and Cartesian cell imprinting.

Given that observations suggest star-forming cores typically produce 2-3 stars (Goodwin & Kroupa 2005), the large number of objects produced in the high-resolution decaying simulations seems somewhat anomalous. However, the issue of initial multiplicity is not well constrained. The protostellar multiplicity is more difficult to determine directly than multiplicity among field stars due to the difficulty of detecting small obscured objects, some of which may have separations below the resolvable limit. Systems with more than two bodies are unstable and decay through gravitational interactions ultimately decreasing the multiplicity of stellar systems over time. We witness exactly this behavior in the decaying turbulence protostellar systems, which expel low-mass members.

Nonetheless, it is likely that a few of these small fragments are numerical products, resulting from our EOS. For example, Boss et al. (2000) and Krumholz et al. (2007b) both find that fragmentation is sensitive to thermal assumptions and the inclusion of radiative transfer, since heating tends to enhance disk stability. Price & Bate (2007) show that magnetic fields tend to suppress and delay both fragmenta-

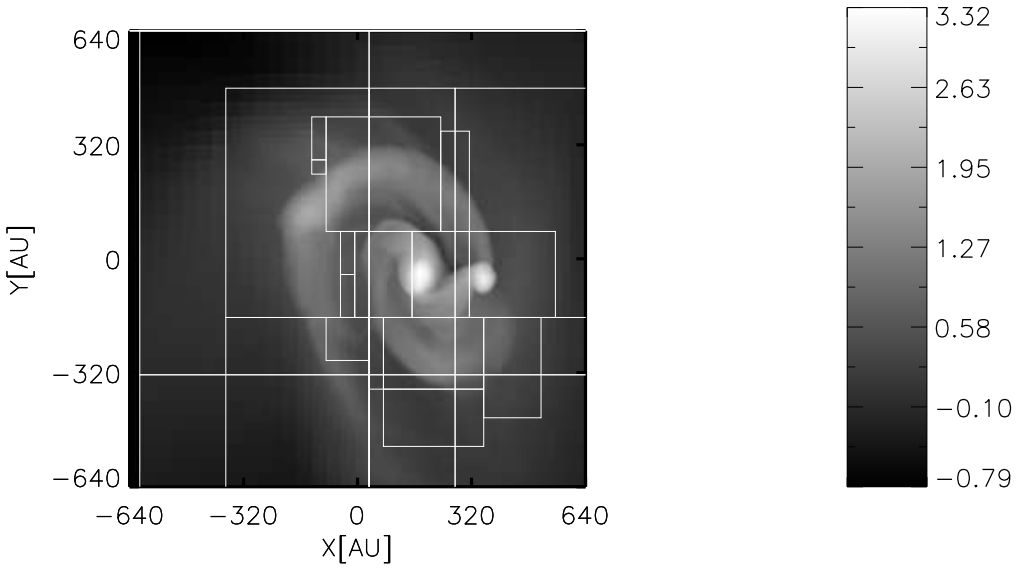

Figure 2.15 The figure shows the log column density (g cm^{-2}) of an accretion disk in run D2 with ll levels of refinement. Two fragments have formed at the edges of the spiral disk structure. The solid white lines denote grid boundaries.

tion and spiral disk structure. It is probable that inclusion of radiative feedback and magnetic fields would suppress some of the small objects that we find in the undriven runs. However, the absence of these objects in the driven simulations indicates a striking difference in the accretion rate, system stability, and fragmentation history with turbulent feedback.

2.5 Conclusions

In this paper we use turbulent simulations with AMR to illustrate distinctions between driven and decaying turbulence. Despite identical initial conditions in the

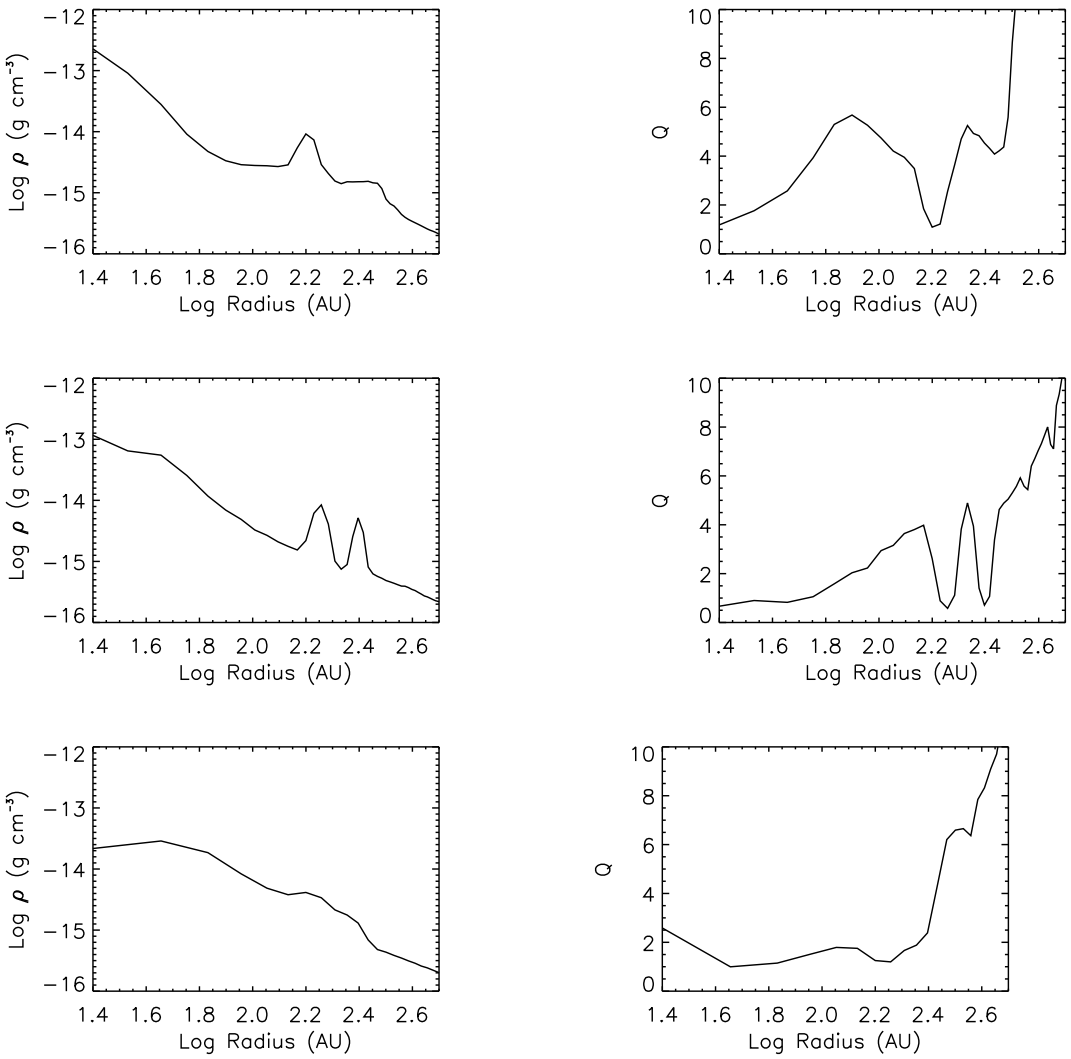

Figure 2.16 The figure shows azimuthally averaged disk properties as a function of log radius (AU) for a disk with $\sim$ 2.5 AU (top), 5.0 AU (middle) and 10.0 AU (bottom) resolution. The left plots show log ρ for a edge -on view of the disk. Plots on the right show log Q vs. log r. The central region corresponding to the sink particle accretion region is excluded from the plots.

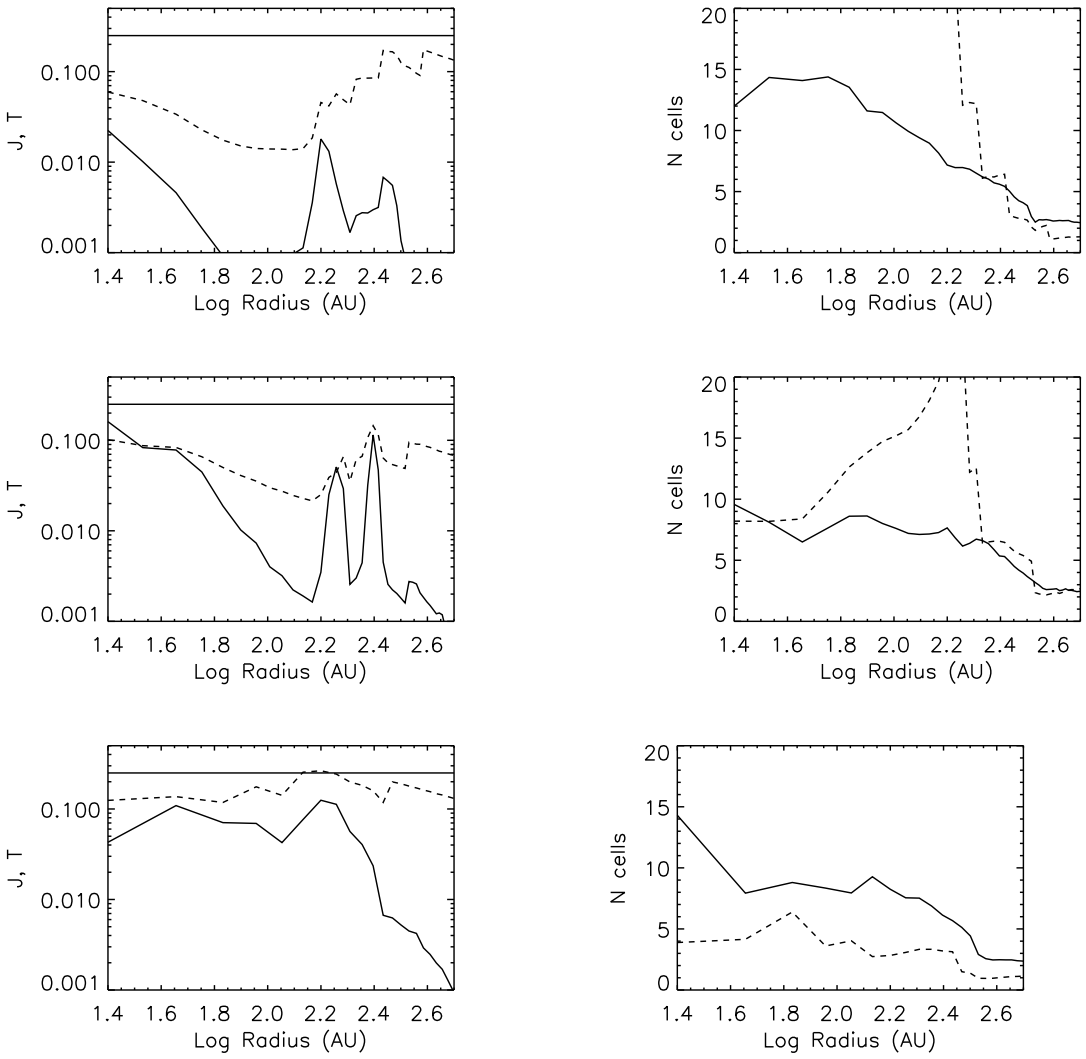

Figure 2.17 The figure shows azimuthally averaged disk properties as a function of log radius (AU) for a disk with $\sim$ 2.5 AU (top), 5.0 AU (middle) and 10.0 AU (bottom) resolution. The first column shows plots of J (dashed line) and T(solid line) vs. $\log r$, where the horizontal line marks the fiducial value of 0.25. The second column shows the number of cells in the disk vertical scale height as a function of $\log r$. The solid line is the required resolution of the vertical scale height according to the Nelson criterion and the dashed line is our resolution. The central region corresponding to the sink particle accretion region is excluded from the plots.

two simulations, we find significant differences between the two cases after one free-fall time. Our simulations neglect the effect of magnetic fields, which are poorly observationally constrained and occupy a place of ambiguous but potentially large importance (Crutcher 1999). Our simulations also lack radiation transfer, instead relying on the barotropic approximation, which may affect the core fragmentation and protostellar multiplicity in our results.

We find that the properties of the cores in driven and decaying turbulence at low-resolution are not sufficiently different to completely dismiss one turbulent environment. This is in part due to the large scatter in our results. For example, we find that the cores in the different environments have similar shapes and mass-size relations. However, we find that cores in the driven simulation have less rotational energy, which is in better agreement with observations (Goodman et al. 1993; Caselli et al. 2002). The linewidth-size relation of the cores forming in driven turbulence is also closer to the observed relation for low-mass regions (e.g., Jijina et al. 1999), while the linewidth-size relation of cores in the decaying simulation is flatter. We find that driven turbulence produces a greater number of cores than decaying turbulence with the potential for new star formation occurring longer than a single dynamical time. In contrast, the decaying simulation stops forming new condensations before one global free-fall time.

The largest differences between the two cases are apparent at high-resolution. We show that our high-resolution simulations are converged and that the resolution is sufficient to capture core fragmentation, despite being marginal for determining the detailed properties of disks. We find that the presence or absence of global virial balance has only a subtle influence on individual accretion rate of the largest object forming in the core at least for the first few core free-fall times. However, the protostars forming in a decaying turbulence environment show clear signs of competitive accretion such that a protostar's accretion rate is tied to its dynamical history and and its location in the clump. This supports the results of Krumholz et al. (2005b) who show that simulations exhibiting competitive accretion do so because of lack of a source of turbulence.

The loss of turbulent feedback in the decaying run affects the dynamic behav-

ior of the forming protostars, resulting in significant disk fragmentation, and BD formation by ejection. This leads to overproduction of BDs in comparison to the observed IMF (Chabrier 2005). In contrast, the driven simulations form few BDs, which can be understood in the context of the turbulent fragmentation model for star formation, which predicts BDs to mainly form from small, highly compressed cores. Observations of low-mass star forming regions do not find large velocity differences or significant spatial segregation between BDs and low-mass objects as obtained in the decaying simulation.

While our simulations of driven and decaying turbulence show some statistically significant differences, particularly in the production of brown dwarfs and core rotation, the uncertainties are large enough that we are not able to conclude whether observations favor one or the other. However, in Paper II we use simulated line profiles to estimate core velocity dispersions and centroid velocities, and we find that decaying turbulence leads to highly supersonic infall onto protostars, which has not been observed. Our results thus give some support to the use of driven turbulence for modeling regions of star formation, but a conclusive determination of which approach is better awaits larger simulations with the inclusion of magnetic fields, protostellar outflows, and thermal feedback.

Acknowledgements

We thank P.S. Li, M. Krumholz and R. Fisher for helpful discussions and suggestions. Support for this work was provided under the auspices of the US Department of Energy by Lawrence Livermore National Laboratory under contacts B-542762 (S.S.R.O.) and DE-AC52-07NA27344 (R.I.K.); NASA ATP grant NNG06GH96G (CFM and RIK); grant AST-0606831 (CFM and RIK); and National Science Foundation under Grant No. PHY05-51164 (CFM and SSRO). Computational resources were provided by the NSF San Diego Supercomputing Center through NPACI program grant UCB267; and the National Energy Research Scientific Computer Center, which is supported by the Office of Science of the U.S. Department of Energy under contract number DE-AC03-76SF00098, though ERCAP grant 80325.

Chapter 3

The Kinematics of Molecular Cloud Cores in the Presence of Driven and Decaying Turbulence: Comparisons with Observations

Offner, Krumholz, Klein, & McKee, 2008, AJ, 136, 4040[1]

3.1 Introduction

The origin of the stellar initial mass function (IMF) is one of the most important problems in astrophysics. Since the discovery of supersonic linewidths in star forming regions, understanding turbulence has been crucial for developing the theoretical framework for molecular cloud (MC) evolution, core formation, and the IMF. Ongoing debate in this field concerns whether the formation and destruction of MCs is dynamic and non-equilibrium (e.g., Elmegreen 2000; Hartmann et al. 2001; Dib et al. 2007) or slow and quasi-equilibrium (Shu et al. 1987; McKee 1999; Krumholz et al. 2006a; Krumholz & Tan 2007; Nakamura & Li 2007). The former mode would

[1]The Astronomical Journal, 136, 404-420, July,

be characterized by transient turbulence, dissipating quickly on timescales comparable to the cloud lifetime so that giant MCs are destroyed within $\sim$ one dynamical time. The latter case corresponds to regenerated turbulence, perhaps injected by the formation of the cloud, protostellar outflows, H II regions, external cloud shearing or supernova blastwaves, that is sufficiently strong to inhibit global gravitational collapse over many dynamical times. As shown by Offner et al. (2008a) and Krumholz et al. (2005a), the presence or absence of turbulent feedback directly relates to the physical mechanism of star formation and determines whether stars form by the formation and collapse of discrete protostellar cores (Padoan & Nordlund 2002; McKee & Tan 2002) or competitive accretion (Bonnell et al. 2001). In the turbulent core model, the cloud remains near virial equilibrium on large scales and collapse occurs only locally in cores that are created and then mass-limited by the initial turbulent compressions. In the competitive accretion model, turbulence generates the initial overdensities, but without turbulent support, the cores are wandering accreting seeds, competing for gas from the cloud, limited only by the size of the MC as a whole.

There have been a number of recent observational papers investigating starless and protostellar core velocity dispersions, envelopes, and relative motions (André et al. 2007; Kirk et al. 2007; Muench et al. 2007; Rosolowsky et al. 2008; Walsh et al. 2004), quantities that provide important clues about the core lifetimes and evolution, and about the turbulent state of the natal MC. All of these results, which include observations of a range of star forming regions in different tracers, indicate that observed low-mass cores have approximately sonic central velocity dispersions, at most transonic velocity dispersions in their surrounding envelopes, and relative motions that are slower than the virial velocity of the parent environment. Such results potentially contradict core properties measured in simulations in collapsing clusters exhibiting competitive accretion (Ayliffe et al. 2007; Klessen et al. 2005; Tilley & Pudritz 2004).

In this paper we analyze the simulations described in Offner et al. (2008a), which follow the evolution of an isothermal turbulent molecular cloud with and without continuous injection of energy to drive turbulent motions. These simula-

tions use the adaptive mesh refinement (AMR) code ORION (Truelove et al. 1998; Klein 1999). The goal of our present work is to explore differences between cores forming in these two environments and to provide predictions of their properties for observational comparison. For this purpose, we simulate observations of our cores using dust continuum and molecular lines, with realistic telescope resolutions. Unlike earlier comparisons of isothermal self-gravitating simulations with observations (Ayliffe et al. 2007; Klessen et al. 2005; Ballesteros-Paredes et al. 2003), we perform more detailed radiative post-processing in order to simulate more accurately synthetic observations of our data. We also compare these observational measures for both driven and decaying turbulence, which has not previously been investigated. Keto & Field (2005) obtain post-processed simulated line profiles of several common tracers modeled with a non-LTE radiative transfer code and find good agreement with observed isolated cores. However, their initial conditions are simple 1D non-turbulent hydrostatic models and they halt the calculations when the central cores velocity exceeds the sound speed. Further, we report core-to-core centroid velocity dispersions of the simulated cores, which has not previously been studied in turbulent simulations. Work by Padoan et al. (2001) comparing observed large-scale gas motions with 128^3 fixed-grid isothermal, non-self-gravitating, MHD simulations found good agreement with the gas centroid velocity dispersion-column density relation. In our higher resolution simulations, we instead focus on the smaller physical scales of self-gravitating cores and their observed properties, and we neglect the effects of magnetic fields.

In section 2, we describe our simulations in detail. Section 3 contains the methods of data analysis we use to simulate observations of our AMR data. In section 4, we present our results on the central core dispersions, relative motions, and dispersions of the surrounding core envelopes. In section 5 we present quantitative comparisons with observational data. Finally, section 6 contains our conclusions.

3.2 Simulation Parameters

As described in Offner et al. (2008a), our two simulations are periodic boxes containing an isothermal, non-magnetized gas that is initially not self-gravitating. We first drive turbulent motions in the gas for two box crossing times, until the turbulence reaches statistical equilibrium, i.e., the power spectrum and probability density function shapes are constant in time. We adopt a 1D Mach number of 4.9 (3D Mach number of 8.5). At the time gravity is turned on, which we label t=0, our two simulations are identical. In one simulation energy injection is halted and the turbulence gradually decays, while in the other turbulent driving is maintained so that the cloud remains in approximate virial equilibrium. The initial virial parameter is defined by

$$\frac{5\sigma_{\rm 1D}^2 R}{GM} = \alpha_{\rm vir} \simeq 1.67, \tag{3.1}$$

where $\sigma_{\rm 1D}$ is the velocity dispersion, M is the cloud mass, and $R = L/2$ is the cloud radius. We use periodic boundary conditions and 4 levels of refinement, which corresponds to an effective 2048^3 base grid for an equal-resolution, fixed-grid calculation.

Isothermal self-gravitating gas is scale free, so we give the key cloud properties as a function of fiducial values for the number density of hydrogen nuclei, $\bar{n}_{\rm H}$, and gas temperature, T. It is then easy to scale the simulation results to the astrophysical region of interest. For the adopted values of the virial parameter and Mach number, the box length, mass, and 1-D velocity dispersion are given by

$$L = 2.9\ {T_1}^{1/2} \bar{n}_{\rm H,3}^{-1/2}\ {\rm pc}\,, \tag{3.2}$$

$$M = 865\ {T_1}^{3/2} \bar{n}_{\rm H,3}^{-1/2}\ {\rm M}_\odot\,, \tag{3.3}$$

$$\sigma_{\rm 1D} = 0.9\ {T_1}^{1/2}\ {\rm km\ s^{-1}}\,, \tag{3.4}$$

$$t_{\rm ff} = 1.37\ \bar{n}_{\rm H,3}^{-1/2}\ {\rm Myr}\,, \tag{3.5}$$

where we have also listed the free-fall time for the gas in the box for completeness.

These equations are normalized to a temperature $T_1 = T/10$ K and average hydrogen nuclei number density $\bar{n}_{\rm H,3} = \bar{n}_{\rm H}/(1 \times 10^3\ {\rm cm^{-3}})$. For the remainder of this paper, all results will be given assuming the fiducial scaling values of $\bar{n}_{\rm H} = 1.1 \times 10^3$ cm^{-3} and $T = 10$ K (Perseus) or $\bar{n}_{\rm H} = 2.0 \times 10^4$ cm^{-3} and $T = 20$ K (ρ Ophiuchus;

see §5) and assuming a mean particle mass of μ=2.33$m_{\rm H}$. These conditions place ρ Ophiuchus slightly above the observed linewidth-size relation (Solomon et al. 1987; Heyer & Brunt 2004):

$$\sigma_{\rm 1D} = 0.5 \left(\frac{L}{1.0{\rm pc}} \right)^{0.5} {\rm km\ s^{-1}}, \tag{3.6}$$

where L is the cloud length (we assume that Perseus lies on this relation–see §3.5).

Note that this relation differs somewhat from the relation given by Heyer & Brunt (2004) since the length scale determined from a Principal Component Analysis is smaller than the actual size of the region being sampled (see McKee & Ostriker 2007). These parameters may be adjusted to different conditions using equations (3.2)-(3.5). However, once we simulate an observation of the data for a given tracer, the scaling is fixed. Using these units, the minimum cell size is $\sim$ 90 AU and 280 AU for ρ Ophiuchus and Perseus, respectively.

In the simulations, we introduce sink particles in collapsing regions that violate the Jeans condition (Truelove et al. 1997) at the finest AMR level (Krumholz et al. 2004), where we adopt a Jeans number of $J = 0.25$. Cores that contain sink particles are analogous to observed protostellar cores, which contain a central source, while cores without sink particles can be considered prestellar. This distinction is an important one in some cases and we discuss some differences in the two simulations in §3.4. Note that due to our resolution and neglect of protostellar outflows, the sink particles represent a mass upper limit for any potentially forming protostar.

3.3 Analysis

Since our goal in this paper is to contrast the simulations and compare them with observations, we must attempt to replicate an observer's view of our simulation. Observations of core kinematics, such as those of André et al. (2007, henceforth A07), Kirk et al. (2007, henceforth K07), and Rosolowsky et al. (2008, henceforth R08), generally trace the gas mass using dust continuum data and obtain velocity information by observing the same region in one or more molecular tracers. We process our simulations using a rough approximation of these techniques as follows. First, we select a fiducial cloud distance of either 125 pc, corresponding to the distance

to the Ophiuchus MC, or 260 pc for comparisons with the Perseus MC. Second, we select an appropriate telescope resolution of 26" or 31" FWHM, corresponding to 0.02 pc and 0.04 pc at our adopted distances, and approximate the telescope beam as Gaussian in shape. We perform all line fits assuming 0.047 km s^{-1} velocity resolution per channel. Increasing the velocity resolution further has little effect on the line fits. For simplicity we adopt the same resolution for observations in dust continuum and in all molecular tracers. Our fiducial resolution is typical of observations of core kinematics (e.g., A07, K07, R08).

For the dust continuum observations, since our gas and dust are isothermal and the simulation domain is everywhere optically thin at typical observing wavelengths of $\sim$ 1 mm, the dust intensity emerging from a given pixel is simply proportional to the column density in that pixel. We therefore define a dust continuum map by computing the column density and convolving the resulting map with the beam. To avoid introducing unnecessary and artificial complications, we neglect observational uncertainties in the conversion from an observed dust continuum intensity to a column density, and assume that the column density can be reconstructed accurately except for beam smearing effects. We identify cores by finding the local maxima directly from the column density data. In the analysis, we consider only local maxima with peak columns greater than 0.1 of the global maximum column of the smeared data. This cutoff corresponds to $\sim$ twice the mean smeared column density.

To model molecular line observations, we choose three representative lines, the $J = 2 \rightarrow 1$ transition of $C^{18}O$, $J = 1 \rightarrow 0$ transition of N_2H^+, and the $NH_3(1,1)$ transition, which have critical densities of 4.7×10^3 cm^{-3}, 6.2×10^4 cm^{-3}, and 1.9×10^3 cm^{-3}, respectively. (For this calculation and all the others presented in this paper, we use molecular data taken from the Leiden Atomic and Molecular Database[2], Schöier et al. 2005). These lines are often used in observing core kinematics because they span a range of densities and, with the exception of $C^{18}O$ along the densest sightlines, are generally optically thin in low-mass star-forming regions. We discuss the issue of optical depths in more detail in § 3.5.2.

We generate a position-position-velocity (PPV) data cube from our simula-

[2]See http://www.strw.leidenuniv.nl/∼moldata

tions in each of these lines using a two step procedure, which combines elements of Krumholz et al. (2007a) and Krumholz et al. (2007b). The first step is to compute the emissivity as a function of density. Since, as we shall see, the density-dependence of the molecular emission has important consequences, we cannot assume that these species are in local thermodynamic equilibrium (LTE). Instead, we assume that the gas is in statistical equilibrium, that it is optically thin, and that radiative pumping by line photons is negligible. Note that the advection time of the gas is large compared to the molecular collisional and radiative time scales, which are on the order of a few years for the mean density of our simulations. Thus, the gas reaches statistical equilibrium essentially instantaneously relative to the gas motion. Collisional excitation dominates over radiative excitation or de-excitation by line photons along lines of sight where the density is above the transition critical density. Since we are particularly interested in the high density regions of the cores, we need not consider radiative pumping in our analysis. However, we do include radiative excitation and de-excitation due to the cosmic microwave background, since this can be significant for lines at very low frequencies such as $NH_3(1,1)$.

For a molecule like $C^{18}O$ with no hyperfine structure, under these approximations the fraction f_i of molecules of a given species in bound state i is given by the equations of statistical equilibrium

$$\begin{aligned} \sum_j (n_{\mathrm{H}_2} q_{ji} + A_{ji} + B_{ji} I_{\mathrm{CMB}}) f_j &= \left[\sum_k (n_{\mathrm{H}_2} q_{ik} + A_{ik} + B_{ik} I_{\mathrm{CMB}}) \right] f_i \\ \sum_i f_i &= 1, \end{aligned} \tag{3.7}$$

where n_{H_2} is the molecular hydrogen number density, q_{ij} is the collision rate for transitions from state i to state j, A and B are the Einstein coefficients for this transition, and I_{CMB} is the intensity of the cosmic microwave background radiation field (which is simply the Planck function for a 2.73 K blackbody) evaluated at the transition frequency. In this expression we adopt the convention that the summations run over all bound states, the spontaneous emission coefficient $A_{ij} = 0$ for $i \leq j$, that B_{ij} is the stimulated emission coefficient for $i > j$, the absorption coefficient for $i < j$, and is zero for $i = j$, and that $q_{ij} = 0$ for $i = j$. For molecules with hyperfine structure,

we show in Appendix 3.7 that with some additional approximations equation (3.7) continues to hold provided that the rate coefficients q_{ij}, A_{ij}, and B_{ij} are understood as statistically-weighted sums over all the hyperfine sublevels of states i and j.

For molecules without hyperfine structure, the net emission minus absorption of the background CMB produced by a parcel of gas along the line of sight is then given by

$$j_{ij} - \chi_{ij} I_{\rm CMB} = \frac{h\nu_{ij}}{4\pi} X n_{\rm H} \times [f_i(A_{ij} + B_{ij} I_{\rm CMB}) - f_j B_{ji} I_{\rm CMB}], \tag{3.8}$$

where χ_{ij} is the extinction of the CMB due to resonant absorption, ν_{ij} is the transition frequency, X is the abundance of the species in question relative to hydrogen nuclei, and $n_{\rm H}$ is the number density of hydrogen nuclei. Physically, this quantity represents the net radiation intensity added by transitioning molecules over and above what one would see at that frequency due to the CMB alone, under the assumption that the line is sufficiently thin that the CMB dominates the intensity at that frequency. It is the intensity one will observe in a line after subtracting off the continuum. In the case of a molecule with hyperfine structure, under the standard assumption that the hyperfine sublevels are populated in proportion to their statistical weight (see Appendix 3.7), the intensity produced by a single transition from level i, hyperfine sublevel α to level j, hyperfine sublevel β is given by

$$j_{i\alpha j\beta} - \chi_{i\alpha j\beta} I_{\rm CMB} = \frac{h\nu_{i\alpha j\beta}}{4\pi} X n_{\rm H} \left[f_i \frac{g_{i\alpha}}{g_i} (A_{i\alpha j\beta} + B_{i\alpha j\beta} I_{\rm CMB}) - \frac{g_{j\beta}}{g_j} f_j B_{j\beta i\alpha} I_{\rm CMB} \right], \tag{3.9}$$

where $g_{i\alpha}$ is the statistical weight of hyperfine sublevel α, $g_i = \sum_\alpha g_i$ is the summed statistical weight of all the hyperfine sublevels of state i, and the combination of subscripts $i\alpha j\beta$ indicates the frequency or radiative coefficient for transitions from level i, hyperfine sublevel α to level j, hyperfine sublevel β. If one neglects the very small differences in frequency between the different hyperfine transitions (i.e., one takes $\nu_{i\alpha j\beta} \approx \nu_{ij}$ independent of α and β) and sums equation (3.9) over hyperfine substates α and β, then it immediately reduces to equation (3.8) provided that the rate coefficients are understood to be statistically-weighted sums of the individual hyperfine transition coefficients (per equations 3.20 - 3.22). Thus equation (3.8) gives

the total intensity summed over all hyperfine components. In either the presence or absence of hyperfine splitting, to compute the intensity from our simulations, we solve the system of equations (3.7)-(3.7) for our fiducial temperature T for a wide range of molecular densities $n_{\rm H_2}$ and tabulate the quantities $(j_{ij} - \chi_{ij} I_{\rm CMB})/X$ or $(j_{i\alpha j\beta} - \chi_{i\alpha j\beta} I_{\rm CMB})/X$ as a function of $n_{\rm H_2}$.

The second step to generate the PPV cube from the simulation data is to compute the emergent intensity in each pixel in each velocity channel using our tabulated net emission function. The specific emissivity minus absorption of the gas at a frequency ν is $(j_{ij} - \chi_{ij} I_{\rm CMB})\phi(\nu)$ or $(j_{i\alpha j\beta} - \chi_{i\alpha j\beta} I_{\rm CMB})\phi(\nu)$, in the absence or presence of hyperfine splitting, where $\phi(\nu)$ is the line shape function. To determine $\phi(\nu)$, we assume that the molecules in each cell have a Maxwellian velocity distribution with dispersion $\sigma_v = \sqrt{k_B T/m}$, where m is the mass of the emitting molecule. For this velocity distribution, the line shape function for a fluid with bulk velocity v is

$$\phi(v_{\rm obs}; v) = \frac{1}{\sqrt{2\pi\sigma_\nu^2}} \exp\left[-\frac{(v - v_{\rm obs})^2}{2\sigma_\nu^2}\right], \tag{3.10}$$

where an observation at velocity $v_{\rm obs}$ is understood to mean an observation at frequency $\nu = (1 - v_{\rm obs}/c)\nu_{ij}$ and where $\sigma_\nu = (\sigma_v/c)\nu_{ij}$. For optically thin emission with no hyperfine structure at an observed velocity $v_{\rm obs}$, a cell of length Δx contributes a specific intensity above the continuum of

$$I_\nu = (j_{ij} - \chi_{ij} I_{\rm CMB})\Delta x \phi(v_{\rm obs}; v), \tag{3.11}$$

where j_{ij} and χ_{ij} are functions of the cell density $n_{\rm H}$ and $\phi(v_{\rm obs}; v)$ is a function of the cell velocity v. The intensity averaged over a velocity channel that covers velocities in the range $v_0 \le v_{\rm obs} \le v_1$ is

$$\begin{aligned}\langle I_\nu \rangle_{\rm chan} = (j_{ij} - \chi_{ij} I_{\rm CMB}) &\frac{c\Delta x}{4(v_1 - v_0)\nu_{ij}} \\ &\times \left[{\rm erf}\left(\frac{v_1 - v}{\sqrt{2}\sigma_v}\right) - {\rm erf}\left(\frac{v_0 - v}{\sqrt{2}\sigma_v}\right)\right].\end{aligned} \tag{3.12}$$

We compute the channel-averaged specific intensity along each line of sight by summing $\langle I_\nu \rangle_{\rm chan}$ over all the cells, each with its own velocity v, along the line of sight. The final step in constructing our PPV data cube is that we take the summed intensity computed in this way and smear each velocity channel using our Gaussian beam.

In the case of molecules with hyperfine structure, the equations are identical except that the subscripts ij are replaced by $i\alpha j\beta$, and we note that, since the hyperfine components are closely spaced in frequency, multiple components may contribute significant intensity at the same frequency. However, in the observations to which we wish to compare our simulations, kinematic information is generally obtained by fitting one or more well-separated individual hyperfine components (e.g., A07, K07, although see R08, who use a more complex procedure). Thus, in practice it is generally not necessary for our purposes to consider more than a single hyperfine component. For optically thin emission in hyperfine components with no significant line overlap, this means that the procedures for molecules with and without hyperfine splitting are the same.

Our procedure determines the emission only up to the unknown abundance X, which in reality will depend on the emitting species and on the density and temperature, and probably also the thermal and density history, of a given fluid element. For example, observations show that in the densest cold regions CO and its isotopomers will be depleted, while the abundance of N_2H^+ stays roughly constant (Tafalla et al. 2004a,b). In order to approximate this effect, we adopt a simple depletion model for each of the chemical species that we simulate. For $C^{18}O$, we assume an abundance of $X = 10^{-7}$ molecules per H_2 molecule with depletion occurring at $n_{H_2} = 5 \times 10^4$ cm^{-3} (Tafalla et al. 2004a). For N_2H^+, we adopt $X = 10^{-10}$ with depletion at $n_{H_2} = 5 \times 10^7$ cm^{-3} (K07; Tafalla et al. 2002). Although depletion in nitrogenous species is not generally observed, it is assumed that N_2 begins to disappear at number densities $n_{H_2} > 10^6$ cm^{-3} (Walmsley et al. 2004). For the NH_3 measurements we compare to in Perseus, we use $X = 10^{-8}$ (Rosolowsky, private communication) with assumed depletion at the same density as N_2H^+.

We use these procedures to produce dust continuum / column density maps and PPV cubes for each of our three molecular lines. To increase our statistics, we generate data sets for each cardinal direction at $t = t_{\rm ff}$, and we treat the three orientations as independent observations. Figure 3.1 shows a dust continuum map in one particular orientation.

3.4 Results

In the decaying simulation, at $1t_{\rm ff}$ we identify a total of 109 cores, 54 of which can be considered protostellar due to the presence of a sink particle within 0.1 pc of the core center. In the driven simulation, we find 214 cores, 92 of which are protostellar. A large central point mass can have a significant effect on the core gas motion, so we separate out the 'starless' cores for comparison. The relative number of starless cores to protostellar cores varies from star-forming cloud to cloud depending upon the advancement of star formation in the region. The ratios of prestellar to protostellar cores that we find in our simulations are similar to the ratios observed in Perseus and Ophiuchus (Young et al. 2006; Enoch et al. 2006). In these simulations, the larger number of cores in the driven run is significant because the ongoing turbulence creates more new condensations, which also collapse more slowly.

For the sake of clarity, we will refer to the centroid velocities of the cores as the "first moments" and the velocity dispersions through the core centers as the "second moments." Thus, in the following sections we will describe the measured distributions of the first and second moments and report the dispersion of the first moments (i.e., the core-to-core velocity dispersion). We define transonic velocities as those falling in the range $c_{\rm s} \leq \sigma \leq 2c_{\rm s}$, while supersonic dispersions have $\sigma > 2c_{\rm s}$.

3.4.1 Central Velocity Dispersions

In this section, we investigate the distribution of second moments (central non-thermal velocity dispersions through the core centers) in N_2H^+, a measure that is useful for determining the level of turbulence and infall motion within the core. The total dispersion along the line of sight is given by

$$\sigma_{\rm LOS} = \sqrt{\sigma_{\rm NT}^2 + \sigma_{\rm T}^2}, \tag{3.13}$$

where $\sigma_{\rm T} = \sqrt{k_{\rm B}T/m}$, and σ_{NT} is the non-thermal component that we discuss here.

We compute $\sigma_{\rm LOS}$ in the simulations by fitting a Gaussian to the spectrum through the core center and then deriving the second moment, $\sigma_{\rm NT}$, from equation

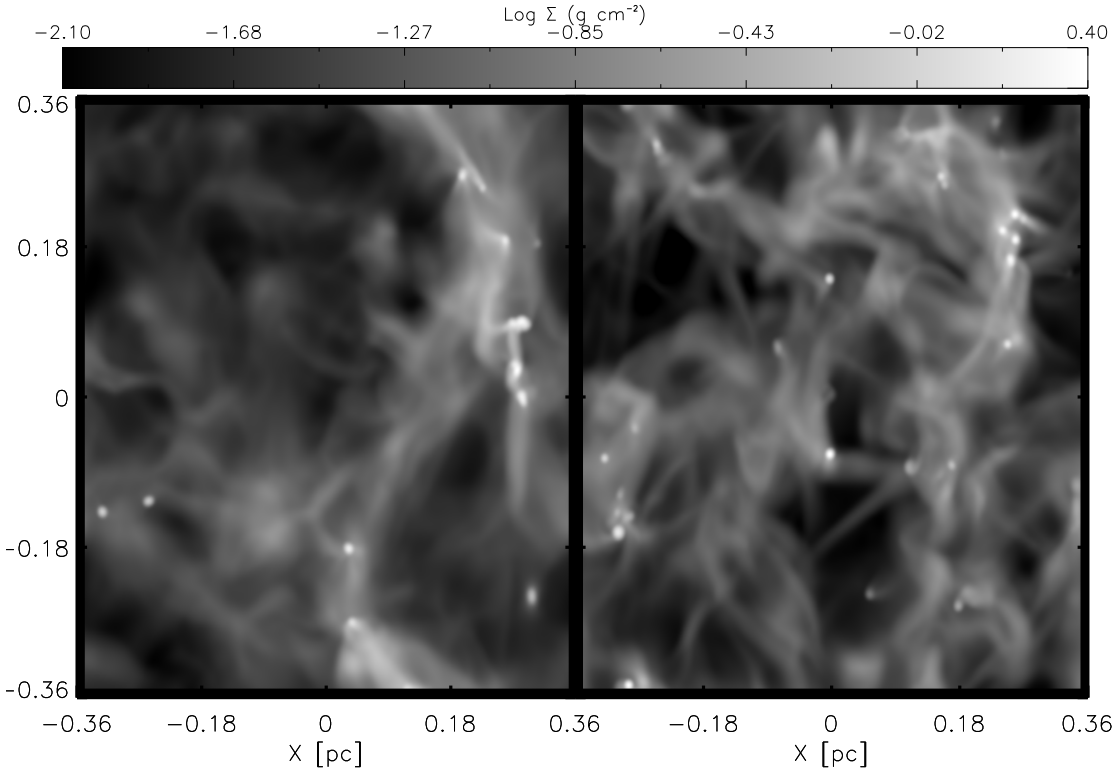

Figure 3.1 The images show the decaying (left) and driven (right) log column densities (g cm^{-2}) 'observed' at a distance of 260 pc with beam size of 31".

Table 3.1. Central velocity dispersion median and mean for the two environments and core types at $1.0t_{\rm ff}$ in N_2H^+ normalized to the conditions in Perseus.

	Decaying			Driven		
	All	Prestellar	Protostellar	All	Prestellar	Protostellar
$N_{\rm cores}$	109	55	54	214	122	92
Median $\sigma_{\rm NT}/c_{\rm s}$	1.0	0.6	2.9	1.1	0.9	2.1
Mean $\sigma_{\rm NT}/c_{\rm s}$	2.2	0.6	3.8	1.8	1.2	2.7

(3.14). Table 3.1 gives the median and means of $\sigma_{\rm NT}/c_{\rm s}$. We plot the total distribution in Figure 3.2 and the prestellar and protostellar distributions in Figures 3.3 and 3.4, respectively. The core populations appear fairly similar in the two simulations, although there is evidence of the elevated turbulence in the driven simulation. Since the cores are created by turbulent compressions in both environments, at early times they should have similar second moments. However, at late times, as the cores collapse and form protostars the distributions are more dissimilar. Indeed, from Figure 3.4 we can see that the protostellar distributions are much broader and less peaked than the prestellar ones. The decaying protostellar core population has almost twice as many cores in the tail ($\sigma_{\rm NT} > 4c_{\rm s}$) of the distribution, while the protostellar driven population is dominated by cores with $\sigma_{\rm NT} < 4c_{\rm s}$.

To better characterize the differences between the two simulations, we perform a Kolmogorov-Smirnov (K-S) test comparing each of the core distributions. The K-S statistic gives 1 minus the confidence level at which the null hypothesis that the two samples are drawn from the same underlying distribution can be ruled out, e.g., a K-S statistic of 0.01 means that we can reject the hypothesis that the two samples were drawn from the same distribution at the 99% confidence level. We find that the net driven and decaying velocity dispersion populations have a K-S statistic of 18%, meaning that we can rule out the hypothesis that they were drawn from the same population only with 82% confidence. Individually, there is large disagreement in both the protostellar populations (4×10^{-2}%) and prestellar core populations (2%).

The difference between the protostellar populations in the two simulations is partially associated with the mass differences between the sink particles: The decaying simulation has a median sink mass that is approximately twice that of the driven simulation such that it has correspondingly larger accretion rates that are associated with higher velocity dispersions.

3.4.2 Core Envelopes and Surroundings

The velocity dispersions of the gas surrounding the central column density maxima yield information about the relative motion between core and envelope, and may also reveal the presence of shocks or strong infall that could limit core boundaries.

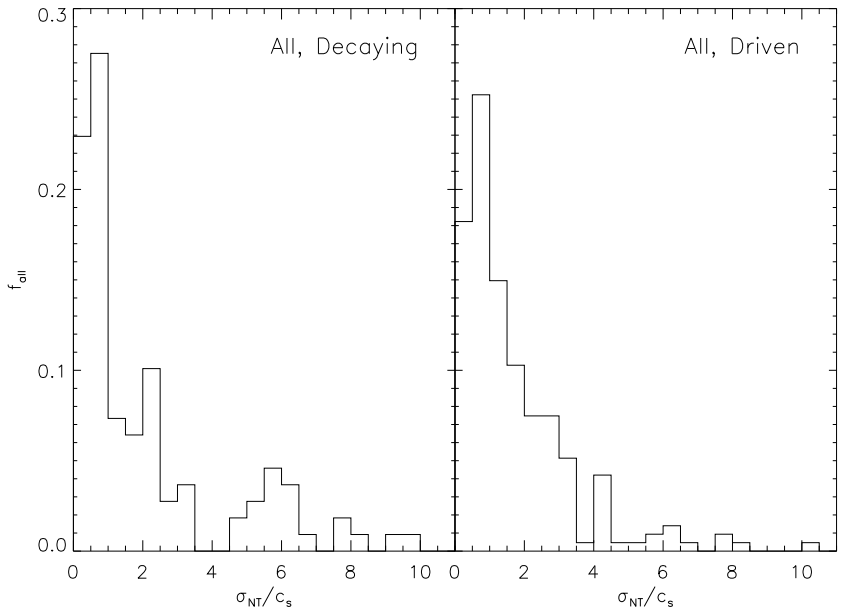

Figure 3.2 Fraction f of all cores binned as a function of second moments (non-thermal velocity dispersion), $\sigma_{\rm NT}$, for a simulated observation of Perseus using N_2H^+. The distribution on the left shows the cores in the decaying turbulence enviornment, while the distribution on the right gives the cores in the driven turbulence enviornment.

Typically, observers find only small differences in velocity between the core and the surrounding gas envelope, which rules out dynamical pictures of core accretion in which protostars may strongly gravitationally interact with their neighbors (K07). In addition, although shocks are postulated to be the origin of the original density compression, close observations have not revealed strong confining shocks surrounding the cores. Generally, our simulations produce prestellar cores that agree with the expectations from observations. However, the decaying protostellar cores exhibit supersonic internal velocities that are not observed in the comparison star-forming regions.

In order to compare the two environments observed with three common tracers, $C^{18}O$, N_2H^+, and NH_3, we calculate the velocity dispersion through each pixel along the line of sight. Figures 3.5 and 3.6 show the velocity dispersion of each pixel in the

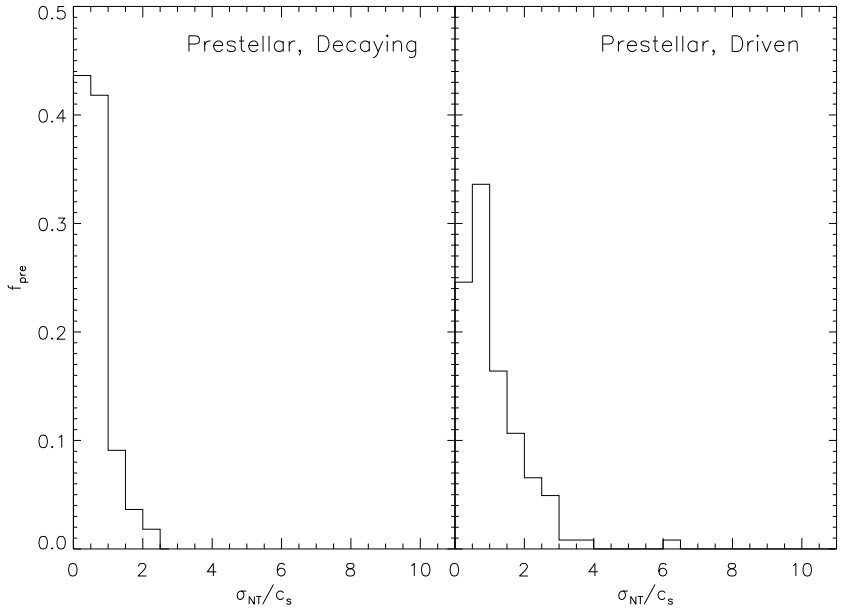

Figure 3.3 Fraction f of starless cores binned as a function of second moments (non-thermal velocity dispersion), $\sigma_{\rm NT}$, for a simulated observation of Perseus using N_2H^+. The distribution on the left shows those cores in the decaying turbulence enviornment, while the distribution on the right gives the cores in the driven turbulence enviornment.

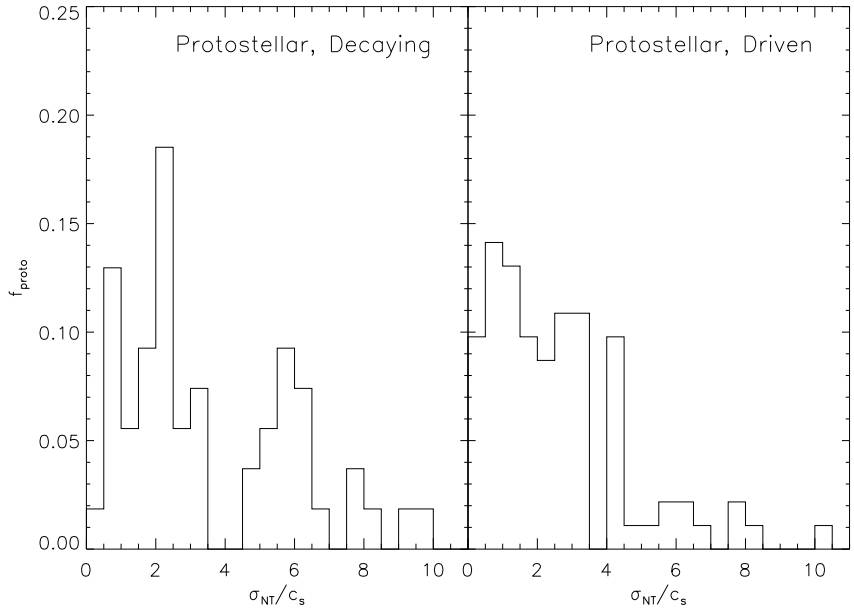

Figure 3.4 Fraction f of protostellar cores binned as a function of second moments (non-thermal velocity dispersion), $\sigma_{\rm NT}$, for a simulated observation of Perseus using N_2H^+. The distribution on the left shows the cores in the decaying turbulence enviornment, while the distribution on the right gives the cores in the driven turbulence enviornment.

vicinity of a single prestellar and protostellar core for decaying turbulence, which represent typical examples of each type from our sample, overlaid with contours of integrated intensity. The large number of cores in our sample makes comparing the populations by eye on an individual basis difficult. In order to consolidate the data sets for each environment, we bin the pixels by radial distance from the core center. We define 20 logarithmic bins that range from 0.005 pc to 0.1 pc in projected distance from the core center and then average together the velocity dispersions of all pixels that fall into a given bin, including all prestellar or protostellar cores in each case. The result is a single averaged core for each tracer and environment. We have plotted this averaged velocity dispersion as a function of distance from core center in Figures 3.7 and 3.8 for starless and protostellar cores, respectively.

There are several interesting points that may be noted from these plots. First,

gas sampled by low density tracers (e.g., $C^{18}O$) around prestellar cores has a higher velocity dispersion than that sampled by higher density tracers. This is reasonable given that the lower-density gas is further from the core center and generally more turbulent. Before collapse ensues, the cores have typically not developed strong high density peaks as is evident in Figure 3.5. This difference between lower and higher density tracers has been frequently exploited observationally to distinguish between the dense core and surrounding envelope (e.g., K07; Walsh et al. 2004). Second, Figure 3.7 shows that the starless cores forming in the driven simulation tend to have a higher average velocity dispersion than those in the decaying simulation. This is mainly apparent in the tracer $C^{18}O$, which traces the more turbulent core envelope. Most importantly, the average prestellar velocity dispersion for both cases and for all tracers are approximately sonic. Even the lowest density tracer, $C^{18}O$, remains, on average, below $2c_s$ for the range of column densities in the core neighborhood. Finally, we note that there is only a small increase in the dispersion with increasing radius. This is consistent with observations by Barranco & Goodman (1998) and Goodman et al. (1998) who find that the velocity dispersion of the cores on the scale of ~ 0.1 pc is approximately constant, with a small increase near the edge of this region of "coherence." The magnitude of the dispersion suggests that starless cores forming in a turbulent medium are not strongly confined by shocks in the range of densities that are traced by observers.

In contrast, some of these conclusions do not hold for protostellar cores when strong infall is evident. As shown in Figure 3.8, protostellar cores exhibit significantly higher average velocity dispersions than the prestellar counterparts. The tracers of the protostellar cores behave differently as well. Due to strong infall predominantly in the densest gas, the higher density tracers, N_2H^+ and NH_3, show higher velocity dispersions than $C^{18}O$, which indicates that the lower density envelope remains transonic.

There is also a clear difference between the protostellar cores in the two environments. Those cores in the driven environment have transonic to slightly supersonic velocity dispersions in all tracers that do not vary significantly with distance from the core center, which is consistent with the coherent core structure observed. This

indicates that the cores still have residual turbulent pressure support at a global free-fall time and collapse more slowly. The protostellar cores in the decaying turbulence environment, lacking this support, have shorter lifetimes and proceed more quickly to collapse and develop much higher, supersonic, central velocity dispersions in N_2H^+ and NH_3 as the cloud gas collapses. However, at large radii the velocity dispersion of the protostellar cores in the decaying enviroment matches the velocity dispersion of cores in the driven environment. A similar time-dependent trend is obtained in decaying simulations by Ayliffe et al. (2007).

In summary, prestellar cores forming in driven turbulence have average dispersions of $\lesssim 1.5c_s$ in all tracers, and this dispersion is either flat or slowly decreasing with increasing radius. In contrast, cores in decaying turbulence show small ($\sigma_{NT} < 1.0c_s$), flat dispersions for prestellar cores, but large and radially decreasing dispersions for protostellar cores. This is most likely due to infall of unbound gas from large distances at late times, which is a signature of competitive accretion. We do not observe this in the driven run because the cloud gas dispersion is too high for Bondi-Hoyle accretion to be efficient over large distances (Krumholz et al. 2006b).

The dispersions we obtain for the cores and their surrounding envelopes are somewhat dissimilar to those obtained by Klessen et al. (2005) in SPH simulations. As we do, Klessen et al. investigate the velocity dispersions of cores forming in an isothermal, large-scale driven turbulent environment. In their study, they derive clump properties when only 5% of the mass is in cores or at $\sim 0.4t_{ff}$, a much earlier time than we use. However, even for prestellar cores with driving, they frequently find strong supersonic shocks with $\sigma_{LOS} \sim 3 - 5c_s$ bounding the cores, which is thus far not supported by observations. In lieu of a simulated observation, they use a column density cutoff to make the dispersion estimates. We find that we obtain higher velocity dispersions calculating the velocity dispersion directly as Klessen et al. do rather than fitting the line profile in the manner of observers. The reason for the difference is that in some cases the spectra resemble a fairly narrow peak, which is well fit by a Gaussian, surrounded by a much broader base around the 10% level. The magnitude of this extra spread is reduced substantially at the higher densities as traced by N_2H^+, and it is likely neglected in the fits performed by observers due

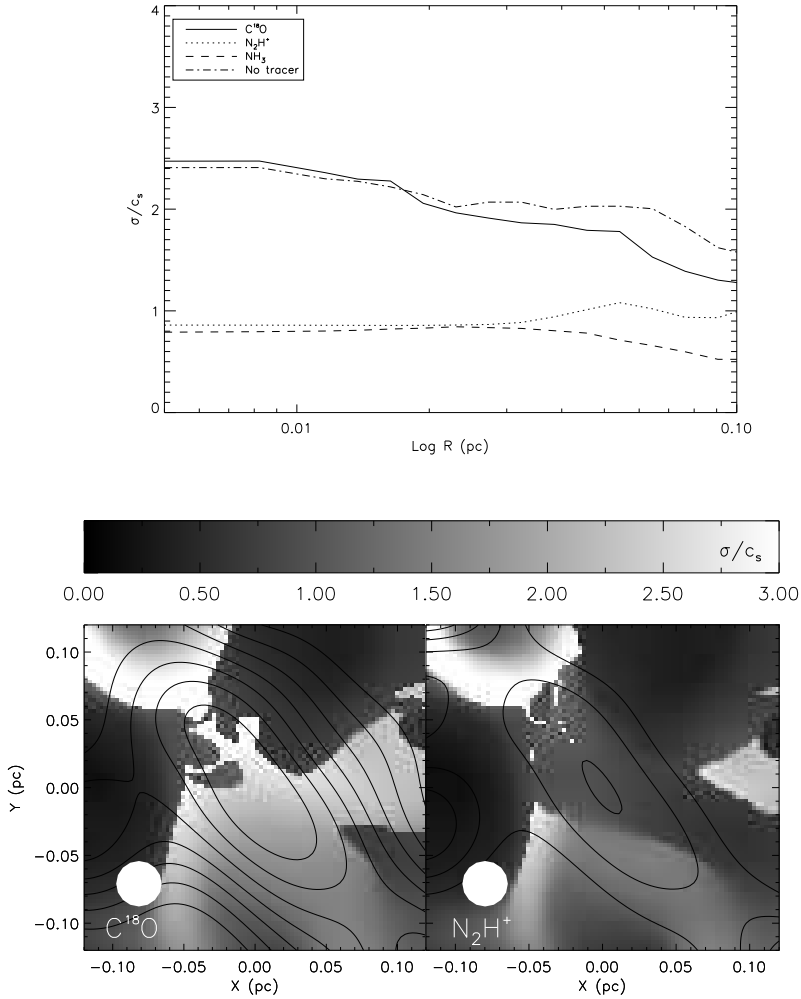

Figure 3.5 The upper plot gives average velocity dispersion versus radius for a decaying starless core at $1t_{\rm ff}$. The images below show a simulated observation in $C^{18}O$ (left) and N_2H^+ (right). Contours indicate integrated intensity where each contour is a 10% linear change from the peak specific intensity in that tracer. The gray scale shows velocity dispersion, $\sigma_{\rm NT}/c_{\rm s}$, and the circle indicates the FWHM beam size.

to the inherent low-level noise in the actual spectra. Another possibility for the difference is the difficulties of SPH in rendering shocks and instabilities, particularly shear flow instabilities (Agertz et al. 2007), that are likely to be present in any compressible turbulent simulation and may seriously affect accuracy. However, the extent that this may contribute to the high dispersions found by Klessen et al. is unclear.

3.4.3 Relative Motions

Observers frequently evaluate an intensity-weighted mean velocity, or first moment, along the line of sight through the core center. While the second moments are indicative of infall motions, the first moments represent the net core advection. The dispersion of the first moments indicates how much the cores move relative to one another. Observations find that the dispersion of first moments is generally smaller than the velocity dispersion of gas that is not in cores, although how much so varies from region to region. For example, A07 conclude that the first moment dispersion is sub-virial by a factor of ~ 4 in ρ Ophiuchus. K07 find that first moment dispersion of starless cores in Perseus is sub-virial by a factor of ~ 2, which does not rule out virialization.

In order to get an unbiased distribution for comparison, it is necessary to subtract out any large gradients in the sample of first moments. Thus, for each region we fit $V = V_0 + \nabla V \cdot x$ as a function of position, x. Generally, this turns out to be a fairly small correction, but the net effect is to decrease the dispersion of first moments relative to the gas.

We plot the distribution of first moments for all cores in both environments in Figure 3.9, and we plot the distributions for prestellar and protostellar cores separately in Figure 3.10. In these, we normalize to the "measured" gas dispersion and correct for the velocity gradient in the box. The dashed line is a Gaussian with the same dispersion as the core distribution. For reference, we also plot a Gaussian with the gas dispersion. Note that in the driven simulation the dispersion inferred from virial arguments and the time-dependent gas dispersion are the same, because by definition we fix the total kinetic energy to maintain virial balance. However, for

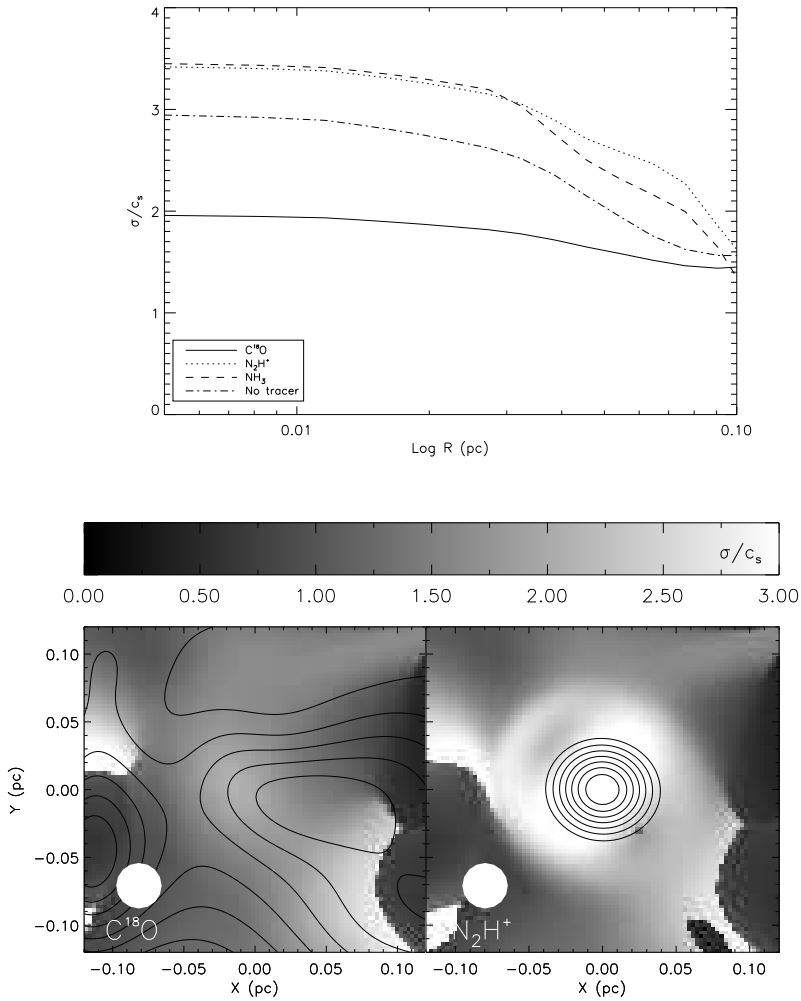

Figure 3.6 The upper plot gives average velocity dispersion versus radius for a decaying protostellar core at $1t_{\rm ff}$. The images below show a simulated observation in $C^{18}O$ (left) and N_2H^+ (right). Contours indicate integrated intensity where each contour is a 10% linear change from the peak specific intensity in that tracer. The gray scale shows velocity dispersion, $\sigma_{\rm NT}/c_{\rm s}$, and the circle indicates the FWHM beam size.

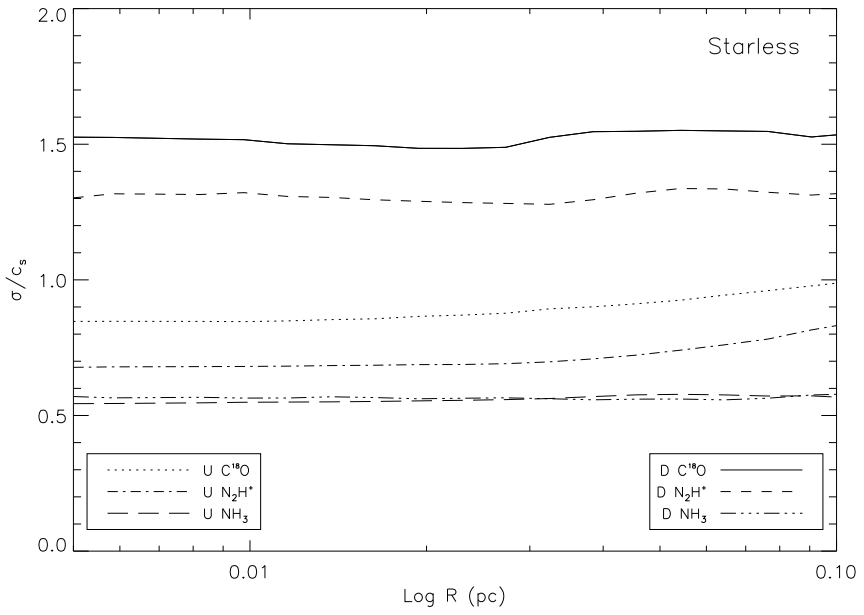

Figure 3.7 The figures show the averaged dispersion of the prestellar cores binned over distance from the central core, where D denotes driven and U denotes undriven turbulence.

the decaying simulation, the time-dependent gas dispersion is lower than would be derived from a virial argument using the total gas mass and cloud size.

As before, we use K-S tests to characterize similarity in the populations, which we report in Table 3.2. A K-S test indicates that driven and decaying distributions of the net first moments agree with 56% confidence, while the prestellar and protostellar core first moments agree with 40% and 13% confidence. This is significant enough to imply that the early core motions are not widely different in the two environments, with the largest difference occurring between the protostellar first moments. Comparing these distributions with a Gaussian dispersion at the gas dispersion yields good agreement for the distributions of the prestellar driven cores (54% confidence) and protostellar decaying cores (56%), but low agreement for the other distributions. In general, low agreement may be because the first moment distributions, although having a similar dispersion to the gas in some cases, are not well represented by a Gaussian distribution.

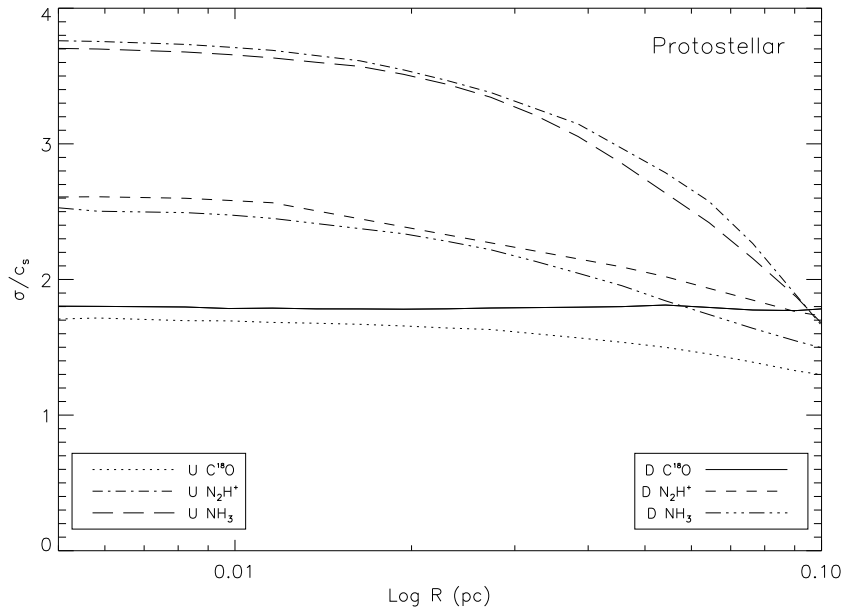

Figure 3.8 The figures show the averaged dispersion of only the protostellar cores binned over distance from the central core, where D denotes driven and U denotes undriven turbulence.

In Table 3.3, we list the first moment dispersions, both corrected and uncorrected for large linear gradients. We find that the corrected net core dispersion for the driven and decaying cores are both sub-virial relative to the gas dispersion. Previous simulations have shown that the dispersion of first moments becomes sub-virial towards higher gas densities (Padoan et al. 2001), so the result is not unexpected. One interesting difference between the simulations is that the decaying *protostellar* cores are approximately virial, while the *prestellar* driven cores are approximately virial. The former suggests that as the cloud loses turbulent support and tends toward global collapse, that either the core interactions increase or that the cores retain some memory of their natal gas dispersion. The inertia of the cores implies that their velocity dispersions will tend to decay more slowly than that of the gas as a whole. This is a potentially testable signature of the competitive accretion model (Bonnell et al. 2001). In the latter case, the prestellar cores may still be forming out of the shocked gas and hence may still have similar motions. In general, the sub-virial dispersion of the cores may imply that they are not scattering sufficiently frequently to virialize within the formation timescale. Elmegreen (2007) reasons that if cores form at the intersection of two colliding shocks, then their initial dispersion should be on average less than the gas dispersion. Overall, our results imply that the forming cores are at least somewhat sensitive to the actual dispersion of the natal gas.

3.5 Observational Comparisons

3.5.1 Scaling to Observed Regions

In this section, we compare our simulated observations with three selections of cores observed in three standard molecular tracers in two different low-mass star-forming regions, ρ Ophiuchus (primarily L1688) and the Perseus MC. This comparison cannot be precise for several reasons: First, the cloud is isolated, whereas our simulation is a periodic box; second, we are using a single simulation with given values of the virial parameter and the Mach number to compare with clouds that have

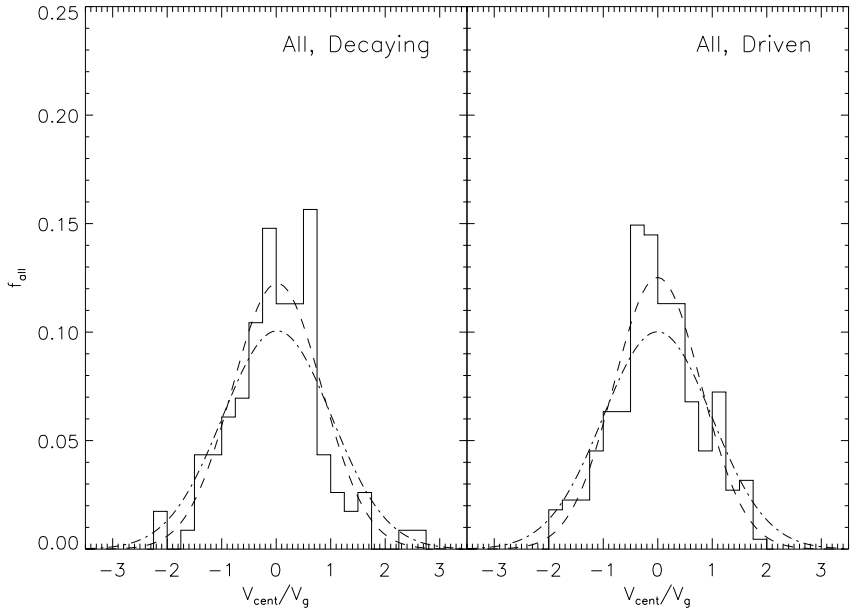

Figure 3.9 Fraction f of all cores binned as a function of first moments, $V_{\rm cent}$, for a simulated observation using N_2H^+ normalized to the large-scale gas dispersion. $V_{\rm g}$, at $t = t_{\rm ff}$. The distribution on the left shows the cores in the decaying turbulence environment, while the distribution on the right gives the cores in the driven turbulence environment. The dashed line is a Gaussian with the same dispersion as the data while the dot-dashed line is a Gaussian with the gas velocity dispersion ($V_{\rm g} = 2.2c_{\rm s}$, $V_{\rm g} = 4.9c_{\rm s}$, for the decaying and driven simulations, respectively).

somewhat different values of each of these parameters; and, finally, our simulation is isothermal, whereas the temperature is observed to vary in the clouds. Furthermore, the actual cloud is magnetized, whereas our simulation is purely hydrodynamic. A variety of possible comparison strategies is possible. We have chosen to use the same mean density in the box as in the cloud, and to make the simulation temperature agree approximately with the typical temperature observed in the cloud cores. The size and mass of the simulation box then follow from equations (3.2) and (3.3). With this approach, the Jeans mass will be about the same in the simulation and in the cloud, but the size and mass of the overall cloud will generally differ between the two.

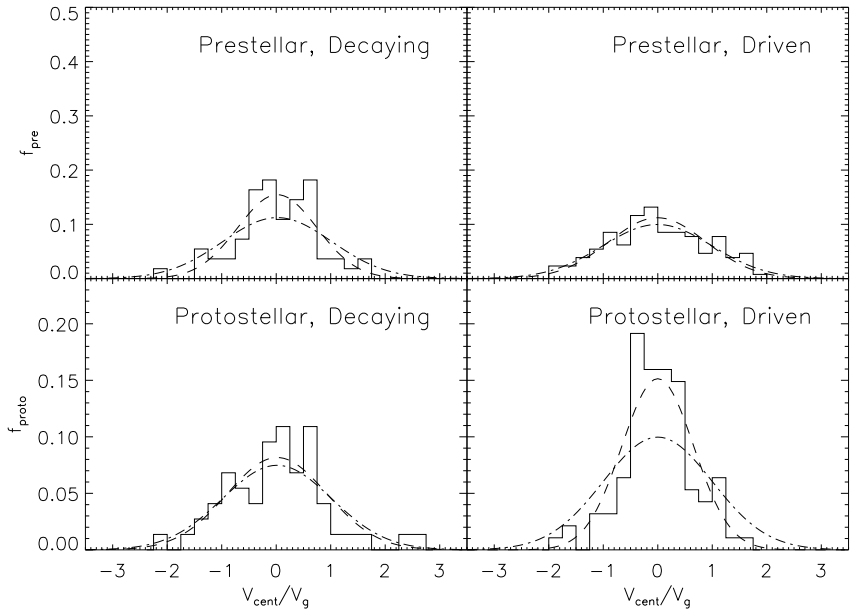

Figure 3.10 Fraction f of prestellar cores (top) and protostellar cores (bottom) binned as a function of first moments, $V_{\rm cent}$, for a simulated observation using N_2H^+ normalized to the large-scale gas dispersion, $V_{\rm g}$. The distribution on the left shows those cores in the decaying turbulence enviornment, while the distribution on the right gives the cores in the driven turbulence enviornment.

A07 observed 41 starless cores in ρ Ophiuchus, clustered in a region of area 1.1 pc^2, and made maps of 26 of them using the tracer N_2H^+ ($J = 1 \rightarrow 0$). The total gas mass in this region with extinction greater than 15 magnitudes is estimated to be ~ 615 M$_\odot$ (Enoch, private communication; Enoch et al. 2007) with peak column densities of N_{H_2}=1-8$\times 10^{23}$ cm^{-2} (Motte et al. 1998). The star-forming area of ρ Ophiuchus is roughly circular with radius $R \simeq 0.6$ pc; the mean density and column density are therefore $\bar{n}_H \simeq 2 \times 10^4$ cm^{-3} and $N_H = 5 \times 10^{22}$ cm^{-2}. As discussed above, we then adopt this density for our simulation. To fix the temperature, we first note that dust temperatures in the prestellar cores range from 12-20 K (A07). On the scale of the entire L1688 cloud, the temperatures as measured by ^{12}CO and ^{13}CO lines are 29 K and 21 K, respectively (Loren 1989a; in his notation, this region is R22). We therefore adopt $T = 20$ K for the simulation. equations (3.2) and (3.3) give $L = 0.9$ pc and $M = 550\ M_\odot$ for the simulation box, comparable to, although somewhat less than, the observed values. The total velocity dispersion measured from the ^{13}CO line is 1.06 km s^{-1} (Loren 1989b), which lies above the standard linewidth-size relation (eq. 3.6). The corresponding 1D Mach number is $\mathcal{M}_{1D} = 3.9$, slightly less than the value 4.9 in the simulation. The virial parameter of the cloud is 1.25, also slightly less than the simulation value of 1.67.

For Perseus, K07 report central velocity dispersions and centroid velocities measured from C^{18}O and N_2H^+ pointings for 59 prestellar and 41 protostellar cores. R08, also making pointed observations of Perseus, obtain velocity dispersions and centroid velocities for 199 prestellar and protostellar cores using NH_3 (2,2), NH_3 (1,1) and C_2S (2,1). They adopt a dust temperature of 11 K, which is slightly lower than the assumed temperature of 15 K used by K07. In comparison to ρ Ophiuchus, the Perseus star-forming region is much larger, 5 pc $\times$ 25 pc, resembles a long chain of clumps with typical column densities of $N_{H_2} \sim 3 \times 10^{22}$ cm^{-2}, and contains a total mass of $\sim$ 18,500 M$_\odot$ (Kirk et al. 2006). Using the total mass and assuming a cylindrical geometry ($L = 25$ pc and $R = 2.5$ pc), we obtain $\bar{n}_H = 1.1 \times 10^3$ cm^{-3}, which we adopt for the simulation. We also assume that Perseus is approximately in the plane of the sky; if it were randomly oriented then the expected value of the longest side of the cloud would be 50 pc. We adopt a temperature of 10 K, since

Table 3.2. K-S statistics for the driven and decaying core first moments (centroid velocities) corrected for large velocity gradients and the gas.

	D: All	D: Starless	D: Proto	Gas: $\mathcal{M}_{1D}$=4.9
U: All	56%	23%	44%	2 %
U: Starless	68%	40%	89%	54%
U: Proto	53%	54%	13%	1 %
Gas: $\mathcal{M}_{1D}$=4.9	14%	14 %	56%	-

Note. — D = driven, U = undriven

Table 3.3. Dispersion of first moments (centroid velocities) normalized to the large-scale gas dispersion.

	All				Protostellar			Prestellar			
	D	U	K07	R08	D	U	K07	D	U	A07	K07
σ_V/σ_g[a]	0.89	0.97	1.62	1.50	0.73	1.04	1.31	1.00	0.90	0.75	1.81
$\sigma_{V_{cor}}/\sigma_g$[b]	0.80	0.82	1.02	0.98	0.66	0.92	0.98	0.89	0.73	0.46	1.03

Note. — D = driven, U = undriven, K07 = Kirk *et al.* (2007), R08 = Rosolowsky *et al.* (2008), A07 = André *et al.* (2007)

[a]Uncorrected for linear gradients

[b]Corrected for linear gradients

Table 3.4. Total optical depth τ through core centers for each normalization and simulated tracer.

	Perseus			ρ Ophiuchus[a]		
$\tau_{\rm tot}$[b]	median	min	max	median	min	max
$C^{18}O$	0.51	0.08	2.46	0.35	0.14	1.05
N_2H^+	0.71	0.07	8.91	7.27	1.72	29.44
NH_3	8.37	0.10	63.49	46.59	10.61	228.73

[a] Optical depths are reported for the distribution of starless cores only.

[b] $\tau_{\rm tot}$ is the sum of the optical depths through line center for each hyperfine transition. For N_2H^+ and NH_3 with 7 and 18 hyperfine transitions, respectively, the optical depth is significantly reduced and generally optically thin for individual transitions.

this is characteristic of the prestellar cores (R08). equations (3.2) and (3.3) then imply that the simulation box has $L = 2.8$ pc and $M = 825\ M_\odot$, which is a relatively small piece of the total cloud. Since we are simulating only a small part of the Perseus cloud, we estimate the velocity dispersion in actual molecular gas from the average linewidth-size relation (eq. 3.6 for $L = 5$ pc), which gives $\sigma = 1.1$ km s^{-1} and $\mathcal{M}_{1D} = 5.9$. In comparison, our simulation box scaled to the Perseus average number density is less turbulent and only half the length of the shorter dimension. This difference in Mach number and cloud side yields a virial parameter for Perseus of $\alpha \simeq 1$, which is about 60% of the value of our simulation box.

3.5.2 Optical Depths

In our analysis we make the assumption that the line transitions are optically thin. This approximation is observationally validated for both the N_2H^+ and NH_3 transitions. For example, according to K07 the total optical depth, $\tau_{\rm tot} \sim 0.1 - 13$, where $\tau_{\rm tot}$ is the sum of the optical depths for each hyperfine transition. Thus, the average optical depth for a given N_2H^+ hyperfine line is $\bar{\tau} = \tau_{\rm tot}/7 \sim 0.01 - 2$, so that the majority of the lines are at least marginally optically thin. In particular, the isolated 101-012 hyperfine component used for velocity fitting has an optical depth of $\tau_{\rm tot}/9$, and is therefore optically thin in all but the very densest cores. A07 report similar N_2H^+ total optical depths of $\tau_{\rm tot} \sim 0.1 - 30$ for ρ Ophiuchus, while R08 find $\tau_{\rm tot} \sim 0.4 - 15$ for NH_3. However, the NH_3 (1,1) complex has 18 hyperfine components so that most of the lines are at least marginally optically thin. For comparison, we report the total optical depth in our simulations for all three tracers in Table 3.4. We derive the optical depth for a given line by solving for the level populations as described in §3.3. Once these are known, the opacity in each cell for photons emitted in the transition from state i to state j is

$$\kappa = nX \frac{f_j B_{ji} \phi(v_{\rm obs}; v)}{4\pi(v_1 - v_0)\nu_{ij}}, \tag{3.14}$$

where n, v, and X are the number density, velocity, and molecular abundance in the cell, B_{ji} and ν_{ij} are the Einstein absorption coefficient and frequency of the transition, and the observation is made in a channel centered at velocity $v_{\rm obs}$ that runs from velocity v_1 to v_0. The optical depth is given simply by computing this quantity in every cell, multiplying by the cell length to obtain the optical depth of that cell, and then summing over all cells along a given line of sight. As the table shows, for the most part the average hyperfine transition is optically thin in all tracers. The main exception is cores traced by NH_3 in ρ Ophiuchus, which are marginally optically thick. As a result, we do not present results for NH_3 using the higher density ρ Ophiuchus scaling; the core velocity dispersion maps in Figures 5-8 are normalized to Perseus.

In all other cases even the strongest hyperfine components have optical depths of order unity, and comparison with more detailed radiative transfer modeling than

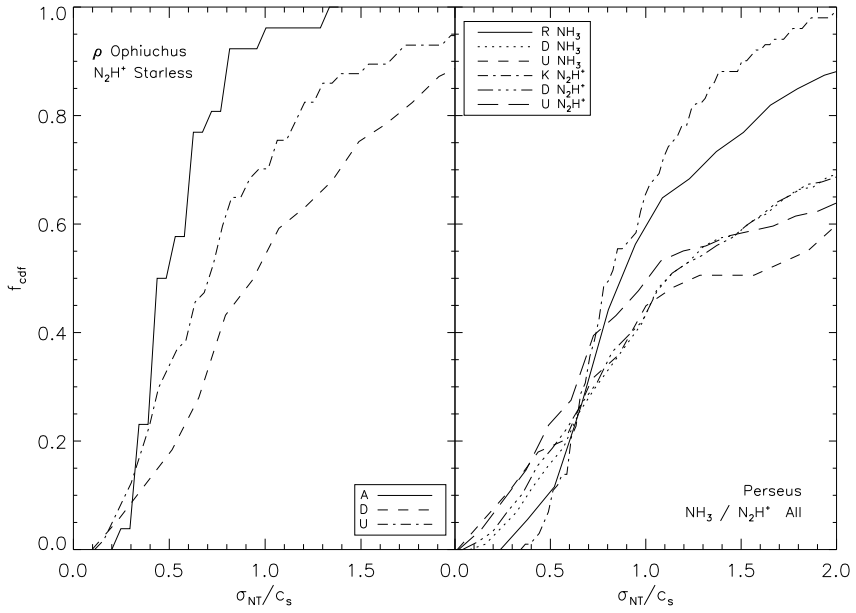

Figure 3.11 Cumulative distribution function showing the total fraction f of cores with second moments, $\sigma_{\rm NT}$, less than or equal to the x coordinate value for simulated observations of ρ Ophiuchus and Perseus in N_2H^+ and NH_3. The legends indicate by first letter whether the distribution is taken from K07, A07, R08, Undriven simulation, or Driven simulation. The tracer is also indicated when two different tracers are used.

we perform indicates this is unlikely to significantly affect our results. For example, Tafalla et al. (2002) model the emission and transfer of the same N_2H^+ and NH_3 lines in a sample of starless cores in Taurus and Perseus whose conditions are similar to those produced by our simulations. They study the interplay between hyperfine splitting and radiative trapping by analyzing the two limiting cases of negligible radiative trapping (which we assume) and neglect of hyperfine splitting (which maximizes radiative trapping). They find that the difference in the level populations they compute under these two assumptions is only a few tens of percent, a level of error comparable to that introduced by uncertainties in the collision rate coefficients. We expect the errors introduced by our optically thin assumption to be comparable.

3.5.3 Comparison of Second Moments

Observationally, the second moments of cores are predominantly subsonic in MCs, apparently independent of the amount of turbulence. For example, A07, measuring second moments in ρ Ophiuchus, find all values are smaller than $2c_s$ with an average $\sigma_{\rm NT}/c_{\rm s} = 0.5$. Likewise, K07 report similar measurements for cores observed in Perseus, finding an average of $\sigma_{\rm NT}/c_{\rm s}= 0.7$ with a maximum value of 1.7. Both our simulations find marginally sub-sonic distributions of second moments with slightly larger means than the observations (see Table 3.1). In comparison, protostellar cores are observed to have a somewhat broader distribution of second moments. K07 find that the protostellar cores in Perseus have a mean second moment of $1.1c_s$ and a maximum of $2.3c_{\rm s}$. The protostellar objects that we observe in our driven simulation tend to have transonic second moments while in the decaying simulation they are supersonic.

We use a K-S test to compare the distribution of second moments for each of the simulation core populations with the observed core populations. We give the results in Table 3.5. Note that the A07 sample is comprised of only prestellar cores, while R08 observe both starless and protostellar cores but do not distinguish between them. Figure 3.11 shows the cumulative distribution functions of the core populations for some of the simulations and observations. Although the medians of some of the second moment distributions are fairly similar, K-S tests of the core

Table 3.5. K-S statistics for the driven and decaying core second moments (velocity dispersions) compared to the observational collections of cores using the appropriate cloud normalization and simulated tracer.

Sample	Cloud	D	U
Starless	ρ Ophiuchus (A07)	$8x10^{-4}$%	2%
	Perseus (K07)	2%	$2x10^{-2}$%
Protostellar	Perseus (K07)	$2x10^{-4}$%	...
All	Perseus (K07)	$1x10^{-3}$%	$8x10^{-4}$
	Perseus (R08)	1%	...

populations show significant disagreement in some cases. Overall, the distribution of second moments for the driven run is closer to observations of Perseus, while the decaying run is a better match for the ρ Opiuchus prestellar second moments.

The physical origin of the poor agreement between the simulations and observations appears to be that the simulated protostellar second moment distributions in either case do not have sufficiently narrow peaks. The protostellar cores in the simulations are regions of supersonic infall, which contradict the observations showing at most transonic contraction. Although the decaying simulation has a larger population of high dispersion protostellar cores, both simulations show almost equally bad agreement with the observations. Tilley & Pudritz (2004), performing smaller decaying turbulent cloud simulations at lower resolution with self-gravity, analyze the linewidths of their cores using a similar simple chemical mode. They also find a number of cores with greater than sonic central linewidths. There are two possibilities for the discrepancy between the observed protostellar cores in our simulation and those observed in Perseus. In reality, forming stars are accompanied by strong outflows that may eject a large amount of mass from the core, leading to efficiency factors of ϵ_{core} =0.25-0.75 (Matzner & McKee 2000). Such outflows reduce the mass of the forming protostar by the same amount. Since we do not include outflows, we

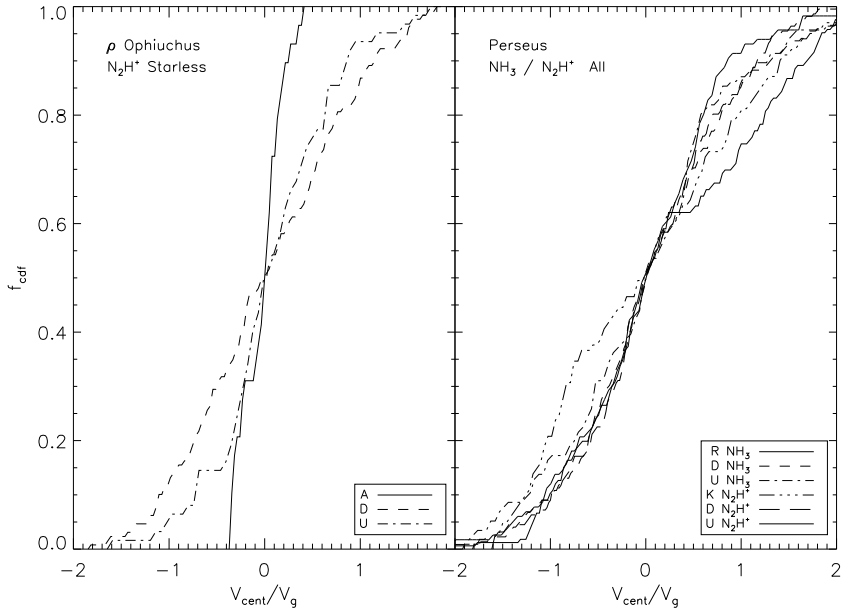

Figure 3.12 Cumulative distribution function showing the total fraction f of cores with first moments, $V_{\rm cent}$, less than or equal to the x coordinate value for simulated observations of ρ Ophiuchus and Perseus in N_2H^+ and NH_3. Each line is normalized to the appropriate large-scale gas dispersion, $V_{\rm g}$, either as measured (simulations) or as derived from the linewidth-size relation in equation (3.6). The legend format is similar to Figure 3.11.

naturally expect our sink particles to overestimate the forming protostellar mass by this factor. This will also effect the maximum infall velocity, characterized by the second moment through core center. If we adopt a sink particle mass correction of 1/3 (Alves et al. 2007), then the infall velocity will decrease by a factor of $\sqrt{3}$. This correction substantially reduces the number of protostellar cores with supersonic second moments from 53% and 70% to 23% and 39% for cores in the driven and decaying simulations, respectively. This correction brings the driven core sample closer in agreement with measurements by R08 and K07. Pressure support from magnetic fields, which we do not include, could also retard collapse and decrease the magnitude of the infall velocities. However, the importance of magnetic effects is difficult to assess without further simulations.

Table 3.6. K-S statistics for the driven and decaying core first moments (centroid velocities) compared to the observational collections of cores using the appropriate cloud normalization and simulated tracer.

Sample	Cloud	D	U
Starless	ρ Ophiuchus (A07)	0.5 %	6%
	Perseus (K07)	48%	12%
Protostellar	Perseus (K07)	6%	85%
All	Perseus (K07)	0.8%	7%
	Perseus (R08)	7%	3%

3.5.4 Comparison of First Moments

When comparing the distributions of first moments, we first subtract out any large gradients in the sample as discussed in §4.3. This is particularly important when comparing to a large elongated cloud such as Perseus. We then shift the distributions so that median centroid velocity falls at 0 and normalize the distribution to the bulk gas dispersion. For Perseus, we infer the bulk gas velocity dispersion for our simulation is $\sigma = 1.1$ km s^{-1} by assuming the cloud falls on the linewidth-size relation and satisfies equation (3.6) with L equal to the transverse size of the cloud. For ρ Ophiuchus, we adopt the ^{13}CO line velocity dispersion of $\sigma = 1.06$ km s^{-1} (Loren 1989b).

In contrast, we find better agreement between simulations and observations for bulk core motions. In Table 3.6, we report the K-S agreement for the first moments of the observations and simulations. Since the simulations themselves are statistically similar to one another, both of the first moment distributions generally either agree or disagree with the observed population. Except in the case of the N_2H^+ driven data for ρ Ophiuchus and the NH_3 decaying data, the velocity-corrected data are fairly statistically similar to the observations. This suggests that the first mo-

ment distributions do not strongly depend upon the details of the turbulence. In Figure 3.12, we have plotted the cumulative distribution function of some of the first moment distributions for comparison. The net core distributions show substantial overlap for both simulations and observated regions. The main source of disagreement with observations is the generally larger dispersions of the first moments in the simulations. In particular, the dispersion of the prestellar core first moments is a factor of ~ 2 larger than the that found by A07 in ρ Ophiuchus. However, because both simulations display sub-virial core-to-core velocity dispersions, we conclude that a sub-virial dispersion of first moments is not necessarily an indicator of global collapse.

In some cases, the direct dispersion of the gas may be poorly observationally constrained and so a virial argument is used to infer the gas dispersion. We find that normalizing the distributions to the virial gas dispersion rather than the measured gas dispersion produces a significantly different result for the decaying simulation. Since the cloud gas is becoming more quiescent with time, the actual gas dispersion is sub-virial at late times. Thus, relative to the virial gas dispersion the decaying dispersion of first moments appears twice as sub-virial.

3.6 Discussion and Conclusions

We use isothermal AMR simulations to investigate the kinematics of cores in environments with and without driven turbulence. We simulate observations of these cores in the tracers $C^{18}O$, N_2H^+, and NH_3 for the star-forming regions ρ Ophiuchus, 125 pc distant, and Perseus, 260 pc distant, with beam sizes of 26" and 31", respectively. From the differences between cores in the two environments and in conjunction with observational results, we are able to draw a number of important conclusions, some of which are relevant for observationally distinguishing between driven and decaying turbulence in star-forming clouds.

We find that in both simulated environments the prestellar second moment distribution is fairly narrow and peaked about the sound speed. Significant broadness of the protostellar second moment distributions is due to strong infall, such that many

cores have central dispersions exceeding $2c_s$. Despite these commonalities, a K-S test indicates that the driven and decaying prestellar and driven and decaying protostellar populations are dissimilar to one another. In contrast to the second moments, a K-S test indicates that the first moment distributions in the two environments have some overlap: 13% confidence for protostellar cores and 44% confidence for prestellar cores. This similarity is an indication that the bulk core advection is decoupled from the gas motions inside the core. The similarity of the K-S tests suggests that core first moments are not a good method for distinguishing the two environments.

Examining the gas dispersion in the core neighborhoods reveals interesting differences in the two simulations. We find that by the end of a global free-fall time the averaged velocity dispersion increases strongly towards the core center for decaying protostellar cores. However, for decaying prestellar cores and all driven cores this trend is fairly flat or slightly increasing. Thus, for both phases the driven cores are coherent, similar to observed cores (Kirk et al. 2007; Barranco & Goodman 1998; Goodman et al. 1998), while the supersonic velocities observed in decaying protostellar cores are inconsistent with observations. Thus, investigating the radial dispersion of protostellar cores may make it possible to discriminate between clouds with and without active turbulent energy injection.

We find that the majority of the combined prestellar and protostellar distribution of second moments for both environments are below $2c_s$, which agrees with the results of A07 and K07. However, neither prestellar core distribution shows a significant confidence level of agreement with the observations.

As shown in Table 5, we obtain sub-virial dispersions of the first moments for both total core populations like A07, however our core-to-core dispersions are approximately a factor of 2 closer to virial. Although both runs produce sub-virial core-to-core dispersions, we have not shown that either driven turbulence or the small virial parameter of decaying turbulence can produce $\alpha_{\rm vir}$ as small as that found by A07.

One interesting finding is that the protostellar cores in the decaying run have a core-to-core dispersion that is higher than the gas dispersion measured after a free-fall time. This is a result of the significantly larger dispersion of the protostellar

cores compared to the prestellar cores, which may be a result of either increased scattering or of memory of the natal higher dispersion gas. This is in contrast to the driven prestellar cores, which have nearly the same dispersion as the gas, and the driven protostellar cores, which have a sub-virial dispersion. Thus, comparing the starless and protostellar core first moment dispersion to the net gas dispersion is potentially a means for distinguishing the two environments.

An effect that we cannot rule out is the importance of magnetic fields, which we do not treat in our simulations. In addition to seeding the initial clump mass spectrum, the turbulence in our simulations provides support against the cloud's self-gravity, a role that could be filled by either sustained turbulence or magnetic fields or both. The very small number of cores observed with supersonic second moments indicates that these cores are collapsing very slowly, a condition that we find is promoted by turbulent support but not throughout the entire core collapse process. At present, little computational work has been done to study line profiles for turbulent cores with magnetic fields. Tilley & Pudritz (2007) present central line profiles for a few cores formed in self-gravitating magneto-hydrodynamic cloud simulations but do not have good statistics. Our simulations also neglect protostellar outflows, which may have an effect on the total core mass and hence the velocity dispersion of the infalling gas in the core center.

Another possible source of the quantitative disagreement between observations and our simulations is geometry. Periodic boundary conditions may do a poor job representing whole, pressure confined molecular clouds. Certainly, the Perseus star-forming region is more filamentary than round. Further, the cloud Mach numbers for both regions are somewhat uncertain, and it may be necessary to match the Mach number of the simulation to the cloud more exactly to get better quantitative agreement.

Overall, we find that the driven simulation agrees better with the cores in Perseus, while the decaying simulation agrees slightly better with the prestellar cores in ρ Ophiuchus (our data do not include protostellar cores there). Our results indicate that the decaying simulation produces a population of protostellar cores with supersonic velocity dispersions that is largely inconsistent with the observations of

protostellar cores in Perseus. To reach a firmer conclusion on the validity of driven or decaying turbulence will require more complete data on a larger sample of clouds as well as simulations that allow for magnetic fields, outflows, and thermal feedback from the protostars.

Acknowledgements

We thank P. André, D. Johnstone, E. Rosolowsky, M. Enoch and H. Kirk for helpful discussions of their observations. Support for this work was provided under the auspices of the US Department of Energy by Lawrence Livermore National Laboratory under contacts B-542762 (S.S.R.O.) and DE-AC52-07NA27344 (R.I.K.); NASA through Hubble Fellowship grant HSF-HF-01186 awarded by the Space Telescope Science Institute, which is operated by the Association of Universities for Research in Astronomy, Inc., for NASA, under contract NAS 05-26555 (M. R. K.); NASA ATP grants NAG 05-12042 and NNG 06-GH96G (R. I. K. and C. F. M.), and the National Science Foundation under Grants No. AST-0606831 and PHY05-51164 (C. F. M. and S. S. R. O). Computational resources were provided by the NSF San Diego Supercomputing Center through NPACI program grant UCB267; and the National Energy Research Scientific Computer Center, which is supported by the Office of Science of the U.S. Department of Energy under contract number DE-AC03-76SF00098, though ERCAP grant 80325.

3.7 Appendix: Statistical Equilibrium for Molecules with Hyperfine Structure

As discussed in Tafalla et al. (2002) and Keto et al. (2004), hyperfine splitting in a molecule introduces two complications on top of the standard calculation of statistical equilibrium. First, hyperfine splitting of a transition reduces its optical depth by breaking the line into multiple components. The frequency separation between the components means that photons generated by a transition from level $i\alpha$ to level $j\beta$, where the Roman index refers to the parent level and the Greek to

its hyperfine sublevel, have a reduced probability of being resonantly absorbed by molecules in state j that are not in hyperfine sublevel β. Under our assumption that all components are optically thin, however, this effect is not significant. We discuss the extent to which this approximation holds, and how our results might be modified in cases where it fails, in § 3.5.2.

A second, practical complication is that collision rate coefficients between different hyperfine sublevels are generally unknown. Only the total rate coefficients summing over all hyperfine states are known. This makes it impossible to perform a true statistical equilibrium calculation without introducing additional assumptions, the most common of which is that the individual hyperfine sublevels are simply populated in proportion to their statistical weights. Observations along some sightlines show that this approximation generally holds for NH_3 and that deviations from it for N_2H^+ are only of order 10% (Tafalla et al. 2002; Keto et al. 2004).

Under the assumption of an optically thin gas, the equation of statistical equilibrium for a molecular species with hyperfine structure is

$$\begin{aligned} \sum_j \sum_\beta (n_{\rm H_2} q_{j\beta i\alpha} + A_{j\beta i\alpha} + B_{j\beta i\alpha} I_{\rm CMB}) f_{j\beta} & \\ = \left[\sum_k \sum_\beta (n_{\rm H_2} q_{i\alpha k\beta} + A_{i\alpha k\beta} + B_{i\alpha k\beta} I_{\rm CMB}) \right] f_{i\alpha} & \quad (3.15) \\ \sum_i \sum_\alpha f_{i\alpha} = 1, & \quad (3.16) \end{aligned}$$

where a set of four subscripts $i\alpha j\beta$ indicates a transition from state i, hyperfine sublevel α to state j, hyperfine sublevel β. The assumption that the hyperfine sublevels are populated in proportion to their statistical weight then enables us to write

$$f_{i\alpha} = \frac{g_{i\alpha}}{g_i} f_i, \quad (3.17)$$

where $g_{i\alpha}$ is the statistical weight of sublevel $i\alpha$, $g_i = \sum_\alpha g_{i\alpha}$ is the total statistical weight of all hyperfine sublevels of level i, and $f_i = \sum_\alpha f_{i\alpha}$ is the fraction of molecules in any of the hyperfine sublevels of level i. If we make this substitution in equations

(3.15) and (3.16), then they become

$$\sum_j \sum_\beta \left[(n_{\rm H_2} q_{j\beta i\alpha} + A_{j\beta i\alpha} + B_{j\beta i\alpha} I_{\rm CMB}) \frac{g_{j\beta}}{g_j} \right] f_j$$

$$= \left[\sum_k \sum_\beta (n_{\rm H_2} q_{i\alpha k\beta} + A_{i\alpha k\beta} + B_{i\alpha k\beta} I_{\rm CMB}) \frac{g_{i\alpha}}{g_i} \right] f_i \tag{3.18}$$

$$\sum_i f_i = 1. \tag{3.19}$$

If the hyperfine sublevels of state i are populated in proportion to their statistical weight, then the total transition rate from all hyperfine sublevels of state i to any of the sublevels of state j are given by

$$q_{ij} \equiv \sum_\alpha \sum_\beta \frac{g_{i\alpha}}{g_i} q_{i\alpha j\beta} \tag{3.20}$$

$$A_{ij} \equiv \sum_\alpha \sum_\beta \frac{g_{i\alpha}}{g_i} A_{i\alpha j\beta} \tag{3.21}$$

$$B_{ij} \equiv \sum_\alpha \sum_\beta \frac{g_{i\alpha}}{g_i} B_{i\alpha j\beta}. \tag{3.22}$$

Now note that (3.18) represents one independent equation for each state i and each of its hyperfine sublevels α. If we fix i and add the equations for each hyperfine sublevel α, then equation (3.18) simply reduces to

$$\sum_j (n_{\rm H_2} q_{ji} + A_{ji} + B_{ji} I_{\rm CMB}) f_j = \left[\sum_k (n_{\rm H_2} q_{ik} + A_{ik} + B_{ik} I_{\rm CMB}) \right] f_i, \tag{3.23}$$

the same as the equation for an optically thin molecule without hyperfine splitting, provided that the rate coefficients are understood to be summed over all hyperfine sublevels.

Chapter 4

The Shapes of Molecular Cloud Cores in Simulations and Observations

Offner & Krumholz, 2009, ApJ, 693, 914 [1]

4.1 Introduction

A successful theory of star formation must explain certain basic characteristics of the early stages of cores and stellar natal conditions. One property of interest is the shape distribution of starless and protostellar cores, which is likely related to the the initial conditions of star formation such as the local turbulent, the magnetic field configuration, and core collapse timescale (see review by McKee & Ostriker 2007). Strong magnetic fields in the early stages of core formation may either support gas perpendicular to the field lines yielding a distribution of oblate cores (Mouschovias 1976) or compress the cores into a prolate geometry (Fiege & Pudritz 2000). The former argument assumes predominantly poloidal magnetic fields, whereas the latter work includes a toroidal field component resulting in a helical field geometry. Independent of magnetic fields, prolate cores may also arise as an artifact of filamentary

[1]The Astrophysical Journal, 693, 914-921, March,

cloud geometry, in which cores fragment at intervals according to the characteristic Jeans length of a cylinder (Hartmann 2002).

Recent large-scale turbulent simulations with and without magnetic fields tend to find distributions of cores that contain predominantly triaxial cores when viewed in 3D (Klessen & Burkert 2000; Gammie et al. 2003; Basu & Ciolek 2004; Li et al. 2004; Offner et al. 2008a). In contrast, simplified numerical studies including ambipolar diffusion find triaxial cores with an inclination towards oblateness (Basu & Ciolek 2004; Ciolek & Basu 2006). Observations of molecular cloud cores in various star forming regions tend to find projected core aspect ratios, $q = a/b$, around 2:1 (Myers et al. 1991; Jijina et al. 1999; Nutter & Ward-Thompson 2007), but comparison of these observations with simulations is hampered by the projection of the observed cores onto the plane of the sky. Some authors have presented analytic work attempting to overcome this difficulty by "de-projecting" the observed cores statistically. For example, Ryden (1996), assuming axisymmetry, finds that cores are significantly more likely to be randomly oriented prolate objects than oblate objects. Tassis (2007, henceforth T07) utilizes a maximum-likelihood method to generate a distribution of ellipsoid axial ratios. He uses two base probability distribution functions and finds that oblate or triaxial cores agree well with observations of cores in Orion (Nutter & Ward-Thompson 2007, hereafter NWT), results which are insensitive to the assumed underlying distribution. Overall, T07 finds that prolate cores are rare, and his method rules out a uniform distribution of oblate, prolate, and triaxial cores with greater than 99% confidence.

Our study is complementary to this previous work, but we perform the core shape comparison in the observational domain rather than the theoretical one. This has a significant advantage over alternative approaches, because it allows us to realistically simulate the effects of finite telescope resolution and sensitivity, and to reduce the simulated observations and fit core shapes using the same methods used for the real data. In this paper, we post-process simulations in this manner and compare with the dataset of Orion reported by NWT, who collate and reanalyze various SCUBA observations of the Orion A and B North and South molecular cloud complexes. They report the masses and sizes for 393 cores. Consequently, this dataset

not only concerns an interesting and well-studied region, but it is also sufficiently large for meaningful statistics.

In section 4.2, we describe the details of the simulations and post-processing. We consider simulations where turbulence is continually driven and where it is allowed to decay. In section 4.3, we present comparisons between the simulations and observations and compare with T07. In section 4.4, we summarize our conclusions.

4.2 Simulated Observations

As described in Offner et al. (2008a,b), our two simulations are periodic boxes containing an isothermal, non-magnetized gas that is initially not self-gravitating. After driving turbulent motions in the gas for two box crossing times, self-gravity is turned on. In one simulation energy injection is halted and the turbulence gradually decays, while in the other turbulent driving is maintained so that the cloud satisfies energy equipartition. A sink particle is introduced when the Jeans condition is exceeded on the finest AMR level, where the cell spacing is Δx=200 AU (Krumholz et al. 2004). Since isothermal self-gravitating gas is scale free, it is easy to normalize the simulations to the conditions observed in Orion using the thermal Jeans length and thermal Jeans mass (see scaling relations in Offner et al. 2008b). For the simulation normalization, we adopt a gas temperature of $T = 20$ K (NWT). We choose a gas density of $\rho = 9.74 \times 10^{-21}$ g cm^3 (number density of hydrogen nuclei $n_H = 4.2 \times 10^3$ cm^{-3}), corresponding to a simulation box length of 2 pc. At this density, the typical box column density is $N_H = 2.6 \times 10^{22}$ cm^{-2}, close to the measured central column density of the Orion B cloud, $N_H = 2.8 \times 10^{22}$ cm^{-2} (Maddalena et al. 1986; Johnstone et al. 2001). Although Maddalena et al. (1986) observe a much larger region than the individual north and south complexes in Orion A and B, column densities are observed to be roughly scale-independent (Larson 1981; Heyer et al. 2008) (although it has been argued that this is a selection effect – e.g., Ballesteros-Paredes & Mac Low 2002). Thus, our normalization is consistent.

We pause at this point to add a caveat about our normalization: our box size is smaller than the individual Orion A and B North and South complexes, which

have projected sizes of $\sim 3-4$ pc. Equivalently, our simulation contains a smaller number of total thermal Jeans masses of gas than the entire Orion A and B North and South complexes. The justification for this is that the periodic geometry of the simulation enables us to model a piece of the cloud rather than the entire cloud. As long as we have the correct mean density, the behavior of structures that are much smaller than the box size such as cores should not depend on the size of the simulation box. Indeed, the similarity between the results for driven and decaying turbulence, and the insensitivity of our results to our assumed density normalization (see below), seem to support the hypothesis that small-scale structure is insensitive to such large-scale features as the total box size and the number of thermal Jeans masses it contains. However, establishing this point definitively would require a suite of simulations with varying total sizes but the same resolution, and such a study is unfortunately too computationally costly to perform. We therefore simply caution readers on this point and proceed.

We run the simulations with gravity for a global free-fall time, $t_{\rm ff}$, and we compare with the observations at $\frac{1}{2}t_{\rm ff}$ and $1t_{\rm ff}$. The column density of the two simulations at $1t_{\rm ff}$ is displayed in Figure 4.1. At these times, the Mach number, $\mathcal{M}$, is 8.4 for the driven simulation and $\mathcal{M} = 5.3$, 4.5 for the decaying simulation. For the driven simulation, this corresponds to half the Mach number of the larger Orion A and B regions that we compare with (Maddalena et al. 1986). However, it is unlikely that the high Mach number flow regions will have a significant effect on the details of the cores, which are generally subsonic to transonic.

It is possible to convert the simulation column density to an observed intensity using the relation

$$I_\nu = N_{\rm H}\Omega_{\rm mb}\mu_{\rm H}\kappa_\nu B_\nu(T_{\rm cloud}), \tag{4.1}$$

where I_ν is the flux density per beam at frequency ν, Ω_{mb} is the solid angle subtended by the beam, μ_H is the mean mass per H atom, κ_ν is the dust opacity at frequency ν, and $\mathrm{B}_\nu(\mathrm{T})$ is the Planck function (Enoch et al. 2007). We set ν=850 μm to match the observations of NWT, and following them we adopt $\kappa_{850} = 0.01$ cm^{2}g^{-1}. Note that equation (4.1) assumes that the gas is optically thin at 850 μm. The densest sightline through the simulation has a column density of $\Sigma = 0.6$ g cm^{-2} or

τ_{850}=0.06, which is safely optically thin.

In order to facilitate comparison with NWT, we post-process the simulation data to have noise and resolution comparable to the SCUBA data. In each projection direction, we integrate along the line of sight and convolve the column density image with a beam of 14" resolution. We assume that the simulated cloud lies at a distance of 400 pc, which is the average distance adopted by NWT. To each pixel in the smoothed image, we add a Gaussian noise distribution with $\sigma_{\rm NWT} = 20$ mJy beam^{-1}, correlated over the FWHM size of the beam. This reproduces the coarser pixel resolution noise inherent in the SCUBA data.

Having generated a simulated column density map, we analyze the data using the same procedure outlined in NWT, which we describe in the following steps. First, from the post-processed simulation data, we generate a large-scale structure map by convolving the data with a beam size of 1'. Second, we subtract this map from the high resolution version to remove large-scale structure and make core identification easier. Third, we define cores as density enhancements within $3\sigma_{\rm NWT}$ contours that contain a peak above $5\sigma_{\rm NWT}$. With few exceptions, core shapes are generally elliptical. Finally, we fit an ellipse around each peak and match to the $3\sigma_{\rm NWT}$ contours "by eye" guided by a sample eye-fit from NWT (D. Nutter, 2008, priv. comm.). An automated fitting algorithm would clearly be preferable to the "by eye" procedure from the standpoint of reproducible comparison between different samples and authors. However, after experimenting with several options we were unable to find an algorithm that adequately reproduced the fits from NWT, while we were able to do so reasonably well by eye. Since the goal of this paper is to compare to the observed sample, we use by eye fits. Based on the elliptical fits we assign each core an axis ratio q. We identify cores that contain a sink particle within 0.05 pc of their core center as "protostellar cores", while cores that do not contain a sink particle are "starless". In the sample of Orion cores, the protostellar cores are identified with the Spitzer IRAC camera.

Figure 4.2 shows one projection through the simulation domain for the driven run, along with the bounding ellipses for all the cores we identify in that projection. For comparison, the unprocessed driven column density is shown in the right panel

of Figure 4.1. To improve the statistics, we include cores from maps in each cardinal direction of the simulation. The Kolmogorov-Smirnov (K-S) test provides a good statistical measure of the agreement of two distributions (Press et al. 1992). It derives 1 minus the confidence level at which the null hypothesis that the two were drawn from the same underlying distribution can be ruled out[2]. In the remainder of the paper, we report the quantity 1 minus the confidence level multiplied by a factor of a 100 to give a percentage. Using a K-S test, we find that core samples from different lines of sight are consistent with being drawn from the same distribution (K-S statistics $\sim 50\%$). This implies that the core ratios in the three projections are statistically indistinguishable, so our procedure of treating each orientation as an independent sample is consistent. The agreement among the orientations also shows that fitting by eye is reasonably reproducible.

We verify that the distribution of core ellipses is not strongly dependent on the details of the normalization by comparing the ellipses in the fiducial case with core samples assuming $\sigma = 0.5\sigma_{\rm NWT}$, and $\sigma = 2\sigma_{\rm NWT}$. This is equivalent to adopting the same contour level while changing the average density of the simulation by a factor of 2. Figure 4.3 shows the fiducial distribution of axes ratios and the two distributions with different contours. We find that the new axis ratio distributions are consistent with being drawn from the same distribution at 99% and 17% confidence, respectively, when comparing samples of equal number. Using a lower or higher contour level respectively increase or decreases, respectively, the number of cores in the population by $\sim$30%.

[2]Formally, the two-sided K-S statistic we use is computed as follows. Consider two sets of N and M measurements of some quantity x (in our case x is the axis ratio, and the two sets of measurements are the simulated and observed values). Let $F_N(x)$ and $G_M(x)$ be the cumulative distribution functions for those measurements, i.e., $F_N(x)$ is the fraction of the N measurements that yield a value less than or equal to x, and similarly for $G_M(x)$. The K-S statistic is then defined as $D_{N,M} = \sup_x |F_N(x) - G_M(x)|$, i.e., the maximum distance between the two cumulative distribution functions. Kolmogorov's Theorem then states that we can reject the null hypothesis that $F_N(x)$ and $G_M(x)$ were drawn from the same parent distribution with a confidence level α if $\sqrt{NM/(N+M)}D_{N,M} > K_\alpha$, where K_α is defined implicitly by the equation $1-\alpha = \Pr(K \leq K_\alpha)$ and $\Pr(K \leq x) \equiv 1 - 2\sum_i^\infty (-1)^{i-1} e^{-2i^2x^2}$. Intuitively, α gives the probability that we could have measured a value of $D_{N,M}$ as large as we did if $F_N(x)$ and $G_M(x)$ were actually drawn from the same parent distribution. The smaller α is, the less likely that our samples would have produced such a large $D_{N,M}$ if the samples were drawn from the same parent distribution.

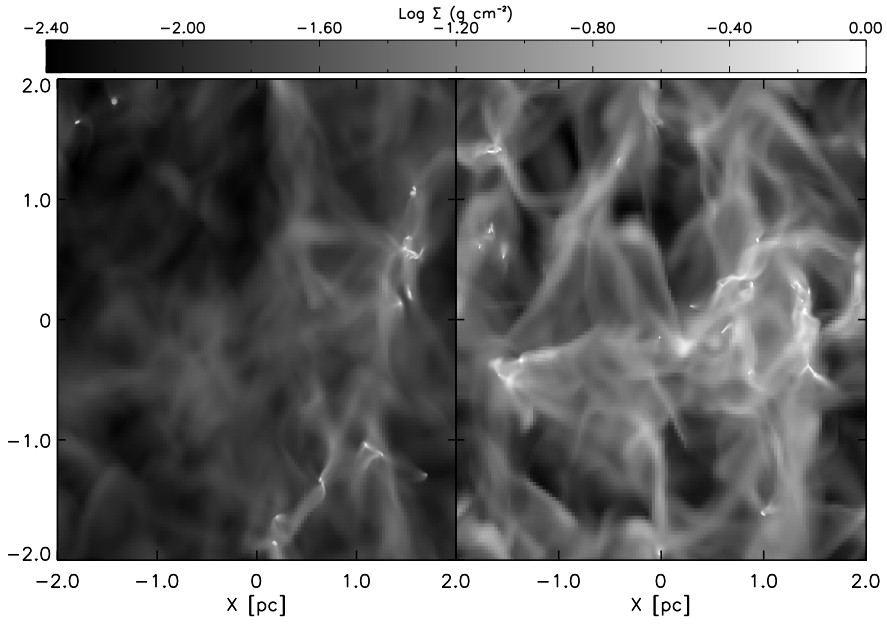

Figure 4.1 Logarithm of the column density, Σ, for one projection of the decaying (left) and driven(right) simulations at $1t_{\rm ff}$.

4.3 Data Comparison

In Table 1 we report a summary of the statistical properties of our cores, including the size of the sample, the absolute sizes of cores, and their aspect ratios. We compute these properties for all cores, for the actual Orion data, and for both the driven and undriven simulations at our two sample times $t = \frac{1}{2}t_{\rm ff}$ and $t = t_{\rm ff}$. In each case we report properties both for the entire population of cores regardless of whether they contain stars and for the starless and protostellar populations separately.

4.3.1 Core Sizes

In this section, we compare the physical sizes of the simulated and observed cores, where the lengths of the semi-major and semi-minor axes are given in Table 4.1. Generally, we find that the medians of the net distribution of simulated core sizes are $\sim 20\%$ smaller. Whereas the simulated starless core sizes are fairly similar to

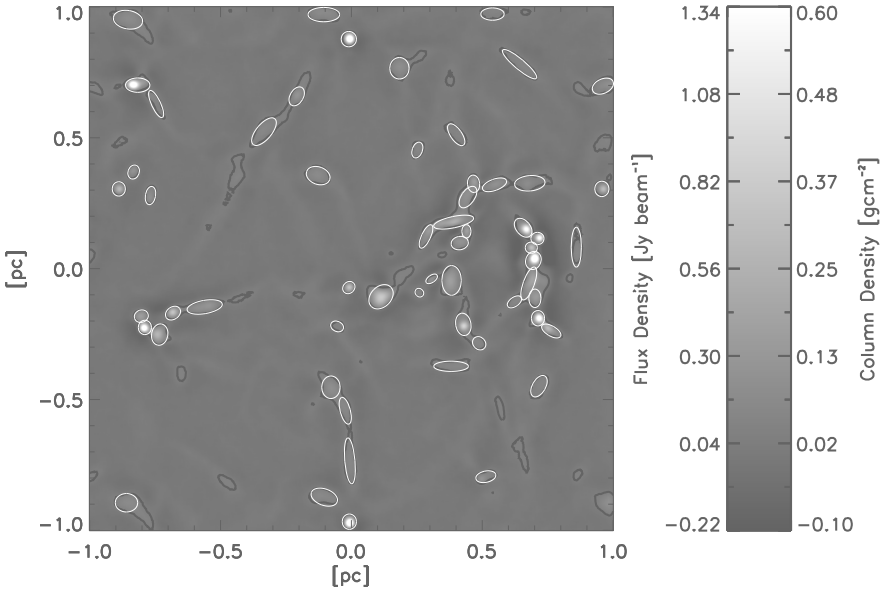

Figure 4.2 Column / flux density for one projection of the post-processed driven simulated cores at $1t_{\rm ff}$. The image includes noise and beam-smearing. The $3\sigma_{\rm NT}$ contours are marked in black and the fitted ellipses are overlaid in white.

observation, the observed protostellar core sizes are much larger than their simulated counterparts. This discrepancy is likely an artifact of the sink particle accretion algorithm: once a core forms a sink particle the surrounding gas is accreted more quickly and to higher masses without losses from outflows, so that the reservoir of bound gas around the sink particle is rapidly depleted. It is also possible that magnetic fields, which we neglect, play a significant role in supporting the protostellar envelopes, thus slowing the collapse process and contributing to the larger sizes of the observed protostellar cores.

As shown in Figure 4.4, the simulation core size distributions have smaller dispersions than the observation. Although some of the difference can be attributed to the smaller sizes of protostellar cores, the smaller core sample and simulation domain size may also contribute. The minimum core size is most likely set by the observation resolution.

We can compensate for the rapid depletion of gas in the outer parts of protostellar cores if we adopt a significantly lower estimate of the telescope noise ($\sigma \sim 0.2\sigma_{\rm NWT}$) and thus a lower contour threshold for defining cores. This has the effect of making the protostellar cores somewhat larger while leaving the starless sizes mostly unchanged, so that the overall size distribution is in better agreement with the observations. Using this lower noise level does not significantly alter the core shape distribution, however, which suggests that the discrepancy in core sizes is not significant for the purpose of determining core shapes. We therefore proceed with our analysis using the real telescope noise level, $\sigma = \sigma_{\rm NWT}$.

4.3.2 Overall Shape Distributions

As shown in Table 4.1, we find similar means and medians for the shape distributions. The characteristic mean falls around $q = 0.6 - 0.7$. The maximum aspect ratio is also very similar in all the cases, around 4:1, and the most elongated core is starless. In the simulations, core elongation is a result of the initial filamentary gas structure out of which the cores form. It is the remnant of the turbulence rather than a signature of magnetic fields.

We next characterize the similarity of the distributions by using a K-S test. One

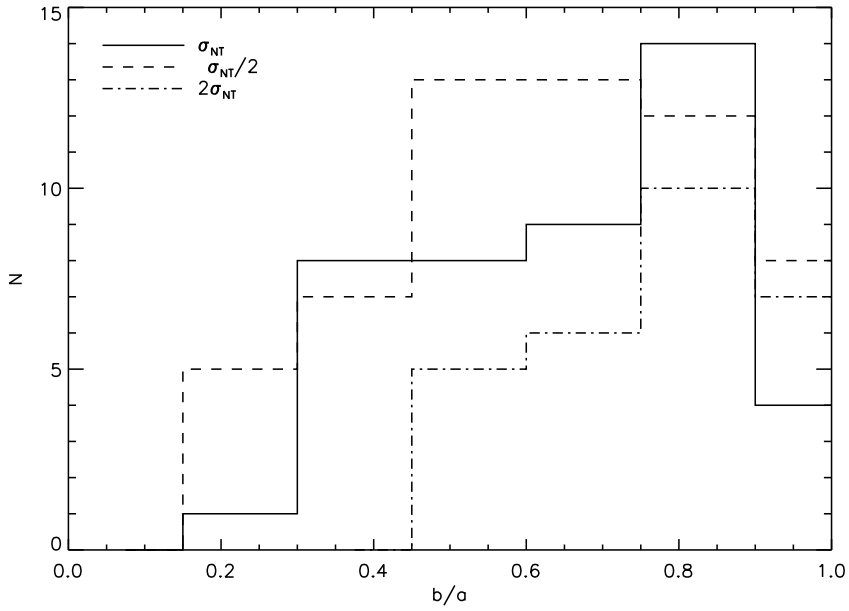

Figure 4.3 Number of cores as a function of axis ratio $q = b/a$ along a single projection for cores defined using the fiducial σ_{NT}, $2\sigma_{\rm NT}$, and $0.5\sigma_{\rm NT}$ at $1t_{\rm ff}$.

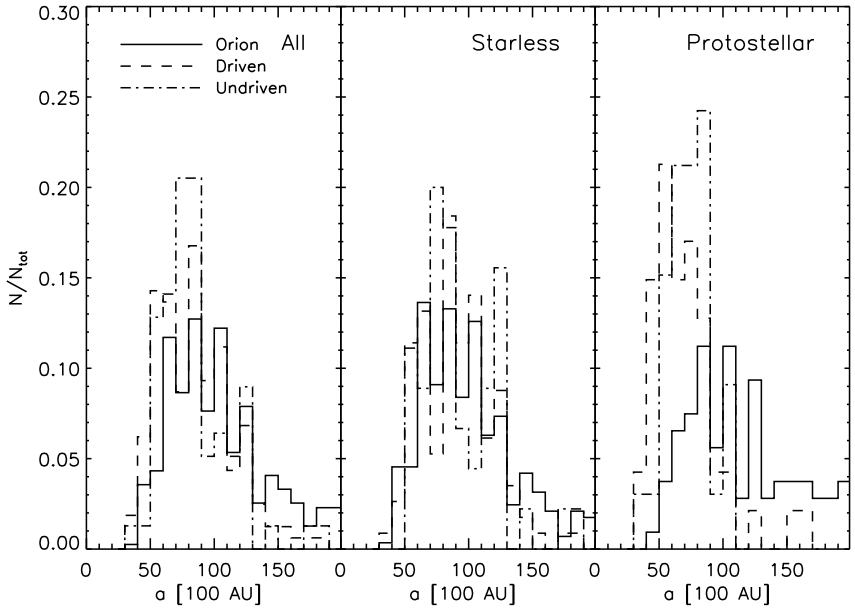

Figure 4.4 The sizes of major axis, a, in units of 100 AU for the total, starless, and protostellar cores, from left to right, at $1t_{\rm ff}$.

Table 4.1. Core axis ratio b/a minimum, median, and mean and median core sizes.

	All				
	O[a]	D_1[b]	$D_{\frac{1}{2}}$[c]	U_1[d]	$U_{\frac{1}{2}}$[e]
$N_{\rm cores}$	393	161	152	78	66
Minimum $\frac{b}{a}$	0.24	0.22	0.23	0.18	0.23
Median $\frac{b}{a}$	0.66	0.68	0.58	0.65	0.65
Mean $\frac{b}{a}$	0.67	0.66	0.61	0.66	0.62
Median a_{100}[f]	100	76	84	80	92
Median b_{100}[f]	64	48	48	52	56

[a]Observed Orion molecular cloud cores (NWT)

[b]Driven turbulence simulation at $1t_{\rm ff}$

[c]Driven turbulence simulation at $\frac{1}{2}t_{\rm ff}$

[d]Undriven turbulence simulation at $1t_{\rm ff}$

[e]Undriven turbulence simulation at $\frac{1}{2}t_{\rm ff}$

[f]Median projected semi-major (a) and semi-minor (b) size in units of 100 AU.

Table 4.2. Core axis ratio b/a minimum, median, and mean and median core sizes.

	Starless					Protostellar				
	O[a]	D_1[b]	$D_{\frac{1}{2}}$[c]	U_1[d]	$U_{\frac{1}{2}}$[e]	O	D_1	$D_{\frac{1}{2}}$	U_1	$U_{\frac{1}{2}}$
$N_{\rm cores}$	286	114	103	45	50	107	47	49	33	16
Minimum $\frac{b}{a}$	0.24	0.22	0.23	0.18	0.23	0.34	0.23	0.26	0.28	0.66
Median $\frac{b}{a}$	0.66	0.66	0.55	0.68	0.57	0.68	0.68	0.74	0.79	0.76
Mean $\frac{b}{a}$	0.66	0.64	0.56	0.58	0.57	0.68	0.68	0.73	0.77	0.80
Median a_{100}[f]	96	88	88	80	104	120	64	68	72	64
Median b_{100}[f]	64	54	48	48	56	76	48	48	52	48

[a]Observed Orion molecular cloud cores (NWT)

[b]Driven turbulence simulation at $1t_{\rm ff}$

[c]Driven turbulence simulation at $\frac{1}{2}t_{\rm ff}$

[d]Undriven turbulence simulation at $1t_{\rm ff}$

[e]Undriven turbulence simulation at $\frac{1}{2}t_{\rm ff}$

[f]Median projected semi-major (a) and semi-minor (b) size in units of 100 AU.

interesting aspect of the Orion dataset is that we can rule out the possibility that the separate Orion A and B populations originate from the same parent population with $> 95\%$ confidence. This disagreement is caused by the higher fraction of elongated cores in Orion B. The physical difference between the North and South regions are otherwise not large: both are sites of high-mass star formation, both have similar average column densities (Maddalena et al. 1986), and the patches surveyed are roughly the same size. However, Orion A has a 25% larger velocity dispersion, 5.1 km s^{-1} as measured in CO (Maddalena et al. 1986). The magnitude of this difference is a useful number to bear in mind when characterizing the extent of agreement or disagreement with the simulations. In comparison, the driven and decaying samples are consistent with being drawn from the same parent population at 88% and 66% confidence for $1t_{\rm ff}$ and $\frac{1}{2}t_{\rm ff}$, respectively.

We note that the K-S statistic is somewhat influenced by the size of the distribution being compared. For example the smaller the samples, the more likely the test will conclude two samples are consistent with being drawn from the same distribution. In general we find if we always compare distributions of the same size (by randomly selecting cores from the larger distribution), K-S agreement rises by $5 - 10\%$.

Table 4.3 shows the K-S statistics for comparisons of the axis ratios in Orion to each of the simulations. Overall, the decaying turbulence simulation agrees better with the Orion populations, although both simulations have fairly high agreement with Orion B. Given the uncertainties in the normalization and the disagreement between the Orion A and B samples, we consider agreement greater than 10% to be encouraging. Interestingly, the disagreement of the driven population is determined mainly by the disagreement of ellipses in one particular projection at $1t_{\rm ff}$, which has an overabundance of elongated cores. Minus the cores in this projection, the driven sample agrees with $\sim 17\%$ confidence at this time. Figure 4.5 shows the cumulative distribution function of the core shapes for the observations and two simulations.

Table 4.3. K-S agreement of simulations with Orion for net populations

	Orion		
	O[a,b] total (%)	A (%)	B (%)
D_1[c]	2.3	1.2	32.9
$D_{\frac{1}{2}}$	0.03	.004	3.7
U_1[d]	25.2	18.0	67.7
$U_{\frac{1}{2}}$	3.8	1.0	16.0

[a]Observed Orion molecular cloud cores (NWT)

[b]Comparison of Orion A with Orion B gives a K-S statistic of 4.6%.

[c]Driven turbulence simulation

[d]Undriven turbulence simulation

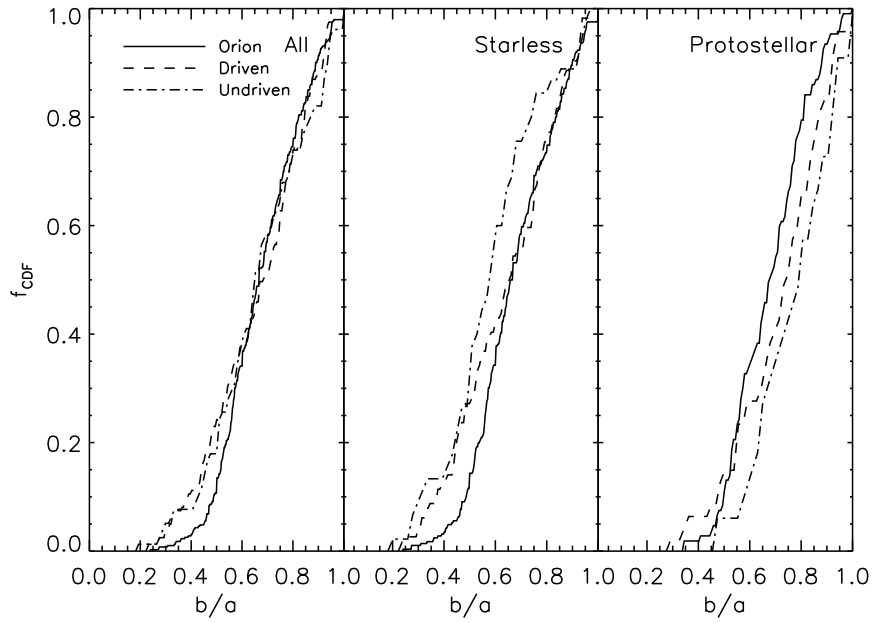

Figure 4.5 Cumulative distribution function of the total, starless, and protostellar shape distribution, from left to right, at $1t_{\rm ff}$.

4.3.3 Starless and Protostellar Core Shapes

K-S agreement for starless and protostellar cores is compared in Table 4.4. We find similar agreement with the Orion data for both the driven and undriven starless core shapes at $1t_{\rm ff}$. In contrast with the observational data, which has a high level of agreement between the Orion starless and Orion protostellar core shapes ($\sim 60\%$) the driven starless and driven protostellar core shapes are only moderately similar ($\sim$13%), while the decaying starless and decaying protostellar core shapes are quite dissimilar ($\sim 0.02\%$). This is illustrated in the second and third panels of Figure 4.5, which show the undriven starless distribution of shapes significantly to the left of the Orion distribution, while the undriven protostellar distribution falls to the right. As a result, the individual simulation starless and protostellar shape distributions can be much less similar to the observed cores than the net simulation shape distribution (see U_1 in Table 4.3 and 4.4). One caveat of this comparison is that the actual goodness of agreement depends not only upon agreement between the net shape distributions but upon the agreement between the individual starless and protostellar

shapes and observations. Figure 4.5 suggests that, particularly for the decaying case, the K-S test may overestimate the overall similarity to observed cores. Observational data bears out the similarity of the distributions of starless and protostellar shapes (Myers et al. 1991; Jijina et al. 1999). In the decaying simulation, the difference is likely due to the more rounded protostellar cores, which are experiencing strong collapse (Offner et al. 2008b).

In Figure 4.6 we plot the number of starless cores as a function of axis ratio, q. For comparison, we also plot the T07 maximum-likelihood curves drawn from normal and beta distributions. In spite of the larger variation in the simulation data (due to the smaller sample size), the simulation data also appears to follow the curves reasonably well. Offner et al. (2008a) report that the protostellar cores in both simulations are mainly trixial, with some preference for prolateness over oblateness. To investigate the 3D shape distribution of the starless cores, which were not examined in Offner et al. (2008a), we first triangulate the 2D projected positions to identify the 3D coordinates of the core center. By setting a minimum density cutoff for cells within 0.1 pc of the core center, we define the gas contained in the core. We adopt a density cutoff of the minimum of $n_{\rm H} = 2 \times 10^4$ cm^{-3} and 0.2 $n_{\rm Hpeak}$, where protostellar cores generally satisfy the former and starless cores the latter. Unlike the core definition in Offner et al. (2008a), we do not require that the gas be bound. We apply principle component analysis to the set of cells comprising each core to identify the eigenvalues of the cardinal axes (Jolliffe 2002). As shown in Figure 4.7, the cores for both simulations are predominately triaxial. The remaining cores are preferentially prolate. However, the ratio of the number of prolate to oblate cores in 3D is somewhat sensitive to the chosen cutoff density. These results appear to be inconsistent with the claim of T07 that the observed core axis distribution implies that prolate cores are rare while oblate cores are more common.

4.3.4 Time Dependence of Core Shapes

We find less K-S agreement between the Orion core shapes and the simulated cores at $\frac{1}{2}t_{\rm ff}$. The origin of the disagreement is mainly due to the smaller mean axes ratios in both the driven and decaying cases as illustrated in Table 4.1. The

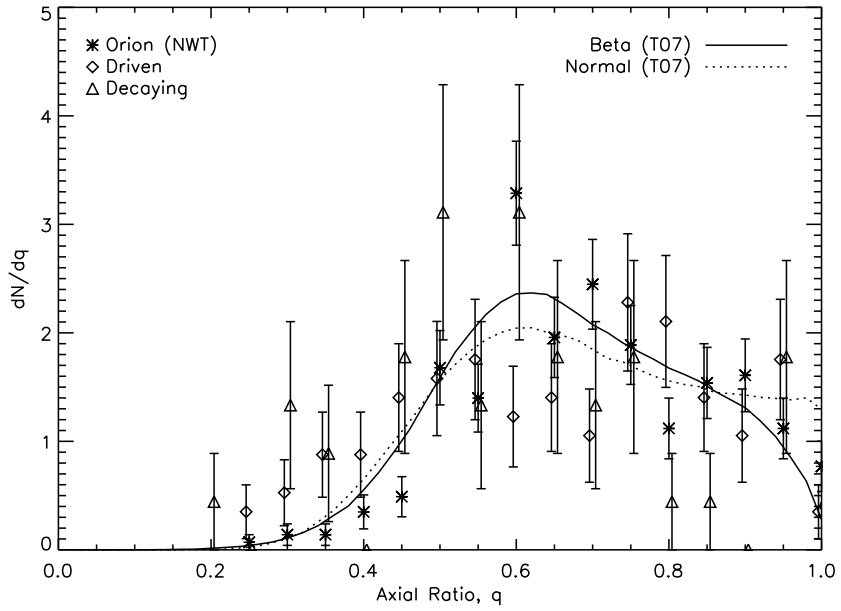

Figure 4.6 Histrogram of starless cores ratios $q = b/a$ at $1t_{\rm ff}$. Results from T07 derived assuming underlying beta and normal distribution for core ratios have been overlaid. The error bars shown on each bin reflect $\sqrt{N}$ counting statistics. The bins for each sample are centered at the same values of q, but the plotted points have been offset slightly to the left or right to allow the error bars to be distinguished.

Table 4.4. K-S agreement of simulations with Orion for starless and protostellar populations

	O[a]Starless (%)		O Protostellar (%)
D_1[b]Starless	1.2	D_1 Proto	20.7
$D_{\frac{1}{2}}$ Starless	2.2×10^{-5}	$D_{\frac{1}{2}}$ Proto	2.5
U_1[c]Starless	1.2	U_1 Proto	2.9
$U_{\frac{1}{2}}$ Starless	0.04	$U_{\frac{1}{2}}$ Proto	0.4

[a]Observed Orion molecular cloud cores NWT

[b]Driven turbulence simulation

[c]Undriven turbulence simulation

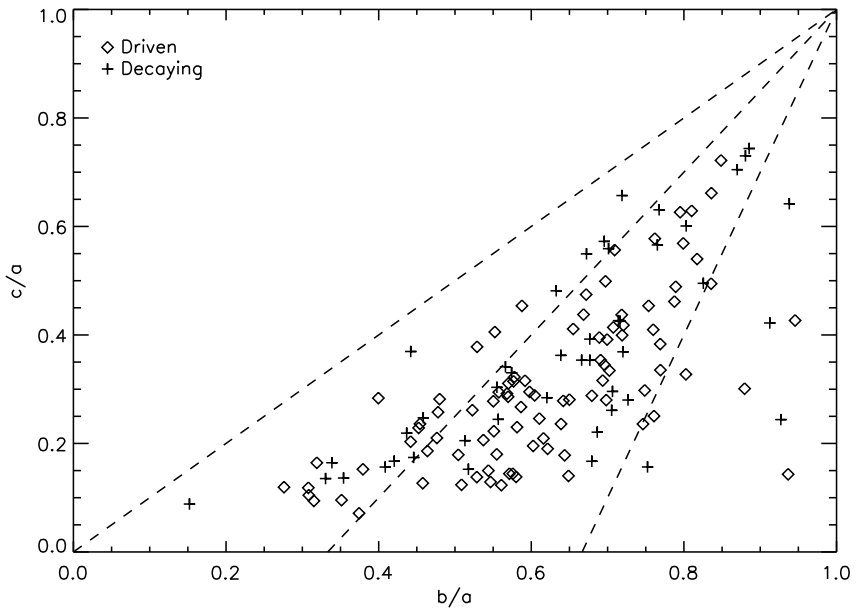

Figure 4.7 Plot of the 3D core aspect ratios c/a vs. b/a at $1t_{\rm ff}$. The dashed lines indicate the boundary between prolate, triaxial, and oblate cores, from left to right.

difference between starless cores and protostellar cores is also more pronounced at this time since the starless cores in both simulations are more elongated and the agreement between the observed and simulated starless distributions is much worse than for the protostellar core distributions. This may be because the simulated protostellar cores are necessarily located in regions of the flow that are dominated by gravitational effects. In contrast, at early times the shapes of starless cores are more strongly influenced by turbulence rather than gravity and so they appear more elongated and filamentary. This suggests that gravitational fragmentation, in addition to turbulence, significantly influences core shapes.

4.4 Conclusions

Overall, we find a high level of similarity between observations of core axis ratios in Orion and simulations of core formation in a self-gravitating, non-magnetized turbulent medium, with either driven or decaying turbulence. We find the best agreement occurs after one dynamical time. The similarity extends from the mean and median core axis ratios to the distributions of starless and protostellar core shapes. We obtain good agreement despite the absence of magnetic fields in the simulations, which may indicate that the local magnetic field in Orion is not strongly influencing the core shapes. This is supported by both turbulent magnetic simulations such as those by (Ballesteros-Paredes & Mac Low 2002) and observations that find the shapes of high density structures are not strongly correlated with the magnetic field direction (Ballesteros-Paredes et al. 2007). Moreover, we find that a population of cores that is intrinsically triaxial, but with a tendency to be more prolate than oblate, can produce an observed distribution of core axis ratios consistent with what is seen in Orion.

The axis ratio distributions are also quite similar in the simulations with driven and decaying turbulence. In fact, we find that the shape distributions of Orion A and Orion B are often more dissimilar (4.6% K-S statistic) to each other than to the simulations. This indicates that the level of turbulence does not play a significant role in determining core shapes. Both simulations compare with larger confidence

to the Orion B core sample, although in terms of statistics, the decaying simulation has slightly better agreement with the total Orion sample of cores.

Increasingly large and complete observational data sets invite important comparisons with simulations, which could shed light on both the theory of star formation and details of the molecular clouds we observe. Our results provide a cautionary note that such comparisons should preferably be done by projecting from simulations into the observational domain, including realistic sensitivities and resolutions. Further simulations concerning the effects of magnetic fields, combined with more detailed simulated observations, would be a beneficial future direction of research.

Acknowledgements

The authors thank K. Tassis and J. Goldston-Peek for helpful discussions and D. Nutter for details and clarifications concerning his recent work on Orion. In addition, helpful suggestions from the referee, J. Ballesteros-Paredes, significantly improved this manuscript. Support for this work was provided by the US Department of Energy at the Lawrence Livermore National Laboratory under contracts B-542762 (S. S. R. O.); NASA through Hubble Fellowship grant HSF-HF-01186 awarded by the Space Telescope Science Institute, which is operated by the Association of Universities for Research in Astronomy, Inc., for NASA, under contract NAS 05-26555 (M. R. K.); the National Science Foundation under Grant PHY05-51164 (S. S. R. O). Computational resources were provided by the NSF San Diego Supercomputing Center through NPACI program grant UCB267; and the National Energy Research Scientific Computer Center, which is supported by the Office of Science of the U.S. Department of Energy under contract number DE-AC03-76SF00098, though ERCAP grant 80325.

Chapter 5

The Effects of Radiative Transfer on Low-Mass Star Formation

Offner, Klein, & McKee, Krumholz, 2009, ApJ, accepted. [1]

5.1 Introduction

On large scales molecular clouds are generally observed to have limited temperature variations, a characteristic that results from the high efficiency of radiative cooling at typical cloud densities. Consequently, simulations of molecular clouds frequently assume constant gas temperature, a convenient approximation for investigations of gas-dynamics, turbulence, and gravitational collapse (Gammie et al. 2003; Bonnell et al. 2003; Li et al. 2004; Tilley & Pudritz 2004; Vázquez-Semadeni et al. 2008). However, an isothermal assumption necessarily neglects the influence of heating due to gas compression, accretion, and stellar sources.

The importance of the local gas temperature to the star formation process is motivated analytically when considered in combination with gravity. The characteristic fragmentation scale for self-graviting gas of density, ρ, and sound speed, $c_{\rm s}$, is

given by the Jeans length:

$$\lambda_J = \sqrt{\frac{\pi c_s^2}{G\rho}} \propto \left(\frac{T}{\rho}\right)^{1/2}. \tag{5.1}$$

Thus, for lower temperatures, gas is prone to gravitational instability at lower densities. In rotating self-gravitating disks, the criterion may be phrased in terms of the local column density Σ:

$$Q = \frac{\kappa_\epsilon c_s}{\sqrt{\pi G \Sigma}} \propto T^{1/2}, \tag{5.2}$$

where the onset of gravitational instability occurs as the Toomre parameter, Q, approaches one and κ_ϵ is the epicyclic frequency. Cold protostellar disks more readily develop spiral structure and become Toomre unstable, influencing protostellar accretion and driving fragmentation (Kratter et al. 2008). Overproducing low-mass objects or brown dwarfs in the stellar initial mass function is one side-effect of increased fragmentation (Bate 2009b; Krumholz et al. 2007b).

Gas eventually becomes optically thick at densities orders of magnitude above the molecular cloud mean, and radiative cooling is no longer efficient. To investigate this transition, Masunaga et al. (1998) modeled a spherically symmetric core collapse including angle-dependent multi-frequency radiative transfer, resolving scales down to the accretion shock. They halted the calculation at the end of the first collapse phase, prior to the dissociation of H_2 and before protostellar feedback commences. The authors reported a characteristic transition density of $\sim 10^{-13}$ g cm^{-3} for initially 10 K gas, above which the temperature increased with increasing density. In many turbulent simulations rudimentary heating due to gas compression is frequently represented using an equation of state (Li et al. 2003; Bate et al. 2003; Bate & Bonnell 2005; Jappsen & Klessen 2005; Bonnell et al. 2006; Offner et al. 2008a; Clark et al. 2008; Bate 2009a). Although such an equation typically fits a more exact radiative transfer solution like that reported by Masunaga et al. (1998), it neglects the instantaneous mean free path, multi-dimensional effects, dust chemistry, and time dependence of stellar sources. In fact, the subsequent paper, Masunaga & Inutsuka (2000), demonstrated that gas temperatures may become significantly warmer as a result of protostellar feedback and that the temperature distribution is quite sensitive to the accretion luminosity.

To compromise between physics and computational expense, a few hybrid methods include heating by solving explicit diffusion approximations, estimating the instantaneous radiative cooling, or extrapolating from previously tabulated temperatures (Stamatellos et al. 2007; Banerjee & Pudritz 2007; Bonnell & Rice 2008). Such methods are computationally cheaper and reproduce radiative heating for simple geometries. However, the suitability of these approximations is unclear for radiative problems involving clustered star formation in a turbulent medium, where the problem is highly non-linear, involves complex geometry, and the column density may not be a good indicator of the cooling rate. In addition, many of these approaches also neglect heating by stellar sources, which are crucial as we will show in this paper. The unknown accuracy of radiation approximations and the deficiencies in handling temporal and spatial variations motivates our use of a full radiative transfer method, albeit one based upon the gray flux-limited diffusion approximation.

Relatively few authors have pursued 3D calculations including radiative transfer. These authors always adopt the flux-limited diffusion approximation and assume that the radiation field is frequency-independent, i.e., gray. By modeling star formation with gray flux-limited diffusion (GFLD), it has been shown that a barotropic or polytropic equation of state (EOS) can underestimate the true heating at high densities even for simple, non-turbulent collapse problems (Boss et al. 2000; Whitehouse & Bate 2006). The issue of radiative feedback is particularly acute for high-mass stars, which emit prodigious luminosities while forming (Krumholz 2006; Krumholz et al. 2007b, 2009). To explore this point, Krumholz et al. (2007b) contrasted simulations of collapsing, turbulent high-mass cores using an isothermal EOS to those using GFLD radiation transfer. The authors demonstrated that simulations with radiative transfer are able to produce a massive star formed from gas accretion, while barotropic or isothermal calculations may only produce a massive star via mergers of many smaller bodies. Comparisons of the temperature distribution, assuming a barotropic EOS in lieu of radiative transfer, showed significant underestimation of the volume of heated gas and a much lower local maximum gas temperature.

In the regime of low-mass star formation, Bate (2009b) modeled several small clusters forming low-mass stars with the SPH radiative transfer method developed

by Whitehouse & Bate (2006). The author compared these with previous published simulations using identical initial conditions and a barotropic EOS. The calculations including radiation transfer showed a substantial decrease in the number of brown dwarfs from 50% of the number of objects to $< 10\%$. This agrees with the prediction of Matzner & Levin (2005), who assert incorrect disk fragmentation may produce brown dwarfs if irradiation is not included. Accretion luminosity, which is emitted at the protostellar surface, generates a significant portion of the luminosity during the early stages of protostar formation. Indeed, Bate (2009b) found increased heating and fewer brown dwarfs at higher resolution but reported little difference in the final stellar distribution for resolutions of 0.5 AU versus 5.0 AU. Since 0.5 AU is much larger than protostellar radii, significant accretion heating was neglected. As Bate (2009b) also neglected deuterium burning, the calculations represent a lower limit on the effects of radiative feedback.

In this paper, we model the formation of low-mass stars in a turbulent molecular cloud including GFLD using the ORION adaptive mesh refinement (AMR) code. We address the issue of radiative feedback, including all the important energy sources, and how it influences low-mass star formation. Our study differs from previous work in that we use source terms to account for accretion luminosity down to the stellar surface and include a stellar evolutionary model (Tan & McKee 2004). We contrast a GFLD simulation to one without radiative transfer. We also perform a less time evolved calculation with resolution eight times higher to characterize the dependence of the solutions with and without radiative transfer on resolution. We describe our method in §5.2. In §5.3, we compare and contrast the four simulations. We discuss caveats to our method in §5.4 and summarize our conclusions in §6.3. Comparisons to observations will appear in a subsequent paper.

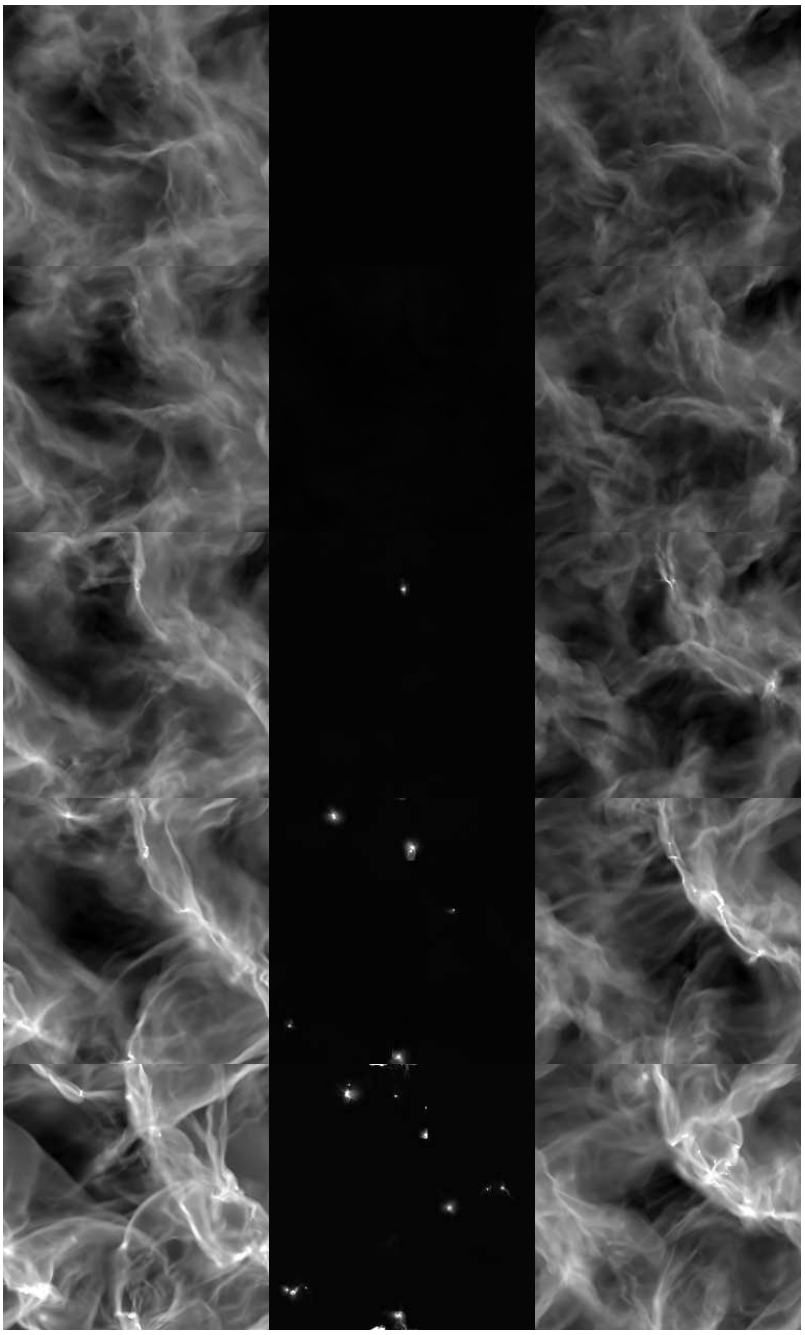

Figure 5.1 Log gas column density of the RT (left) and NRT (right) simulations at 0.0, 0.25, 0.5, 0.75, 1.0 $t_{\rm ff}$. The log density weighted gas temperature for the RT is shown in the center. The color scale for the column density ranges from $10^{-1.5} - 10^{0.5}$ g cm^{-2} and $10 - 50$ K for the gas temperature. Animations of the left and right panels, as well as color figures, are included in the online version.

5.2 Methodology and Initial Conditions

5.2.1 Numerical Methods

For the purpose of comparison, we perform two calculations with identical resolutions and characteristic parameters. The first, which we denote RT, includes radiative transfer and feedback from stellar sources. The second, henceforth NRT, uses an EOS to describe the thermal evolution of the gas. We perform both simulations using the parallel AMR code, ORION. ORION utilizes a conservative second order Godunov scheme to solve the equations of compressible gas dynamics (Truelove et al. 1998; Klein 1999):

$$\frac{\partial \rho}{\partial t} + \nabla \cdot (\rho \mathbf{v}) = 0, \tag{5.3}$$

$$\frac{\partial (\rho \mathbf{v})}{\partial t} + \nabla \cdot (\rho \mathbf{v}\mathbf{v}) = -\nabla P - \rho \nabla \phi, \tag{5.4}$$

$$\frac{\partial (\rho e)}{\partial t} + \nabla \cdot [(\rho e + P)\mathbf{v}] = \rho \mathbf{v} \nabla \phi - \kappa_R \rho (4\pi B - cE), \tag{5.5}$$

where ρ, P, and $\mathbf{v}$ are the fluid density, pressure, and velocity, respectively. The total fluid energy is given by $e = 1/2\rho\mathbf{v}^2 + P/(\gamma - 1)$, where $\gamma = 5/3$ for a monatomic ideal gas[2]. The total radiation energy density is denoted by E, and B is the Planck emission function. ORION solves the Poisson equation for the gravitational potential ϕ using multi-level elliptic solvers with multi-grid iteration:

$$\nabla^2 \phi = 4\pi G[\rho + \sum_n m_n \delta(\mathbf{x} - \mathbf{x}_n)], \tag{5.6}$$

where m_n and $\mathbf{x}_n$ are the mass and position of the nth star.

ORION solves the non-equilibrium flux-limited diffusion equation using a parabolic solver with multi-grid iteration to determine the radiation energy density (Krumholz et al. 2007c):

$$\frac{\partial E}{\partial t} - \nabla \cdot (\frac{c\lambda}{\kappa_{\rm R}\rho} \nabla E) = \kappa_{\rm P}\rho(4\pi B - cE) + \sum_n L_n W(\mathbf{x} - \mathbf{x}_n), \tag{5.7}$$

[2]Most of the volume of the domain is too cold to excite any of the H_2 rotational or vibrational degrees of freedom, and thus the gas acts as if it were monatomic.

where $\kappa_{\rm R}$ and $\kappa_{\rm P}$ are the Rosseland and Planck dust opacities, and L_n is the luminosity of the nth star. W is a weighting function that determines the addition of the stellar luminosity to the grid (see Appendix A for details of the star particle algorithm). The flux-limiter is given by $\lambda = \frac{1}{R}(\coth R - \frac{1}{R})$, where $R = |\nabla E/(\kappa_{\rm R}\rho E)|$ (Levermore & Pomraning 1981).

We assume that the dust grains and gas are thermally well-coupled, an approximation we discuss further in Section 4.2. We obtain the dust opacities from a linear fit of the Pollack et al. (1994) dust model, which includes grains composed of silicates, trolites, metallic iron, organics, and H_2O ices. For gas temperatures $10 \leq T_g \leq 350$ K, the linear fit is given by:

$$\kappa_R = 0.1 + 4.4(T_g/350) \text{ cm}^2 \text{ g}^{-1}, \quad (5.8)$$

$$\kappa_P = 0.3 + 7.0(T_g/375) \text{ cm}^2 \text{ g}^{-1}. \quad (5.9)$$

These fits give $\kappa_{\rm R} = 0.23$ cm^2 g^{-1} and $\kappa_{\rm P} = 0.49$ cm^2 g^{-1} at the minimum simulation temperature, 10 K. Work by Semenov et al. (2003) explores the effect of dust composition, porosity, and iron content on the Planck and Rosseland average opacities. For the different models, they find a spread of more than an order of magnitude in the opacity at 10 K. The simplest model, based upon the assumption that dust grains are homogenous spheres, produces the lowest value for the Rosseland opacity, $\kappa_R \simeq 0.02$ cm^2 g^{-1}, while the most porous and non-homogenous grain models produce 10 K opacities as large as $\kappa_R \simeq 0.7$ cm^2 g^{-1}. For temperatures above 100 K, the different dust models are more converged and the opacities are generally within a factor of 2. As a result, the temperature range from 10 K to 100 K is the most sensitive to dust assumptions. In this range, homogenous models increase roughly quadratically with temperature, while fluffier grain models increase linearly. Our opacity fits are then close to the mean value of $\kappa_R = 0.16$ for the Semenov et al. (2003) models, although this value is more representative of porous and aggregate grains. As a result, our dust model is reasonable for the higher density regions of $n \gtrsim 10^7$ cm^3 typical of protostellar cores, but we may overestimate the dust opacity in the lower density cold gas by as much as a factor of 10.

In studies of low-mass star formation, it is reasonable to neglect pressure exerted

by the radiation field on the dust and gas. This is because the advection of radiation enthalpy is small compared to the rate the radiation diffuses through the gas:

$$\frac{\nabla \cdot \left(\frac{3-R_2}{2}\mathbf{v}E\right)}{\nabla \cdot \left(\frac{c\lambda}{\kappa_R \rho}\nabla E\right)} \ll 1, \tag{5.10}$$

where $R_2 = \lambda + \lambda^2 R^2$ is the Eddington factor.

Without radiative transfer, the energy exchange term in (5) disappears, and we close the system of equations with a barotropic EOS for the gas pressure:

$$P = \rho c_{\rm s}^2 + \left(\frac{\rho}{\rho_{\rm c}}\right)^{\gamma} \rho_{\rm c} c_{\rm s}^2, \tag{5.11}$$

where $c_{\rm s} = (k_{\rm B}T/\mu)^{1/2}$ is the isothermal sound speed, $\gamma = 5/3$, the average molecular weight $\mu = 2.33 m_{\rm H}$, and the critical density, $\rho_{\rm c} = 2 \times 10^{-13}$ g cm^{-3}. The value of μ reflects an assumed gas composition of $n_{\rm He} = 0.1 n_{\rm H}$. The critical density determines the transition from isothermal to adiabatic regimes, and we adopt a value to agree with the full angle-dependent 1D radiation-hydrodynamic calculation by Masunaga et al. (1998) that agrees with the collapse solution prior to H_2 dissociation.

We use the Truelove criterion to determine the addition of new AMR grids so that the gas density in the calculations always satisfies:

$$\rho < \rho_{\rm J} = \frac{J^2 \pi c_{\rm s}^2}{G(\Delta x_l)^2}, \tag{5.12}$$

where Δx_l is the cell size on level l, and we adopt a Jeans number of $J = 0.25$ (Truelove et al. 1997). In the case with radiative transfer, it is important to adequately resolve spatial gradients in the radiation field. Radiation gradients are primarily associated with collapsing regions hosting a star but are not covered by the Jeans gravitational criterion. We find that we adequately resolve the radiation field and avoid effects such as grid imprinting by refining wherever $\nabla E/E > 0.25$. Although the simulation box and gas behavior is periodic, we adopt Marshak boundary conditions for the radiation field. This allows the radiation to escape from from the box as it would from a molecular cloud.

We insert sink, or star, particles in regions of the flow that have exceeded the Jeans density on the maximum level (Krumholz et al. 2004). These particles mark

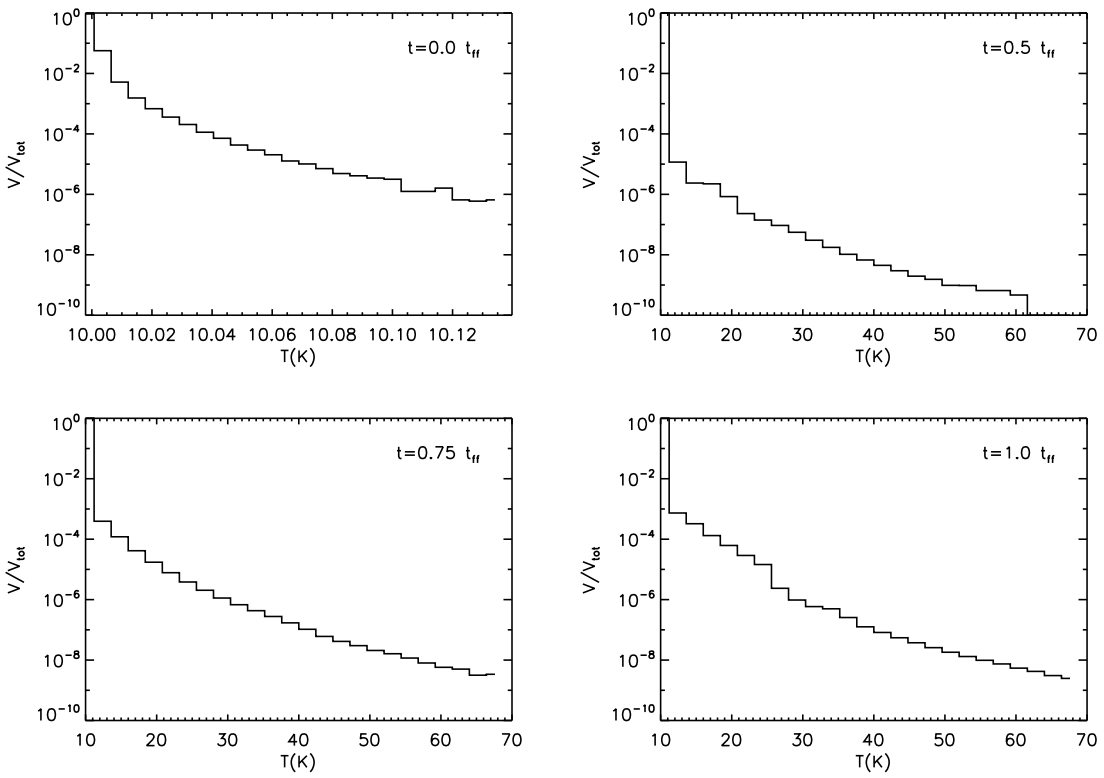

Figure 5.2 Histogram of the gas temperatures weighted by volume fraction for RT at 0.0, 0.5, 0.75, and 1.0 t_{ff}.

collapsing regions and also represent protostellar objects. In the simulation with radiative transfer, the particles act as radiative sources, and they are endowed with a sub-grid stellar model. We describe the details of this model and its implementation in Appendix B. By construction, stars that approach within eight cells are merged together. Small sink particles, such as those generated by disk fragmentation, tend to accrete little mass and frequently merge with their more substantial neighbors within a few orbital times.

5.2.2 Initial Conditions

We chose a characteristic 3D turbulent Mach number, $\mathcal{M}$=6.6, and assume that the cloud is approximately virialized:

$$\alpha_{\rm vir} = \frac{5\sigma^2}{GM/R} \simeq 1. \tag{5.13}$$

The initial box temperature is $T = 10$ K, length of the box $L = 0.65$ pc and the average density is $\rho = 4.46 \times 10^{-20}$ g cm^{-3}, so that the cloud satisfies the observed linewidth-size relation (Solomon et al. 1987; Heyer & Brunt 2004). The total box mass is 185 M$_\odot$.

To obtain the initial turbulent conditions, we begin without self-gravity and apply velocity perturbations to an initially constant density field using the method described in Mac Low (1999). These perturbations correspond to a Gaussian random field with flat power spectrum in the range $1 \leq k \leq 2$ where $k = k_{\rm phys}L/2\pi$ is the normalized wavenumber. At the end of three cloud crossing times, the turbulence follows a Burgers power spectrum, $P(k) \propto k^{-2}$, as expected for hydrodynamic systems of supersonic shocks. We denote this time $t = 0$. We then turn on gravity and follow the subsequent gravitational collapse for one global freefall time:

$$\bar{t}_{ff} = \sqrt{\frac{3\pi}{32G\bar{\rho}}} = 0.315 \text{ Myr}, \tag{5.14}$$

where $\bar{\rho}$ is the mean box density. We continue turbulent driving in the simulations, using a constant energy injection rate to ensure that the turbulence does not decay and the cloud maintains approximate energy equipartition.

The calculations have a 256^3 base grid with 4 levels of factors of 2 in grid refinement, giving an effective resolution of 4096^3, where $\Delta x_4 = 32$ AU. In section 3.2, we describe the results of a high-resolution core study using 7 levels of refinement for an effective resolution of $65,536^3$ and minimum cell size $\Delta x_7 = 4$ AU. Generally, the calculations run on 128-256 CPUs.

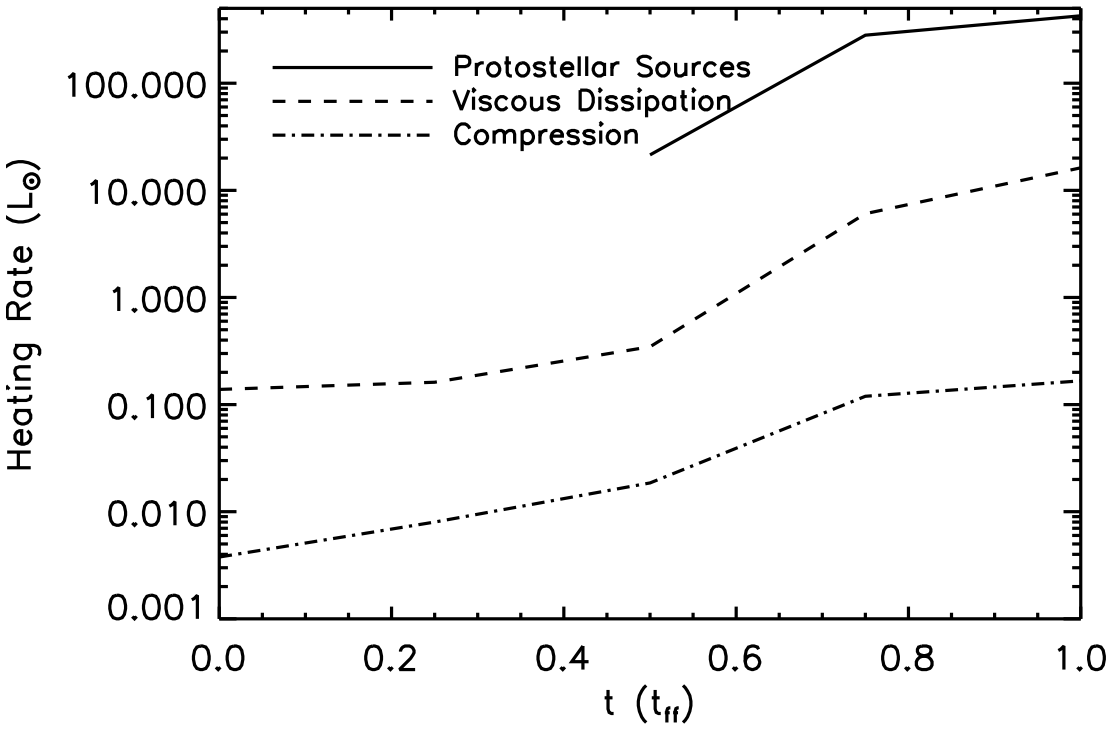

Figure 5.3 The magnitude of the heating rate due to all stellar sources, viscous dissipation, and gas compression at the times shown in Figure 5.1.

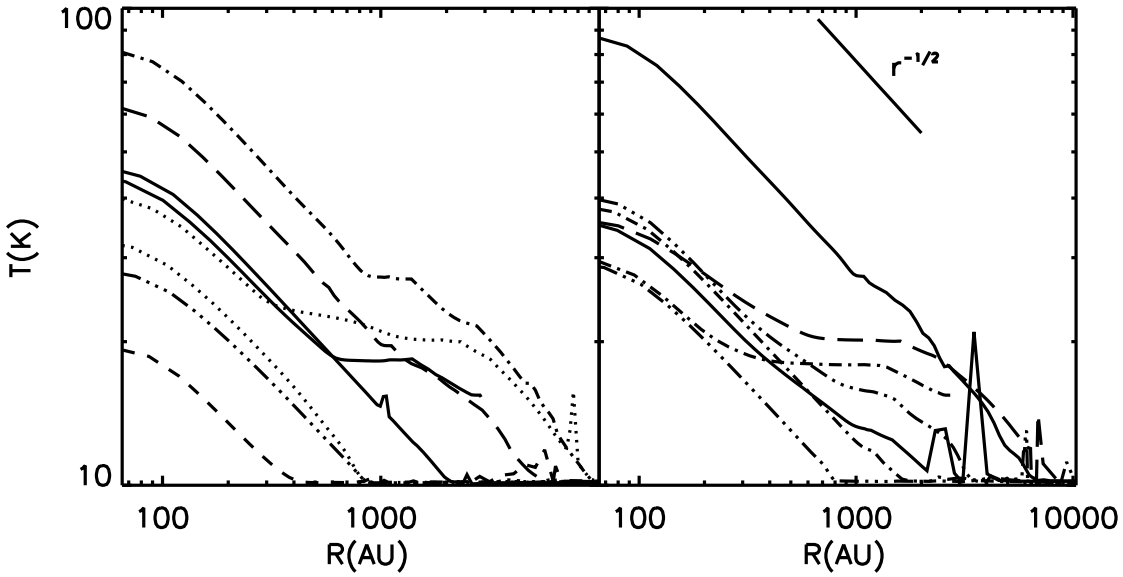

Figure 5.4 The gas temperature as a function of distance from the source for all sources in the RT simulation at 1.0 t_{ff}. The sources are separated into two plots for viewing, where the earlier forming sources are on the left. The line indicates $T \propto r^{-1/2}$.

5.3 Results

5.3.1 Radiative Transfer and Non-Radiative Transfer Comparison

In order to quantify the effects of radiative feedback on low-mass star formation, we compare a simulation including radiative transfer with a non-radiative one using an EOS. The latter simulation is essentially isothermal throughout since the highest density allowed by the Truelove criteria at the fiducial maximum AMR level corresponds to $\rho \simeq 5 \times 10^{-15}$ g cm^{-3}. With the adopted EOS, gas of this density is not heated above 11 K.

Images of the two simulations at different times are shown in Figure 5.1. Although the simulations use identical forcing patterns applied at the same Mach number, the details of the turbulence differ as the two calculations have slightly different time steps and turbulent decay rates. Both calculations begin at $t = 0$ with a centrally condensed region that forms the first stars, an imprint of the large wavenumber driving. Once gravity is turned on, we continue driving the simulations with the same energy injection rate, yielding 3D Mach numbers of 7.0 and 8.6 at 1 $t_{\rm ff}$ for the NRT and RT calculations, respectively. Because gravitational collapse causes non-turbulent velocity motions, we chose to fix the energy injection rate rather than the total kinetic energy. Thus, the root-mean-squared gas velocity no longer exactly indicates the total turbulent energy, and the Mach number increases above the initial value. In Tables 5.1 and 5.2, we list the properties of the stars formed in each calculation at $1t_{\rm ff}$.

Temperature Distribution

At $t = 0$, the RT simulation is nearly isothermal and gas temperatures, are distributed between 10-11 K (Figure 5.2). Evaluated at the mean box density, the gas is quite optically thin with an average optical depth though the box of $\tau_{\rm L} = L \times \kappa_{\rm R}\rho = 0.65$ pc $\times\, 4.46 \times 10^{-20}$ g cm^{-3} $\times\, 0.2$ cm^2 g^{-1} ~ 0.02. Since the box is so transparent, the gas cools very efficiently. Small temperature variations arise in the

Table 5.1. RT protostar properties at 1 $t_{\rm ff}$

m ($M_\odot$)	$\dot{m}_f$ ($\mathrm{M_\odot\ yr^{-1}}$)[a]	$\dot{m}_{f,2500}$ ($\mathrm{M_\odot\ yr^{-1}}$)[b]	$\bar{\dot{m}}$ ($\mathrm{M_\odot\ yr^{-1}}$)[c]	L ($L_\odot$)	Age (Myr)[d]
1.52	4.2×10^{-9}	1.1×10^{-7}	8.7×10^{-6}	7.2	0.18
0.45	2.0×10^{-8}	3.9×10^{-8}	4.0×10^{-6}	0.9	0.11
0.09	1.4×10^{-7}	1.3×10^{-7}	8.0×10^{-7}	0.3	0.11
2.91	8.1×10^{-7}	1.7×10^{-5}	2.9×10^{-5}	177.5	0.10
0.35	5.6×10^{-7}	2.0×10^{-7}	3.5×10^{-6}	1.3	0.10
2.21	6.0×10^{-7}	4.2×10^{-6}	2.4×10^{-5}	45.2	0.09
1.54	4.0×10^{-6}	7.5×10^{-6}	1.7×10^{-6}	74.6	0.09
1.17	9.8×10^{-6}	1.7×10^{-5}	1.4×10^{-5}	69.4	0.09
0.43	1.2×10^{-6}	2.8×10^{-6}	6.0×10^{-6}	8.6	0.09
0.48	3.2×10^{-6}	7.2×10^{-6}	6.9×10^{-6}	19.4	0.08
0.65	1.6×10^{-6}	9.9×10^{-6}	1.1×10^{-5}	12.9	0.08
0.80	5.7×10^{-6}	1.7×10^{-5}	1.5×10^{-5}	67.6	0.06
0.33	2.1×10^{-5}	2.2×10^{-5}	2.3×10^{-5}	79.1	0.02
0.06	4.7×10^{-6}	5.1×10^{-6}	7.4×10^{-6}	3.9	0.01
0.01	3.0×10^{-6}	1.1×10^{-5}	8.6×10^{-6}	0.8	0.003

[a]Instantaneous final accretion rate.

[b]Accretion rate averaged over the last $\sim$ 2500 yrs.

[c]Mean accretion rate averaged over the protostar lifetime.

[d]Age calculated from the time of particle formation.

Table 5.2. NRT protostar properties at 1 $t_{\rm ff}$

m ($M_\odot$)	$\dot{m}_f$ ($M_\odot$ yr^{-1})[a]	$\dot{m}_{f,2500}$ ($M_\odot$ yr^{-1})[b]	$\bar{\dot{m}}$ ($M_\odot$ yr^{-1})[c]	Age (Myr)[d]
3.92	7.2×10^{-6}	1.2×10^{-5}	2.2×10^{-5}	0.15
4.77	1.6×10^{-6}	2.7×10^{-5}	2.6×10^{-5}	0.15
2.91	1.0×10^{-5}	1.2×10^{-5}	2.6×10^{-5}	0.11
4.84	2.1×10^{-5}	2.3×10^{-5}	4.4×10^{-5}	0.11
0.66	2.5×10^{-7}	2.7×10^{-7}	7.6×10^{-6}	0.09
1.13	1.3×10^{-5}	1.3×10^{-5}	2.1×10^{-5}	0.05
0.66	8.9×10^{-7}	9.0×10^{-7}	1.2×10^{-5}	0.05
0.55	9.3×10^{-7}	1.0×10^{-6}	1.1×10^{-5}	0.05
0.71	5.9×10^{-6}	5.6×10^{-6}	1.4×10^{-5}	0.05
1.32	1.2×10^{-5}	1.4×10^{-5}	7.8×10^{-5}	0.02
0.08	2.7×10^{-5}	6.6×10^{-6}	5.9×10^{-6}	0.02
0.49	1.1×10^{-5}	1.1×10^{-5}	3.6×10^{-5}	0.02
0.26	5.0×10^{-6}	1.2×10^{-5}	2.0×10^{-5}	0.02
0.04	5.8×10^{-6}	1.1×10^{-5}	2.8×10^{-6}	0.02
0.02	2.6×10^{-9}	1.1×10^{-8}	1.2×10^{-6}	0.02
0.12	1.3×10^{-6}	1.5×10^{-6}	9.3×10^{-6}	0.02
0.04	2.7×10^{-6}	2.7×10^{-6}	4.2×10^{-6}	0.01
0.01	8.6×10^{-12}	5.5×10^{-12}	1.8×10^{-6}	0.01
0.09	6.4×10^{-6}	5.1×10^{-6}	1.3×10^{-5}	0.01
0.14	1.9×10^{-5}	1.9×10^{-5}	2.3×10^{-5}	0.01
0.02	2.7×10^{-6}	7.0×10^{-6}	5.5×10^{-6}	0.01
0.05	2.4×10^{-5}	1.5×10^{-5}	1.6×10^{-5}	0.01

[a]Instantaneous final accretion rate.

[b]Accretion rate averaged over the last $\sim$ 2500 yrs.

[c]Mean accretion rate averaged over the protostar lifetime.

[d]Age calculated from the time of particle formation.

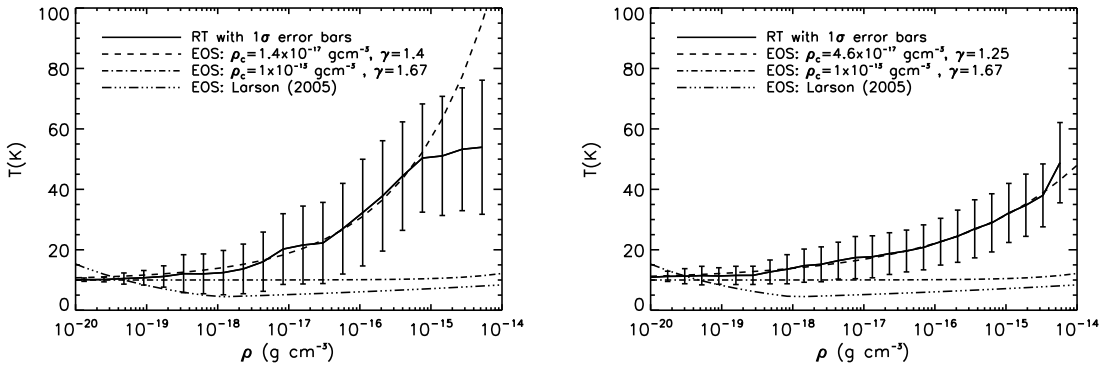

Figure 5.5 The average gas temperature at 0.8 t_{ff} and 1.0 t_{ff} as a function of density. The error bars give the temperature dispersion in each bin. The dashed line is a least-sqares fit of equation (5.11) which returns $\rho_{\rm c}$ and γ. The dot-dashed line plots equation (5.11) with the original parameters: $\rho_{\rm c} = 1 \times 10^{-13}$ g cm^{-3} and $\gamma = 1.67$. The power law density-temperature relation from Larson (2005) is also plotted.

initial state due to the distribution of strong shocks. For reference, gas compressed by a Mach 10 shock at 10 K will undergo net heating of < 0.1 K during a time step. Qualitatively, the change is so small because the radiative cooling time is a factor of $\sim 10^3$ smaller than the time step.

Under the influence of gravity, collapsing regions begin to become optically thick, where individual cells at the maximum simulation densities reach optical depths of $\tau \simeq 3$ when $T = 100$ K. Figure 5.2 shows the evolution of the gas temperature distribution over a freefall time. There are three processes that result in heating. First, there is the direct contribution from the protostars, which we add as a source term in the radiation energy equation. Second there is heating due to viscous dissipation, which is given by:

$$\dot{e}_{\rm vis} = -(\sigma' \cdot \nabla) \cdot \mathbf{v}, \tag{5.15}$$

where σ' is the viscous stress tensor, $\sigma' = \eta(S - \frac{2}{3} I \nabla \cdot v)$ and $S = \nabla v + (\nabla v)^T$ (Landau & Lifshitz 1987). We assume that the dynamic viscosity $\eta = \rho |\mathbf{v}| \Delta x / \mathcal{R}e_g$, where the Reynolds number, $\mathcal{R}e_g \simeq 1$, at the dissipation scale. However, turbulent dissipation occurs over a range of the smallest scales on the domain, where the largest amount

of dissipation occurs on the size scale of a cell. Thus, we expect this formula to be uncertain to within a factor of two. Third, the net heating due to gas compression is given by:

$$\dot{e}_{\rm comp} = -P(\nabla \cdot \mathbf{v}); \tag{5.16}$$

the heating is negative (i.e., cooling occurs) in rarefactions. Figure 5.3 shows the heating contributions summed over the entire domain. At $t = 0$, the only source of heating is turbulent motions. The figure demonstrates that after star formation commences protostellar output rather than compression is responsible for the majority of the heated gas, and at $1t_{\rm ff}$ protostellar heating dominates by an order of magnitude relative to viscous dissipation and four orders of magnitude relative to gas compression. Viscous dissipation dominates the heating prior to star formation. After star formation is underway, viscous dissipation occurs in the protostellar disks. In contrast, turbulent shocks then contribute very little to the total.

Figure 5.2 shows the evolution of the gas temperature distribution over a freefall time. The amount of heated gas ($T > 12$ K) increases with the number of stellar sources from 0.06% of the volume for one protostar at 0.5 $t_{\rm ff}$ to $\sim 4\%$ at 1 $t_{\rm ff}$. The corresponding mass fractions of the heated gas are slightly higher at 0.3 % and 5%, respectively. As we have seen in the previous figure, most of this heating is directly related to the protostars, and it comprises a relatively small volume filling fraction.

The temperature distribution as a function of distance from the sources is shown in Figure 5.4. As illustrated, heating is local and occurs within ~ 0.05 pc of the protostar. Since the remainder of the cloud remains near 10 K, additional turbulent fragmentation is not affected by pre-existing protostars. However, radiative feedback profoundly influences the evolution of the protostars, accretion disks, and stellar multiplicity as we will show (see sections 5.3.1.2-3.1.3). Our temperature profiles are qualitatively similar to those of Masunaga & Inutsuka (2000), who model 1D protostellar collapse with radiative transfer. During the formation of the low-mass protostar, Masunaga & Inutsuka (2000) also find that heating above 10 K is confined within 0.05 pc of the central source and that significant variation in temperature occurs as a function of density and time. Additional studies using GFLD (Whitehouse & Bate 2006) or approximate radiative transfer methods (Stamatellos

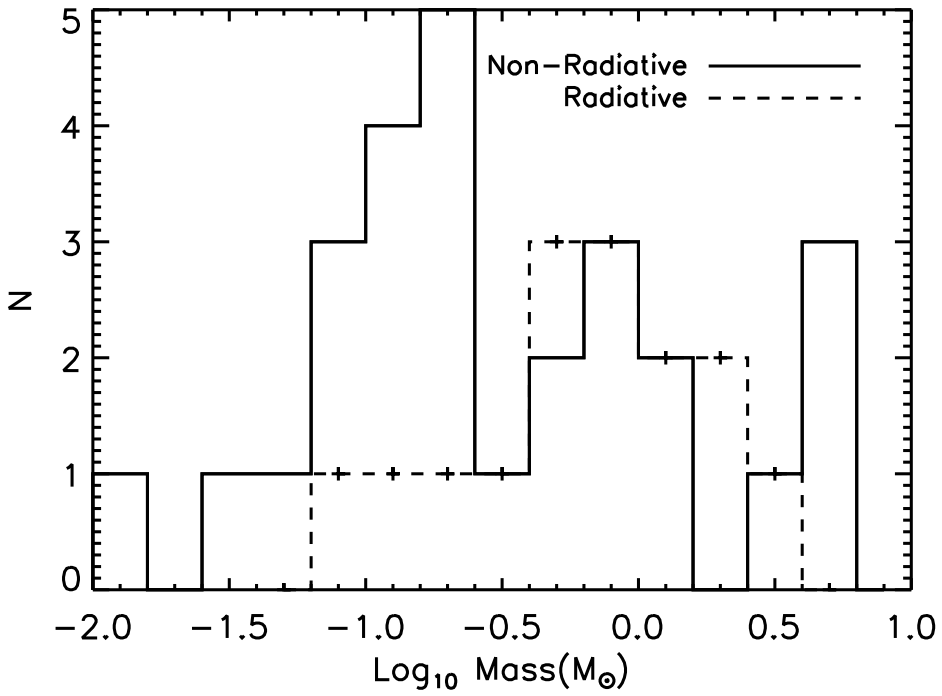

Figure 5.6 The distribution of masses (star + disk) for the two simulations at 1.0 t_{ff}. The solid and dashed-cross lines indicate the NRT and RT simualtions, respectively.

et al. 2007; Forgan et al. 2009) find similar heating beyond that expected from a barotropic EOS.

Due to temperature variation with both density and time, we find that the gas temperature is poorly represented by a single EOS with characteristic critical density and γ. Figure 5.5 shows the distribution of cell temperatures as a function of cell density. For reference, we also plot our fiducial EOS for the NRT simulation as well as the EOS presented by Larson (2005). We find that many cells at lower densities are heated due to close proximity with a source. In fact, for both the EOS described in section 5.2, which only includes the heating due to gas compression, and the Larson (2005) EOS, none of the cells are predicted to heat much above the initial 10 K temperature.

Nonetheless, at any given time a representative EOS can be formulated by fitting the mean grid cell temperature binned as a function of density. Figure 5.5 shows a least-squares fit of the temperature data for two different times. The magnitude of the error bars is given by the standard deviation of the temperatures in each density bin. Because such an equation fits the average temperature, there is necessarily a large scatter as illustrated by the error bars. The two fits return different effective critical densities and gamma values. Thus, a single EOS results in a large fraction of cells unavoidably at the wrong temperature.

Since accretion luminosity is predominantly emitted at the stellar surface, a low simulation resolution, when not augmented for the missing source contribution, can significantly neglect a large part of the heating (e.g., Bate 2009b). Typical pre-main sequence protostellar radii are expected to range from 3-5 $R_{\odot}$ for low-mass stars (Palla & Stahler 1993; Robitaille et al. 2006). Thus, the temperature at a distance, r, from an emitting source, L_*, is given by:

$$T = \left(\frac{L_*}{4\pi\sigma_B r^2} \right)^{1/4}, \tag{5.17}$$

where $\sigma_{\rm B}$ is the Stefan-Boltzman constant, and the gas distribution is assumed to be spherically symmetric. Then the difference in accretion luminosity for a simulation with minimum resolution of $R_{\rm res} = 0.5$ AU versus a simulation resolving down to the stellar surface at $R_* = 5\ R_{\odot}$ is given by:

$$\Delta L = \frac{Gm\dot{m}}{R_{res}} \times \left(\frac{R_{\rm res}}{R_*} - 1 \right) \simeq \frac{Gm\dot{m}}{R_{\rm res}} \times (20). \tag{5.18}$$

Thus, the actual accretion luminosity at the higher resolution is a factor of 20 larger! Since we adopt a stellar model to calculate the protostellar radii self-consistently, we include the entire accretion luminosity contribution down to the stellar surface in our simulations. From (5.18), the difference in luminosity corresponds to a factor of $(20)^{1/4}$ or ~ 2 underestimation of the gas temperature. Nonetheless, this estimate is conservative since it does not include the additional luminosity emitted by the protostar, which may become significant during the Class II and late Class I phase. Thus, we expect the simulation of Bate (2009b) may overestimate the extent of small scale fragmentation and BDs formed in disks.

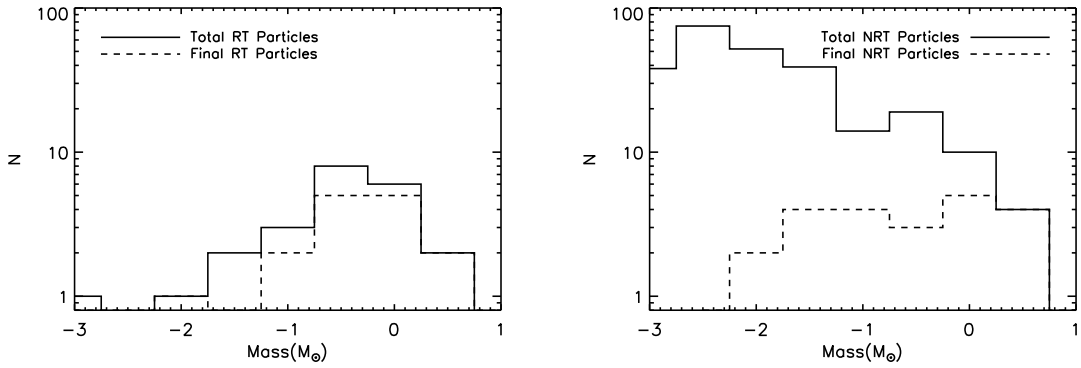

Figure 5.7 The figures show the distribution of particles formed as a function of mass for the RT(left) and NRT(right) simulations (solid line). These include the particles that are merged, where the total particle number with final masses greater than 10^{-3} $M_{\odot}$is 23 and 251, respectively. The dashed lines show the distributions of stellar masses at the final time output.

Stellar Mass Distribution

The large temperature range in the RT simulation has a profound effect on the stellar mass distribution. Figure 5.6 depicts the total mass of the star-disk systems in each simulation, were we define the surrounding disk as cells with $\rho > 5 \times 10^{-17}$ g cm^{-3}. We find that this cutoff selects gas within a few hundred AU of the protostars, visually identified with the disk, while excluding the envelope gas. Increased thermal support in the protostellar disk acts to suppress disk instability and secondary fragmentation in the core. In contrast, protostellar disks in the NRT calculation suffer high rates of fragmentation. Most of these small fragments are almost immediately accreted by the central protostar, driving temporarily large accretion rates onto the central source. If we define the star formation rate per freefall time as

$$\mathrm{SFR}_{ff} = \frac{\dot{M}_*}{M/\bar{t}_{ff}}, \tag{5.19}$$

(Krumholz & McKee 2005) then the total star formation rate in the NRT simulation is 13% versus 7% in the RT simulation. Thus, the RT $\mathrm{SFR}_{\mathrm{ff}}$ is almost half the NRT value and agrees better with observations (Krumholz & Tan 2007). Since the

simulations have the same numerical resolution, thermal physics must be directly responsible. In the RT simulation, cores containing protostars experience radiative feedback that slows collapse and accretion.

Due to the small number statistics, we do not directly compare with the shape of the observed initial mass function. Accurate comparison is also problematic because many of the late forming protostars are still actively accreting. As shown in Table 5.1, by $1t_{\rm ff}$ in the RT case, about a third, or 5 of the protostars, have accretion rates that are at least 5 times smaller than their individual mean accretion rate, indicating that the main accretion phase has ended. Adopting an efficiency factor of $\epsilon_{\rm core} = \frac{1}{3}$ to account for mass loss due to outflows (Matzner & McKee 2000; Alves et al. 2007; Enoch et al. 2008), we find that the mean protostellar mass of these protostars is $\bar{m} = 0.4\ M_{\odot}$, which is comparable to the expected mean mass of the system initial mass function of $\sim 0.5\ M_{\odot}$(Scalo 1986; Chabrier 2005).

The dynamics of close bodies and embedding gas are difficult to accurately resolve inside a small number of grid cells, so we merge particles that pass within 8 cells. Without this limit, some of the small fragments would dynamically interact with the central body and be ejected from the stellar system. These brown dwarf size objects are commonly produced in simulations that do not include a merger criterion, typically in larger numbers than are observed in the stellar IMF (e.g., Bate et al. 2003; Bate & Bonnell 2005; Bate 2009a). As a result, the simulation IMF only resolves wide binaries with separations > 300 AU.

Figure 5.7 shows a histogram of all created fragments in both simulations, including the final mass of the objects that are merged. Due to the low-resolution of the disks in the simulations, ~ 10 cells, the many small bodies shown in the NRT distribution indicate numerical disk instability rather than small bodies forming from gravitational collapse. The large number of particles that are created in the NRT case is directly related to the nearly isothermal EOS. Gravitational instability in disks results in filamentary spiral arms. If the gas is isothermal, the filaments undergo indefinite collapse irrespective of the numerical resolution (Truelove et al. 1997, 1998; Larson 2005; Inutsuka & Miyama 1992). In a numerical calculation, this means that all the cells along a filament exceed the Jeans criterion nearly simul-

taneously and trigger refinement. Once the maximum refinement level is reached, sink particles are introduced in cells with densities violating the Truelove criterion (Truelove et al. 1997). Since our sink particle algorithm is formulated to represent a collapsing sphere, it is not well suited to filament collapse. Kratter et al. (2009, in preparation) have addressed this issue in their predominantly isothermal simulations by transitioning from an isothermal to an adiabatic EOS once the density reaches a factor of four below the density at which sink particles are created. This has the effect of forcing filaments to fragment into quasi-spherical blobs prior to sink particle creation, thereby allowing the collapsing objects to be faithfully represented by point-like sink particles. At higher resolution, the barotropic nature of our EOS is invoked and so much of this fragmentation disappears (see Section 5.3.2). Similarly, in radiative calculations filamentary collapse is halted by heating due to radiative feedback, so that fragmentation is described by spherical rather than filamentary collapse. For either representation of heating, although numerical fragmentation in filaments is restricted, physical fragmentation may yet occur.

The creation and fragmentation of filaments in the simulations is a result of gravitational instability driven by rapid accretion. The criterion for the onset of instability is similar to the classic Toomre $Q < 1$ condition, slightly modified by the non-axisymmetry of the instabilities and the finite scale height of the disks, which is a result of turbulence driven by the accretion. This sort of gravitational instability has been investigated by Kratter et al. (2008, 2009 in preparation), who point out that the presence or absence of instability depends largely on the accretion rate onto the disk. The rate of mass transport through an α disk is

$$\dot{m} = 3\left(\frac{\alpha}{Q}\right)\frac{c_{\rm s,disk}^3}{G}, \tag{5.20}$$

where Q is the Toomre parameter for the disk and $c_{\rm s,disk}$ is the sound speed within it. Gravitational instabilities produce a maximum effective viscosity $\alpha \sim 1$. At early times, we find that the accretion rate from a core onto the disk forming within it can be $\gg c_{\rm s,core}^3/G$, where $c_{\rm s,core}$ is the sound speed in the core. If the sound speeds in the disk and core are comparable, $c_{\rm s,disk} \sim c_{\rm s,core}$, as is the case in the low-resolution NRT simulation, then the disk can only deliver matter to the star at a rate $\sim c_{\rm s,core}^3/G$ while

still maintaining $Q > 1$. As a result matter falls onto the disk faster than the disk can deliver it to the star, and the disk mass grows, driving Q toward 1 and producing instability and fragmentation, as illustrated by the NRT simulation. Conversely, if the disk is warmed, either by radiation or by a switch from an isothermal to an adiabatic equation of state, then $c_{\rm s,disk} > c_{\rm s,core}$ and the rate at which the disk can deliver gas to the star increases. If the disk is sufficiently warm then it can process all the incoming material while still maintaining $Q > 1$. As a result the disk does not fragment, as is seen in both the low- and high-resolution RT simulations and in high-resolution NRT simulation. This shows that the fragmentation in the low-resolution NRT simulation is indeed numerical rather than physical in origin, and that it is a result of the density-dependence of the equation of state rather than of the resolution directly.

This analysis also sheds light on the importance of numerical viscosity. Krumholz et al. (2004) show that in the inner few cells of disks, numerical viscosity can cause angular momentum transport at rates that correspond to $\alpha \gtrsim 1$. However, as the analysis above shows, increasing α tends to suppress fragmentation rather than enhance it. We find that fragmentation is more prevalent in the low-resolution NRT simulation than the high-resolution one, which is exactly the opposite of what we would expect if numerical angular momentum transport were significantly influencing fragmentation. Therefore we conclude that numerical angular momentum transport is not dominant in determining when fragmentation occurs in our simulations.

In isothermal calculations, the issue of filamentary collapse is a problem for all sink particle methods and it is not unique to grid-based codes. Due to the filamentary fragmentation in the NRT case, we prefer to merge close particle pairs in the simulations rather than follow their trajectories. Note that particles are inserted with the mass exceeding the Truelove criterion rather than the net unstable mass in the violating cells. Particles created within a discrete bound mass typically gain size quickly. Most particles formed in the unstable disk regions form in a spiral filament and do not have significant bound mass, so the particle mass is tiny when they are accreted by the central object. However, if several small particles are created within the merging radius each time step around a particular protostar, their merging can

significantly increase the instantaneous accretion rate. As illustrated by the figure, there are only a handful of objects that form and approach within a merging radius in the RT simulation, whereas the NRT simulation produces a plethora of such bodies.

Bate (2009b) finds a similar reduction in protostar number with the addition of radiative transfer. As in our calculation, the final number of stars including radiative transfer is sufficiently small that a statistical comparison with the IMF is problematic. Instead, we base our comparison on the mean stellar mass. Using a resolution of 0.5 AU, Bate (2009b) finds $\bar{m} \sim 0.5$ $M_\odot$, which does not include outflows or any scaling factor accounting for their presence. Adopting a scaling factor of $\epsilon_{\rm core} = 1/3$ would produce a mean of $\bar{m} \sim 0.2$ $M_\odot$, lower than our RT mean mass and the mean mass of either the system or individual stellar initial mass function reported by Chabrier (2005). However, in Bate (2009b) a number of the protostars are continuing to accrete and have not reached their final mass. In addition, Bate (2009b) demonstrates that the mean stellar mass increases as calculations approach higher resolution and include a larger portion of the accretion luminosity. This result is most likely because disk fragmentation decreases as the gas becomes hotter, thus increasing accretion onto primary objects. It is possible that if Bate (2009b) had included all the accretion and stellar luminosity, the mean mass obtained would be closer to the value we find.

Observations suggest that BDs compose $\sim 30\%$ of the total population of clusters (Andersen et al. 2006). Despite the merger criterion we adopt, the NRT calculation produces a significant number of BDs, $> 30\%$ sans scaling with $\epsilon_{\rm core}$, resulting in a slightly lower mean mass than the RT run. In comparison, Bate et al. (2003) find that approximately half of the objects formed are BDs, resulting in a mean mass of ~ 0.1 $M_\odot$. This result persists for barotropic calculations modeling more massive clusters with superior resolution (Bate 2009a). Calculations using a modified EOS that includes effects due to the internal energy and dissociation of H_2, ionization state of H, and approximate dust cooling find increased disk fragmentation, leading to numerous BDs (Attwood et al. 2009). Thus, the overproduction of BDs in non-radiative simulations substantiates the importance of radiative transfer and feedback from protostars in accurately investigating fragmentation and the initial

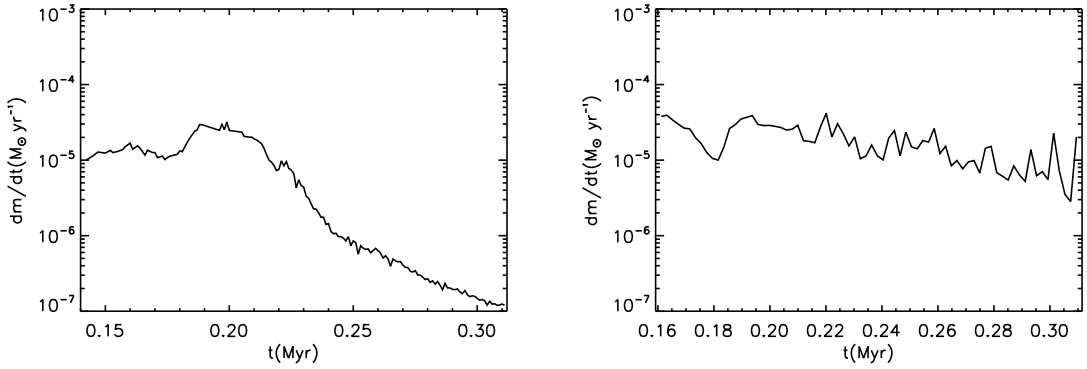

Figure 5.8 The accretion rate, $\dot{M}$, as a function of time for the first forming object in the RT (left) and NRT (right) simulations. We average both simulations over 1 kyr for consistency.

mass function.

Accretion Rates

As indicated by the Toomre criterion given by equation (5.2), the local gas temperature is key to the stability of disks. Clumpiness in the disks is directly reflected in the variability of the protostellar accretion rate. Figure 5.8 shows the accretion rates for the two first-forming protostars in each calculation as a function of time. The RT protostellar accretion in the left panel illustrates that once a protostar has accreted most of the mass in the core envelope, its accretion rate diminishes significantly. Protostars in both simulations show evidence of variable accretion on short timescales. However, the accretion bursts in the NRT simulation may vary by an order of magnitude, while in the RT case variability is generally only a few. Disk clumpiness may be magnified due to dynamical perturbations by nearby companions. For the cases shown, the RT protostar is single, while the NRT protostar has several companions. Similar variability to the NRT protostellar accretion rate is also observed by Schmeja & Klessen (2004). In their turbulent isothermal runs, Schmeja & Klessen (2004) show that the magnitude of the initial particle accretion rate is comparable to our calculations at $\dot{m} \sim$ few $\times 10^{-5}$ M$_{\odot}$ yr^{-1}

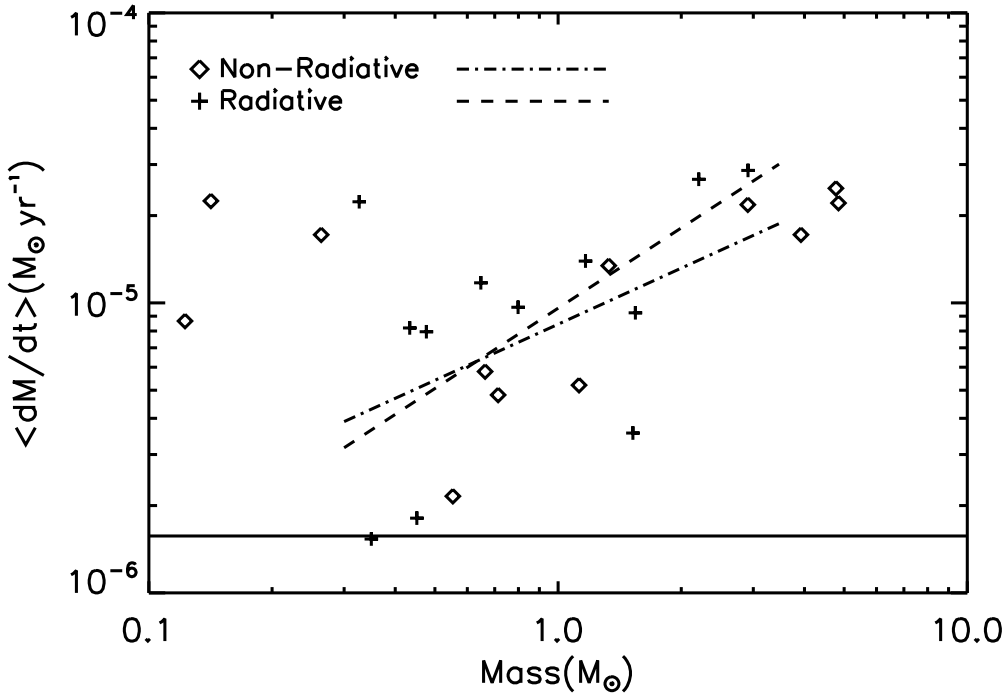

Figure 5.9 The plot shows the distribution of average accretion rates (crosses) as a function of final star mass at 1 $t_{\rm ff}$. The horizontal line indicates the Shu (1977) accretion rate $c_{\rm s}^3/G$ at 10K. The dashed and dot-dashed lines indicate the age weighted fit of the average accretion rates for the RT and NRT runs, respectively.

with variability by factors of 5-10. However, the reported accretion rates appear to significantly decrease within 0.1 Myr.

In principle, a sizable amount of the protostellar mass may be accreted during the periods of high accretion. We define a burst as an increase of 50% in the accretion rate over 1000 years, where mergers of another protostar of mass $m > 0.1$ $M_\odot$ are excluded. Using this metric, the NRT protostars accrete from 0-13 % of their mass during the bursts with a median of 5%. The RT protostars accrete 0.0-9 % of their mass during bursty accretion with a median amount of 1%. Thus, variable accretion is not significant. Our data analysis is limited by the coarse level time step of ~ 100 yrs, so that accretion rate variability on shorter timescales will not be resolved in the analysis. For comparison, Vorobyov & Basu (2006), modeling the formation and accretion history of a protostar in two-dimensions, find that > 50 % of the protostellar mass is gained in short intense accretion bursts. In their simulations, accretion occurs smoothly until $t \simeq 0.15$ Myr, where variability on timescales < 100 yrs begins, corresponding to accretion of ~ 0.05 $M_\odot$ clumps. Although their time resolution is finer, sampling at longer time increments, as in our calculation, is unlikely to miss persistent cyclical variability of four to five orders of magnitude in accretion rate. We find that when the stellar mass is about half the final mass, large variability in the RT accretion rates is rare, while it is more common in the NRT case. RT protostars with ages comparable to $t \simeq 0.15$ Myr experience the most variable accretion occurring over 1-2 orders of magnitude. However, by this time, the majority of the envelope mass has been accreted and accretion rates are $\bar{\dot{m}} \sim 10^{-7}$ $M_\odot$ yr^{-1}, so that accreting significant mass is unlikely.

In Vorobyov & Basu (2009), the authors demonstrate that simulations with a stiffer equation of state and warmer disk exhibit variability over at most two orders of magnitude. This finding is more consistent with our results, and it supports the differences in accretion we find between the NRT and RT calculations. However, bursty accretion due to disk instability also depends upon the core rotation and the rate at which mass is fed into the disk from the envelope(Vorobyov & Basu 2006; Boley 2009). Thus, we expect that radiative effects alone cannot completely determine accretion behavior. Since the disks in our low-resolution calculations

are not well resolved, it is possible that we may not be able to resolve the disk clumpiness observed by Vorobyov & Basu (2006). Their innermost cell is placed at 5 AU, which is comparable to the cell size in our high-resolution runs, however, they adopt logarithm spacing to concentrate cells in the inner region of the disks. We note that their method also includes an approximate treatment of magnetic fields that could influence their results and which we neglect in our calculations.

Figure 5.9 shows that the NRT simulation exhibits slightly higher average accretion. Note that we subtract the accretion spikes caused by significant mergers. The mean accretion rate over the protostars lifetime for the final protostars is $\sim 1 \times 10^{-5}$ $M_\odot$ yr^{-1} versus $\sim 6 \times 10^{-6}$ $M_\odot$ yr^{-1} for the RT run. Without the added thermal support from radiation feedback and with increased fragmentation, the NRT protostars accrete their envelope mass more quickly. However, the protostars in both calculations satisfy the same accretion-mass relationship, with accretion increasing approximately linearly with star mass. Using a least-squares fitting technique, we obtain power-law relationships $\bar{\dot{m}} \propto m^{0.92}$ and $\bar{\dot{m}} \propto m^{0.64}$ for the RT and NRT data, respectively, which have χ^2 values of 67.6 and 18.0.[3]We include masses $m \geq 0.1$ $M_\odot$in the fit and weight the data by the ages of the protostars. Thus, young protostars with only a short accretion history are weakly weighted. As Figure 5.9 shows, there is a significant amount of scatter about the fits. Schmeja & Klessen (2004) find a similar trend between the mean accretion rate and final masses for protostars forming in their isothermal driven turbulence simulations.

The apparent correlation between stellar mass and average accretion rate occurs because protostars forming in more massive cores tend to be more massive and also have higher accretion rates. McKee & Tan (2003) derive a self-similar solution for the accretion rate where the pressure and density each have a power-law dependence on r, such that $\rho \propto r^{-k_\rho}$ and $P \propto \rho^{\gamma_P} \propto r^{-k_P}$, where $\gamma_P = 2k_P/(2 + k_P)$ and $k_\rho = 2/(2 - \gamma_P)$. Although the simulated cores are not self-similar, it is possible to fit a power-law to the pressure of the core envelope in most cases. Both RT and NRT cores have exponents in the range $k_P \simeq 0 - 5$ at a few thousand AU from the

[3]The χ^2 value for the fit is given by: $\chi^2 = \sum_{i=1}^{N} \frac{y_i - A - Bx_i}{\sigma_y^2}$, where y_i are the age-weighted accretion rates, x_i are the masses, A and B are the fit coefficients, and σ_y is the standard deviation of the y_i values.

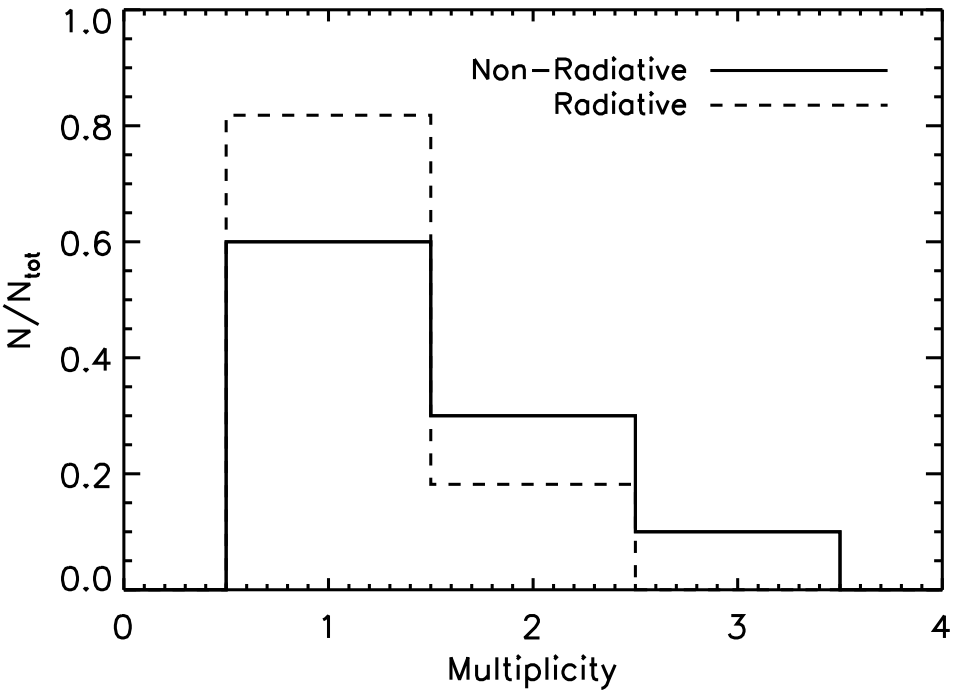

Figure 5.10 The plot shows the system multiplicity for the two calculations, where N is the number of stellar systems, and the plot is normalized to the total number of systems. The multiplicity on the x-axis is the number of stars in each system.

protostar, with an average value of $k_P \sim 1$ or $k_\rho = 1.5$. McKee & Tan (2003) show that the accretion rate is then:

$$\dot{m}_* = 5.5 \times 10^{-6} \phi_* A^{1/8}, k_P^{1/4} \epsilon_{\rm core}^{1/4} \left(\frac{m_{*f}}{1\ {\rm M}_\odot} \right)^{3/4} \times \left(\frac{P_{s,{\rm core}}/k_B}{10^6\ {\rm K\ cm^{-3}}} \right) \left(\frac{m_*}{m_{*f}} \right)^{3(2-k_\rho)/[2(3-k_\rho)]} {\rm M}_\odot\ {\rm yr}^{-1}, \quad (5.21)$$

where m_{*f} is the final stellar mass , $P_{s,{\rm core}}$ is the core surface pressure, ϕ_* and A are order unity constants describing the effect of magnetic fields on accretion and the isothermal density profile, respectively. Since we weight the fit by the protostellar age, this selects for the case where $m_* \simeq m_{*f}$. Assuming that $\Sigma_{\rm cl}$ is roughly constant, $\dot{m}_* \propto m_{*f}^{3/4}$, that is similar to the slopes produced by the least-squares fit.

Multiplicity

The number of stars with stellar companions is an important observable that may directly relate to the initial conditions of star-forming regions. Among the population of field stars, most systems are single with the number of systems containing multiple stars increasing as a function of stellar mass (Lada 2006). Young pre-main sequence stellar populations are observed to contain more multiple systems than field stars suggesting that the multiplicity fraction evolves over time (Duchêne et al. 2007). Unfortunately, the initial stellar multiplicity is challenging to directly measure due to the difficulty of resolving close pairs and limited sample sizes (Duchêne et al. 2007). The two dominant effects influencing multiplicity are fragmentation and N-body dynamics. While fragmentation in a collapsing core may result in multiple stars, systems with three or more bodies are dynamically unstable, causing higher-order stellar systems to rapidly lose members. Multiple stellar systems can also occur via stellar capture, a mechanism most applicable to high-mass stars forming in very clustered environments (Moeckel & Bally 2007). Goodwin & Kroupa (2005) suggest that that observed higher-order multiple systems are initially members of open stellar clusters rather than arising from the fragmentation of a single core. In general, the number of such systems is observed to be small, with only 1 in every 50 systems in the field having at least four members (Duquennoy & Mayor 1991).

The RT and NRT calculations present very different pictures of the initial stellar multiplicity. The large differences in temperature and fragmentation have a significant effect on the fractions of stars in single and multiple systems. As shown in Figure 5.10, the majority of stars formed in the RT calculation are single, while in the NRT calculation the majority of stars live in systems with 2 or more stars. This is mainly due to continued disk fragmentation rather than long-lived stable orbital systems. The field single star fraction (SSF), defined as the ratio of the number of primary stars without a *stellar* companion to the total number of stellar systems, is observed to be $\sim 70\%$ (Lada 2006)[4]. The RT calculation produces an SSF of 0.8 $+0.2/-0.4$, while the NRT calculation has an SSF of 0.6 ± 0.4, where the uncertainty is given by the poisson error. Due to the resolution of our calculation, we can only

[4]The SSF does not include brown dwarfs in estimating multiplicity.

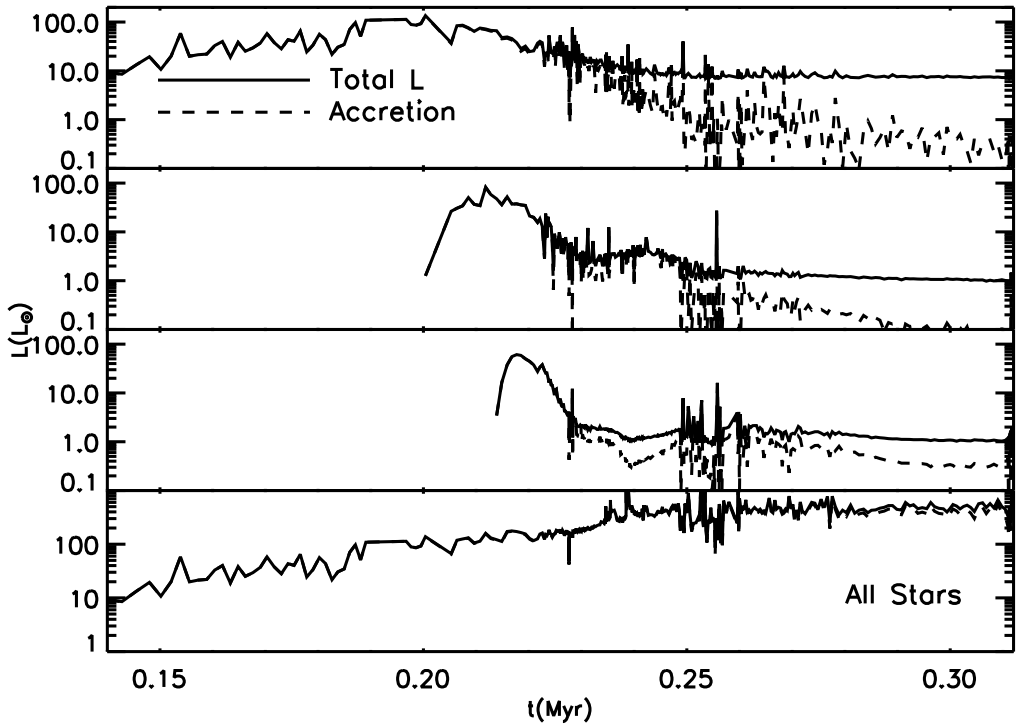

Figure 5.11 The plot shows the total luminosity as a function of time for three stars in the RT simulation. The accretion luminosity contribution is shown by the dashed line, and the masses are 1.5, 0.45, and 0.35 $M_{\odot}$, respectively. The bottom plot shows the total luminosity including all the protostars.

capture wide binary systems of $r > 300$ AU. However, a number of protostars have undergone significant mergers, which we define as those in which the smaller mass exceeds 0.1 $M_{\odot}$. We find that about a third of the stars in the RT simulation and a tenth of stars in the NRT simulation have experienced significant past mergers. Assuming that these would have resulted in multiple stellar system revises the SSF values to 0.5±0.3 and 0.6±0.4, respectively. Unfortunately, this is a very uncertain estimate as we have small statistics, and we cannot know whether the systems with significant mergers would have resulted in bound or unbound systems in the absence of the mergers.

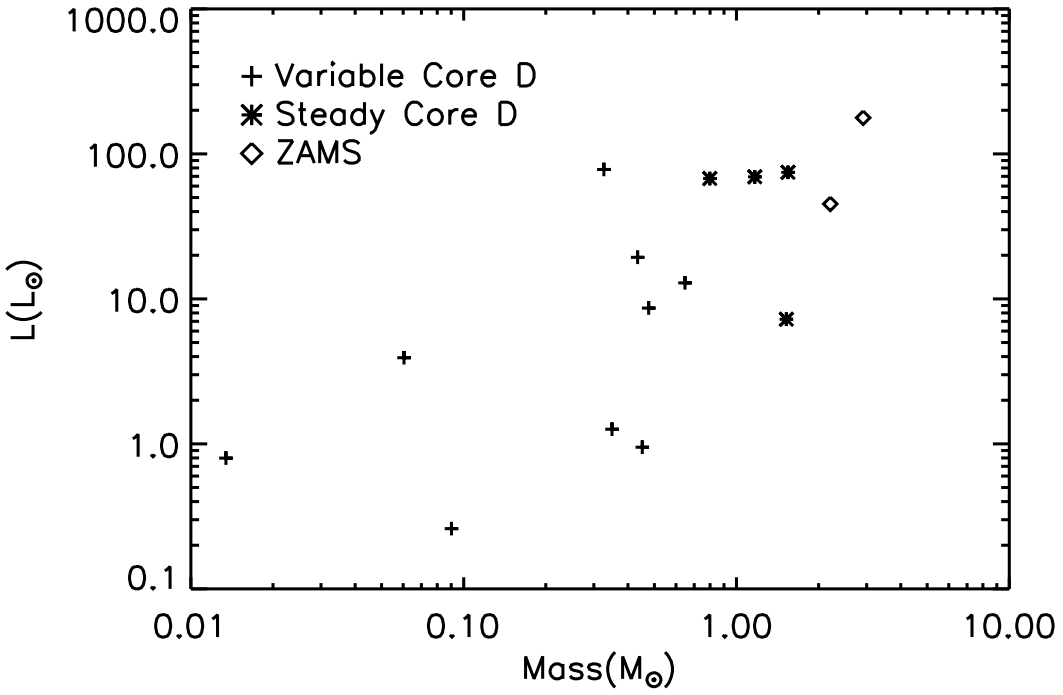

Figure 5.12 The plot shows the distribution of luminosities (crosses) in the RT simulation as a function of final star mass at 1.0 $t_{\rm ff}$. The crosses, stars, and diamonds refer to stars undergoing variable core deuterium burning, undergoing steady core deuterium burning, or reaching the zero-age main sequence.

Stellar Feedback

Our model includes accretion luminosity and a sub-grid stellar model estimating the contribution from Kelvin-Helmholz contraction and nuclear burning (see Appendix 5.7) The stellar model includes four evolutionary stages. The earliest stage occurs when the protostar begins burning deuterium within the core at a sufficient rate to maintain a constant core temperature. Once the initial deuterium in the core is depleted, burning occurs at the rate that new matter convects inwards; this is the steady core deuterium state. In the third stage, the star burns the deuterium remaining in the outer layers of the protostar. Finally, the star ceases contracting and reaches the zero-age main sequence (ZAMS).

Figure 5.11 shows the luminosity as a function of time for three different protostars. At early times, accretion dominates the luminosity, and variability in accretion is strongly reflected in the total luminosity. At late times, accretion slows and Hayashi contraction begins to make a substantial contribution. In general, the total luminosity summed over all the stars is dominated by those protostars with the highest accretion rates. For these young sources, the stellar luminosity is quite small in comparison to the accretion luminosity. Thus, the last panel in Figure 5.11 shows that for all times, accretion luminosity is the main source of luminosity.

For comparison, luminosity due to other physical processes such as compression and viscous dissipation is small (see Figure 5.3). Figure 5.12 shows the final luminosity as a function of source mass. The luminosity increases roughly linearly with mass but has a fairly large scatter. As indicated on the plot, two of the stars have reached the ZAMS, which was due to increased accretion resulting from significant mergers. Even in this low-mass stellar cluster, there are individual stars with contributions larger than the net viscous dissipation. This demonstrates that any heating due to viscous dissipation is exceeded by modest protostellar feedback.

5.3.2 Resolution and Convergence

The AMR methodology allows flexibility in both the depth and breadth of resolution. An insufficient amount of resolution may give inaccurate results, so it is

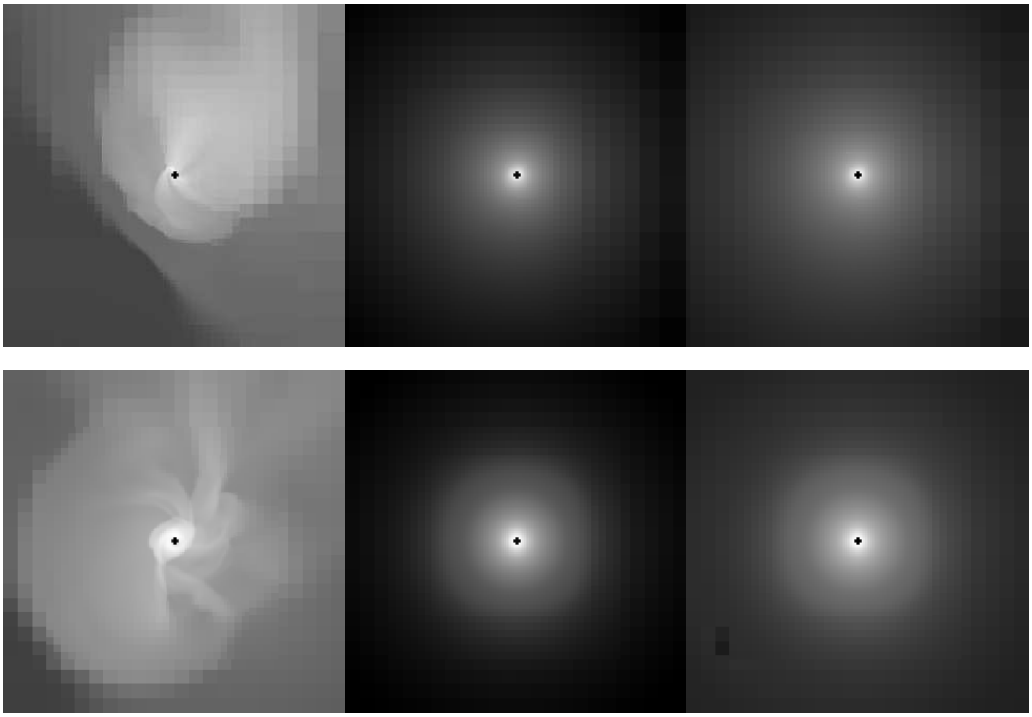

Figure 5.13 From left to right, the images show the log density, log radiation temperature, $T_{\rm r} = (E_{\rm r}/a)^{1/4}$, and log gas temperature for an RT protostellar system at $\sim 0.6\ t_{\rm ff}$ followed with $dx = 4$ AU resolution (top) and $dx = 32$ AU (bottom). The image is 0.03 pc on a side, where we denote the star position with a black cross. The color scale ranges are given by $10^{-19} - 10^{-14}$ g cm^{-3}, $1 - 100$ K, and $1 - 100$ K, respectively.

important to gauge the sensitivity of the result to the resolution. The large scope of the problem and the expense of the radiative transfer methodology limits the depth or maximum resolution of our calculation, where the RT calculation cost is $\sim$ 70,000 CPU hrs on 2.3 GHz quad-core processors. To quantify the effects of resolution on the solution, we run second RT and NRT calculations that evolve the first formed object to a resolution eight times higher than the overall calculation. We run these simulations for 0.12 $t_{\rm ff}$ after the formation of the protostar. We adopt a fixed number of cells for the closest resolved approach between two particles, so that the high-resolution simulations have a merging radius of 32 AU, a factor of eight smaller than the low-resolution cases.

High-Resolution Study with Radiative Feedback

The high-resolution and low-resolution calculations both form single objects with stable, thermally supported disks. Figure 5.13 shows a comparison of the densities, temperatures, and radiation fields. The effective radiation temperature differs by only a few percent outside the inner cells of the low-resolution calculation. In both cases, the gas and radiation temperatures are well coupled such that $T_{\rm gas} \simeq T_{\rm rad}$. However, the gas in the high resolution case is more centrally concentrated, and the disk radius appears smaller. At the final time, the high-resolution star has accreted 0.54 $M_\odot$, while the low-resolution case has reached 0.50 $M_\odot$. During the course of the run, the lower resolution case forms a few fragments in the disk, which are almost immediately accreted by the primary, while in the high-resolution case, no additional particles are formed.

Figure 5.14 shows a comparison of the accretion and luminosity as a function of time. Accretion is generally smooth, and the rates are generally within a factor of two. The luminosity in the low-resolution run has slightly larger variation, but the two approach a similar value at later times. Although there are deviations in the history between the two runs, the evolution is not significantly different at the higher resolution. Certainly, even higher resolution is preferable for investigation of disk properties, but our main result–*that radiative feedback is important to the formation of low-mass stars*–is insensitive to the simulation resolution. High-resolution

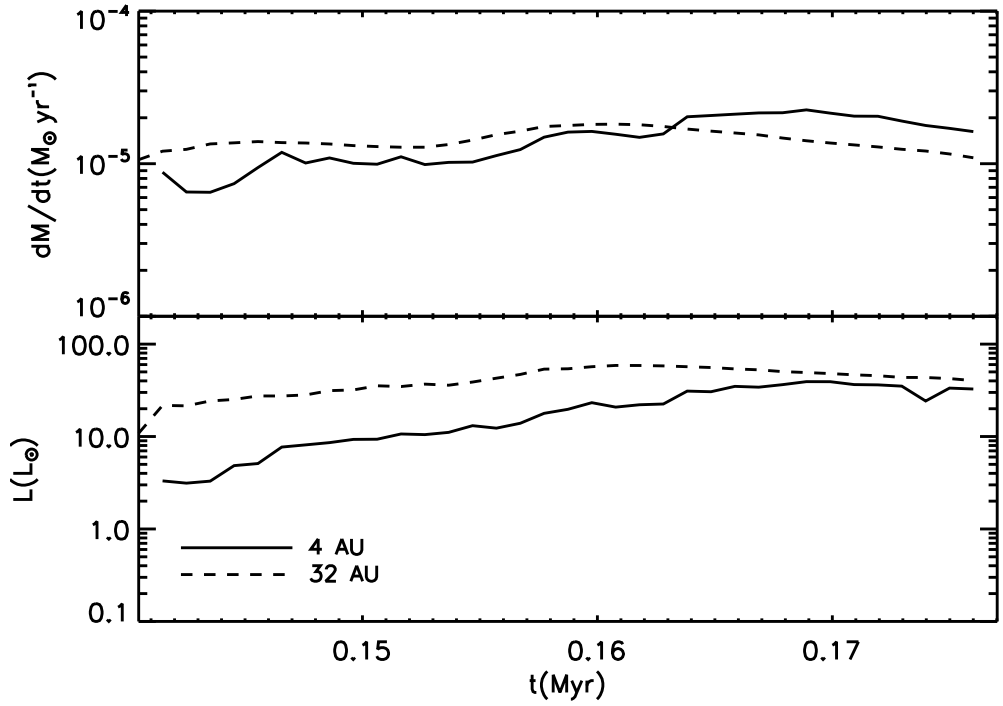

Figure 5.14 The plot shows the accretion rate and luminosity as a function of time for the first formed star in the RT calculation and the same object followed with $dx = 4$ AU resolution. Temporal bins of 1kyr are used.

radiation-hydrodynamics simulations of low-mass disks including irradiation confirm that such disks, with properties similar to ours, are stable against fragmentation (Cai et al. 2008). Gravitational instability is expected to occur only in the regime where the mass of the disks is comparable to the stellar mass (Cai et al. 2008; Stamatellos & Whitworth 2008, 2009).

High-Resolution Study with a Barotropic EOS

This higher resolution non-radiative study achieves maximum densities $> 5 \times 10^{-13}$ g cm^{-3}, several times higher than the barotropic critical density. Consequently, dense gas is heated to temperatures of $\sim 20 - 25$ K. During the time we compare the non-radiative simulations, both the high-resolution barotropic calculation and the first collapsing core in low-resolution NRT calculation form a similar mass primary

object with protostellar disk (see Figure 5.15). However, the low-resolution NRT system experiences significantly more fragmentation. We find that the protostellar disk in the NRT case fragments during approximately half of the time steps, while in the higher resolution barotropic case fragmentation occurs very rarely, taking place in less than <0.1% of the time steps.

Since the low-resolution NRT disks are essentially isothermal, we conclude that heating due to the barotropic approximation is largely responsible for decreasing the number of fragments. In contrast, the higher resolution disks are heated to ~ 20 K. However, this is still significantly less heating than in the RT case, and we find that numerical instability is not suppressed completely even with high-resolution. The radiative high-resolution case experiences no disk fragmentation, underscoring our conclusion that radiative feedback is crucial to representing fragmentation or lack thereof in the star formation process.

Despite different merger radii, in both non-radiative cases all of the fragments are eventually merged with the primary protostar so that the end result in both calculations is a single protostar. This suggests that the fragmentation taking place at low-resolution is largely numerical rather than physical. We emphasize that both significantly higher resolution than we use and additional physics are required to study accretion disk properties.

Convergence

The minimum breadth of resolution is determined by the Truelove criterion. Due to the radiation gradient refinement criterion we apply to resolve the radiation field, at 1 $t_{\rm ff}$ the RT simulation has $\sim$ 80 % more cells, generally concentrated near the protostars, than the NRT calculation. This extra refinement improves the resolution regions near protostellar sources. Inverting (5.12) yields an expression for the effective Jeans number for each cell as a function of density, resolution, and sound speed:

$$J_{\rm eff} = \frac{(\rho G)^{1/2} \Delta x_l}{c_s \pi^{1/2}}. \tag{5.22}$$

As shown in Figure 5.16, the RT simulation is shifted to lower $J_{\rm eff}$, where the vast majority of cells in both calculations are resolved to better than $J_{\rm eff} = 0.1$. The

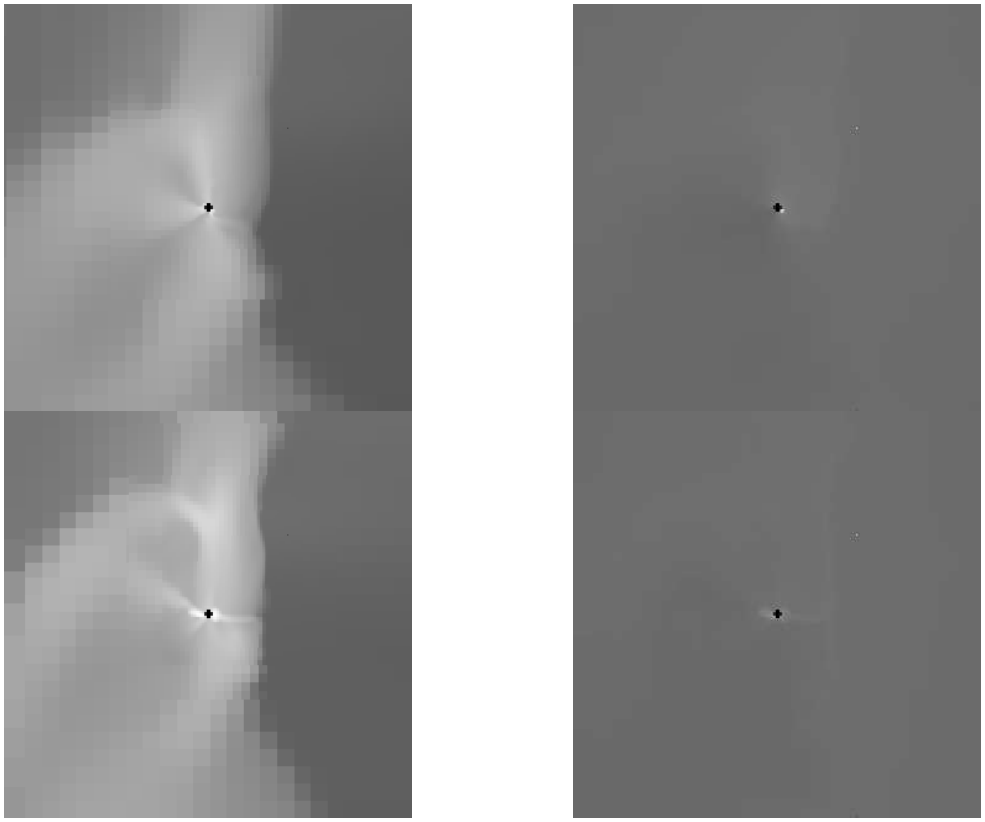

Figure 5.15 The images show the log density (left) and log gas temperature (right) for a NRT protostellar system at $\sim 0.5\ t_{\rm ff}$ followed with $dx = 4$ AU resolution (top) and $dx = 32$ AU (bottom). The image is 0.03 pc on a side, where we denote the star position with a black cross. The color scale ranges are given by $10^{-19} - 10^{-14}$ g cm^{-3} and $1 - 50$ K, respectively.

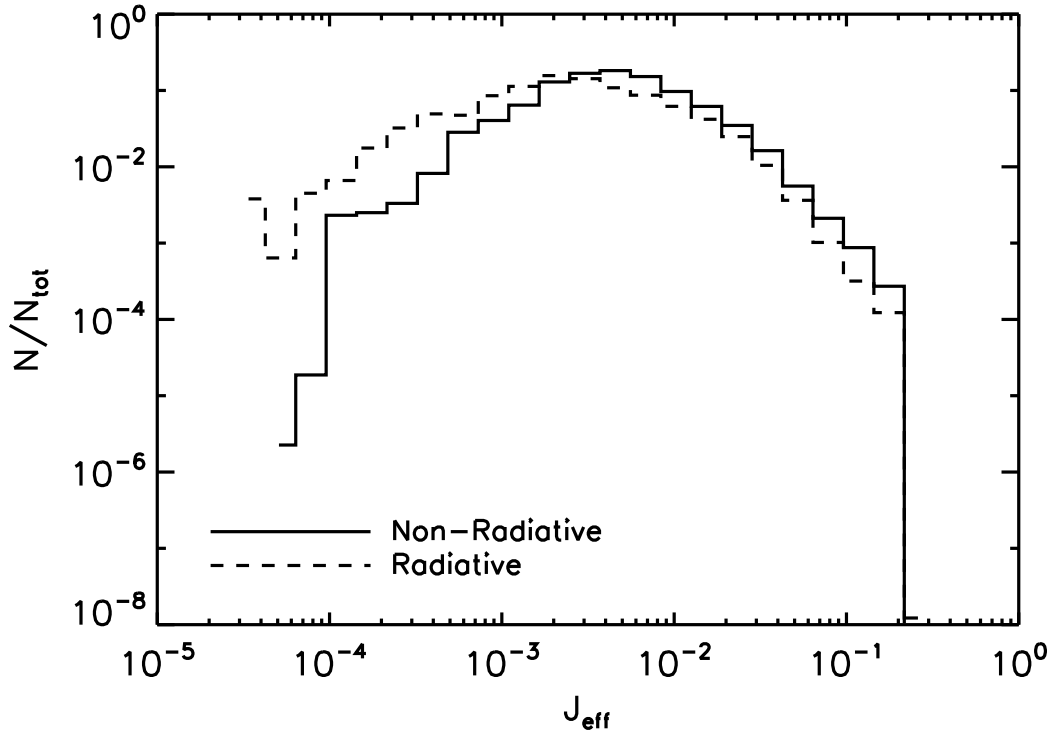

Figure 5.16 Histogram of the effective Jeans number, $J_{\rm eff}$ at 1.0 t_{ff}. The solid and dashed lines indicate the NRT and RT simulations, respectively. Each histogram is normalized to the total number of cells.

choice of base grid resolution guarantees that $J_{\rm eff}$ is typically much smaller than J for most of the cells on the domain. We use a fiducial value of $J = 0.25$ to trigger additional refinement in both simulations, so no cell has $J_{\rm eff}$ exceeding 0.25. Cells in the highest $J_{\rm eff}$ bin are exclusively found on the maximum AMR level, and they are generally at the highest gas densities. These cells, many located in the disks around the protostars, are at the same resolution in both calculations. Thus, the fragmentation results of the RT and NRT calculations are not dissimilar due to differences in effective resolution but are solely a result of differences in thermal physics.

5.4 Simplifying Assumptions

These numerical calculations neglect a number of arguably crucial physical processes in low-mass star formation. In this section, we discuss the implications for our results.

5.4.1 Chemical Processes

Dust Morphology

Our dust model neglects the evolution of dust grains due to coagulation and shattering. In cold dense environments, such as protostellar disks, the aggregation of dust grains may significantly increase grain sizes on timescales as short as 100 years (Schmitt et al. 1997; Blum et al. 2002). Observations of Class 0 protostars indicate significant evolution of the dust size distribution at average densities of $n \simeq 10^7$ cm^{-3} by the Class 0 phase (Kwon et al. 2009). Since we adopt a single dust model for the entire domain, we are likely to either overestimate or underestimate dust grain size in different regions.

To examine the effect of the dust model on gas temperature, we repeat the turbulent driving phase (without gravity) using a conservative model more typical for non-aggregate dust grains:

$$\kappa_R = 0.015(T_g^2/110) \text{ cm}^2 \text{ g}^{-1} \text{ for } T_g \leq 110 \tag{5.23}$$

$$\kappa_P = 0.10(T_g^2/110) \text{ cm}^2 \text{ g}^{-1} \text{ for } T_g \leq 110. \tag{5.24}$$

Using this model, we find that shocked gas may be heated as high as 18 K after a crossing time. In comparison, gas in the fiducial case is only heated to ∼11 K at the same densities (see Figure 5.2 for the temperature distribution due to the fiducial dust opacity model). However, the extent of the additional heating is quite small since only 0.003% of the mass is heated above 11 K and thus differs from the fiducial case. This suggests that the simulations may underestimate the gas temperature in low density regions outside of cores ($n_H < 10^7$) where the dust distribution is not expected to evolve due to coagulation. Significant discrepancy between the gas temperatures of the two models is mainly confined to a small number of cells and is

mitigated by the importance of molecular cooling in these regions, which we discuss in Section 4.1.2.

Gas Temperature at Low Density

To simplify the dust-gas interaction, we assume that dust and gas are perfectly collisionally coupled such that their temperatures are identical. In molecular clouds, there can be significant variation between the dust and gas temperatures. For example, dust in close proximity to stellar sources is radiatively heated, while in strongly shocked regions of the flow, dust acts as a coolant for compressionally heated gas. Below we will discuss both the regime where dust cooling dominates, i.e., $T_g > T_d$, and where molecular cooling dominates, i.e., $T_d > T_g$.

When the gas is shock-heated, the perfect coupling approximation remains valid as long as the rate of energy transfer between the gas and dust is balanced by the cooling rate of the dust. The dust cooling per unit grain area by photon emission is:

$$F(a, T_d) = 4 < Q(a, T_d) > \sigma_B T_d^4, \tag{5.25}$$

where T_d is the dust temperature, a is the grain size, and $< Q(a, T_d) >$ is the Planck-averaged emissivity (Draine & Lee 1984). Then for an ensemble of grains with dust opacity, κ_P, the dust cooling is given by:

$$n^2 \Lambda_d \simeq 4\kappa_P \rho \sigma_B T_d^4 \tag{5.26}$$

$$\simeq 9 \times 10^{-21} \left(\frac{n_H}{1.6 \times 10^4 \text{ cm}^{-3}} \right) \left(\frac{T_d}{10 \text{ K}} \right)^6 \text{ ergs cm}^{-3}\text{s}^{-1}. \tag{5.27}$$

In equation (5.27), we substitute Equation (7.3) for $\kappa_{\rm P}$ and assume that $T_g \sim T_d$. The rate at which energy is transferred from the gas to the dust is given by:

$$\begin{aligned} n\Gamma_d &= 9 \times 10^{-34} {n_H}^2 T_g^{0.5} \left[1 - 0.8 e^{\left(-\frac{75\text{K}}{T_g}\right)} \right] \times \\ &\quad (T_g - T_d) \left(\frac{\sigma_d}{2.44 \times 10^{-21} \text{ cm}^{-3}} \right) \\ &\simeq 7.3 \times 10^{-24} \left(\frac{n_H}{1.6 \times 10^4 \text{ cm}^{-3}} \right)^2 \left(\frac{T_g}{10 \text{ K}} \right)^{3/2} \left[1 - 0.8 e^{\left(-\frac{75\text{K}}{T_g}\right)} \right] \\ &\quad \left(1 - \frac{T_d}{T_g} \right) \text{ erg cm}^{-3} \text{ s}^{-1}, \end{aligned} \tag{5.28}$$

where we adopt $\sigma_d = 2.44 \times 10^{-21}$ cm^{-2} for the dust cross section per H nucleus (Young et al. 2004). For a gas temperature of 10 K the exponential term is very small, so we neglect it in the following equation. Equating these expressions and solving for the gas density at which heating and cooling balance gives:

$$n_H \simeq 2 \times 10^7 \left(\frac{T_d}{10 \text{ K}}\right)^6 \left(\frac{T_g}{10 \text{ K}}\right)^{-3/2} \left(1 - \frac{T_d}{T_g}\right)^{-1} \text{cm}^{-3}. \tag{5.29}$$

Thus, we demonstrate that the dust and gas are well coupled as long as the gas densities are sufficiently high.

However, even in regions where the dust and gas may not be well coupled, molecular line cooling is important. For gas densities in the range $n_{\rm H} = 10^3 - 10^5$ cm^{-3}, CO is the dominant coolant. For these densities, the cooling rate per H, $\Lambda/n_{\rm H}$, is approximately constant with density at fixed temperature. To compare to the magnitude of dust cooling consider a 2 km s^{-1} shock that heats the gas above 100 K. The cooling rate at 100 K is given by $n^2\Lambda_{\rm mol} \simeq 5 \times 10^{-27} n_{\rm H}$ ergs cm^{-3} s^{-1}, where we adopt the cooling coefficient from Neufeld et al. (1995). The characteristic cooling time is $\sim$ 1000 yrs at the average simulation density, which is approximately half the cell-crossing time of such a shock, implying that molecules cool the gas relatively efficiently. Since the shock temperatures on our domain are limited by our resolution, which is much larger than the characteristic cooling length, post-shock temperatures do not surpass 20 K. In this regime, the dust cooling for perfect dust-gas coupling is at least an order of magnitude larger than the estimated molecular cooling. As a result, we likely under-estimate the temperatures in low-density strongly shocked gas in comparison to similar shocks in molecular clouds.

In the regions near protostars, the perfect coupling assumption is valid provided that gas heating by dust is balanced by molecular cooling. This case is discussed by Krumholz & McKee (2008), where the authors demonstrate that the dust and gas temperature remain within a degree provided that:

$$T_d - T_g \simeq \frac{3.5 \times 10^5}{n_{\rm H}} \text{ K} \tag{5.30}$$

for gas temperatures around 10 K. For higher gas temperatures around 100 K, we adopt the molecular cooling coefficient above and find that the dust and gas are well

coupled provided $n_{\rm H}$ exceeds $\sim 2 \times 10^8$ cm^{-3}. Number densities of this magnitude are exceeded in collapsing cores, so that regions near protostars are guaranteed to have well-coupled dust and gas.

Thus, gas temperatures in our RT simulation are fairly accurate for densities larger than the average density, but they may be underestimated by a factor of ~ 2 in strong shocks when the molecular cooling rate is much smaller than the implemented dust cooling rate. Since gas heating suppresses fragmentation, our results may actually overestimate the amount of fragmentation. Consequently, our finding that radiative feedback reduces fragmentation would generally be strengthened by a better treatment of the thermodynamics.

5.4.2 Magnetic Fields

Observations indicate the presence of magnetic fields in nearby low-mass star-forming regions (Crutcher 1999). However, the magnitude of the fields and their importance in the star formation process remain uncertain. Observations by Troland & Crutcher (2008) suggest that the energy contributed by magnetic fields on core scales is subdominant to the gravitational and turbulent energies. On smaller scales, magnetic fields are believed to be associated with disk accretion and the generation of protostellar outflows (Shu et al. 1994; Königl & Pudritz 2000).

Numerical simulations have demonstrated that the presence of magnetic fields may suppress disk fragmentation by supplying additional pressure support (Machida et al. 2008; Price & Bate 2007, 2008). We find that the inclusion of radiative transfer has a similar stabilizing influence on disks.

5.4.3 Multi-frequency Radiative Transfer

Due to the expense of the calculations, we adopt a gray radiative transfer flux-limited diffusion approximation. By averaging over angles and frequencies to obtain the total radiation energy density, we sacrifice the direction and frequency information inherent in the radiation field. As discussed in Krumholz et al. (2009), these approximations touch on several competing effects that influence the radiation spec-

trum. Since radiation pressure is negligible for low-mass stars, it does not affect the gas dynamics. Instead, our main consideration is the extent to which radiative heating may differ for a more sophisticated radiative treatment. As we have discussed in previous sections, the gas temperature and corresponding thermal pressure alone have a significant relationship with accretion and fragmentation.

The first effect to consider is a more exact treatment of dust opacity, which is strongly frequency dependent in the infared and increases towards lower wavelengths (e.g., Ossenkopf & Henning 1994). Since long-wavelength radiation has a lower optical depth, in a multi-frequency calculation the longest wavelengths would be able to escape the core. Anisotropies in the radiation field may also facilitate cooling. Radiative beaming, for example via an outflow cavity, may allow photons to escape along the poles (Krumholz et al. 2005a). Thus, both these effects will likely decrease the temperature in protostellar cores.

The gray radiative transfer method also assumes that the radiation field is thermalized, producing a Planckian radiation spectrum everywhere. Although this is a fair assumption in opaque regions where the number of mean-free-paths is large, it fails in optically thin regions. Since thermalization softens the radiation spectrum, the assumed Planck spectrum is likely to under-predict the heating rate.

Since the net affect of the approximations is somewhat unclear, comparison with more sophisticated radiative treatments would be ideal. However, there have been no 2D or 3D non-gray simulations of low-mass star formation. To date, the most thorough investigation of protostellar formation is presented by Masunaga & Inutsuka (2000). These spherically symmetric simulations follow the formation of 0.8 and 1.0 $M_\odot$ protostars. At radii of 60 AU, they find temperatures ranging from 20-250 K during the main accretion phase, while we find $T_{\max} \sim 90$ K. Their maximum protostellar luminosity is 25 $L_\odot$, which is entirely due to accretion. A few of the protostars in the RT simulation have higher masses and higher maximum luminosities, but the gas temperature distributions on average appear similar (see Figure 5.4). However, the disparity in maximum temperature may be attributable to either differences in the radiation schemes or initial conditions and geometry. Future work will investigate the effects of 3D multi-frequency radiative transfer on low-mass

star formation.

5.5 Conclusions

We perform gravito-radiation-hydrodynamic simulations to explore the effect of radiation feedback on the process of low-mass star formation. We compare our calculation with a similar one using an approximately isothermal equation of state in lieu of radiative transfer. We find that the inclusion of radiative transfer has a profound effect on the gas temperature distribution, accretion, and final stellar masses.

We confirm the finding of Bate (2009b) that additional heating provided by radiative transfer stabilizes protostellar disks and suppresses small scale fragmentation that would otherwise result in brown dwarfs. However, we also find that the vast majority of the heating comes from protostellar radiation, rather than from compression or viscous dissipation. Thus calculations that neglect radiative feedback from protostars, either because they use approximations for radiative effects that are incapable of including it (e.g., Bate et al. 2003; Clark et al. 2008) or because the explicitly omit it (e.g., Bate 2009b), significantly underestimate the gas temperature and thus the strength of this effect. More generally, we find that, due to significant variations in the temperature with time, no scheme that does not explicitly include time-dependent protostellar heating is able to adequately follow fragmentation on scales smaller than $\sim$0.05 pc.

We find that due to the increased thermal support in the protostellar disks, accretion is smoother and less variable with radiative feedback. However, we show that for low-mass star formation the heating is local and limited to the volume within the protostellar cores. As a result, pre-existing sources do not inhibit turbulent fragmentation elsewhere in the domain.

We find that the mean accretion rate increases with final stellar mass so that the star formation time is only a weak function of mass. This is inconsistent with the standard Shu (1977) picture, but it is qualitatively consistent with the McKee & Tan (2003) result for the turbulent core model, where the star formation time varies

as the final stellar mass to the 1/4 power.

The magnitude and variability of protostellar luminosity is of significant observational interest. If accretion contributes a substantial portion of the total luminosity emitted by young protostars, then upper limits for protostellar accretion rates can be inferred directly from the observed luminosity. This may give clues about the formation timescale and the accretion process while the protostars are deeply embedded and cannot be directly imaged. In a future paper we will examine the "luminosity problem" and compare with embedded Class 0 and Class I protostars.

Our larger NRT and RT simulations are performed at a maximum resolution of 32 AU, so it is possible that a few of our cores form stars that otherwise would have become thermally supported or turbulently disrupted in a higher resolution calculation. Thus, higher resolution calculations would be desirable for further work. Although we find that the inclusion of radiative transfer has a similar impact as magnetic fields on fragmentation and accretion, simulations examining the interplay of magnetic fields and radiative transfer are important. To asses the accuracy of our radiative transfer approximations, further simulations with multi-frequency treatment in multi-dimensions with improved dust modeling are also necessary.

Acknowledgements

The authors acknowledge helpful discussions with Andrew Cunningham and Kaitlin Kratter. Support for this work was provided by the US Department of Energy at the Lawrence Livermore National Laboratory under contracts B-542762 (S. S. R. O) and DE-AC52-07NA27344 (R. I. K.) and the National Science Foundation under Grant PHY05-51164 (C. F. M., & S. S. R. O.); the National Science Foundation grant AST-0807739 and NASA through the Spitzer Space Telescope Theoretical Research Program, provided by a contract issued by the Jet Propulsion Laboratory (M. R. K.); the National Science Foundation grant AST-0606831 (C. F. M & S. S. R. O). Computational resources were provided by the NSF San Diego Supercomputing Center through LRAC program grant UCB267; and the National Energy Research Scientific Computer Center, which is supported by the Office of Science of the U.S. Department of Energy under contract number DE-AC03-76SF00098,

though ERCAP grant 80325.

5.6 Appendix A: The Star Particle Algorithm

In this appendix we describe the details of our "star particle" algorithm we use to represent protostars. Appendix 5.6 describes how the star particle algorithm functions within the larger ORION code, while Appendix 5.7 describes the protostellar evolution code that we use to determine the luminosities of our stars. This division is useful because, from the standpoint of the ORION code, a star particle is characterized by only four quantities: mass, position, momentum, and luminosity. The luminosity is determined by the protostellar evolution model outlined in Appendix 5.7 that is attached to each star particle, but the only output of this model that is visible to the remainder of the code is luminosity.

In a calculation using star particles, we add a set of additional steps to every update cycle on the finest AMR level, so that the cycle becomes

1. Hydrodynamic update for gas
2. Gravity update for gas
3. Radiation update, including stellar luminosity
4. Star particle update
   (a) Sink particle update
   (b) Stellar model update

Steps (1) – (3) are the ordinary parts of the update that we would perform even if no star particles were present. In steps (1) and (2) star particles have no direct effect (since they do not interact hydrodynamically, and we handle their gravitational interactions with the gas in an operator split manner in step (4a).

In step (3), star particles act as sources of luminosity, as indicated in equation (5.7). We implement this numerically as follows: let L_n and $\mathbf{x}_n$ be the luminosity

and position of star particle n. Our code uses the Krumholz et al. (2007c) radiation-hydrodynamic algorithm, in which we split the radiation quantities into those to be handled explicitly and those to be handled implicitly. We therefore write the evolution equation to be solved during the radiation step as

$$\frac{\partial \mathbf{q}}{\partial t} = \mathbf{f}_{\rm e-rad} + \mathbf{f}_{\rm i-rad}, \tag{5.31}$$

where $\mathbf{q} = (\rho, \rho\mathbf{v}, \rho e, E)$ is the state vector describing the gas and radiation in a cell, the explicit update vector $\mathbf{f}_{\rm e-rad}$ is the same as in the standard Krumholz et al. algorithm (their equation 52)[5], and the implicit update is modified to be

$$\mathbf{f}_{\rm i-rad} = \begin{pmatrix} 0 \\ 0 \\ -\kappa_{\rm P}\rho(4\pi B - cE) \\ \nabla \cdot \left(\frac{c\lambda}{\kappa_{\rm R}\rho}\nabla E\right) + \kappa_{\rm P}(4\pi B - cE) + \sum_n L_n W(\mathbf{x} - \mathbf{x}_n). \end{pmatrix}. \tag{5.32}$$

Here $W(\mathbf{x} - \mathbf{x}_n)$ is a weighting function that depends on the distance between the location of the cell center $\mathbf{x}$ and the location of the star $\mathbf{x}_n$. The weighting function has the property that the sum of $W(\mathbf{x} - \mathbf{x}_n)$ over all cells is unity, and that $W(\mathbf{x} - \mathbf{x}_n) = 0$ for $|\mathbf{x} - \mathbf{x}_n|$ larger than some specified value. For the computations we present in this paper we use the same weighting function as we use for accretion (equation (13) of Krumholz et al. 2004). However, we have experimented with other weighting functions, including truncated Gaussians, top-hats, and delta functions, and we find that the choice makes very little difference because radiation injected into a small volume of the computational grid almost immediately relaxes to a configuration determined by diffusion. With this modification to $\mathbf{f}_{\rm i-rad}$, our update procedure is the same as described in Krumholz et al. (2007c).

Step (4a) is the ordinary sink particle method of Krumholz et al. (2004), so we only summarize it here and refer readers to that paper for a detailed description and the results of numerous tests. We first create new particles in any cell whose density

[5]Note that our notation here differs slightly from that of Krumholz et al. (2007c), in that we follow the standard astrophysics convention in which κ is the specific opacity, while Krumholz et al. (2007c) follow the radiation-hydrodyanmic convention in which κ is the total opacity. As a result, any opacity κ that appears in the Krumholz et al. (2007c) equations is replaced by $\kappa\rho$ here.

exceeds the Jeans density on the maximum AMR level (i.e., where equation (5.12) is not satisfied.) Next we merge star particles whose accretion zones, defined to be 4 cells in radius, overlap. This ensures that we combine multiple sink particles created in adjacent cells that simultaneously exceed the Jeans density, or multiple sink particles created in the same cell during consecutive time steps. Then we transfer mass from the computational grid onto existing sink particles. Accretion happens within a radius of 4 cells around each sink particle. The amount of mass that a sink particle accretes is determined by fitting the flow around it to a Bondi flow, reduced to account for an angular momentum barrier that would prevent material from reaching the computational cell in which the sink particle is located. The division of mass accreted among cells inside the 4-cell accretion zone is determined by a weighting function. The accretion process leaves the radial velocity, angular momentum, and specific internal energy of the gas on the computational grid unchanged (in the frame co-moving with the sink particle), and it conserves mass, momentum, and energy to machine precision. Next we calculate the gravitational force between every sink particle and the gas in every cell using a direct $1/r^2$ force computation (since the number of particles is small), and modify the momenta of the sink particles and the momenta and energies of the gas cells appropriately. Finally we update the positions and velocities of each sink particle under their mutual gravitational interaction, using a simple N-body code. Forces are again computed via direct $1/r^2$ sums.

Once the sink particle update is complete, we proceed to update the protostellar evolution model that is attached to each star particle.

5.7 Appendix B: Protostellar Evolution Model

Step (4b) of the update cycle described in Appendix 5.6 involves advancing the internal state of each star particle. The primary purpose of this procedure is to determine the stellar luminosity for use in step (3). We determine the luminosity using a simple one-zone protostellar evolution model introduced by Nakano et al. (1995) and extended by Nakano et al. (2000) and Tan & McKee (2004). The model has been calibrated to match the detailed numerical calculations of Palla & Stahler

(1991, 1992), and it agrees to $\sim 10\%$. The numerical parameters we use for the calculations in this paper are based on this calibration, but we note that after we began this work Hosokawa & Omukai (2009) published calculations suggesting that slightly different values would improve the model's accuracy. We recommend that Hosokawa & Omukai's values be used in future work.

Before diving into the details of the numerical implementation, it is helpful to give an overview of the model. The model essentially treats the star as a polytrope whose contraction is governed by energy conservation. The star evolves through a series of distinct phases, which we refer to as "pre-collapse", "no burning", "core deuterium burning at fixed T_c", "core deuterium burning at variable T_c", "shell deuterium burning", and "main sequence". The "pre-collapse" phase corresponds to the very low mass stage ($m \lesssim 0.01$ $M_\odot$) when the collapsed mass is not sufficient to dissociate H_2 and produce second collapse to stellar densities (Masunaga & Inutsuka 2000). During this phase the object is not yet a star. "No burning" corresponds to the phase when the object has collapsed to stellar densities, but has not yet reached the core temperature $T_c \approx 1.5 \times 10^6$ K required to ignite deuterium, and its radiation is powered purely by gravitational contraction. During this phase the star is imperfectly convective. The next stage, "core deuterium burning at fixed T_c", begins when the star ignites deuterium. While the deuterium supply lasts, core deuterium burning acts as a thermostat that keeps the core temperature fixed and the star fully convective. Once the deuterium is exhausted, the star begins the "core deuterium burning at variable T_c" phase, during which the core temperature continues to rise. The star remains fully convective, and new deuterium arriving on the star is rapidly dragged down to the center and burned. The rising core temperature reduces the star's opacity, and eventually this shuts off convection in the stellar core, beginning the "shell deuterium burning" phase. At the start of this phase the star changes to a radiative structure and its radius swells; deuterium burning continues in a shell around the radiative core. Finally the star contracts enough for its core temperature to reach $T_c \approx 10^7$ K, at which point it ignites hydrogen and the star stabilizes on the main sequence, the final evolutionary phase in our model.

In the following sections, we give the details of our numerical implementation

of this model.

5.7.1 Initialization and Update Cycle

When a star is first created, its mass is always below 0.01 $M_\odot$ and thus in the "pre-collapse" state. We do not initialize our protostellar evolution model until the mass exceeds 0.01 $M_\odot$ – prior to this point star particles are characterized only by a mass and have zero luminosity. On the first time step when the mass exceeds 0.01 $M_\odot$, we change the state to "no burning". Thereafter each star particle is characterized by a radius r, a polytropic index n, and a mass of gas from which deuterium has not yet been burned, m_d. We initialize these quantities to

$$r = 2.5 R_\odot \left(\frac{\Delta m / \Delta t}{10^{-5} M_\odot \text{ yr}^{-1}} \right)^{0.2} \tag{5.33}$$

$$n = 5 - 3 \left[1.475 + 0.07 \log_{10} \left(\frac{\Delta m / \Delta t}{M_\odot \text{ yr}^{-1}} \right) \right]^{-1} \tag{5.34}$$

$$m_d = m, \tag{5.35}$$

where Δt and Δm are the size of the time step when the star passes 0.01 $M_\odot$ and the amount of mass accreted during it. If this produces a value of n below 1.5 or greater than 3.0, we set $n = 1.5$ or $n = 3.0$. These fitting formulae are purely empirical calibrations designed to match Palla & Stahler (1991, 1992). The choice of n intermediate between 1.5 and 3.0 corresponds to imperfect convection.

Once a star particle has been initialized and its state set to "no burning", during each time step we perform the following operations:

1. Update the radius and the deuterium mass
2. Compute the new luminosity
3. Advance to the next evolutionary phase

We describe each of these operations below.

5.7.2 Evolution of the Radius and Deuterium Mass

Once a star reaches the "main sequence" evolutionary phase, we simply set its radius equal to the radius of a zero-age main sequence star of the same mass, which we compute using the fitting formula of Tout et al. (1996) for Solar metallicity. Before this point we treat the star as an accreting polytrope of fixed index. For such an object, in a time step of size Δt during which the star gains a mass Δm, the radius changes by an amount Δr given by a discretized version of equation (5.8) of Nakano et al. (2000):

$$\Delta r = 2\frac{\Delta m}{m}\left(1 - \frac{1-f_k}{a_g\beta} + \frac{1}{2}\frac{d\log\beta}{d\log m}\right)r - 2\frac{\Delta t}{a_g\beta}\left(\frac{r}{Gm^2}\right)\left(L_{\rm int} + L_I - L_D\right)r \quad (5.36)$$

Here $a_g = 3/(5-n)$ is the coefficient describing the gravitational binding energy of a polytrope, β is the mean ratio of the gas pressure to the total gas plus radiation pressure in the star, f_k is the fraction of the kinetic energy of the infalling material that is radiated away in the inner accretion disk before it reaches the stellar surface, $L_{\rm int}$ is the luminosity leaving the stellar interior, L_I is the rate at which energy must be supplied to dissociate and ionize the incoming gas, and L_D is the rate at which energy is supplied by deuterium burning.

In this equation we adopt $f_k = 0.5$, the standard value for an α disk. For β, the low-mass stars we discuss in this paper have negligible radiation pressure and so $\beta = 1$ to very good approximation. In general, however, we determine β and $d\log\beta/d\log m$ by pre-computing a table of β values for polytropes as a function of polytropic index n and mass m, and then interpolating within that table. For $n = 3$ interpolation is unnecessary and we instead obtain β by solving the Eddington quartic

$$P_c^3 = \frac{3}{a}\left(\frac{k_B}{\mu m_{\rm H}}\right)^4 \frac{1-\beta}{\beta^4}\rho_c^4, \quad (5.37)$$

where P_c and ρ_c are the central pressure and density of the polytrope (which are also stored in a pre-computed table as a function of n), and $\mu = 0.613$ is the mean molecular weight for fully ionized gas of Solar composition.

For the luminosity emanating from the stellar interior we adopt

$$L_{\rm int} = \max\left(L_{\rm ms}, L_{\rm H}\right), \quad (5.38)$$

where $L_{\rm ms}$ is the luminosity of a main sequence star of mass m, which we compute using the fitting formula of Tout et al. (1996) for Solar metallicity, and $L_{\rm H} = 4\pi r^2 \sigma T_{\rm H}^4$ is the luminosity of a star on the Hayashi track, with a surface temperature $T_{\rm H} = 3000$ K. For the luminosity required to ionize and dissociate the incoming material we use

$$L_I = 2.5\ L_\odot \frac{(\Delta m/\Delta t)}{10^{-5}\ M_\odot\ {\rm yr}^{-1}}, \tag{5.39}$$

which corresponds to assuming that this process requires 16.0 eV per hydrogen nucleus. The deuterium luminosity depends on the evolutionary stage. In the "pre-collapse" and "no burning" phases, $L_D = 0$. In the "core burning at fixed T_c" phase, we set the deuterium luminosity to the value required to keep the central temperature at a constant value $T_c = 1.5 \times 10^6$ K. This is (equation (5.13) of Nakano et al. 2000)

$$L_D = L_{\rm int} + L_I + \frac{Gm}{r}\frac{\Delta m}{\Delta t}\left\{1 - f_k - \frac{a_g \beta}{2}\left[1 + \frac{d\log(\beta/\beta_c)}{d\log m}\right]\right\}, \tag{5.40}$$

where $\beta_c = \rho_c k_B T_c/(\mu m_{\rm H} P_c)$ is the ratio of gas pressure to total pressure at the center of the polytrope. In all subsequent phases, deuterium is burned as quickly as it is accreted, so we take

$$L_D = 15\ L_\odot \frac{(\Delta m/\Delta t)}{10^{-5}\ M_\odot\ {\rm yr}^{-1}}, \tag{5.41}$$

which corresponds to assuming an energy release of 100 eV per gram of gas, appropriate for deuterium burning in a gas where the deuterium abundance is D/H $= 2.5 \times 10^{-5}$. Finally, we update the mass of material that still contains deuterium simply based on L_D. The change in unburned mass is

$$\Delta m_d = \Delta m - 10^{-5} M_\odot \left(\frac{L_D}{15\ L_\odot}\right)\left(\frac{\Delta t}{\rm yr}\right). \tag{5.42}$$

5.7.3 Computing the Luminosity

From the standpoint of the rest of the code, the only quantity of any consequence is the luminosity, since this is what enters as a source term in step (3). The luminosity radiated away from the star consists of three parts:

$$L = L_{\rm int} + L_{\rm acc} + L_{\rm disk}, \tag{5.43}$$

where $L_{\rm int}$ is the luminosity leaving the stellar interior as defined above, $L_{\rm acc}$ is the luminosity radiated outward at the accretion shock, and $L_{\rm disk}$ is the luminosity released by material in traversing the inner disk. These in turn are given by

$$L_{\rm acc} = f_{\rm acc} f_k \frac{Gm\Delta m/\Delta t}{r} \tag{5.44}$$

$$L_{\rm disk} = (1 - f_k) \frac{Gm\Delta m/\Delta t}{r}, \tag{5.45}$$

where $f_k = 0.5$ as defined above, and $f_{\rm acc}$ is the fraction of the accretion power that is radiated away as light rather than being used to drive a wind. Although we do not explicitly include a protostellar outflow in this calculation, we take $f_{\rm acc} = 0.5$ so that we do not overestimate the accretion luminosity by assuming that the all the accretion power comes out radiatively rather than mechanically. Thus, we assume a total radiative efficiency of 75%. Although this value is consistent with x-wind models (Ostriker & Shu 1995), neither x-wind or disk-wind models definitively constrain the total conversion of accretion energy into radiation, and we treat this as a free parameter.

5.7.4 Advancing the Evolutionary State

The final pieces of our protostellar evolution model are the rules for determining when to change the evolutionary state, and for determining what happens at such a change. Our rules are as follows: if the current state is "no burning", then at the end of each time step we compute the central temperature by numerically solving the equation

$$P_c = \frac{\rho_c k_B T_c}{\mu m_{\rm H}} + \frac{1}{3} a T_c^4, \tag{5.46}$$

where P_c and ρ_c are determined from the current mass, radius, and polytropic index. If $T_c \geq 1.5 \times 10^6$ K, we change the evolutionary state to "core burning at fixed T_c" and we change the polytropic index to $n = 1.5$.

If the current evolutionary state is "core burning at fixed T_c", then we check to make sure that $m_d \geq 0$ after we update the unburned deuterium mass with equation (5.42). If not, then the deuterium has been exhausted and we change the state to "core burning at variable T_c".

If the current state is "core burning at variable T_c", we decide whether a radiative zone has formed by comparing the luminosity being generated by deuterium burning, L_D, to the luminosity of a zero-age main sequence star of the same mass, $L_{\rm ms}$. We switch the state to "shell deuterium burning" when $L_D/L_{\rm ms} > f_{\rm rad} = 0.33$. At this point we also change the polytropic index to $n = 3$ and increase the radius by a factor of 2.1, representing a swelling of the star due to formation of the radiative barrier.

Finally, if the state is "shell burning", we compare the radius r at the end of every time step to the radius of a zero-age main sequence star of the same mass. Once the radius reaches the main sequence radius, we switch the state to "main sequence", our final evolutionary state.

Chapter 6

Luminosity Distributions of Low-Mass Protostars: Comparison with Observations

6.1 Introduction

Low-mass protostars are typically divided into four observational classes that can roughly be mapped to evolutionary stages (Andre et al. 2000). Class 0 protostars are both dim and heavily obscured by a dusty envelope, such that most of the radiation falls in the sub-mm band. During the Class I phase the protostar, while still embedded, becomes less obscured and may be surrounded by a thick circumstellar accretion disk. By the Class II phase, the now pre-main sequence star has accreted or expelled most of the initial envelope mass. The remaining gas lies in thin accretion disk surrounding the star. Signatures of outflows may be apparent during both the Class I and Class II phases. During Class III, accretion finishes and the remaining debris disk begins the planet formation process.

These classes are observationally distinguished using the bolomentric temperature of the observed spectral energy distribution (Enoch et al. 2009). However, cataloguing sources and definitively mapping them to a physical stage is complicated since edge-on Class II protostars may be misclassified as Class I (Robitaille

et al. 2006). More simply, measurements of the mm emission as a proxy for the envelope mass can be used to distinguish between embedded, i.e., Class 0 and Class I objects, and non-embedded, Class II objects.

The majority of the accretion process occurs while the protostar is deeply embedded. Consequently, the high extinction and significant radiation reprocessing during the Class 0 and Class I phases hinder detailed study and the protostellar properties are poorly constrained. However, if accretion contributes a substantial portion of the total luminosity, then upper limits for the accretion rates may be inferred directly from the observed luminosity. This gives clues about the formation timescale and the accretion process while the protostars are deeply embedded and cannot be directly imaged. As a result, the magnitude and variability of protostellar luminosity, particularly during for the earliest classes, is of significant observational interest.

For a source accreting at $\dot{M}_*$ with mass M_* and radius R_*, the luminosity generated via accretion is given by:

$$L_{acc} = f_{acc}\frac{GM_*\dot{M}_*}{R_*}, \tag{6.1}$$

where $f_{\rm acc}$ is the fraction of the total accretion energy converted to radiation versus absorbed by the star or channeled into an outflow (McKee & Ostriker 2007). Standard protostellar properties and lifetimes suggest that many sources have lower accretion rates as inferred from their luminosity than expected (Enoch et al. 2009; Evans et al. 2009). This discrepancy, first noted by Kenyon et al. (1990), is generally referred to as the "luminosity problem."

Most recently, Enoch et al. (2009) reports a mean protostellar luminosity of $\sim$ 2 $L_\odot$, which corresponds to a final mean stellar mass given by:

$$M_* \simeq \dot{M}_* t_{acc} = 0.41 \left(\frac{L_{bol}}{2.0\ \mathrm{L}_\odot}\right) \left(\frac{\bar{M}_*}{0.25\ M_\odot}\right)^{-1} \left(\frac{f_{acc}}{0.75}\right)^{-1} \left(\frac{R_*}{3.0\ \mathrm{R}_\odot}\right) \left(\frac{t_{acc}}{0.4\ \mathrm{Myr}}\right) \mathrm{M}_\odot, \tag{6.2}$$

where all the luminosity is derived from accretion. A lifetime of $\sim$ 0.5 Myr is derived from the observed number of Class 0, I, and II objects (Evans et al. 2009). However, the lifetime decreases to $\sim$ 0.4 Myr when the observations are corrected for extinction. If the mean final stellar mass is 0.5 $M_\odot$, then the mean stellar mass over its

formation, $\bar{M}_*$, is half the final mass or ~ 0.25 M$_\odot$. This estimate apears reasonable given that the mean mass of the system IMF is ~ 0.5 M$_\odot$ (Chabrier 2005). However, this picture is simplified by assuming that sources have constant luminosity over the duration of the embedded phase and that all luminosity derives from accretion, which may significantly decrease the estimates. Source confusion in which edge-on Class II protostars are misclassified as Class I may also lower the embedded lifetime. Many late Class I or early Class II sources lack detectable mm emission, which suggests that they are no longer embedded within an envelope. Such sources likely have significantly diminished accretion rates such that their luminosity output is dominated by the stellar contribution (White & Hillenbrand 2004; Muzerolle et al. 1998).

Some authors have suggested that the large spread in observed source luminosities may be attributed to variability in accretion (Kenyon et al. 1990; White & Hillenbrand 2004; Evans et al. 2009). For example, Evans et al. (2009) find that if protostars spend 7% of their Class I lifetime in a high-accretion phase, then it is possible to form a 0.7 M$_\odot$ star. However, this analysis also neglects the stellar luminosity. Star formation models including both stellar luminosity and accretion luminosity generally estimate significantly higher bolometric luminosities than observed (Young & Evans 2005). Evans et al. (2009) find that the Myers et al. (1998) formation model including the stellar contribution compares favorably with observations. However, the authors assume a somewhat contrived accretion proscription, where accretion decreases exponentially with time.

In this chapter, we investigate the nature of the luminosity problem, by comparing a radiation-hydrodynamics simulation of protostars forming in a turbulent molecular cloud (see Chapter 5) to observations of low-mass protostars. In section 6.2 we compare to recent observations of embedded protostars obtained by Enoch et al. (2009). Section 6.3 contains conclusions.

6.2 Comparison to Observations

In this section, we directly compare our radiative transfer (RT) simulation with Enoch et al. (2009), henceforth E08, who report observations of embedded protostellar sources in three low-mass star-forming regions. All three clouds have similar mean protostellar luminosities of a couple $L_\odot$. We confine our comparison to protostars in the Perseus molecular cloud, which has the best statistics.

6.2.1 Simulation Model

We begin by constructing a simple expression to estimate the dependence of the total luminosity on various parameters, including the core efficiency and binary fraction, which are fixed in our simulation. We write this expression as a function of the simulated values that have been calculated self-consistently using the McKee & Tan (2003) model, which we use as a sub-grid model to describe the evolution of the protostellar properties as a function of mass. Although the simulation neglects outflows and it is limited by resolution, these effects can be included during post-processing.

Observations of starless cores indicate that the core mass function shares a similar shape with the stellar mass function but is shifted to higher masses by a factor of three (Alves et al. 2007; Enoch et al. 2008). This difference is generally interpreted as an efficiency factor reflecting the amount of gas launched and entrained in outflows (Matzner & McKee 2000). Since we do not include stellar winds, we adopt $\epsilon_{core} = \frac{1}{3}$, which acts to reduce both the simulated protostellar masses and instantaneous accretion rates. We also consider the effect of unresolved close binaries on the luminosity. For example, two equal mass stars accreting at a combined accretion rate of $\dot{M}_*$ have half the luminosity of a single star with the same total mass and accretion rate. Low-mass stars observed in binaries have a distribution of mass ratios that peaks around 2:1 (Mazeh et al. 2003). Since the accretion luminosity is proportional to the mass squared, this suggests an average binary correction factor of

$$f_{bin} = \frac{(M_1^2 + M_2^2)}{M_{\rm tot}^2} = \frac{(\frac{2}{3}M_{\rm tot})^2 + (\frac{1}{3}M_{\rm tot})^2}{(M_{\rm tot})^2} \simeq 0.56 \tag{6.3}$$

for those protostars with a close companion. We include this correction for all protostars in the RT simulation that have undergone a major merger ($M > 0.1 M_\odot$) during their evolution. We adopt a value of $f_{acc} = 0.75$ from Tan & McKee (2004), which is directly included in the simulation accretion luminosity. The luminosity generated as the protostar contracts along the Hayashi track, L_*, must also be included in the total luminosity, where $L_* = 4\pi\sigma_B r^2 T_s^4$. While post-processing, we adopt $T_{\rm s} = 3000$ K for all protostars, since this is the minimum stable surface temperature. We estimate the stellar radius assuming a mass of $\epsilon_{core} M$ with an average accretion rate of $\bar{\dot{M}} = 1 \times 10^{-6}$ M$_\odot$ yr^{-1}. The protostellar radius estimated by the simulations depends upon the time-history of the accretion rate. For simplicity, we adopt the average accretion rate for the post-processing, and we find that in fact this radius, $r_{\rm eff}$, is not overly sensitive to the value of the mean accretion rate, $\bar{\dot{M}}$, varied by a factor of 10. A simple estimation of the luminosity including these factors is then given by:

$$L_{acc,*,bin} = \epsilon_{core}^2 f_{binary} L_{acc,sim} + \left(\frac{r_{\rm eff}(\bar{\dot{M}}, \epsilon_{core} M, f_{binary})}{r(\dot{M}, M, 1)} \right)^2 L_{*,sim}, \tag{6.4}$$

where $L_{acc,sim}$ and $L_{*,sim}$ denote the simulation accretion luminosity and stellar luminosity, respectively. There are two dominant competing effects: a lower core efficiency factor works to reduce the luminosity, while a smaller protostellar radius increases it. With the fiducial values, the net effect is to reduce the RT protostellar luminosities by a factor of ~ 5.

For most of the early protostellar formation, the accretion luminosity is an order of magnitude larger than the stellar luminosity. Once accretion diminishes to $\lesssim 10^{-7}$ M$_\odot$ yr^{-1}, the stellar luminosity may surpass the accretion luminosity (Offner et al. 2009).

6.2.2 Comparison

Since observations can give no direct information about protostellar masses or radii, we instead use the envelope mass for comparing sources. To derive the simulation envelope masses, we use the E08 beam size of 31" at 1.1 mm, which

corresponds to a physical diameter of ~ 0.04 pc at 250 pc. If we use an envelope mass of 0.1 $M_\odot$ to distinguish between Class I and Class II sources, then we find that two protostars in the simulation are no longer deeply embedded and would therefore be considered Class II objects. We exclude these from the data comparison. The remaining protostars correspond to Class 0 and early Class I objects.

Figure 6.1 shows the Perseus Class 0 and Class I bolometric luminosities reported by E08 and the estimated RT luminosities as a function of envelope mass. For reference, we plot the accretion luminosity, $L_{\rm acc}$, the total stellar and accretion luminosity, $L_{\rm acc,*}$, and the net luminosity corrected for significant mergers, $L_{\rm acc,*,bin}$. We find a mean accretion luminosity of 3.9 $L_\odot$, which is almost twice the observed mean. We quantify the similarity of the two distributions using a two-variable Kolmogorov-Smirnov (K-S) test. Comparing the net accretion and protostellar luminosities with the bolometric luminosities, we find a K-S statistic of 0.17. Some of the disagreement may be due to the lack of resolution of close binaries. If we assume that all the stars with past mergers greater than 0.1 $M_\odot$ are in fact two stars with a 2:1 mass ratio that would be distinguishable observationally, then the K-S statistic increases to 0.22. Adopting a higher core efficiency of $\epsilon_{core} = 0.5$ decreases the agreement to 0.05.

In our simulations, the mean protostellar mass at the final time is $\sim 0.4 M_\odot$, which includes objects that are still actively accreting and reflects the expected core efficiency (Offner et al. 2009). In comparison, the Chabrier (2005) system stellar IMF gives a mean final mass of ~ 0.5 $M_\odot$ for small clusters with maximum stellar mass of a few solar masses.

We have shown that our simulations can reproduce the observed luminosity distribution reasonably well assuming a typical core efficiency factor. However, it is also interesting to ask the question in reverse: How well do the accretion rates inferred from observed luminosities using equation (6.1) compare to the true accretion rates produced in our simulations? We plot the accretion rates inferred from the observed bolometric luminosities and the RT instantaneous accretion rates as a function of envelope mass in Figure 6.2. The observational accretion rates are derived using equation (6.1), where we assume that all objects have mass of 0.25 $M_\odot$,

averaging over their accretion history, and radius of 3 $R_{\odot}$. For the largely uncertain distribution of stellar masses and significant span of accretion rates, a wide range of protostellar radii are possible. To our knowledge, a mass averaged value for the mean stellar radius has not been rigorously calculated, although stellar radii of 3-5 $R_{\odot}$ are typically derived in 1D evolutionary models of low-mass pre-main sequence stars (Palla & Stahler 1993; Robitaille et al. 2006). Our code model reproduces the Palla & Stahler (1993) results fairly well, although it tends to underestimate the stellar radii for $M < 0.3$ M$_{\odot}$ by ~ 30 %. This occurs because Palla & Stahler (1993) assume that the protostellar radii limit to a fixed value of 2.5 M$_{\odot}$ for arbitrarily small masses. We plot the post-processed values for the radii in Figure 6.3 as a function of the gas envelope mass. We expect the derived observational accretion rates are uncertain to within a factor of ~ 2.

We find that the youngest protostars in our simulation have accretion rates that are on average slightly higher than observed. For example Enoch et al. (2009) estimate that typical Class 0 and Class I accretion rates are $1 - 2 \times 10^{-6}$ M$_{\odot}$ yr^{-1}, while we find an average rate of $\sim 4 \times 10^{-6}$ M$_{\odot}$ yr^{-1}. As a result, the K-S statistic for all the sources compared with observation is 0.004, while comparison with only the first forming 7 RT sources gives a K-S statistic of 0.09. In general, the RT luminosities agree better observationally than the RT accretion rates, since the RT simulation accretion rates for the youngest protostars are clustered around $\dot{M} \sim 10^{-6} - 10^{-5}$ $M_{\odot}$yr^{-1}. Observations of sources with envelope masses of $M_{\rm env} \sim 1$ M$_{\odot}$ appear to have a larger dispersion of accretion rates, assuming that the luminosity is due entirely to accretion. However, the observational accretion rates should be considered very approximate since the actual protostellar masses, radii, and evolutionary stages are unknown.

The RT simulation supports the idea that accretion dominates the luminosity for young (e.g., Class 0) sources, while stellar luminosity dominates once protostars have accreted most of their envelopes (e.g., Class II). Consequently, assuming that nearly all of these observed sources are dominated by accretion luminosity is likely a good approximation (Offner et al. 2009). Although we are thus able to get reasonable agreement with observed luminosities, this agreement is somewhat sensitive to

both the protostellar radius and the binary fraction of stars formed in the simulation. Due to uncertainties in the protostellar evolutionary model, the estimated luminosity may be uncertain to within a factor of ~ 2 or ~ 4 depending upon whether accretion or stellar luminosity dominates the total. Since we do not resolve pairs with separations of less than 300 AU, we also cannot conclude whether the mergers would have otherwise resulted in close binaries or unbound neighbors that would be observationally resolved. We note that the Spitzer IRAC band has a beam resolution of ~ 500 AU in Perseus, which is larger than our stellar separation resolution, such that existing close binaries present in the observational sample are similarly unresolved.

6.3 Conclusions

We find that for a reasonable core efficiency factor, the RT simulation produces protostellar luminosities that are in reasonable agreement with observations. The agreement is further improved by accounting for mergers of large protostars, which cannot be followed at our resolution. Although our luminosities do tend to be slightly systematically higher than the observed ones, we do not conclude that a significant luminosity problem exists.

We find less good agreement between inferred accretion rates and simulation accretion rates. This comparison is complicated by the need to assume a fixed radius for the observed protostars. Since the actual observed protostellar properties such as mass and radius are poorly constrained, it is unsurprising that the observed and simulated accretion distributions are dissimilar.

The main uncertainty in our comparison is the degree to which protostellar winds affect accretion. The fiducial efficiency factor effectively lowers the simulation luminosities by a factor of ~ 5. Without this correction factor, the simulations would over-predict the observed luminosities. Further simulations which self-consistently include the effects of winds are necessary to for future studies.

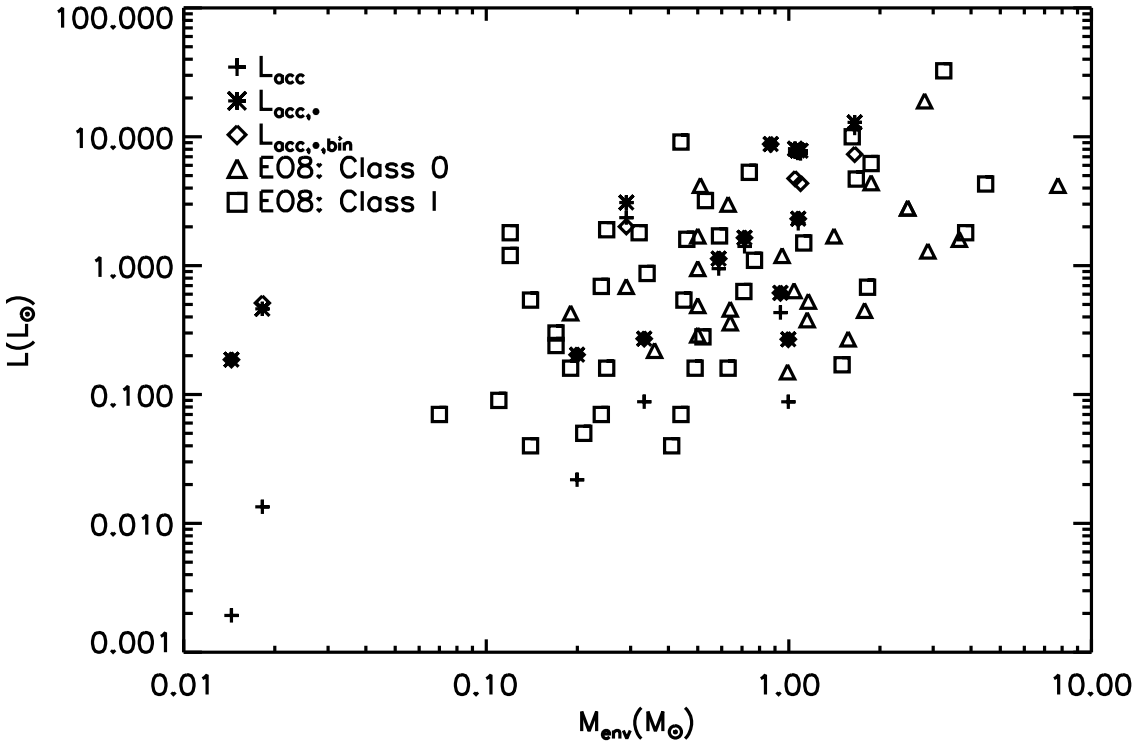

Figure 6.1 The figure shows the RT luminosities as a function of envelope mass. The luminosity due to accretion, accretion plus stellar, and accretion and stellar corrected for binaries is given by the crosses, stars, and diamonds, respectively. The bolometric luminosity of Class 0 and Class I sources observed in Perseus by E08 is given by the triangles and squares, respectively.

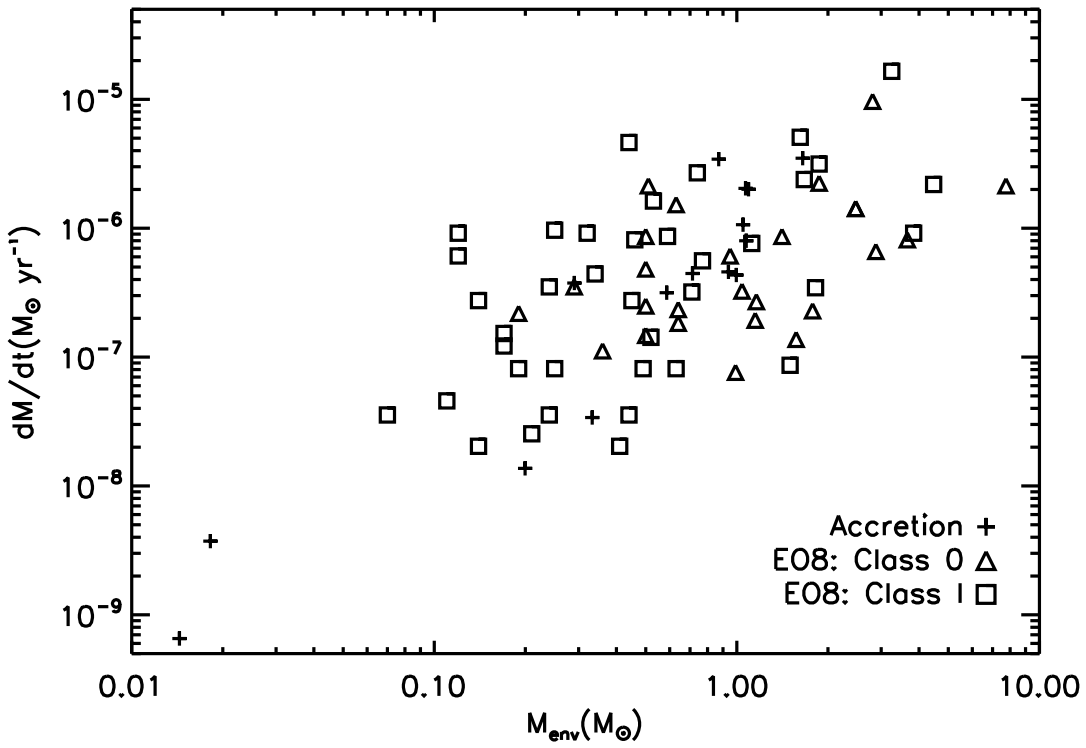

Figure 6.2 The figure shows the instantaneous RT accretion rates as a function of envelope mass (crosses). The accretion estimated from the bolometric luminosity of Class 0 and Class I sources observed in Perseus by E08 is given by the triangles and squares, respectively.

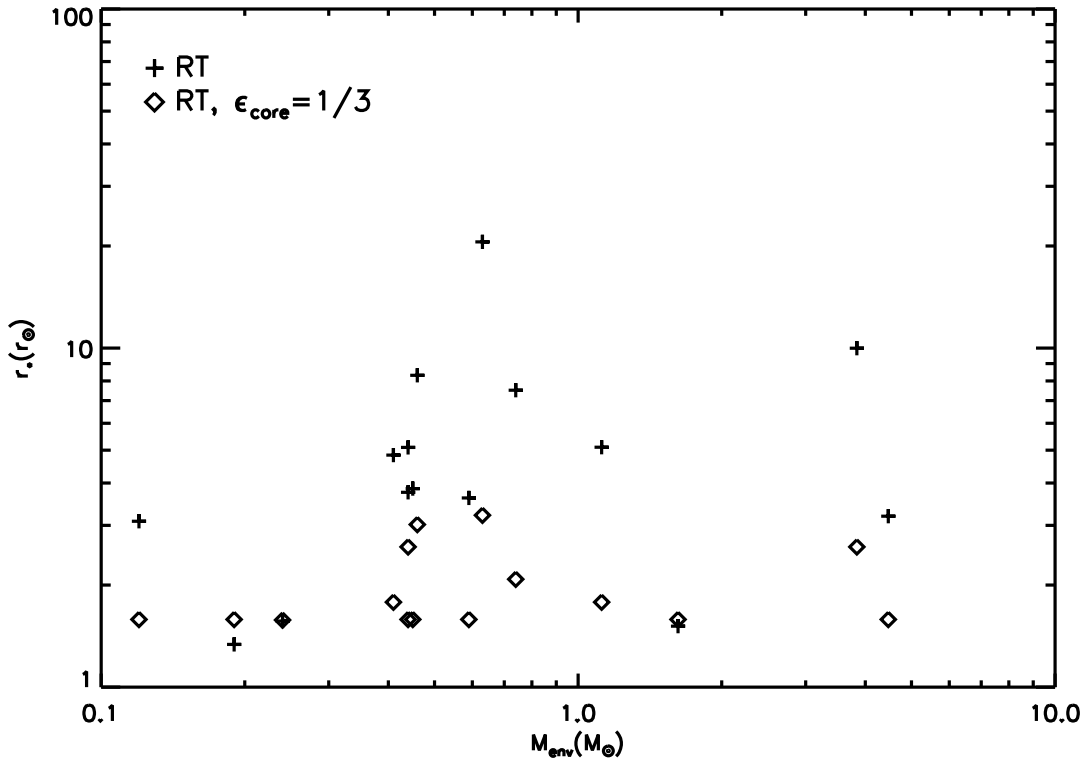

Figure 6.3 The figure shows the protostellar radius as a function of envelope mass. The crosses indicate the RT simulation values without correction. The diamonds indicate post-processed values for the same protostars assuming that $\epsilon_{\rm core} = \frac{1}{3}$.

Chapter 7

Multigroup Radiative Transfer

7.1 Introduction

Radiative processes pose a complex, nonlinear physics problem. Obtaining the solution for time-dependent, three-dimensional conditions can be extremely computationally challenging. This intractability essentially demands the introduction of various approximations to the radiative transfer equation in order to obtain a solution. The adaptive mesh refinement (AMR) gray radiative transfer method derived by Krumholz et al. (2007a) and used by Offner et al. (2009) is a precursor and simplification of the multigroup method discussed in this chapter. In section 7.2, we review the multigroup approach to the radiation transfer problem, which is described thoroughly in Shestakov & Offner (2007). In section 7.3, we present tests of the multigroup diffusion method implemented in ORION. In section 7.4, we discuss the future application of multifrequency methods to problems in star formation.

7.2 Equations

The multigroup diffusion (MGD) equations stem from a discretization of the multifrequency radiation energy equations. For a static medium where radiation pressure is negligible, these equations are given by (Mihalas & Weibel-Mihalas 1999):

$$\partial_t u_\nu = \nabla \cdot c/(\rho\kappa_\nu)\,\nabla u_\nu + c\,\rho\,\kappa_\nu\,(B_\nu - u_\nu)\,, \tag{7.1}$$

$$\rho\,\partial_t e \;=\; -c\,\rho\int_0^\infty d\nu\,\kappa_\nu\,(B_\nu - u_\nu)\;, \tag{7.2}$$

where u_ν and e represent the spectral radiation energy density and specific thermal energy, respectively. The former quantity is a function of position, time, and frequency, ν, while e is a function of the density, ρ, and gas temperature, T, quantities which also depend on position and time. Here, κ_ν is the opacity, and B_ν is the Planck function, which is given by:

$$B_\nu = \frac{(8\pi\,h/c^3)\,\nu^3}{e^{\frac{h\nu}{kT}} - 1} \quad \text{erg sec}^{-1}\ \text{cm}^{-3}\ \text{Hz}^{-1}\,, \tag{7.3}$$

where c is the speed of light and h and k are the Planck and Boltzmann constants, respectively. Since the evolution of the density is determined by hydrodynamics, it remains fixed during the solution of the transfer equations. Equations (7.1-7.2) are obtained in the diffusion limit by assuming that the gas is optically thick, which suppresses the directional dependence of the radiation intensity. In the limit that the gas becomes optically thin, a flux-limiter is used to correct the equations and obtain the appropriate radiation propagation speed. Equation (7.1) must be solved for each frequency of interest, where the frequencies are coupled together via equation (7.2). The solution of the equations must be iterated until the gas temperature as well as the radiation energies has converged.

To sufficiently model the radiation spectrum, a large number of frequencies may be required, incurring a prohibitive computational cost. However, the number of equations can be reduced by discretizing the frequency domain into G frequency spans, ν_i, or groups of frequencies (Shestakov & Offner 2007). For example, the energy in each group is denoted:

$$u_g(x,\,t) = \int_g u_\nu = \int_{\nu_{g-1}}^{\nu_g} d\nu\,u_\nu\,. \tag{7.4}$$

Equations (7.1-7.2) can then be integrated over each frequency span to obtain the MGD equations:

$$\partial_t u_g \;=\; \nabla\cdot c/(\rho\kappa_g)\,\nabla u_g + c\,\rho\,\kappa_g\,(B_g - u_g)\,, \tag{7.5}$$

$$\rho\,\partial_t e \;=\; -c\,\rho\sum_{g=0}^{G}\kappa_g\,(B_g - u_g)\;, \tag{7.6}$$

where B_g is the Planck function integrated over the gth group and κ_g is the average opacity for the group. In comparison, the gray radiation diffusion equation, a further simplification of equation (7.5), is essentially a one-group system that is derived by integrating over all frequencies (Krumholz et al. 2007a). For a frequency-independent opacity, the MGD equations and the gray equations produce identical results, independent of the number of groups. In the limit of many groups, the MGD solution approaches the more exact multifrequency solution. The MGD equations thus bestow significant computational advantage, allowing the user to concentrate groups in interesting regions of the frequency domain, while covering low radiation energy density regions of the spectrum more coarsely.

Although many methods for solving these equations have been previously constructed, recently Shestakov & Offner (2007) implemented a 3D multigroup flux-limited radiative diffusion method within an AMR framework. Implemented in the AMR ORION code, this method enables multi-physics simulations including radiation-hydrodynamics, gravitation, and point mass sources with an unprecedented amount of resolution and accuracy. The actual method and implementation utilizing pseudo transient continuation (PTC) have been described in great detail by Shestakov & Offner (2007) and will not be repeated here.

7.3 Test Problems

Characterizing the accuracy of a scheme is an integral and informative part of code development. Verification of radiation transfer methods is particularly challenging because exact analytic frequency-dependent solutions simply do not exist. Historically, benchmark testing occurs through comparison with solutions generated by previous codes or via trivial problems that do not fully evaluate the method. Recently, Shestakov & Bolstad (2005) obtained a semi-analytic solution to the 1D multifrequency diffusion problem by replacing the Planck function with the more tractable Wien function. This solution constitutes a rigorous test for multigroup and multifrequency methods. In addition, the substitution of the radiation emission function is simple to implement without modifying the underlying scheme. Unfor-

tunately, analytic tests for multifrequency radiation-hydrodynamics remain nonexistent, so we test ORION by investigating a classic shock-tube problem and comparing to known physical limits. We describe and present the results of these two tests in the following subsections.

7.3.1 Wien Diffusion Test

The initial conditions for the Wien diffusion test consist of a gas with constant density, ρ_0, along a 1D extent with initially zero radiation field (Shestakov & Offner 2007). The gas temperature is initialized to T_0 for $0 \leq x \leq x_0$ and 0 elsewhere. At $t = 0$ gas is heated in a region near the origin such that the gas and radiation fields are out of equilibrium. The opacity of the gas is given by $\kappa = \kappa_0(\nu/\nu_0)^{-3}$ cm^2 g^{-1}, where the configuration is optically thick for most frequencies. As the state evolves with time, energy diffuses into the cold region while the gas and radiation fields equilibrate. Thus, the problem tests the frequency dependent diffusion of the radiation field as well as the energy transfer due to the gas and radiation coupling equation.

In order to derive a semi-analytic solution to the multifrequency equations, Shestakov & Bolstad (2005) replace the Planck function (equation 7.3) with its form in the limit that $h\nu >> kT$. Thus, equation (7.3) reduces to the Wien function:

$$W_\nu = (8\pi\, h/c^3)\, \nu^3 e^{\frac{-h\nu}{kT}} \quad \text{ergs s cm}^{-3}. \tag{7.7}$$

The choice for the opacity conveniently eliminates the coefficient frequency dependence in the product $\kappa W_\nu \propto e^{(-h\nu/kT)}$. This expression is then easy to integrate, so that equations 7.1 -7.2 can be evolved semi-analytically.

As described in Shestakov & Bolstad (2005), the Wien diffusion problem can be written in terms of dimensionless parameters describing length, time, and radiation energy densities, respectively:

$$l_0 = \tfrac{\nu_0^3}{\kappa_0}, \quad x_0 = \tfrac{l_0}{\sqrt{3}}, \quad t_0 = \tfrac{l_0}{c} \quad u_0 = \tfrac{8\pi h}{n u_0^3/c^3},\, E_0 = T_0^4,$$

where the characteristic frequency is given by $\nu_0 = kT_0/h$ and $e = c_v T$, where the specific heat capacity for an ideal gas is $c_v = 9.99 \times 10^7$ ergs K^{-1} g^{-1}. As a

consequence, the solution is conveniently independent of the initial choices for T_0, κ_0, and ρ_0. For running the test with ORION, we adopt fiducial values of $T_0 = 100$ eV, $\kappa_0 = 7.40 \times 10^{38}$ cm^{-1} s^{-3}, and $\rho_0 = 1.82 \times 10^{-5}$ g cm^{-3}. These correspond to a characteristic length and time of $x = 2 \times 10^5$ cm and $t_0 = 1.16 \times 10^{-5}$ s, respectively. Although the derivation of the analytic solution assumes that the initial radiation energy density on the domain and gas temperature at $x > x_0$ are exactly zero, we set these to small floor values that are negligible compared to the solution.

To model the frequency evolution, ORION uses 64 groups that span $0.0 \leq h\nu \leq 1500.0$ eV with spacing that increases incrementally by a factor of $\alpha = 1.1$. The lowest span width is $\Delta\nu_0 = 0.05$ eV. The frequency limits are chosen based on the characteristic minimum and maximum temperatures in the problem, where the integral of the emission function evaluated at these temperatures over the frequency range must include most of the energy, i.e., for the Wien function:

$$\int_0^\infty W(\nu, T_{max}) d\nu \simeq \int_{\nu_0}^{\nu_{max}} W(\nu, T_0) d\nu. \tag{7.8}$$

The adopted group structure contains more than 99.98% of the energy for the expected range of temperatures.

We adopt a symmetry boundary condition for the left domain boundary at $x/x_0 = 0$. The right boundary at $x/x_0 = 4$ uses an outflow boundary condition, which allows the radiation to propagate freely out of the domain. We verify that the solution is not affected by the placement of the boundary edge for solution times on the order of t_0.

In Figure 7.1, we show the ORION solution of the gas temperature and radiation energy density at $t = 1.0\ t_0$ with the analytic solution overlaid. The solution is sufficiently accurate that the predicted and actual solutions are indistinguishable by eye. For reference, the bottom two panels in Figure 7.1 show the relative error in the two quantities. The ORION solution is generally accurate to better than one part in 1000, with the worst agreement occurring just to the right of the initial gas temperature discontinuity, which corresponds to the location of the largest temperature gradient. The radiation energy density, which is inherently diffusive, is an order of magnitude more accurate in this region.

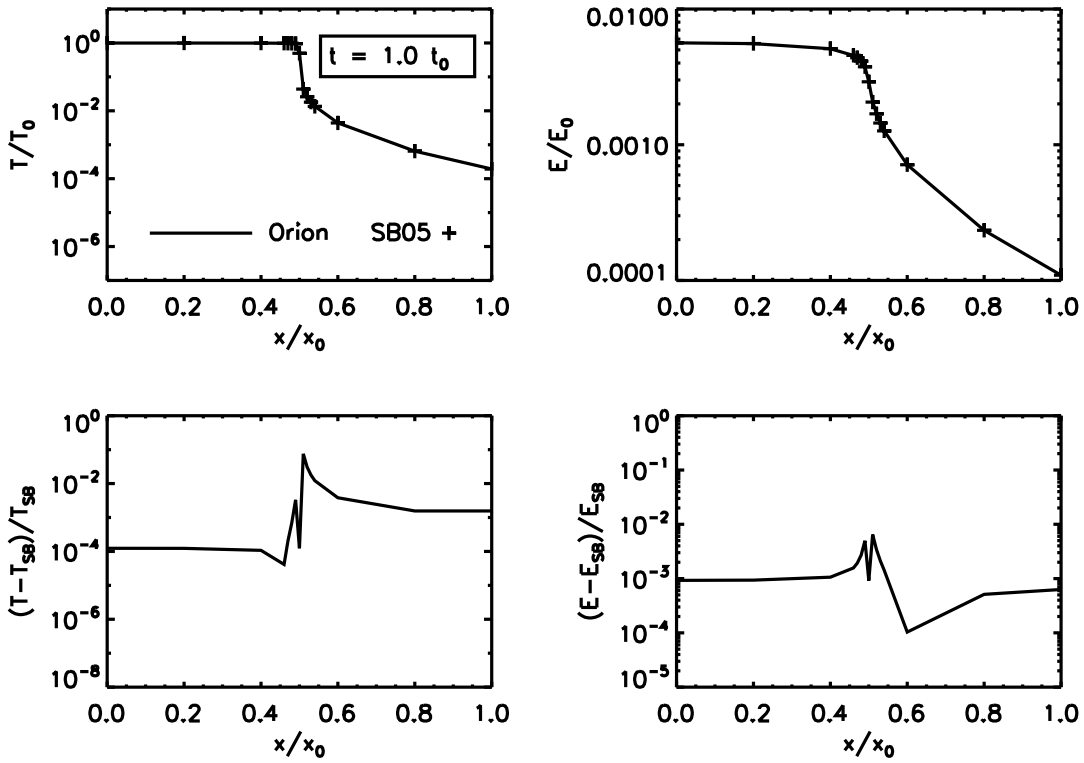

Figure 7.1 The top images show the normalized gas temperature, T, and total radiation energy density, E, as a function of position at $t = 1.0\ t_0$. The crosses indicate the semi-analytic solution derived by Shestakov & Bolstad (2005). The bottom plots show the relative error in the two quantities as a function of position.

The net radiation energy density derived by ORION is given by the sum of the energies contained in all frequency groups. As shown in Figure 7.1, the individual group energies have widely different solutions depending on the typical mean-free path of the group. By 1 t_0, the few highest frequency groups have propagated past the edge of the domain. However the energy in these groups is tiny in comparison to the solution by construction, so the accuracy is not compromised. As illustrated in Figure 7.1, the peak of the energy spectrum occurs in the groups 40-48, where $h\nu \simeq kT_0$.

7.3.2 Colliding Flows Test

Despite the power of the Wien diffusion test to directly validate the accuracy of multifrequency radiative transfer methods, it is nonetheless limited to a static medium. It is also important to check the veracity of the radiation solver within the framework of a multi-physics problem. In the colliding flows test, we examine the outcome of a strongly shocked flow in the optically thin and optically thick limits of the radiation regime. When the gas is optically thin, efficient cooling occurs and the gas acts as if it were isothermal. When the gas is optically thick, the shocked gas cools slowly such that the gas behaves adiabatically. In these two regimes, we can compare to the analytic purely hydrodynamic solution for strong shocks with effective values of $\gamma = 1.001$ and $\gamma = 5/3$, respectively.

ORION solves the radiation-hydrodynamic equations of compressible gas dynamics (Truelove et al. 1998; Klein 1999; Krumholz et al. 2007b):

$$\frac{\partial \rho}{\partial t} + \nabla \cdot (\rho \mathbf{v}) = 0, \tag{7.9}$$

$$\frac{\partial (\rho \mathbf{v})}{\partial t} + \nabla \cdot (\rho \mathbf{v}\mathbf{v}) = -\nabla P, \tag{7.10}$$

$$\frac{\partial (\rho e)}{\partial t} + \nabla \cdot [(\rho e + P)\mathbf{v}] = -\kappa_R \rho (4\pi B - cE), \tag{7.11}$$

$$\frac{\partial u_g}{\partial t} - \nabla \cdot (\frac{c\lambda}{\kappa_{\mathrm{R,g}} \rho} \nabla u_g) = \kappa_{\mathrm{P,g}} \rho (4\pi B_g - c u_g). \tag{7.12}$$

These equations are leading-order accurate in v/c provided that radiation pressure terms are negligible, which is indeed true in our problem.

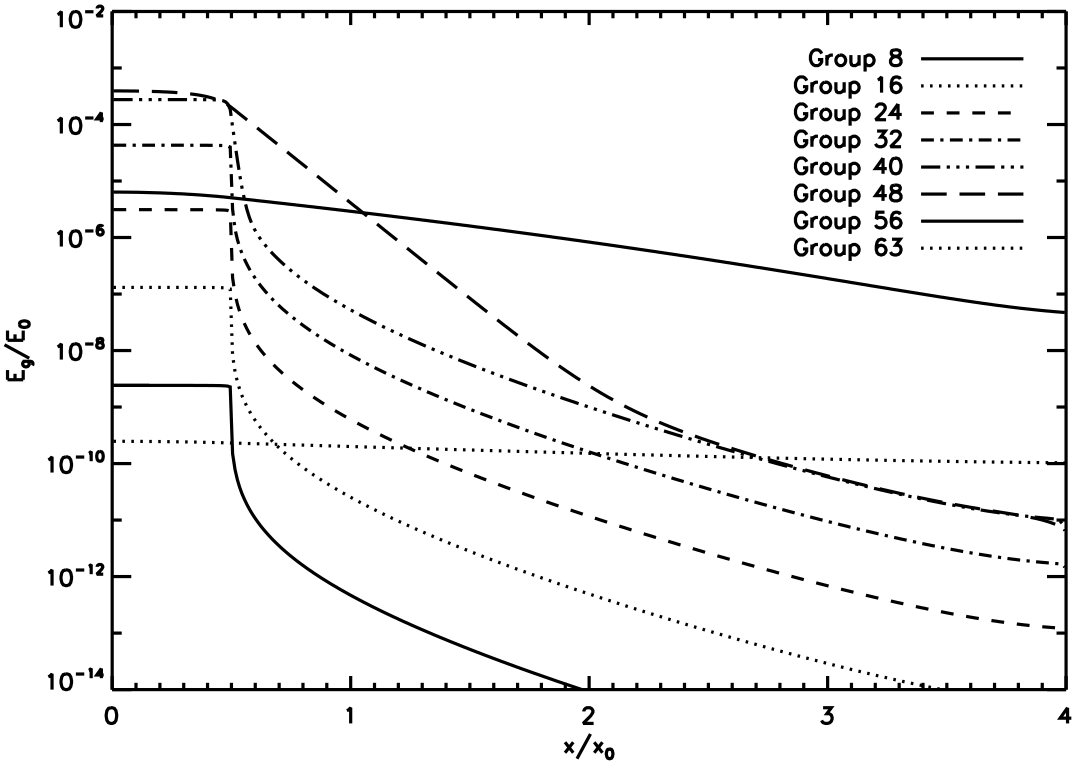

Figure 7.2 The image shows the normalized radiation energy density in selected frequency groups, E_g, as a function of position at $t = 1.0\ t_0$. The frequency increases with increasing group number, where the group boundaries are given by: 0.58 eV $< \nu_0 <$ 0.68 eV; 1.79 eV $< \nu_0 <$ 2.0 eV; 4.58 eV $< \nu_0 <$ 4.9 eV; 10.0 eV $< \nu_0 <$ 11.1 eV; 22.1 eV $< \nu_0 <$ 24.4 eV; 50.0 eV $< \nu_0 <$ 52.9 eV; 104.1 eV $< \nu_0 <$ 113.9 eV; 204.0 eV $< \nu_0 <$ 222.4 eV. Note that the line pattern repeats, so that the first and last two consecutive groups share the same pattern. Of these, the last two groups can be distinguished by their high diffusivity.

For ease of comparison, we adopt the characteristic physical values used by Whitehouse et al. (2005). The initial flow conditions consist of 1D slab with uniform density, $\rho_0 = 1 \times 10^{-10}$ g cm^{-3}, and length, $x_0 = 2 \times 10^{15}$ cm. The gas and radiation temperatures are fixed at $T = 1500$ K, where the effective radiation temperature is defined as $T_r = (E/a)^{0.25}$. The gas with $x \leq x_0/2$ has an initial velocity of $v_0 = c_s = 3.2 \times 10^5$ cm s^{-1}, while the gas with $x > x_0/2$ has an initial velocity of $v_0 = -3.2 \times 10^5$ cm s^{-1}. The opposing flow causes a strong shock to immediately form at the domain center. We use inflow boundary conditions at the domain edges, so that gas continually enters the grid with velocity $\pm v_0$.

We examine the solution for the opacities $\kappa = 40.0$, 0.4, 4.0×10^{-3}, and 4.0×10^{-5} cm^2 g^{-1}, where the two extremes recover the adiabatic and isothermal limits, respectively. We use $N_{\rm cells} = 100$ cells with width $dx = 2 \times 10^{13}$ cm. For the group structure, we use 8 groups logarithmically spaced to cover the frequency range from $0 \leq h\nu \leq 1500$ eV. Since the opacity is constant, this is not a challenging multigroup problem, but it serves to demonstrate that the ORION radiation-hydrodynamcs scheme is working properly.

Neglecting the complexity of the radiative transfer, an analytic solution may be obtained from the hydrodynamic jump conditions as a function of the ratio of specific heats, γ. Solving for the shock speed gives:

$$s = \frac{(\gamma - 3)v_0 + \sqrt{(\gamma + 1)^2 v_0^2 + 16 c_s^3}}{4}. \tag{7.13}$$

The density behind the shock, ρ_1, is given by:

$$\rho_1 = \rho_0(1 + v_0/s). \tag{7.14}$$

This corresponds to a pressure, P_1, given by:

$$P_1 = P_0 \frac{(\gamma + 1)\frac{\rho_1}{\rho_0} - (\gamma - 1)}{(\gamma + 1) - (\gamma - 1)\frac{\rho_1}{\rho_0}}. \tag{7.15}$$

The gas temperature inside the shocked region, T_1, is then:

$$T_1 = T_0 \left(\frac{P_1 \rho_0}{P_0 \rho_1} \right). \tag{7.16}$$

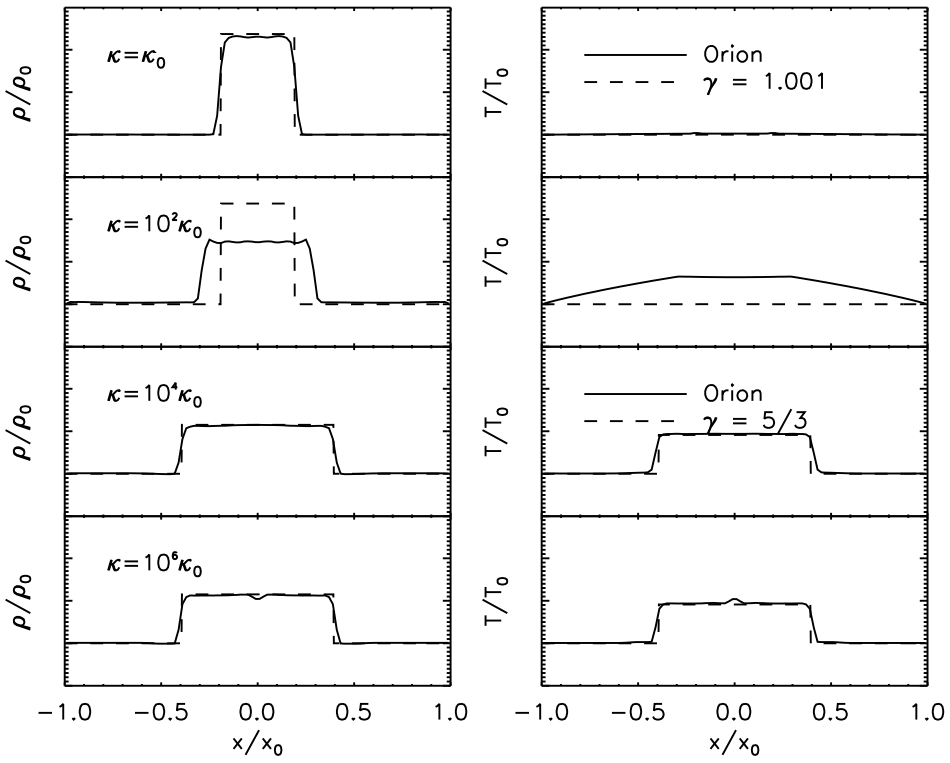

Figure 7.3 The images show the normalized gas density (left) and temperature (right) as a function of position at $t = 1.0 \times 10^9$ sec where $\kappa_0 = 4 \times 10^{-5}$ cm^2 g^{-1} and $N_{\rm cells}$ = 100. The analytic solution for $\gamma = 1.001$ is shown by the dashed line in the top two panels, while the analytic solution for $\gamma = 5/3$ is shown by the dashed line in the bottom panels.

As gas continues to amass behind the shock, the thickness of the central region of post-shock gas increases as $\Delta x = 2s \times t$.

Figure 7.3 shows the solution obtained by ORION with the analytic solution overlaid for the limits where the gas is optically thick or optically thin. ORION, even with this fairly minimal resolution, reliably reproduces the solution in the two limits as expected. The intermediate solutions show the progression between the two cases. In particular, the marginally optically thin $\kappa = 100\kappa_0$ calculation exhibits a solution that does not agree well with either the analytic isothermal or adiabatic cases, which is to be expected. The other opacity values render the gas sufficiently optically thick or thin to be effectively adiabatic or isothermal, respectively. The temperature bump that appears at the origin in the very optically thick case is a product of wall-heating.

There are several interesting differences in the shock-tube solution reported by ORION and the published solution by Whitehouse et al. (2005) using an SPH radiative transfer method. Most obviously, ORION renders the shock jumps more accurately with only ~ 3 cells across the discontinuity, while the SPH method, using the same parameters and resolution, requires ~ 10 cells. Presumably, Whitehouse et al. (2005) could achieve similar shock resolution by using three times the number of particles. This difference is unsurprising given that higher-order Godunov methods generally have superior shock-capturing to SPH methods, which are more diffusive (Klein et al. 2007). However, due to the low numerical dissipation of the scheme, ORION exhibits small amplitude oscillations of a few percent behind that shock for the $\kappa = 4.0, 0.4$ cm^2 g^{-1} cases, which are apparently absent in the SPH results. Whitehouse et al. (2005) observe more substantial wall-heating, which first becomes noticeable for $\kappa = 4 \times 10^{-3}$ cm^2 g^{-1}. In contrast, ORION exhibits no wall-heating for $\kappa = 4 \times 10^{-3}$ cm^2 g^{-1}, and for $\kappa = 4 \times 10^{-5}$ cm^2 g^{-1}, the magnitude of the effect is half that of the SPH method.

Figure 7.4 shows the density and gas temperature for $\kappa = 4 \times 10^{-5}$ cm^2 g^{-1} with four times higher resolution. Except for the few cells located in the shock, the relative error is generally smaller than 10^{-2}. The solution shows a small amount of ringing inside the shock, which can be reduced by increasing the numerical diffusion

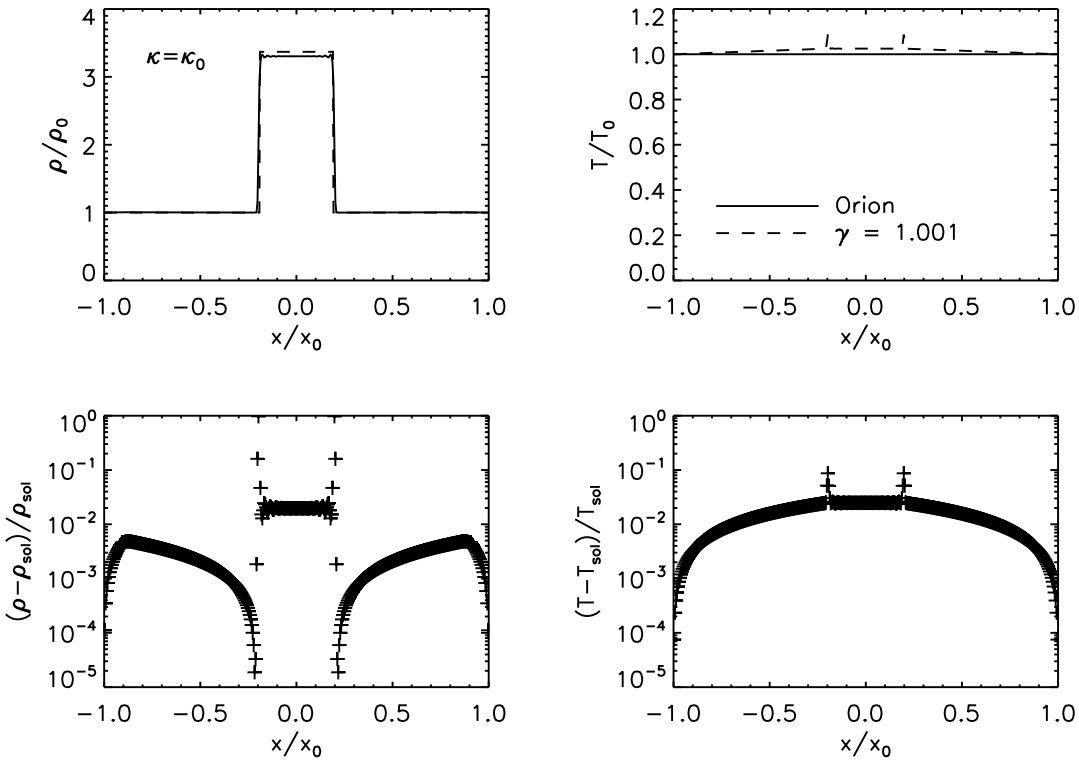

Figure 7.4 The top images show the normalized gas density and temperature as a function of position at $t = 1.0 \times 10^9$ sec with $\kappa = 4 \times 10^{-5}$ cm^2 g^{-1} and $N_{\rm cells} = 400$. The analytic solution for $\gamma = 1.001$ is shown by the dashed line. The bottom plots show the relative error in the two quantities as a function of position.

coefficient.

7.4 Future Work: Applications of Multifrequency Radiative Transfer to Star Formation

7.4.1 Overview of Past Work

To date, no 3D multifrequency hydrodynamic studies of either high-mass or low-mass star formation have been completed. The dearth of such studies is a testament to the difficulty and computational expense of the radiative transfer problem. Past modeling has instead sacrificed dimensionality or introduced approximations such as the gray flux-limited diffusion approximation discussed in Chapter 5. Nonetheless, the conclusions of past work have hinted that non-axisymmetric frequency-dependent radiative transfer modeling may be crucial for understanding unsolved problems in star formation, including the formation process and mass limit of massive stars, core fragmentation, and stellar multiplicity.

The most thorough investigation of low-mass star formation including multifrequency radiative transfer is presented by Masunaga et al. (1998) and Masunaga & Inutsuka (2000). The two successive papers modeled the collapse of a spherically symmetric cloud through the formation of a protostar and accretion of the initial envelope. Their method solves the full angle-dependent and frequency-dependent transfer equation without any diffusion approximation. In Masunaga et al. (1998), the authors continued the calculation only through the first collapse phase (hydrogen molecules are not dissociated). They varied the initial mass, temperature, and dust opacity to investigate the role of these parameters on the solution. They demonstrated that the radius, $R \sim 5$ AU, and mass, $M \sim 0.05\ M_{\odot}$, of the first core are independent of the initial temperature and density. In Masunaga & Inutsuka (2000), the calculation is continued from the birth of the protostar through the termination of the main accretion phase. This second set of calculations illustrate that the luminosity peaks just after the formation of the protostar and declines with the accretion rate towards late times for an initially homogeneous cloud. The authors

argue that the homogeneous cloud reproduces the observations more accurately than hydrostatic initial conditions.

The high fidelity of the radiation transfer method used by Masunaga et al. guarantees that the temperature and density distributions are obtained with good accuracy. However, disks and wind cavities, which cannot be represented in 1D, play an important role in the star formation process (Shu et al. 1987). The calculations also neglect the production of nuclear energy, which would begin to be significant in comparison to the accretion luminosity towards the end of the main accretion phase.

Yorke & Sonnhalter (2002) modeled the formation of a high-mass star using 2D axi-symmetric multifrequency radiative-hydrodynamic calculations. They found that the existence of lower density regions generated by core rotation and aligned with the rotational axis facilitated the escape of radiation, promoting accretion along the plane of the disk. Ultimately Yorke & Sonnhalter (2002) found that this flashlight effect alone was not sufficient to overcome radiation pressure in the high-mass case, and accretion was halted by radiation pressure at $\sim 42 M_{\odot}$. However, they demonstrated that a multifrequency approach allowed nearly twice as much mass to accrete onto the star as an identical simulation using a GFLD method.

As discussed in Krumholz et al. (2009), multifrequency treatment in 3D may influence and improve the radiation spectrum over a gray approach in several ways. Although low-mass star formation is insensitive to radiation pressure effects, radiative beaming, for example via an outflow cavity, may allow photons to escape along the poles (Yorke & Sonnhalter 2002; Krumholz et al. 2005a). This may lead to significantly lower temperatures in the accretion disk. As we have discussed in previous chapters, the gas temperature and corresponding thermal pressure alone have a significant relationship with accretion and fragmentation, so that multifrequency treatment may produce a qualitatively different result every for low-mass stars.

MGD studies are also important because the gas and dust become opaque at high frequencies, while remaining transparent at low frequencies due to the frequency squared opacity dependence in the far infared. As a result, the spectrum may have significant deviations from a black-body form. Approximations, such as GFLD, adopt Planck or Rosseland averaged opacities, which integrate the dust opacity over

all frequencies. The Rosseland opacity represents a weighted average that accounts for some of this frequency-dependent effect. However, the calculation assumes a thermal spectrum, so that the average is likely to incorrectly estimate the opacity in the cases where the thermalization assumption fails. In optically thick regions with a large numbers of photon scatterings, a Planckian radiation spectrum is a good approximation. However, this may not be true within the dust-destruction radius or inside an outflow cavity.

The net affect of radiation approximations on star formation studies remains unclear, particularly in the 3D case where the problem geometry is the most complex. Thus, 3D multifrequency simulations are important to our understanding of both low-mass and high-mass star formation.

7.4.2 Multigroup Modifications for Modeling Star Formation

In addition to multigroup radiative transfer, there are several additional details that must be implemented for modeling low-mass star formation problems.

Radiative Sources

It remains computationally unrealistic to resolve the collapse of gas from cloud densities of 10^2 cm^{-3} to stellar interior densities of $> 10^{22}$ cm^{-3} in 3D and evolve the subsequent protostellar evolution for a significant fraction of its formation. A typical solution to this problem involves replacing the unresolved gas mass with a point particle. Among star formation methods, the most sophisticated of these sink particles advect within the grid, accrete gas, and include sub-grid protostellar models to represent stellar evolution (Krumholz et al. 2004, 2009).

Within the MGD framework, star particles serve as frequency-dependent radiative source terms. Thus, the diffusion equation, 7.5, with stellar sources becomes:

$$\partial_t u_g(\,x,\,t) = \nabla \cdot c/(\rho\kappa_g)\,\nabla u_g + c\,\rho\,\kappa_g\,(B_g - u_g)\; + \sum_i L_{g,i}\delta(\mathbf{x} - \mathbf{x}_i), \qquad (7.17)$$

where $L_{g,i}$ is the luminosity of the ith particle in group g at position x_i. This term

is independent of u_g and T_g and, like ρ, remains constant throughout the iterations. To facilitate convergence, the source radiation is not injected into a single cell, but added to the grid within a volume of 8^3 cells weighted by a gaussian distribution.

The ORION sub-grid stellar model we adopt is based upon Tan & McKee (2004). It is straightforward to modify the model to derive the radiation energy added to each radiation group rather than the integrated luminosity. The Tan & McKee (2004) model consists of two main components, namely, the accretion luminosity, and the stellar luminosity due to deuterium and nuclear burning. Thus, the change in radiation energy per timestep in each group is the sum of these contributions: $L_{g,i} = L_{acc,g,i} + L_{*,g,i}$.

The accretion luminosity for a protostar of mass M_* accreting at $\dot{M}_*$ with radius R_* is given by:

$$L_{acc} = f_{acc}\frac{GM_*\dot{M}_*}{R_*}, \tag{7.18}$$

where $f_{\rm acc}$ indicates the fraction of accretion energy radiated by the protostar rather than used to drive an outflow; we adopt $f_{\rm acc} = 0.75$ (McKee & Ostriker 2007). The radiation due to accretion is emitted at the stellar surface behind the accretion shock. The protostellar surface is well-within the dust destruction radius, $r_d \sim 1$ AU (Chakrabarti & McKee 2005), and the emitted radiation spectrum may significantly deviate from a Plankian. However, our treatment of this term is simplified since the cell resolution is generally much larger than r_d. Thus, for $r > r_d$ the accretion photons are absorbed and re-emitted by the dust at some effective temperature producing a more thermal spectrum. Most species of dust typically sublimate around ~ 1100 K (Pollack et al. 1994; Semenov et al. 2003), and therefore we adopt $T_d = 1100$ K for the temperature of the thermalized spectrum of the accretion luminosity. The accretion component of the group luminosity can then be described by:

$$L_{acc,g,i} = L_{acc,i}\frac{\int_g B(\nu, T_d)d\nu}{B(T_d)}. \tag{7.19}$$

The second component of the net luminosity is stellar. Happily, stars emit as near perfect black bodies, which can be described as a function of an effective surface temperature, T_{eff}. We obtain the stellar luminosity from the Tan & McKee (2004) model, which records the amount of deuterium in the protostar and self-consistently

models the deuterium burning as a function of time. This model also includes Kelvin-Helmholz contraction, and it connects smoothly to the zero-age main-sequence luminosity and radius once all the deuterium is depleted. Consequently, the stellar component of the group luminosity is given by:

$$L_{*,g,i} = L_{*,i} \frac{\int_g B(\nu, T_{eff}) d\nu}{B(T_{eff})}. \tag{7.20}$$

During the early stages of star formation, the protostar is deeply embedded in an optically thick dusty envelope, so that all the luminosity generated by the protostar is heavily processed. After the embedded phase, which lasts $\sim 5 \times 10^5$ yrs (Evans et al. 2009), accretion diminishes and the stellar component dominates the total luminosity (White & Hillenbrand 2004). At these later stages, our approximation using an assumed T_d may break down since the optical depth through most sightlines is small. However, once the main accretion phase has ended, the accretion luminosity will contribute only a small part of the radiation spectrum.

In the event of calculations with very high frequency resolution, $B(\nu, T_{eff})$ can be directly replaced by tabulated stellar spectra (Kurucz 1999). However, for our purposes the blackbody assumption is adequate given that frequency resolution will be coarse and the stellar radiation will be strongly processed by the surrounding protostellar envelope.

Dust Chemistry

Dust grains found in molecular clouds play an important role in heating and cooling the gas. In dense regions near protostars, the dust and gas are collisionally coupled so that radiatively heated grains may directly transfer energy to the gas. In shock heated regions, dust serves as important cooling agent (Offner et al. 2009). Dust grains post-processes the radiation field in crucial ways, as we discussed in the previous section, emitting primarily in the infrared.

The grain size distribution and chemical composition are both important to calculating the absorbed and emitted wavelengths of radiation. Much work has been devoted to estimating optical coefficients and opacities calculated from various sizes, shapes, and mixtures of graphite and silicate grains (e.g., Draine & Lee 1984; Pollack

et al. 1985, 1994; Semenov et al. 2003). In the range $10\ \mu\text{m} \leq \lambda \leq 3\ \text{mm}$, most models agree that the dust opacity goes as a strong powerlaw with frequency, $\kappa \propto \nu^2$ (Draine & Lee 1984). GFLD methods typically skirt this issue by adopting averaged dust opacities as a function of the local density and gas temperature (Pollack et al. 1985). With MGD, we include this frequency dependence explicitly to more accurately capture the evolution of the radiation field and the gas temperature.

For a small number of groups, a complicated dust model is unnecessary since we cannot resolve fine structure in frequency space. Thus, we adopt the simplest model for the opacity:

$$\kappa = \kappa_0 \left(\frac{\nu}{\nu_0} \right)^2, \tag{7.21}$$

where $\kappa_0 = 0.54\ \text{cm}^2\ \text{g}^{-1}$ per unit mass of gas (Chakrabarti & Whitney 2007). Equation (7.21) has been normalized to an opacity twice that of the diffuse interstellar medium (e.g., Weingartner & Draine 2001) to account for icy grain mantles. For calculations involving a large number of groups such that the far-infrared spectrum is well resolved, the simple opacity power-law can be replaced by detailed opacity tables such as those published by Ossenkopf & Henning (1994). These opacities are also calculated as a function of gas density from $n = 10^5 - 10^8\ \text{cm}^{-3}$ typical of molecular cloud cores. Changes in the opacities as a function of density reflect evolution of the dust grain distribution due to coagulation and shattering of dust grains.

7.4.3 Future Work

MGD is an important step for better modeling and understanding star formation, however further physics and additional advances are necessary for a complete computational picture.

In the short term, multifrequency modeling of high-mass star formation in 3D will be possible with the addition of radiation pressure terms to the MGD method. Recent GLFD studies with explicit treatment of radiation pressure have shown that although radiation pressure plays an important role in the formation of high-mass stars, it cannot halt accretion and limit the final stellar mass (Krumholz et al. 2009). Such studies will need to be revisited with more accurate multifrequency radiation

treatment and dust modeling, which can be accomplished with further extension of the MGD method.

Finally, the MGD method described in this chapter nonetheless relies on the flux-limited diffusion approximation. A Monte-Carlo radiative transfer approach is currently the most promising for following both the frequency and angle-dependence of the radiation field in both optically thick and thin regimes. Currently, such methods are commonly used for static modeling and post-processing (Whitney et al. 2003; Robitaille et al. 2006; Chakrabarti & Whitney 2007; Stamatellos & Whitworth 2005). However, adequate sampling of the probability distributions requires that the number of photons be comparable to the number of grid-points (Chakrabarti & Whitney 2007). Even with parallelization, these methods currently remain too time consumptive to be feasible within a time-advanced operator-split framework. In the future, clever modifications will be necessary in addition to increases in computational performance for full Monte-Carlo radiative transfer simulations of star formation.

Bibliography

Adams, F. C. & Shu, F. H. 2007, ApJ, 671, 497

Agertz, O., Moore, B., Stadel, J., Potter, D., Miniati, F., Read, J., Mayer, L., Gawryszczak, A., Kravtsov, A., Nordlund, Å., Pearce, F., Quilis, V., Rudd, D., Springel, V., Stone, J., Tasker, E., Teyssier, R., Wadsley, J., & Walder, R. 2007, MNRAS, 380, 963

Alves, J., Lombardi, M., & Lada, C. J. 2007, A&A, 462, L17

Andersen, M., Meyer, M. R., Oppenheimer, B., Dougados, C., & Carpenter, J. 2006, AJ, 132, 2296

André, P., Belloche, A., Motte, F., & Peretto, N. 2007, A&A, 472, 519

Andre, P., Ward-Thompson, D., & Barsony, M. 2000, Protostars and Planets IV, 59

Attwood, R. E., Goodwin, S. P., Stamatellos, D., & Whitworth, A. P. 2009, A&A, 495, 201

Ayliffe, B. A., Langdon, J. C., Cohl, H. S., & Bate, M. R. 2007, MNRAS, 374, 1198

Ballesteros-Paredes, J., Gazol, A., Kim, J., Klessen, R. S., Jappsen, A.-K., & Tejero, E. 2006, ApJ, 637, 384

Ballesteros-Paredes, J., Klessen, R. S., Mac Low, M.-M., & Vazquez-Semadeni, E. 2007, in Protostars and Planets V, ed. B. Reipurth, D. Jewitt, & K. Keil, 63–80

Ballesteros-Paredes, J., Klessen, R. S., & Vázquez-Semadeni, E. 2003, ApJ, 592, 188

Ballesteros-Paredes, J. & Mac Low, M.-M. 2002, ApJ, 570, 734

Banerjee, R. & Pudritz, R. E. 2006, ApJ, 641, 949

—. 2007, ApJ, 660, 479

Barranco, J. A. & Goodman, A. A. 1998, ApJ, 504, 207

Basu, S. & Ciolek, G. E. 2004, ApJ, 607, 39

Bate, M. R. 2009a, MNRAS, 392, 590

—. 2009b, MNRAS, 392, 1363

Bate, M. R. & Bonnell, I. A. 2005, MNRAS, 356, 1201

Bate, M. R., Bonnell, I. A., & Bromm, V. 2002, MNRAS, 336, 705

—. 2003, MNRAS, 339, 577

Bate, M. R. & Burkert, A. 1997, MNRAS, 288, 1060

Blum, J., Wurm, G., Poppe, T., Kempf, S., & Kozasa, T. 2002, Advances in Space Research, 29, 497

Boley, A. C. 2009, ApJ, 695, L53

Bonnell, I. A. 1994, MNRAS, 269, 837

Bonnell, I. A., Bate, M. R., Clarke, C. J., & Pringle, J. E. 1997, MNRAS, 285, 201

—. 2001, MNRAS, 323, 785

Bonnell, I. A., Bate, M. R., & Vine, S. G. 2003, MNRAS, 343, 413

Bonnell, I. A., Clarke, C. J., & Bate, M. R. 2006, MNRAS, 368, 1296

Bonnell, I. A. & Rice, W. K. M. 2008, Science, 321, 1060

Bonnell, I. A., Vine, S. G., & Bate, M. R. 2004, MNRAS, 349, 735

Boss, A. P., Fisher, R. T., Klein, R. I., & McKee, C. F. 2000, ApJ, 528, 325

Cai, K., Durisen, R. H., Boley, A. C., Pickett, M. K., & Mejía, A. C. 2008, ApJ, 673, 1138

Caselli, P., Benson, P. J., Myers, P. C., & Tafalla, M. 2002, ApJ, 572, 238

Chabrier, G. 2005, in Astrophysics and Space Science Library, Vol. 327, The Initial Mass Function 50 Years Later, ed. E. Corbelli, F. Palla, & H. Zinnecker, 41–+

Chakrabarti, S. & McKee, C. F. 2005, ApJ, 631, 792

Chakrabarti, S. & Whitney, B. 2007, ArXiv e-prints, 711

Ciolek, G. E. & Basu, S. 2006, ApJ, 662, 442

Clark, P. C., Bonnell, I. A., & Klessen, R. S. 2008, MNRAS, 386, 3

Clark, P. C., Klessen, R. S., & Bonnell, I. A. 2007, MNRAS, 379, 57

Crutcher, R. M. 1999, ApJ, 520, 706

di Francesco, J., Evans, II, N. J., Caselli, P., Myers, P. C., Shirley, Y., Aikawa, Y., & Tafalla, M. 2007, in Protostars and Planets V, ed. B. Reipurth, D. Jewitt, & K. Keil, 17–32

Dib, S., Kim, J., Vázquez-Semadeni, E., Burkert, A., & Shadmehri, M. 2007, ApJ, 661, 262

Draine, B. T. & Lee, H. M. 1984, ApJ, 285, 89

Duchêne, G., Delgado-Donate, E., Haisch, Jr., K. E., Loinard, L., & Rodríguez, L. F. 2007, in Protostars and Planets V, ed. B. Reipurth, D. Jewitt, & K. Keil, 379–394

Duquennoy, A. & Mayor, M. 1991, A&A, 248, 485

Durisen, R. H., Boss, A. P., Mayer, L., Nelson, A. F., Quinn, T., & Rice, W. K. M. 2007, in Protostars and Planets V, ed. B. Reipurth, D. Jewitt, & K. Keil, 607–622

Elmegreen, B. G. 2000, ApJ, 530, 277

—. 2007, ApJ, 668, 1064

Elmegreen, B. G. & Scalo, J. 2004, ARA&A, 42, 211

Enoch, M. L., Evans, N. J., Sargent, A. I., & Glenn, J. 2009, ApJ, 692, 973

Enoch, M. L., Evans, II, N. J., Sargent, A. I., Glenn, J., Rosolowsky, E., & Myers, P. 2008, ApJ, 684, 1240

Enoch, M. L., Glenn, J., Evans, Neal J., I., Sargent, A. I., Young, K. E., & Huard, T. L. 2007, ApJ, 666, 982

Enoch, M. L., Young, K. E., Glenn, J., Evans, II, N. J., Golwala, S., Sargent, A. I., Harvey, P., Aguirre, J., Goldin, A., Haig, D., Huard, T. L., Lange, A., Laurent, G., Maloney, P., Mauskopf, P., Rossinot, P., & Sayers, J. 2006, ApJ, 638, 293

Evans, N. J., Dunham, M. M., Jørgensen, J. K., Enoch, M. L., Merín, B., van Dishoeck, E. F., Alcalá, J. M., Myers, P. C., Stapelfeldt, K. R., Huard, T. L., Allen, L. E., Harvey, P. M., van Kempen, T., Blake, G. A., Koerner, D. W., Mundy, L. G., Padgett, D. L., & Sargent, A. I. 2009, ApJS, 181, 321

Fiege, J. D. & Pudritz, R. E. 2000, ApJ, 534, 291

Forgan, D., Rice, K., Stamatellos, D., & Whitworth, A. 2009, MNRAS, 394, 882

Gammie, C. F., Lin, Y.-T., Stone, J. M., & Ostriker, E. C. 2003, ApJ, 592, 203

Goodman, A. A., Barranco, J. A., Wilner, D. J., & Heyer, M. H. 1998, ApJ, 504, 223

Goodman, A. A., Benson, P. J., Fuller, G. A., & Myers, P. C. 1993, ApJ, 406, 528

Goodwin, S. P. & Kroupa, P. 2005, A&A, 439, 565

Goodwin, S. P., Kroupa, P., Goodman, A., & Burkert, A. 2007, in Protostars and Planets V, ed. B. Reipurth, D. Jewitt, & K. Keil, 133–147

Hartmann, L. 2002, ApJ, 578, 914

Hartmann, L., Ballesteros-Paredes, J., & Bergin, E. A. 2001, ApJ, 562, 852

Hennebelle, P. & Chabrier, G. 2008, ArXiv e-prints, 805

Hennebelle, P., Whitworth, A. P., Cha, S.-H., & Goodwin, S. P. 2004, MNRAS, 348, 687

Heyer, M., Krawczyk, C., Duval, J., & Jackson, J. M. 2008, ArXiv e-prints

Heyer, M. H. & Brunt, C. M. 2004, ApJ, 615, L45

Hosking, J. G. & Whitworth, A. P. 2004, MNRAS, 347, 1001

Hosokawa, T. & Omukai, K. 2009, ApJ, 691, 823

Hujeirat, A., Camenzind, M., & Yorke, H. W. 2000, A&A, 354, 1041

Inutsuka, S.-I. & Miyama, S. M. 1992, ApJ, 388, 392

Jappsen, A.-K. & Klessen, R. S. 2005, å, 423, 1

Jijina, J., Myers, P. C., & Adams, F. C. 1999, ApJS, 125, 161

Johnstone, D., Fich, M., Mitchell, G. F., & Moriarty-Schieven, G. 2001, ApJ, 559, 307

Jolliffe, I.-T. 2002, Principle Component Analysis, 2nd edn.

Kenyon, S. J., Hartmann, L. W., Strom, K. M., & Strom, S. E. 1990, AJ, 99, 869

Keto, E. & Field, G. 2005, ApJ, 635, 1151

Keto, E., Rybicki, G. B., Bergin, E. A., & Plume, R. 2004, ApJ, 613, 355

King, A. R., Pringle, J. E., & Livio, M. 2007, MNRAS, 376, 1740

Kirk, H., Johnstone, D., & Di Francesco, J. 2006, ApJ, 646, 1009

Kirk, H., Johnstone, D., & Tafalla, M. 2007, ApJ, 668, 1042

Kirk, J. M., Ward-Thompson, D., & André, P. 2005, MNRAS, 360, 1506

Klein, R. I. 1999, Journal of Computational and Applied Mathematics, 109, 123

Klein, R. I., Inutsuka, S.-I., Padoan, P., & Tomisaka, K. 2007, in Protostars and Planets V, ed. B. Reipurth, D. Jewitt, & K. Keil, 99–116

Klessen, R. S. 2001, ApJ, 556, 837

Klessen, R. S., Ballesteros-Paredes, J., Vázquez-Semadeni, E., & Durán-Rojas, C. 2005, ApJ, 620, 786

Klessen, R. S. & Burkert, A. 2000, ApJS, 128, 287

—. 2001, ApJ, 549, 386

Klessen, R. S., Burkert, A., & Bate, M. R. 1998, ApJ, 501, L205+

Königl, A. & Pudritz, R. E. 2000, Protostars and Planets IV, 759

Kratter, K. M., Matzner, C. D., & Krumholz, M. R. 2008, ApJ, 681, 375

Krumholz, M. R. 2006, ApJ, 641, L45

Krumholz, M. R., Klein, R. I., & McKee, C. F. 2007a, ApJ, 665, 478

—. 2007b, ApJ, 656, 959

Krumholz, M. R., Klein, R. I., McKee, C. F., & Bolstad, J. 2007c, ApJ, 667, 626

Krumholz, M. R., Klein, R. I., McKee, C. F., Offner, S. S. R., & Cunningham, A. J. 2009, Science, 323, 754

Krumholz, M. R., Matzner, C. D., & McKee, C. F. 2006a, ApJ, 653, 361

Krumholz, M. R. & McKee, C. F. 2005, ApJ, 630, 250

—. 2008, Nature, 451, 1082

Krumholz, M. R., McKee, C. F., & Klein, R. I. 2004, ApJ, 611, 399

—. 2005a, ApJ, 618, L33

—. 2005b, Nature, 438, 332

—. 2006b, ApJ, 638, 369

Krumholz, M. R. & Tan, J. C. 2007, ApJ, 654, 304

Kurucz, R. 1999, 1999 TiO linelist from Schwenke (1998). Kurucz CD-ROM No. 24. Cambridge, Mass.: Smithsonian Astrophysical Observatory, 1999., 24

Kwon, W., Looney, L. W., Mundy, L. G., Chiang, H.-F., & Kemball, A. J. 2009, ApJ, 696, 841

Lada, C. J. 2006, ApJ, 640, L63

Lada, C. J., Muench, A. A., Rathborne, J., Alves, J. F., & Lombardi, M. 2008, ApJ, 672, 410

Landau, L. D. & Lifshitz, E. M. 1987, Course of Theoretical Physics, Vol. 6, Fluid Mechanics, 2nd edn. (Reed Educational and Professional Publishing Ltd.)

Larson, R. B. 1981, MNRAS, 194, 809

—. 2005, MNRAS, 359, 211

Levermore, C. D. & Pomraning, G. C. 1981, ApJ, 248, 321

Li, P., L., N. M., M.-M., M., & F, H. 2004, ApJ, 605, 800

Li, Y., Klessen, R. S., & Mac Low, M.-M. 2003, ApJ, 592, 975

Li, Z.-Y. & Nakamura, F. 2006, ApJ, 640, L187

Loren, R. B. 1989a, ApJ, 338, 902

—. 1989b, ApJ, 338, 925

Luhman, K. L., Joergens, V., Lada, C., Muzerolle, J., Pascucci, I., & White, R. 2007, in Protostars and Planets V, ed. B. Reipurth, D. Jewitt, & K. Keil, 443–457

Mac Low, M.-M. 1999, ApJ, 524, 169

Mac Low, M.-M. & Klessen, R. S. 2004, Reviews of Modern Physics, 76, 125

Mac Low, M.-M., Smith, M. D., Klessen, R. S., & Burkert, A. 1998, Ap&SS, 261, 195

Machida, M. N., Matsumoto, T., Hanawa, T., & Tomisaka, K. 2006, ApJ, 645, 1227

Machida, M. N., Tomisaka, K., & Matsumoto, T. 2004, MNRAS, 348, L1

Machida, M. N., Tomisaka, K., Matsumoto, T., & Inutsuka, S.-i. 2008, ApJ, 677, 327

Maddalena, R. J., Morris, M., Moscowitz, J., & Thaddeus, P. 1986, ApJ, 303, 375

Masunaga, H. & Inutsuka, S.-i. 2000, ApJ, 531, 350

Masunaga, H., Miyama, S. M., & Inutsuka, S.-I. 1998, ApJ, 495, 346

Matzner, C. D. & Levin, Y. 2005, ApJ, 628, 817

Matzner, C. D. & McKee, C. F. 2000, ApJ, 545, 364

Mazeh, T., Simon, M., Prato, L., Markus, B., & Zucker, S. 2003, ApJ, 599, 1344

McKee, C. F. 1999, in NATO ASIC Proc. 540: The Origin of Stars and Planetary Systems, ed. C. J. Lada & N. D. Kylafis, 29–+

McKee, C. F. & Ostriker, E. 2007, ARA&A, 45, 565

McKee, C. F. & Tan, J. C. 2002, Nature, 416, 59

—. 2003, ApJ, 585, 850

McLaughlin, D. E. & Pudritz, R. E. 1997, ApJ, 476, 750

Mihalas, D. & Weibel-Mihalas, B. 1999, Foundations of Radiation Hydrodynamics (Dover Publications, Inc.)

Moeckel, N. & Bally, J. 2007, ApJ, 661, L183

Motte, F., Andre, P., & Neri, R. 1998, A&A, 336, 150

Mouschovias, T. C. 1976, ApJ, 207, 141

—. 1977, ApJ, 211, 147

Muench, A. A., Lada, C. J., Rathborne, J. M., Alves, J. F., & Lombardi, M. 2007, ApJ, 671, 1820

Muzerolle, J., Hartmann, L., & Calvet, N. 1998, AJ, 116, 2965

Myers, P. C., Adams, F. C., Chen, H., & Schaff, E. 1998, ApJ, 492, 703

Myers, P. C., Fuller, G. A., Goodman, A. A., & Benson, P. J. 1991, ApJ, 376, 561

Nakamura, F. & Li, Z.-Y. 2007, ApJ, 662, 395

Nakano, T., Hasegawa, T., Morino, J., & Yamashita, T. 2000, ApJ, 534, 976

Nakano, T., Hasegawa, T., & Norman, C. 1995, Ap&SS, 224, 523

Nelson, A. F. 2006, MNRAS, 373, 1039

Neufeld, D. A., Lepp, S., & Melnick, G. J. 1995, ApJS, 100, 132

Nutter, D. & Ward-Thompson, D. 2007, MNRAS, 374, 1413

Offner, S. S. R., Klein, R. I., & McKee, C. F. 2008a, ApJ, 686, 1174

Offner, S. S. R., Klein, R. I., McKee, C. F., & Krumholz, M. R. 2009, ArXiv e-prints

Offner, S. S. R., Krumholz, M. R., Klein, R. I., & McKee, C. F. 2008b, AJ, 136, 404

Onishi, T., Mizuno, A., Kawamura, A., Tachihara, K., & Fukui, Y. 2002, ApJ, 575, 950

Ossenkopf, V. & Henning, T. 1994, A&A, 291, 943

Ostriker, E. C. & Shu, F. H. 1995, ApJ, 447, 813

Padoan, P., Goodman, A., Draine, B. T., Juvela, M., Nordlund, Å., & Rögnvaldsson, Ö. E. 2001, ApJ, 559, 1005

Padoan, P. & Nordlund, Å. 1999, ApJ, 526, 279

—. 2002, ApJ, 576, 870

—. 2004, ApJ, 617, 559

Padoan, P., Nordlund, Å., Kritsuk, A. G., Norman, M. L., & Li, P. S. 2007, ApJ, 661, 972

Palla, F. & Stahler, S. W. 1991, ApJ, 375, 288

—. 1992, ApJ, 392, 667

—. 1993, ApJ, 418, 414

Plume, R., Bensch, F., Howe, J. E., Ashby, M. L. N., Bergin, E. A., Chin, G., Erickson, N. R., Goldsmith, P. F., Harwit, M., Kleiner, S., Koch, D. G., Neufeld, D. A., Patten, B. M., Schieder, R., Snell, R. L., Stauffer, J. R., Tolls, V., Wang, Z., Winnewisser, G., Zhang, Y. F., Reynolds, K., Joyce, R., Tavoletti, C., Jack, G., Rodkey, C. J., & Melnick, G. J. 2000, ApJ, 539, L133

Pollack, J. B., Hollenbach, D., Beckwith, S., Simonelli, D. P., Roush, T., & Fong, W. 1994, ApJ, 421, 615

Pollack, J. B., McKay, C. P., & Christofferson, B. M. 1985, Icarus, 64, 471

Press, W. T., Teukolsky, S. A., Vetterling, W. T., & Flannery, B. P. 1992, Numerical Recipes 2nd Edition: The Art of Scientific Computing, 2nd edn. (Cambridge University Press)

Price, D. J. & Bate, M. R. 2007, MNRAS, 377, 77

—. 2008, MNRAS, 385, 1820

Reipurth, B. & Clarke, C. 2001, AJ, 122, 432

Robitaille, T. P., Whitney, B. A., Indebetouw, R., Wood, K., & Denzmore, P. 2006, ApJS, 167, 256

Rosolowsky, E. W., Pineda, J. E., Foster, J. B., Borkin, M. A., Kauffmann, J., Caselli, P., Myers, P. C., & Goodman, A. A. 2008, ApJS, 175, 509

Ryden, B. S. 1996, ApJ, 471, 822

Scalo, J. M. 1986, Fundamentals of Cosmic Physics, 11, 1

Schmeja, S. & Klessen, R. S. 2004, A&A, 419, 405

Schmitt, W., Henning, T., & Mucha, R. 1997, A&A, 325, 569

Schöier, F. L., van der Tak, F. F. S., van Dishoeck, E. F., & Black, J. H. 2005, AAP, 432, 369

Semenov, D., Henning, T., Helling, C., Ilgner, M., & Sedlmayr, E. 2003, A&A, 410, 611

Shestakov, A. I. & Bolstad, J. H. 2005, JQSRT, 91, 133

Shestakov, A. I. & Offner, S. S. R. 2007, JCP, 227, 2154

Shu, F., Najita, J., Ostriker, E., Wilkin, F., Ruden, S., & Lizano, S. 1994, ApJ, 429, 781

Shu, F. H. 1977, ApJ, 214, 488

Shu, F. H., Adams, F. C., & Lizano, S. 1987, ARA&A, 25, 23

Solomon, P. M., Rivolo, A. R., Barrett, J., & Yahil, A. 1987, ApJ, 319, 730

Stamatellos, D. & Whitworth, A. P. 2005, A&A, 439, 153

—. 2008, A&A, 480, 879

—. 2009, MNRAS, 392, 413

Stamatellos, D., Whitworth, A. P., Bisbas, T., & Goodwin, S. 2007, A&A, 475, 37

Stone, J. M., Ostriker, E. C., & Gammie, C. F. 1998, ApJ, 508, L99

Swift, J. J. & Welch, W. J. 2008, ApJS, 174, 202

Tafalla, M., Myers, P. C., Caselli, P., & Walmsley, C. M. 2004a, A&A, 416, 191

—. 2004b, Ap&SS, 292, 347

Tafalla, M., Myers, P. C., Caselli, P., Walmsley, C. M., & Comito, C. 2002, ApJ, 569, 815

Tan, J. C., Krumholz, M. R., & McKee, C. F. 2006, ApJ, 641, L121

Tan, J. C. & McKee, C. F. 2004, ApJ, 603, 383

Tassis, K. 2007, MNRAS, 379, 50

Testi, L. & Sargent, A. I. 1998, ApJ, 508, L91

Tilley, D. A. & Pudritz, R. E. 2004, MNRAS, 353, 769

—. 2007, MNRAS, 382, 73

Tout, C. A., Pols, O. R., Eggleton, P. P., & Han, Z. 1996, MNRAS, 281, 257

Troland, T. H. & Crutcher, R. M. 2008, ApJ, 680, 457

Truelove, J. K., Klein, R. I., McKee, C. F., Holliman, II, J. H., Howell, L. H., & Greenough, J. A. 1997, ApJ, 489, L179+

Truelove, J. K., Klein, R. I., McKee, C. F., Holliman, II, J. H., Howell, L. H., Greenough, J. A., & Woods, D. T. 1998, ApJ, 495, 821

Vázquez-Semadeni, E., González, R. F., Ballesteros-Paredes, J., Gazol, A., & Kim, J. 2008, MNRAS, 390, 769

Vázquez-Semadeni, E., Ryu, D., Passot, T., González, R. F., & Gazol, A. 2006, ApJ, 643, 245

Vorobyov, E. I. & Basu, S. 2006, ApJ, 650, 956

—. 2009, MNRAS, 393, 822

Walmsley, C. M., Flower, D. R., & Pineau des Forêts, G. 2004, A&A, 418, 1035

Walsh, A. J., Myers, P. C., & Burton, M. G. 2004, ApJ, 614, 194

Ward-Thompson, D., André, P., Crutcher, R., Johnstone, D., Onishi, T., & Wilson, C. 2007, in Protostars and Planets V, ed. B. Reipurth, D. Jewitt, & K. Keil, 33–46

Weingartner, J. C. & Draine, B. T. 2001, ApJ, 548, 296

White, R. J. & Hillenbrand, L. A. 2004, ApJ, 616, 998

Whitehouse, S. C. & Bate, M. R. 2006, MNRAS, 367, 32

Whitehouse, S. C., Bate, M. R., & Monaghan, J. J. 2005, MNRAS, 364, 1367

Whitney, B. A., Wood, K., Bjorkman, J. E., & Cohen, M. 2003, ApJ, 598, 1079

Whitworth, A. P., Chapman, S. J., Bhattal, A. S., Disney, M. J., Pongracic, H., & Turner, J. A. 1995, MNRAS, 277, 727

Whitworth, A. P. & Stamatellos, D. 2006, A&A, 458, 817

Williams, J. P. & Andrews, S. M. 2006, ApJ, 653, 1480

Williams, J. P., de Geus, E. J., & Blitz, L. 1994, ApJ, 428, 693

Williams, J. P. & McKee, C. F. 1997, ApJ, 476, 166

Wu, J., Evans, II, N. J., Gao, Y., Solomon, P. M., Shirley, Y. L., & Vanden Bout, P. A. 2005, ApJ, 635, L173

Yorke, H. W. & Sonnhalter, C. 2002, ApJ, 569, 846

Young, C. H. & Evans, II, N. J. 2005, ApJ, 627, 293

Young, K. E., Enoch, M. L., Evans, II, N. J., Glenn, J., Sargent, A., Huard, T. L., Aguirre, J., Golwala, S., Haig, D., Harvey, P., Laurent, G., Mauskopf, P., & Sayers, J. 2006, ApJ, 644, 326

Young, K. E., Lee, J.-E., Evans, II, N. J., Goldsmith, P. F., & Doty, S. D. 2004, ApJ, 614, 252